

Sheffield Hallam University

Vibrational Spectroscopy and Atomic Force Microscopy Studies of Silane Adsorption onto Silicon and Glass.

BANGA, Reena.

Available from the Sheffield Hallam University Research Archive (SHURA) at:

<http://shura.shu.ac.uk/19310/>

A Sheffield Hallam University thesis

This thesis is protected by copyright which belongs to the author.

The content must not be changed in any way or sold commercially in any format or medium without the formal permission of the author.

When referring to this work, full bibliographic details including the author, title, awarding institution and date of the thesis must be given.

Please visit <http://shura.shu.ac.uk/19310/> and <http://shura.shu.ac.uk/information.html> for further details about copyright and re-use permissions.

SHEFFIELD HALLAM UNIVERSITY LIBRARY
CITY CAMPUS POND STREET
SHEFFIELD S1 1WB

101 522 594 2 367237



Sheffield Hallam University

REFERENCE ONLY

ProQuest Number: 10694191

All rights reserved

INFORMATION TO ALL USERS

The quality of this reproduction is dependent upon the quality of the copy submitted.

In the unlikely event that the author did not send a complete manuscript and there are missing pages, these will be noted. Also, if material had to be removed, a note will indicate the deletion.



ProQuest 10694191

Published by ProQuest LLC (2017). Copyright of the Dissertation is held by the Author.

All rights reserved.

This work is protected against unauthorized copying under Title 17, United States Code
Microform Edition © ProQuest LLC.

ProQuest LLC.
789 East Eisenhower Parkway
P.O. Box 1346
Ann Arbor, MI 48106 – 1346

**Vibrational Spectroscopy and Atomic Force Microscopy
Studies of Silane Adsorption onto Silicon and Glass**

Reena Banga

A thesis submitted in part fulfilment of the requirement of
Sheffield Hallam University
for the degree of Doctor of Philosophy

September 1995

Collaborating Organisation: Pilkington plc

ACKNOWLEDGEMENTS.

My thanks go to my supervisor, Prof. Jack Yarwood, at Sheffield Hallam University for his help, advice and encouragement. Thanks also go to the staff at the Pilkington Technology Centre, particularly to my supervisors, Dr. Paul Holmes and Tony Morgan, whose help was invaluable throughout my PhD. I would also like to thank Pilkington plc and EPSRC for their financial support for both my project and foreign conference fees.

I owe a lot to my friends at Durham, who helped me through the traumas of moving university, particularly, Chris, Rorie, Leela and Penny.

For the light entertainment, which made life at Sheffield so interesting, I thank the fellas and the players, namely Nigel, Chris, Jason, Franny, Jolyon, Sohail, Bryan and Russell. Keep playing on.

For accompanying me to all those horrendous aerobics classes, in a vain attempt to keep fit, I thank Anita. Last but not least, my warm thanks go to my housemate, Linda, who gave me support throughout my final year in Sheffield.

ABSTRACT.

Vibrational Spectroscopy and Atomic Force Microscopy Studies of Silane Adsorption onto Silicon and Glass.

The adsorption of two surfactants, n-octadecyltrichlorosilane and perfluorodecyl(ethyl)trichlorosilane, onto silica surfaces, was investigated by Fourier transform infrared attenuated total reflection, (FTIR-ATR), spectroscopy and by atomic force microscopy, (AFM). The rate of formation of the monolayers and the effect of surface coverage on the packing of these long-chain molecules was studied by both methods and the results compared. The silica surface was provided by the native silicon oxide layer on the surface of the silicon ATR prism for FTIR-ATR spectroscopy and by float glass substrates for AFM.

Polarized radiation was used in the FTIR-ATR experiments to determine the relative dichroic ratios of cast and self-assembled films on silicon, and these results were compared with a theoretical model. The conclusion was that the cast silane layers were orientationally disordered, whilst the self-assembled layers showed a greater orientational order.

In situ FTIR-ATR spectroscopy was employed to study the adsorption of these long-chain silanes at a silica-deuterated toluene interface. The silica surface was provided by the native oxide layer on a silicon ATR prism. The experiment required careful calibration in order to determine the Gibbs surface excess of these silanes on this surface. The Gibbs surface excess was calculated over a variety of silane concentrations, enabling the area occupied by the silane molecules to be calculated. The rates of formation of the monolayers were also determined and compared to the results obtained from the AFM and FTIR-ATR experiments, (not *in situ*).

FTIR-ATR and Raman spectroscopy and microscopy were employed to investigate the interactions in silicon (or quartz)/silane/poly(vinylchloride) laminates. Specifically, (3-aminopropyl)trimethoxysilane and (3-mercaptopropyl)triethoxysilane were the silanes studied. Confocal Raman microscopy was used to discover whether interdiffusion of the silanes into the polymer overlayers had occurred, and also to determine the distribution of the silane molecules over the polymer surface. This was successfully achieved with the laminate containing the mercaptosilane.

CONTENTS.

CHAPTER 1	INTRODUCTION	1
	Introduction	1
1.1.	The Nature of the Surfaces of Silicon and Silica	2
1.2	Sample Preparation	5
1.2.1.	Adsorption Mechanisms of Surfactants	5
1.2.2.	Formation of Polymer Overlayers	6
1.3.	The Reactions of N-octadecyltrichlorosilane and Perfluorodecyl(ethyl)trichlorosilane with Silica and Silicon	8
1.3.1.	Infrared, Ellipsometric and X-ray Measurements	10
1.3.2.	Atomic Force Microscopy, AFM, of Long-Chain Alkyl Silanes	13
1.4.	The Reactions of (3-Aminopropyl)trimethoxy and (3-Mercaptopropyl)triethoxy Silanes with Silicon and Silica	14
1.5.	The Reactions of Silane Coupling Agents with Polymers and Epoxy Resins	20

CHAPTER 2	THEORY	25
Introduction		25
2.1.	Infrared Spectroscopy Background Theory	25
2.1.1.	Classical Theory of Light	25
2.1.2.	Quantum Theory of Light	26
2.1.3.	Sources of Infrared Radiation	26
2.1.4.	Absorption of Infrared Radiation by Molecules	27
2.1.4.1.	Quantum Mechanical Harmonic Oscillator	27
2.1.4.2.	Selection Rules for Quantum Mechanical Harmonic Oscillator	28
2.1.4.2.1.	Dipole Moment Change	28
2.1.4.2.2.	Absorption Process	28
2.1.4.2.3.	The Harmonic Oscillator Selection Rule	28
2.1.4.3.	Anharmonicity and Overtones	29
2.1.4.4.	Lineshape and Frequency Changes	30
2.2.	Fourier Transform Infrared, FTIR, Spectroscopy	33
Introduction		33
2.2.1.	Michelson Interferometer	33
2.2.2.	Advantages of Interferometry	36
2.2.2.1.	The Multiplex, (Fellgett), Advantage	36
2.2.2.2.	The Throughput, (Jacquinot), Advantage	37
2.2.2.3.	Connes Advantage	38
2.2.2.4.	Mirror Movement Averaging	38
2.2.3.	Disadvantages of Interferometry	38
2.2.4.	Instrument Parameters	39
2.2.4.1.	Resolution	39
2.2.4.2.	Mirror Travel Rate	39
2.2.4.3.	Apodisation	40
2.2.4.4.	Phase Corrections	41

2.3.	Attenuated Total Reflection, ATR, Spectroscopy	43
	Introduction	43
2.3.1.	Total Internal Reflection	43
2.3.2.	Depth of Penetration and the Effective Thickness	46
2.3.3.	Advantages of ATR	54
2.3.4.	Disadvantages of ATR	54
2.3.5.	Linear Dichroism Theory	54
2.3.6.	Surface Excess Concentrations in Inhomogeneous Systems	60
2.3.7.	Calibration of the Internal Reflection Element	63
2.4.	Raman Spectroscopy	66
	Introduction	66
2.4.1.	Classical Theory	67
2.4.2.	Quantum Theory	68
2.4.3.	Polarisability	69
2.4.4.	Intensities	69
2.4.5.	Raman Instrumentation	69
2.4.5.1.	The Renishaw Raman Imaging Microscope	70
2.5.	Atomic Force Microscopy	76
	Introduction	76
2.5.1.	Atomic Force Microscopy Theory	76
2.5.2.	Components of the Atomic Force Microscope	77
2.5.3.	Atomic Resolution	79
2.5.4.	Roughness Average	80
2.5.5.	Advantages and Disadvantages of Atomic Force Microscopy	81

CHAPTER 3	ATTENUATED TOTAL REFLECTION	83
	SPECTROSCOPY OF THE <i>EX SITU</i> ADSORPTION	
	OF LONG-CHAIN SILANES ONTO SILICON	
Introduction		83
3.1.	Experimental	83
3.1.1.	Chemicals	83
3.1.2.	Substrates	83
3.1.3.	Preparation of Solutions	84
3.1.4.	Preparation of Samples	85
3.1.5.	Spectroscopic Measurements	86
3.1.6.	Linear Dichroic Ratio Calculations	87
3.2.	Results and Discussion	88
3.2.1.	N-octadecyltrichlorosilane	88
3.2.1.1.	Cast Films of OTS on Silicon	88
3.2.1.2.	Self-Assembled Films of OTS on Silicon	90
3.2.2.	Perfluorodecyl(ethyl)trichlorosilane	107
3.2.2.1.	Cast Films of F8 on Silicon	107
3.2.2.2.	Self-Assembled Films of F8 on Silicon	109
3.3.	Conclusions	118
3.3.1.	N-octadecyltrichlorosilane	118
3.3.2.	Perfluorodecyl(ethyl)trichlorosilane	119

CHAPTER 4	ATTENUATED TOTAL REFLECTION	121
	SPECTROSCOPY OF THE <i>IN SITU</i> ADSORPTION	
	OF LONG-CHAIN SILANES ONTO SILICON	
Introduction		121
4.1.	Experimental	121
4.1.1.	Chemicals	121
4.1.2.	Substrates	121
4.1.3.	Calibration of the Silicon ATR Prisms	122
4.1.4.	Preparation of Solutions	124
4.1.5.	Preparation of Samples	124
4.1.6.	Spectroscopic Measurements	126
4.1.7.	Determination of the Gibbs Surface Excess and the Separation of Bulk and Surface Components in the System	127
4.2.	Results and Discussion	128
4.2.1.	Calibration of Silicon ATR Prisms	128
4.2.2.	N-octadecyltrichlorosilane	130
4.2.2.1.	Molar Absorption Coefficient	130
4.2.2.2.	Self-Assembled Films of OTS on Silicon	131
4.2.3.	Perfluorodecyl(ethyl)trichlorosilane	152
4.2.3.1.	Molar Absorption Coefficient	152
4.2.3.2.	Self-Assembled Films of F8 on Silicon	153
4.3.	Conclusions	174

CHAPTER 5 ATOMIC FORCE MICROSCOPY OF THE *EX SITU* 177

**ADSORPTION OF LONG-CHAIN SILANES ONTO
SILICON**

Introduction	177
5.1. Experimental	177
5.1.1. Chemicals	177
5.1.2. Substrates	177
5.1.3. Preparation of Solutions	178
5.1.4. Preparation of Samples	178
5.1.5. Atomic Force Microscopy Measurements	179
5.2. Results and Discussion	181
5.2.1. Pilkington Float Glass	181
5.2.2. N-octadecyltrichlorosilane	181
5.2.3. Perfluorodecyl(ethyl)trichlorosilane	206
5.3. Conclusions	229
5.3.1. Float Glass	229
5.3.2. N-octadecyltrichlorosilane	230
5.3.3. Perfluorodecyl(ethyl)trichlorosilane	231

CHAPTER 6	VIBRATIONAL SPECTROSCOPY AND	233
	MICROSCOPY OF THE CHEMICAL	
	INTERACTIONS IN POLYMER/SILANE/SiO₂	
	LAMINATES	
Introduction		233
6.1.	Experimental	233
6.1.1.	Chemicals	233
6.1.2.	Substrates	233
6.1.3.	Preparation of Solutions	234
6.1.4.	Preparation of Silane Films	234
6.1.5.	Preparation of Polymer Films	235
6.1.6.	Spectroscopic Measurements	235
6.2.	Results and Discussion	236
6.2.1.	Raman Spectroscopy Results	236
6.2.2.	Infrared Spectroscopy Results	260
6.3.	Conclusions	274

CHAPTER 7	DISCUSSION AND CONCLUSIONS	277
	Introduction	277
7.1.	Adsorption of Long-Chain Silanes onto Silicon and Glass	278
7.1.1.	Comparison of <i>ex situ</i> FTIR-ATR Spectroscopy and Atomic Force Microscopy Results	279
7.1.2.	Comparison of <i>ex situ</i> and <i>in situ</i> FTIR-ATR Spectroscopy Results	282
7.1.3.	Comparison of <i>in situ</i> FTIR-ATR Spectroscopy Data with XRD and AFM Results, (previous researchers' work).	283
7.2.	Physical and Chemical Interactions in SiO ₂ / Short-Chain Silane/ Polymer Laminates	286
7.3.	Conclusions	288
7.4.	Future Work	290
	REFERENCES	292
	CONFERENCES ATTENDED	301
	PAPERS PUBLISHED	303

CHAPTER.1. INTRODUCTION.

Introduction.

The work discussed in this thesis has been carried out in conjunction with Pilkington plc, who coordinated and partly sponsored the research. Pilkington plc have a commercial interest in various coatings for hydrophilic glass substrates. These include hydrophobic, oleophobic coatings and coatings which provide a means of laminating glass sheets together. The former are mainly used in the car and aircraft industries, as 'rain-shedding' coatings for windscreens and the latter are used for front 'safety' windscreens in the motor vehicle industry.

The main aim of this introduction is to outline the objectives and detail the background theory of relevance to the research reported in this thesis. The coatings in question are all based on various derivations of alkyl-chain silane surfactants. The hydrophobic, oleophobic coatings are formed from long-chain alkyl or perfluoro-alkyl trisubstituted silanes. A large amount of research has been conducted on the adsorption of these surfactants onto silica or silicon, using infrared spectroscopy, [1-15], particularly for n-octadecyltrichlorosilane, OTS. However, fewer results have been obtained for the adsorption of perfluoro-alkyl silanes onto silica or silicon.

In order to produce a glass coating which will facilitate the lamination of two glass sheets, two stages need to be considered. Firstly, a 'thick', (200 nm), short amino- or mercapto- substituted alkyl silane layer has to be deposited over one side of each glass sheet. Secondly, a polymer, which may or may not interact chemically with the silane, has to be laminated at high temperature and pressure, in an autoclave, between the two pieces of coated glass. The silanes used for this process are termed coupling agents, since they provide a means of joining two separate oxide layers together. The resulting laminate is termed an encapsulation. A large amount of research has been performed on the adsorption of these coupling agents onto glass and silicon by vibrational spectroscopic techniques.

However, there are few published results on the lamination process described above.

The main aims and objectives of this project are to determine the following:

- (i) The dipping time for formation of monolayers of the hydrophobic coatings, produced by the self-assembly of various long-chain alkyl and perfluoro-alkyl silanes onto silicon and glass substrates.
- (ii) The degree of orientational ordering of the above-mentioned silanes as a function of surface coverage of the substrate.
- (iii) The distribution of these silane molecules at submonolayer, monolayer and 'above' monolayer coverages.

These systems have been monitored both *in situ* and *ex situ* by Fourier Transform infrared, FTIR-ATR, spectroscopy and *ex situ* by atomic force microscopy, AFM. *In situ* experiments involve obtaining data whilst the substrate is in the silane solution. *Ex situ* experiments involve obtaining data after the substrate has been removed from the silane solution.

- (iv) The diffusion behaviour of short-chain aminopropyl or mercaptopropyl substituted silanes, deposited onto silicon and glass substrates, into a polymer overlayer.
 - (v) The distribution of the short-chain silane over the polymer overlayer.
- (iv) and (v) have been investigated by FTIR-ATR and Raman spectroscopy.

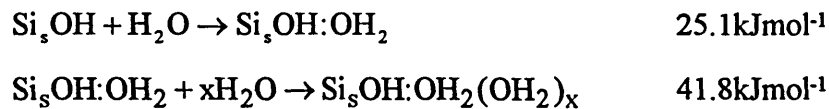
The following subsections will summarise the literature results obtained so far, which are relevant to the studies in this thesis. The detailed spectroscopy and microscopy theory will be given in chapter 2.

1.1. The Nature of the Surfaces of Silicon and Silica.

An excellent study of the properties of various silica surfaces can be found in Iler's book on the subject, [16]. Silicon oxide is a very widely used compound in,

for example, heterogeneous catalysis, microelectronics, optical fibres and chromatography, [16]. There are many types of silica including glass, quartz and colloidal silicas, whose properties vary according to their method of preparation. The glass used in these studies is Pilkington float glass, which has been manufactured by floatation on hot tin. Therefore one side of this glass has a higher proportion of tin incorporated into its structure than glasses prepared by other methods. Silica has a tendency to trap sodium atoms into its structure, [17]. The sodium produces a negatively charged oxide surface, which can be etched by aqueous hydrofluoric acid, but returns to the surface from the bulk silica within a few weeks, at room temperature.

The silica surface is known to have silanol groups on it, of which there are many different types, [1]. On a fully hydroxylated silica surface, physisorbed water will cover the silanol groups. Water will physisorb more strongly onto hydrogen-bonded silanol groups than onto isolated silanol groups, and the energies for these reactions are as follows:



Si_s = surface silicon. The water forms clusters of 5 or 6 molecules which are as stable as bulk water.

Various studies have been carried out to determine the number of silanol groups on the surface of different silicas, [18-27]. At room temperature there are approximately 5 silanol groups per nm^2 , covered with adsorbed water, [18]. Armistead et al, [27], determined the infrared adsorption bands corresponding to different types of OH or water groups on pyrogenic silica. These are reported in table.1.1.

The silicon surface is generally doped either p or n and naturally has an ambient coverage of silicon oxide, [28-29]. Chemically it resembles boron and

germanium and has a tendency to react with oxygen as opposed to other elements. Unoxidised silicon is uncommon, even in nature. Pure silicon is hydrophobic, however oxidised silicon is hydrophilic, [28]. Silicon oxide can also be deposited onto silicon by CVD, [30-31], and plasma deposition or grown on the silicon by thermal oxidation, [32-33].

A mixture of nitric, acetic and hydrofluoric acids will dissolve pure silicon. Hot concentrated solutions of alkalis will also dissolve silicon with the evolution of hydrogen, [34]. In the microelectronics industry, silicon is generally cleaned using a cleaning method called the RCA clean, [35]. This consists of a rigorous treatment in two hot solutions, the first alkaline, the second acidic. In the infrared, silicon absorbs light at approximately 1150 cm^{-1} . Therefore all Si-O-Si and Si-Cl bands are obscured. Silica will absorb light at approximately 1400 cm^{-1} in the infrared.

Table.1.1. Infrared Absorption Band Positions for OH and Water Adsorbed onto Silica.

Silanol Group /Water	Absorption frequency / cm^{-1}
Isolated, single OH on surface	3750
Isolated, paired OH groups on surface which are mutually hydrogen-bonded, (vicinal)	3650-3660
Internal OH groups, hydrogen-bonded	3650
Molecular water	3400, 1627
Adjacent pairs of silanol groups with hydrogens bonded to each other	3540-3550
Water molecule on above	3400-3500

Both silica and silicon surfaces are hydrophilic and possess surface silanol groups, covered with adsorbed water. For this reason, they readily react with surfactants with a polar head group, such as OTS, $\text{CH}_3(\text{CH}_2)_{17}\text{SiCl}_3$, F8, $\text{CF}_3(\text{CF}_2)_7(\text{CH}_2)_2\text{SiCl}_3$, A1891, $\text{SH}(\text{CH}_2)_2\text{Si}(\text{OEt})_3$ or A1100, $\text{NH}_2(\text{CH}_2)_2\text{Si}(\text{OMe})_3$. The non-polar end groups provide the coated substrate with varying properties, which will be described in the following sections of this chapter.

1.2. Sample Preparation Techniques.

1.2.1. Adsorption Mechanisms of Surfactants.

The formation of a monolayer of a surfactant, from solution, onto a substrate, can be obtained in several ways. These include deposition from a Langmuir trough, casting or self-assembly. The Langmuir-Blodgett technique involves floating a monolayer of the required surfactant on a tank of water. A well-ordered monolayer can be formed by simply moving the substrate through the surfactant/water interface once. This cannot work of course if the surfactant will not float over the liquid in the tank or if it reacts in any way with the liquid in the tank or if it dissolves or polymerises.

The casting technique involves depositing a quantity of surfactant, in solution, onto a substrate and allowing the solvent to evaporate slowly. This method can be used to produce monolayers or much thicker layers, relatively easily. However the drawback of this technique is that it inherently produces layers with a disordered structure.

The self-assembly method involves dipping the substrate into the surfactant solution and allowing the surfactant to self-assemble onto the surface, (see figure.1.1). Using this technique, well-ordered monolayers of long-chain alkyl silanes have been produced, [1-13, 36-44].

For the long-chain alkyl and perfluoro-alkyl silanes, considered here, the Langmuir-Blodgett technique is not appropriate, since these particular silanes

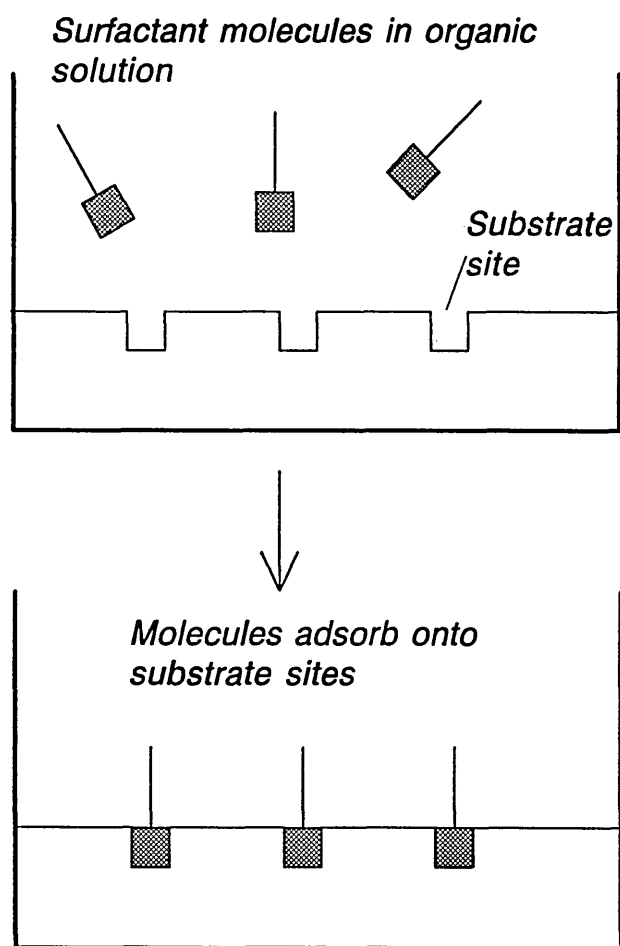
polymerise when in contact with water, which renders them of little use for producing monolayers on the silica substrates. The casting method is clearly of no use since a disordered layer will inevitably be produced by this technique. Therefore, for the formation of mono - and submonolayers of long-chain alkyl and perfluoro-alkyl silanes onto silica substrates, the self-assembly method is preferred.

For production of the 'thicker' layers of amino- or mercapto- substituted silanes onto silica substrates, where degree of order is not an important issue, the casting technique is perfectly acceptable.

1.2.2. Formation of Polymer Overlayers.

There are several methods of depositing a polymer onto a substrate. These include spin-coating, casting and dipping. The dipping method involves the use of a dip motor, whose speed is controllable. This tends to form uneven wedge-like layers. The casting method will form a more even layer, provided that the polymer is dried slowly, to prevent irregularities in the film. The best method of formation of an even polymer film is the spin-coating technique. This forms an evenly distributed thin film, relatively quickly.

Figure.1.1. Self-Assembly Technique.



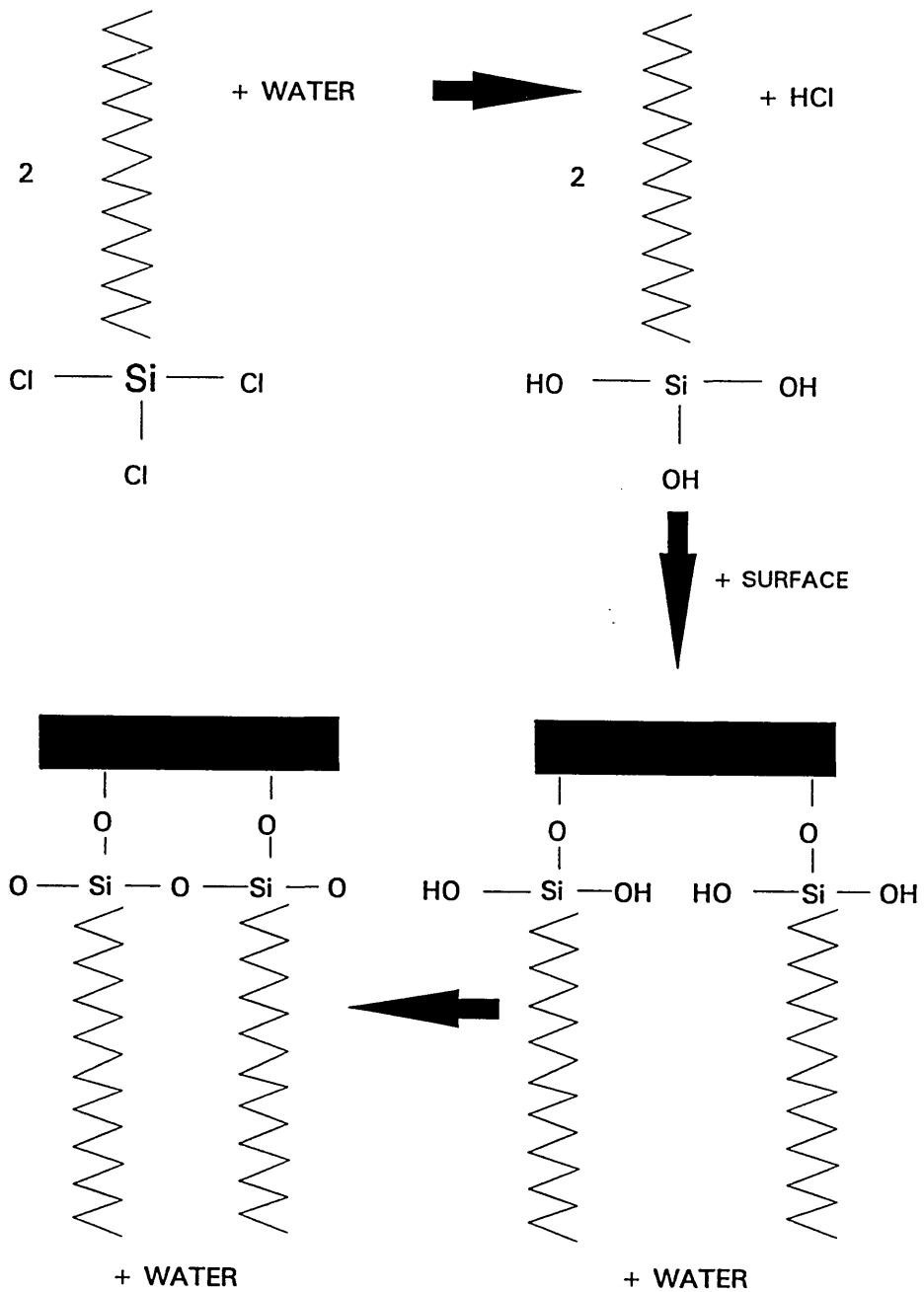
1.3. The Reactions of n-Octadecyltrichlorosilane and Perfluorodecyl(ethyl)trichlorosilane with Silicon and Silica.

Adsorption of amphiphilic molecules onto a polar substrate leads to the formation of hydrophobic, oleophobic, closely packed, monomolecular films. Many silanes exhibit amphiphilic properties including n-octadecyltrichlorosilane, OTS, [1-13, 36-44], and perfluorodecyl(ethyl)trichlorosilane, F8, [14-15, 46-49]. These surfactant coatings, primarily used in the car and aircraft windscreen industries, are constantly being developed. A summary of the major literature results so far is given here.

OTS has been used for a variety of other purposes, including use in HPLC to reduce the polarity of the stationary silica phase, and in anion chromatography, [50]. F8 is a stronger agent than OTS for producing hydrophobic coatings, since the CF_3 end group is a better hydrophobe than the OTS end group, CH_3 . This is shown from the contact angle data obtained for monolayers of the two silanes on silica substrates. OTS exhibits a water contact angle of $114 \pm 3^\circ$, [1], while F8 has a higher water contact angle value of $119.4 \pm 0.7^\circ$, [15].

The reaction of OTS with the silanol groups of a silicon or silica surface can be seen in figure.1.2. The SiCl groups on the silane are first hydrolysed. They then condense with the SiOH groups on the silica surface and then cross-link with silanol groups of adjacent silane molecules. This self-assembly reaction has been investigated by many researchers, [1, 7, 9, 36-37], who have found that the presence of water on the surface of the substrate was necessary for the success of the reaction. Some authors believe that OTS reacts with the adsorbed water and not the surface silanol groups, and that if the amount of water in the silane solution is decreased, the rate of adsorption of the OTS onto the silicon is also decreased, [37].

Figure.1.2. Reaction of Long-Chain Silane with Silica.



Tripp and Hair, [14], have compared the reaction of $\text{CF}_3(\text{CH}_2)_2\text{SiCl}_3$ and $\text{CH}_3(\text{CH}_2)_2\text{SiCl}_3$ with silica at room temperature, using DRIFT spectroscopy, and discovered that the non-fluorinated compound would not react with the silica while the fluorinated silane would. They attributed this to the electron withdrawing effect of the CF_3 groups, which made the hydrolysis of the SiCl groups on the fluorinated silane possible, (an $\text{S}_{\text{N}}2$ reaction with OH^- as the nucleophile). In the non-fluorinated silane, an opposite induction effect prevented the hydrolysis of the SiCl groups from occurring. This would indicate that a fluorinated silane is more likely to react or will react faster than the corresponding non-fluorinated silane, under similar conditions. Tillman et al, [5], investigated the effect of chain length on the reaction of various long-chain alkyl silanes with silicon. They discovered that longer dipping times and more immersions, of the silicon substrate in the solutions of TTS and UTS were required to form monolayers, than in the OTS solution. TTS and UTS are shorter alkyl-chain silanes than OTS. TTS is an abbreviation for tridecyltrichlorosilane, $\text{CH}_3(\text{CH}_2)_{12}\text{SiCl}_3$ and UTS is an abbreviation for undecyltrichlorosilane, $\text{CH}_3(\text{CH}_2)_{10}\text{SiCl}_3$. Therefore they discovered that the rate of adsorption of long-chain alkyl silanes onto silicon was increased by increasing the chain length.

1.3.1. Infrared, Ellipsometric and X-Ray Measurements.

Monolayers of n-octadecyltrichlorosilane on silica and silicon have been characterised by Fourier transform infrared attenuated total reflection spectroscopy, [1-5, 8, 10, 12-13], by reflection infrared spectroscopy, [7, 9, 11] and by ellipsometry, contact angle and X-ray measurements, [12-13, 39, 42, 44, 47, 51-53]. One of the most important objectives of this research is to determine the degree of orientational order of OTS and F8 on silicon and glass. Maoz and Sagiv conducted an intensive study into the formation of OTS monolayers on a variety of substrates, including silicon, [4]. They calculated the perfect and

random orientational linear dichroic ratios, A_{TE}/A_{TM} , for a monolayer of OTS on silicon from Harrick's equations for a thin film, as follows: Random = 0.897, perfect = 1.094, (see chapter 2 for details). They discovered that the tilt angle of molecules in a monolayer to the surface normal could not be calculated accurately. This is because the accuracy required in the experimental data to do this, could not be obtained. For the same reason they could not calculate the dichroic ratio values for submonolayers of OTS. The dichroic ratio values they did obtain, from experimental data, did not match their calculated values because they did not take account of the silicon oxide interlayer in the calculation. Gun and Sagiv, [2], later reported that OTS monolayers formed in stages by self-assembly, were ordered but not as well ordered as those prepared in one step. They also recommended rinsing the OTS films, on removal from the silane solution, with a highly volatile solvent, such as chloroform, to prevent solvent retention in the films.

The dipping time for formation of an OTS monolayer depends on its method of formation. Kallury and Thompson, [38], found that it took 80 to 90 minutes to form an OTS monolayer film, from a 1mM toluene solution of the silane, on silicon. The reaction was followed by ellipsometry, and the monolayer thickness was found to be 2.5 ± 0.1 nm. Tillman, [5], studied the adsorption of OTS onto silicon wafers, silicon ATR prisms and aluminium surfaces using ellipsometry, contact angle and FTIR grazing incidence techniques. The best water contact angle they obtained, (on silicon), was 111° and the OTS thickness was measured as 2.5 ± 0.2 nm. The FTIR measurements showed that the positions of the ν (CH_2) stretching bands moved to lower wavenumber as the film coverage increased from a partial layer to a monolayer. They attributed this shift to the decreasing fluidity and increasing order of the alkyl chains as the coverage increased from partial monolayer to monolayer. Another important issue is how the monolayer formation occurs. Some authors, [39, 47, 53], believe that at submonolayer coverage there is a liquid-like randomly distributed structure.

Sagiv, however, believes that the orientational and conformational order in the submonolayer is not much different from that of the monolayer and that the initial adsorbed molecules act as nucleation sites for further deposition, [41]. Whitesides et al, [39], determined, from X-ray measurements, that the area per molecule of OTS on silicon was $21 \pm 3 \text{ \AA}^2$. Allara et al, [51], discovered that OTS monolayers formed on silicon below 28°C , exhibited a structure with closely packed islands of densely packed nearly all-trans alkyl chains arranged almost perpendicular to the surface.

As previously stated, the monolayers produced by perfluorinated silanes, such as F8, are more hydrophobic than those prepared from non-fluorinated silanes, such as OTS. There are numerous patents on the uses of the perfluorinated silanes. Some infrared measurements have been conducted on the adsorption of perfluorinated alkyltrichlorosilanes, onto silica or silicon, [14-15]. Ellipsometric and X-ray systems have also been employed to study these silanes, [45, 47]. From surface-free energy calculations, [46], a monolayer of F8 was found to form after 5 minutes immersion time of a glass substrate in a 0.17% silane solution in freon 113. Tada and Nagayama, [15], used FTIR-ATR and XPS to show that F8 forms monolayers on porous glass, exposing the CF_3 group to the atmosphere. The infrared absorption bands that are usually identified for characterisation of OTS are the $\nu(\text{CH}_2)$ stretching bands. These occur in the infrared spectrum at approximately 2920 and 2850 cm^{-1} , for the ν_{as} and ν_{s} bands, respectively. These will shift depending upon the degree of conformational order of the OTS alkyl chains. More gauche, 'liquid-like', molecules will exhibit higher $\nu(\text{CH}_2)$ band positions than more trans, 'solid-like', molecules, [54-56]. The important infrared bands in the F8 spectrum are those at approximately 1213 and 1204 cm^{-1} . These are due to the antisymmetric CF_2 stretching and rocking modes. There are also bands due to the $\nu_{\text{s}}(\text{CH}_2)$ stretches in the F8 molecule but these are very weak in comparison to the $\nu_{\text{s}}(\text{CF}_2)$ bands. Any bands at

approximately 1150 cm^{-1} are obscured by the absorptions due to the silicon substrate.

1.3.2. Atomic Force Microscopy, AFM, of Long-Chain Alkyl Silanes.

As will be explained later, (in chapter 2), AFM is an ideal technique for analysing the topography of organic monolayers on semi-conductor or insulating surfaces. This section will deal with some of the important AFM results that have been reported in the literature recently.

AFM has been utilised to characterise the adsorption of long-chain alkyl and perfluoro-alkyl silane molecules on a variety of substrates, including silicon and silica, [57-62] and mica, [63-66]. Molecularly and atomically resolved AFM images of various other surfactants have also been obtained, [67-77], and the interest in this area is ongoing.

Fuji et al, [57], have silanized silicon with OTS and with F8 and determined the areas per molecule from AFM images. The OTS was found to occupy $0.43 \pm 0.07 \text{ nm}^2$ and the F8 was found to occupy $0.5 \pm 0.08 \text{ nm}^2$. Therefore the fluorocarbon chain occupies an area 15% larger than the hydrocarbon chain.

Yoon et al, [58-59], looked at the adsorption of OTS submono- and mono-layers on silica surfaces. They found that at submonolayer coverage, the OTS adsorbs in patches, whose size did not significantly increase with increasing coverage. They believed this meant that there was an increase in the number of patches with increased coverage and that the patches at low coverage did not act as nucleation sites for further growth. Wasserman et al, have used X-ray reflection studies to determine the distribution of OTS on aluminium substrates, [39,47,53], and their results agree with this theory. (Sagiv, however, using infrared spectroscopy, [41], does not agree with this theory).

Grunze et al, [60], produced monolayers of OTS on silicon and characterised them using AFM and XPS. They found that irreproducible results were obtained unless the samples were prepared under class 100 clean room conditions. They

attributed this to the fact that dust particles may get trapped under the samples prepared outside the clean room. It can be seen from these results that samples destined for AFM analysis, require careful preparation.

Marchant et al, [61], have shown that OTS forms smooth monolayers on a glass coverslip, with a roughness greater than the usual mica substrate. They believe this is achieved by the entropy-driven alignment reaction of the OTS molecules, through the formation of intermolecular siloxane linkages, Si-O-Si. This means that not all the OTS molecules need to be bonded to the glass substrate beneath. The root mean square, (RMS), roughness value obtained for a monolayer of OTS on a glass coverslip was 0.18 ± 0.02 nm.

Grunze et al, [62], reported that the surface preparation used by Fujii et al, [57], may have reduced the silanol group density on the silicon surface and therefore may have produced an area per molecule for OTS, greater than that reported by Whitesides et al, [39].

1.4. The Reactions of (3-Aminopropyl)-trimethoxy and (3-Mercaptopropyl)-triethoxy silanes with Silica and Silicon.

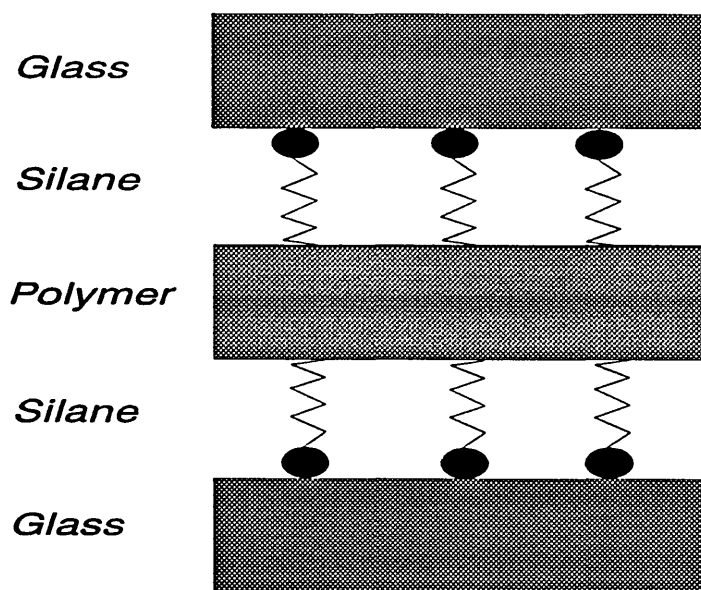
(3-Aminopropyl)trimethoxy and (3-mercaptopropyl)triethoxy silanes, (A1100 and A1891, respectively), are well known coupling agents, which adsorb onto oxidised substrates in a variety of ways, depending upon conditions. Silane coupling agents are so called because they provide a method of bonding a polymer or resin to an oxidised substrate or a method of cross-linking polymer chains, via chemical interactions between the end groups of the silane and the polymer backbone. This produces a much stronger structure than if the silane was omitted. For example the shear strength and the lifetime of fibre-glass reinforced plastics has been improved by cross-linking them with silane coupling agents, [78].

In a laminate, (see figure 1.3), used as 'safety' glass in a car windscreen, the silane used depends upon the degree of adhesion required. The silanes mentioned

above would provide high adhesion. Other silanes which will give strong adhesion are A189, the trimethoxy version of A1891 and A1110, the triethoxy version of A1100. For optimum conditions a mixture of silanes with intermediate adhesion would be ideal.

There are many factors which affect the reactions of silane coupling agents with oxidised substrates, including the availability of water, the pH of the silane solution, the curing conditions, the concentration of the silane solution and the age of the silane solution, [79]. Therefore it is very important to control the conditions.

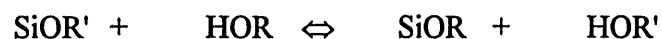
Figure.1.3. 'Safety'-Glass Laminate.



The base-catalysed or acid-catalysed reactions of organoalkoxysilanes have been described previously, [79], as follows:

Base-catalysed: For example, for a silane in solution in a water/ammonia/ethanol mixture at room temperature, two reactions are seen to occur in solution:

(1) HYDROLYSIS



(2) CONDENSATION



R = H, R' = Et

In the hydrolysis reaction, (1), base-catalysis proceeds through a bimolecular nucleophilic attack on the silicon atom which leads to a negatively charged pentacoordinated transition state, (S_N2 reaction). The nucleophile attacking the silicon in the hydrolysis reaction is OH^- . If the concentration of OH^- increases, the rate of the reaction increases. The steric and inductive effects of the silicon substituents also affect the reaction rate. Hydrolysis and condensation decrease the electron density on the silicon atom as follows: In hydrolysis, the more electron withdrawing group, OH^- , replaces EtO^- . This decrease in electron density of the silicon atom stabilises the negatively charged transition state and leads to an increase in hydrolysis rate for each subsequent hydrolysis step. Steric hindering effects of the ethoxy or methoxy groups increase this trend. If the ethoxy or methoxy groups on the silicon atom are replaced by alkyl groups, the opposite inductive effect is produced i.e. the electron density of the silicon increases.

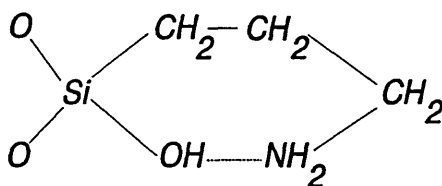
In condensation the reaction occurs through a base-catalysed nucleophilic attack on the silicon atom, (OR replaced by OSi), which gives a pentacoordinated transition state with negative charge. This resembles the mechanism for the hydrolysis reaction. Therefore steric hindrance and

concentration effect the rate of condensation in the same way that they effect the rate of hydrolysis.

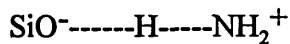
The acidity of the silanol groups is important in the formation of highly condensed siloxane structures. In the condensation reaction the nucleophile is a deprotonated silanol group, SiO^- . The acidity of a silanol group belonging to a more condensed silicon atom increases rapidly with degree of condensation. This is due to the electron withdrawing effects of the siloxane bonds in the condensed species. Just as in hydrolysis, the electron donating character of an alkyl group reduces the condensation rate of organoalkoxysilanes relative to tetraalkoxysilanes by destabilising the transition state. The decreased acidity of the silanol group thus decreases the nucleophile concentration. Therefore, for these reasons acid -catalysed reactions are preferred for organoalkoxysilanes. Acid-catalysis reverses all induction effects.

A1100 and A1110 have properties which make their behaviour exceptional, as follows: In aqueous solution aminopropyltrialkoxysilanes hydrolyse very rapidly and the infrared band due to NH_2 deformation shifts from 1600 to 1575 cm^{-1} . On drying, the NH_2 absorption shifts back to 1600 cm^{-1} . The band at 1575 cm^{-1} corresponds to hydrogen bonded NH_2 and the band at 1600 cm^{-1} corresponds to free NH_2 . Hydrolysed A1110 or A1100 can exist as an extended non-ring structure and as a cyclic hydrogen bonded amine structure, (see figure.1.4.). The ring structure explains the stability in water.

Figure.1.4. Hydrogen-bonded Aminosilane in Water at pH 10.6.



It is believed that partial proton transfer has occurred in this ring:



The pH of A1110 in water is 10.6. Decreasing the pH causes this ring structure to break up, [80].

Monolayers of aminopropylsilanes can be produced on oxidised substrates by immersing the substrate in a very dilute solution of the silane in a dry organic solvent or even in water, followed by incubating in water for 24 hours and / or curing in an oven at 200°C for 24 hours. Vandenberg et al, [81], have produced monolayers on silicon oxide substrates and studied them using FTIR and XPS as follows: The silicon substrates were cleaned using an RCA clean, [82]. The aminosilane, A1110, was redistilled before use and 0.4% solutions were made in toluene. Thick films, (30 nm), were made by submerging the silicon in the silane solution for 24 hours. Thin films, (0.3 to 1 nm), were prepared by submerging the silicon in the silane solution for 1 hour. The films were cured in a variety of ways and the effect of using different solvents was also investigated. They discovered that the first layer of silane covalently bonds to the surface. Then partially polymerised material deposits over this. The partially polymerised silane could easily be washed away by water. They also produced thick layers of aminosilanes on oxidised substrates by using concentrated solutions, (20% w/w), of the silane in polar liquids, [83-85]. These layers were composed of three sections: The silane/substrate layer, a high molecular weight polysiloxane, the middle section, a oligomeric siloxane and the air/silane section, a high molecular weight polysiloxane. On exposure to 95% humidity for long periods of time, the oligomeric layer was found to polymerise and form siloxane polymers.

The effect of carbon dioxide in the atmosphere on the reaction of A1110 in solution in deionised water, 2% w/w, with glass surfaces has been studied by Koenig et al, [85], using FTIR spectroscopy. They discovered that when the silane molecule bonds to the glass through the silicon end of the molecule, the carbon dioxide in the atmosphere will react with the non-bonded amine end of

the molecule to produce an amine bicarbonate salt, $\text{HCO}_3^- \text{NH}_3^+\text{R}$. The infrared bands due to this species are at 1630, 1575, 1488 and 1332 cm^{-1} . These correspond to the HCO_3^- mode of the bicarbonate salt, the antisymmetric and symmetric deformations of NH_3^+ and to the CH_2 bending mode respectively. The amine bicarbonate salt formation occurs mainly in the drying process. Very little reaction with carbon dioxide occurs in the bulk silane solution. The bicarbonate salt is unstable to heat treatment. Heating for 2 minutes at 100°C will remove the bicarbonate formed in the drying stage. At low pH, the amine group of the silane reacts with the added acid forming the amine salt, NH_3^+Cl^- . The SiO^- concentration of the surface of the silicon decreases and the silicon surface silanol concentration increases. Therefore the tendency of the NH_3^+Cl^- to react with SiO^- surface species is reduced. At the pH of A1110 in water, (pH = 10.6), the SiO^- concentration is higher which attracts the positively charged amine group. At this pH the amine bicarbonate salt is seen and the amine group is hydrogen bonded to the silicon surface. At high pH, greater than pH 11, some of the aminosilane silanol groups may be in the form of SiO^- which will repel the surface SiO^- groups. The amine is mainly in the form of NH_2 , ie. no salt is formed.

In general, when using a coupling agent to bond polymers and resins to glass or metal surfaces, the acid-catalysed reaction of amino and mercapto silanes are preferable for many reasons. No bicarbonate salt is formed, (if HCl is the acid), with carbon dioxide in the atmosphere. The silicon end of the silane molecule bonds to the surface as oppose to the amine end, leaving the amine end free to bond with another species. Condensation of the silanes is reduced.

Koenig et al, [86], have obtained Raman spectra of A1110 and of A189 before and after deposition onto glass substrates from 2% volume solutions at a pH of 3.5 to 4.0. The strongest bands in the spectrum of the aminosilane deposited onto the glass were due to the NH_2 stretching and CH_2 bending modes. In the spectrum of the mercaptosilane on glass, the dominant features were the band at

2564 cm^{-1} , due to the SH stretching mode and the bands at 650 and 690 cm^{-1} due to the SC stretching modes, (See table.1.2). The bands mentioned above were easily identified before and after hydrolysatation and adsorption onto the glass. The Raman and Infrared spectra of A1110 and A189 have been studied extensively, [80-81, 83-84, 86-122]. Some important Raman and Infrared frequencies can be found in Table.1.2

Table.1.2. Raman and Infrared Frequencies of A1100 and of A1891.

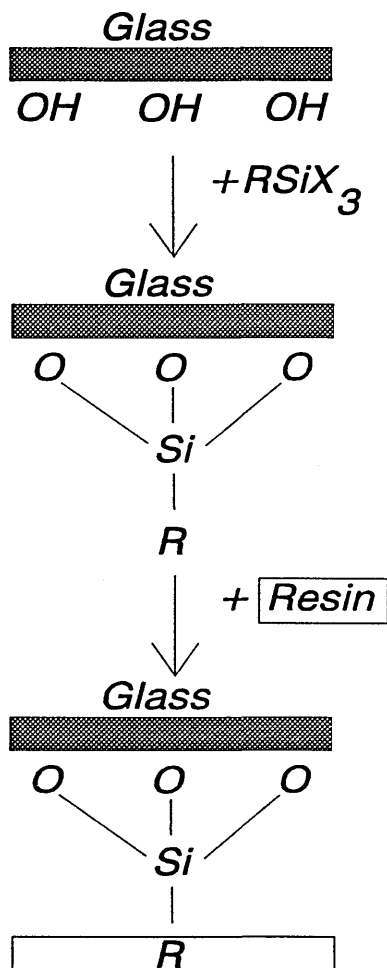
Silane	Band	Raman Frequency/ cm^{-1}	Infrared Frequency/ cm^{-1}
A1100	$\nu(\text{NH})$	3367, 3300	3370, 3295
A1100	$\delta(\text{NH}_2)$	1610, 1584	1600
A1100	$\nu(\text{CN})$	1409, 1414	
A1100	$\delta(\text{CH}_2)$	1455	1483
A1891	$\nu(\text{HS})$	2564	2550
A1891	$\rho(\text{CH}_2)$	903, 943	
A1891	$\nu(\text{SC})$	690, 650	620-715

1.5. The Reactions of Silane Coupling Agents with Polymers and Epoxy Resins.

Going back to the diagram in figure.1.3, it can be seen that a polymer is necessary to complete the laminate. In this case, the polymer used is PVC, which industrially will contain up to 30% additives, including heat stabilisers, lubricants, fillers and plasticisers. If too high a concentration of stabiliser is used, (greater than 1%), or if the laminate is left too long before autoclaving, then the stabiliser will diffuse to the surface. Also if the laminate is placed in a humidity cabinet, the edges of the PVC tend to peel away from the glass. This may be due to the layers of silane being washed away.

The reactions of coupling agents such as A1110 and A189 with epoxy resins and cross-linkage with polymers such as PVC have been well studied, [119,123-128]. Pluddemann et al, [123], first produced glass/silane/polyester laminates in the sixties. They stated that almost all functional groups are capable of reacting with an epoxy resin or its curing agent in an epoxy laminate. For example condensation reactions may occur between mercapto or amino groups on silicon with the hydroxyl groups of a polyester. A schematic of one of these reactions can be seen in figure.1.5.

Figure.1.5. Condensation between a Silane Coupling Agent and a Polyester.



R = alkyl chain with a mercapto or aminofunctional group

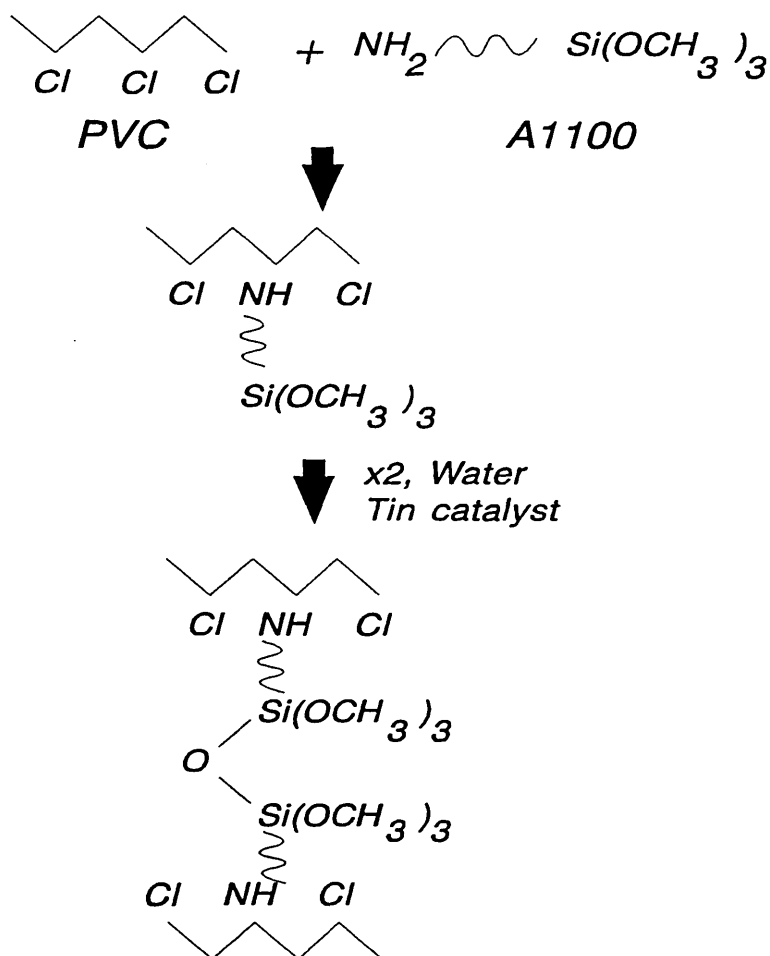
X = ethoxy or methoxy group

Koenig et al, [89], studied the reaction of epoxy resins with amines. They described the interpenetrating networks theory which states that a matrix resin can penetrate into a silane phase to form a network with the silane. This is of particular use with epoxy resins as they gain their maximum mechanical properties when they are completely cured in a system. It has been reported that secondary aminosilanes are more effective as cross-linking agents than primary aminosilanes and that A1110 would not react with epoxy resins below 200°C,

[129]. However improvements in the mechanical properties of epoxy resins have been reported with A1100 as the cross-linking agent, [80].

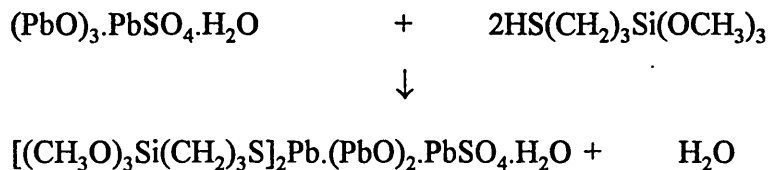
Gilbert et al, [124], have cross-linked PVC with A1100, using a tin catalyst at 80°C in water, as in figure.1.6.

Figure.1.6. Cross-Linking of PVC with A1100.

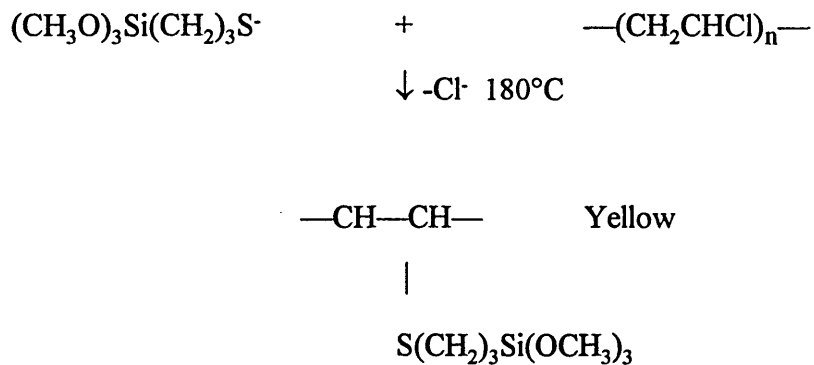


Kelnar and Schatz, [122], have grafted mercaptopropylalkoxysilanes onto plasticised and unplasticised PVC, stabilised with various thermal stabilisers. The grafting only occurred in the presence of basic lead salts, (due to their ability to form a nucleophilic agent from the mercaptosilane, with a poorly reactive thiol group). The reaction can be seen in figure.1.7, below:

Figure 1.7. Reaction of A189 with PVC.



Dissociation of this at processing temperatures leads to the formation of a thiolate anion which is capable of substituting for a chlorine atom in the PVC chain:



Now that the background of the surfactant systems has been described, it is necessary to explain how to obtain spectroscopic and microscopic measurements of these systems. This will be done in the following chapter.

CHAPTER.2. THEORY.

Introduction.

In this chapter, the basic principles of infrared and Raman spectroscopy, and of atomic force microscopy will be discussed. The details of the sampling techniques; attenuated total reflection infrared spectroscopy and depth profiling Raman microscopy and spectroscopy will be described in detail.

2.1. Infrared Spectroscopy Background Theory.

Infrared spectroscopy theory has been well covered by a variety of authors, [128-131]. Infrared radiation occurs between 0.7 and 500 μm in the electromagnetic spectrum, between microwave and visible radiation. The infrared absorption arises from the infrared radiation interacting with a fluctuating dipole of a molecule, during vibrations. The mid infrared is the most useful for spectroscopists as this is the region of the electromagnetic spectrum where most chemical vibrational bands appear. The infrared absorptions of systems at a molecular level are of interest here. A summary of infrared spectroscopy theory is given in the following sub- sections of this chapter.

2.1.1. Classical Theory of Light.

Light is considered, classically, to be an alternating electric field of high frequency moving in the direction of light propagation. This moving electric field has a magnetic field perpendicular to it and the electric field motion is depicted as wave motion with wavelength, λ . The wavelength is the linear distance between two consecutive maxima or minima of the wave motion. The frequency of radiation, ν , is defined, classically, in the following equation:

$$E = L \sin 2\pi\nu t \quad (2.1)$$

E = Instantaneous electric vector

L = Vector of length proportional to (light intensity)^{1/2}

t = Time

In a vacuum all electromagnetic radiation moves with a constant velocity, $c = 3 \times 10^{10} \text{ cms}^{-1}$ and is related to λ and ν as follows:

$$\lambda\nu = c \quad (2.2.)$$

Therefore if λ is fixed, ν can be determined and vice-versa.

Classical theory depicts light as being a *continuous wave motion*.

2.1.2. Quantum Theory of Light.

The classical concept of light radiation being a continuous wave motion fails to explain "blackbody" radiation experimental data. A blackbody is an object which is completely absorbing in the spectral region concerned. Classical theory, (Rayleigh-Jeans), suggests that the energy emitted by a body at finite temperature becomes infinitely large as λ goes to zero, which is not seen experimentally. Planck assumed that radiation was not continuous but was emitted in 'quanta'. Both quantum theory and experiment show that the energy of a single quantum of light is given by the following equation:

$$E = h\nu \quad (2.3)$$

$h = \text{Planck's constant} = 6.62 \times 10^{-34} \text{ Js}$

The relationship $\lambda\nu = c$ still applies. Infrared spectra are usually quoted in 'frequency' units, cm^{-1} , where $\frac{1}{\lambda} \text{ cm}^{-1} = \frac{\nu}{c}$ (2.4)

2.1.3. Sources of Infrared Radiation.

'Light' emitted from a blackbody heated to a temperature at which it becomes incandescent is a good source of infrared radiation. The radiation emitted has an intensity distribution which is a function of frequency, ν , according to Planck's radiation law:

$$E\nu d\nu = \left(\frac{8\pi h\nu^3}{c^3 [\exp(h\nu / kT) - 1]} \right) d\nu \quad (2.5)$$

$E\nu d\nu = \text{Energy density}$

$k = \text{Boltzmann constant} = 1.38 \times 10^{-23} \text{ JK}^{-1}$

2.1.4. Absorption of Infrared Radiation by Molecules.

The systems that are described in this thesis are anharmonic, so only a brief summary of the harmonic oscillator will be given. More detail will be given on the way that lineshapes and widths of infrared bands are effected.

2.1.4.1. Quantum Mechanical Harmonic Oscillator.

In quantum mechanics a mathematical operator operates on a function. Here we are interested in operators associated with energy and functions of Cartesian coordinates, which describe the position of the particle. The Schrödinger wave equation can be written as follows:

$$\hat{H}\Psi(x, y, z) = E\Psi(x, y, z) \quad (2.6)$$

\hat{H} = Hamiltonian operator

$\Psi(x, y, z)$ = Eigenfunction or wave function of coordinates

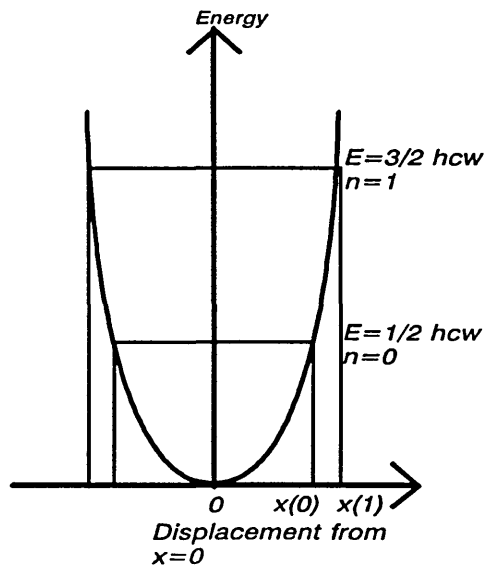
E = Energy Eigenvalues

There are only a very few discrete values of E for which the Schrödinger equation is valid i.e. there are only certain allowed energy levels, (see figure.2.1).

The system is not continuous as in the classical case. For a one-dimensional harmonic oscillator, the Schrödinger wave equation is written as follows:

$$\left(\frac{h}{8\pi^2 m} \frac{d^2}{dx^2} + \frac{kx^2}{2} \right) \Psi(x) = E\Psi(x) \quad (2.7)$$

Figure.2.1. Quantum Mechanical Harmonic Oscillator.



For a quantum mechanical harmonic oscillator the energy levels are equally spaced.

2.1.4.2. Selection Rules for the Quantum Mechanical Harmonic Oscillator.

2.1.4.2.1. Dipole Moment Change.

An infrared spectrum is only produced when the infrared radiation interacts with a molecule that has a fluctuating dipole.

2.1.4.2.2. Absorption Process.

Consider a vibrating molecule which is irradiated by an infrared beam. In order for the molecule to absorb the electromagnetic energy, the energy absorbed must be of a specific value to cause the molecule to just reach a higher energy value = $h\nu_{\text{vibration}}$.

2.1.4.2.3. The Harmonic Oscillator Selection Rule.

Transitions between non-adjacent energy levels in a system are not allowed.

2.1.4.3. Anharmonicity and Overtones.

Molecular vibrations are not strictly harmonic. (See figure.2.2). At small displacements, the curve follows the harmonic parabola but for higher energy states, it deviates away from the harmonic curve. For higher energy states:

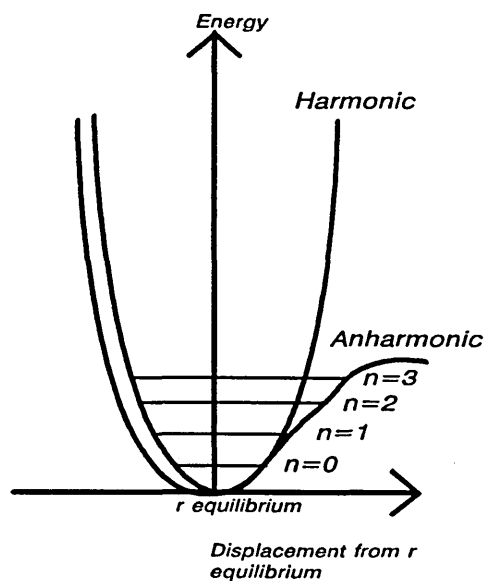
$$E = hc\omega \left[\left(n + \frac{1}{2} \right) - \left(n + \frac{1}{2} \right)^2 x_e \right] \quad (2.8)$$

x_e = Anharmonicity constant

$n = 0, 1, 2, 3, \dots$

Positive anharmonicity occurs when x is positive and the energy spacing between successive energy levels decreases as n increases. Transitions from states 0 to 2 and 0 to 3, which are not allowed in the simple harmonic oscillator approximation, do occur and are called the first and second overtones respectively. The intensity of these transitions is usually lower than for the fundamental transition.

Figure.2.2. Anharmonic Oscillator.

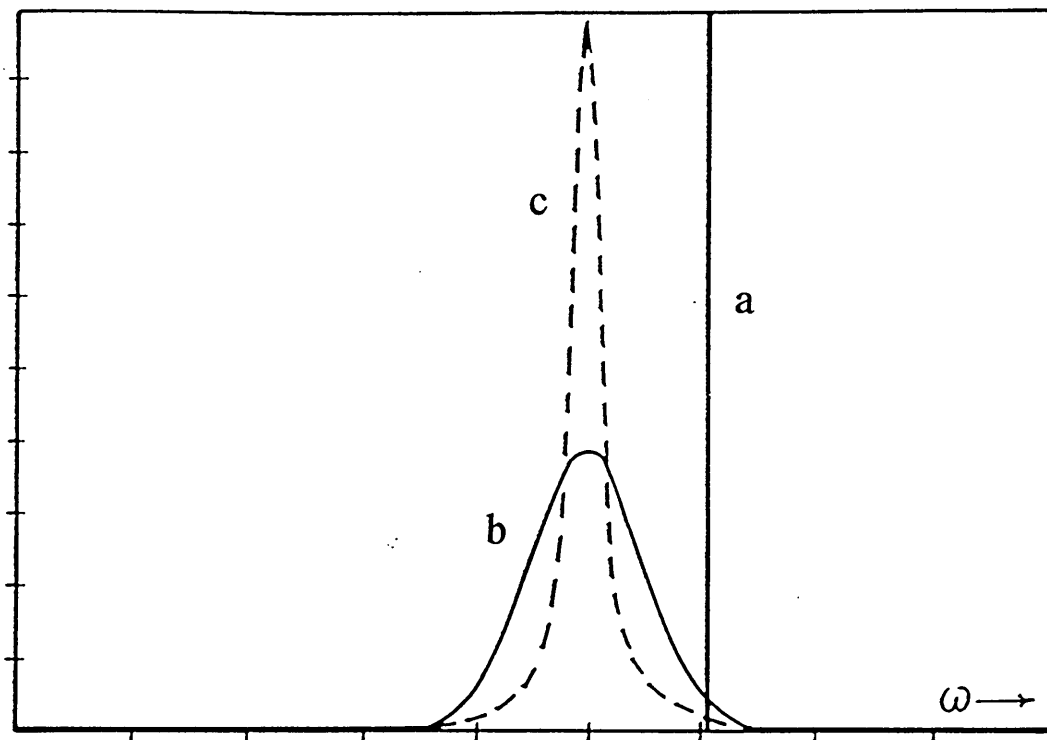


2.1.4.4. Lineshape and Frequency Changes.

The observed bands in an infrared spectrum are not necessarily 'sharp' lines and there are many factors which control the broadening and narrowing of the band.

An unbroadened line, expected for an allowed transition between energy states, (using a time independent Hamiltonian), e.g. a dilute gas, can be seen in figure.2.3.(a)

Figure 2.3. Band Shapes, [132].



There are several contributions to the broadening of infrared bands. These include the instrument linewidth, time dependent processes, (relaxation processes), inter-molecular forces and intra-molecular coupling.

The instrument bandwidth will contribute to bandwidths in a spectrum and can be measured from any dilute gas spectrum.

Time dependent processes include Doppler broadening, lifetime broadening and motional narrowing. Doppler broadening occurs mainly in gaseous samples and has a line shape which is dependent on the Maxwell distribution of speeds of the molecules in the gas. Lifetime broadening arises from the fact that it is impossible to determine the energy and lifetime of an energy state simultaneously. That is, if a system survives for time, t , its energy levels are uncertain to an extent, ΔE .

$$\text{Lifetime broadening} = \Delta E \Delta t \approx h/2\pi \quad (2.9)$$

The shorter the lifetime of the states involved in the transition, the broader the band which arises from transitions between them.

The vibrational energy states involved in the initial and final states can be changed by intermolecular interaction. These interactions will vary from molecule to molecule, since the liquid is disordered. This means that there is no longer one transition energy but a transition energy 'range' of variable size, due to phase fluctuations among the oscillators. This effect is called inhomogeneous broadening. Figure.2.3.(b) shows a band due to a liquid with slow molecular motions and little motional narrowing,(a band which has undergone inhomogeneous broadening). For solid systems, interactions of molecules with other molecules in the same solid or with molecules of other solids, e.g. at an interface, also gives rise to inhomogeneous broadening of the vibrational band.

Figure.2.3.(c) shows the effect of motional narrowing on an inhomogeneously broadened band. This represents a liquid with more rapid molecular motions and significant motional narrowing. Motional narrowing arises from the fact that the intermolecular interactions fluctuate very quickly, due to fast translational and rotational motions of molecules in a liquid. This causes partial averaging of all the initial and final states because the spectroscopic experiment does not show the instantaneous situation of the liquid sample. Fast relaxation processes give broad bands and slow processes give narrow bands unless the system is already in the motionally narrowed limit.

Homogeneous broadening, (where all the molecules have the same frequency), is due to intermolecular collisions and can be reduced by working at lower pressure in the gas phase.

Because of the strong interactions between molecules in a liquid, excitation energy is sometimes observed to shift from one molecule to another by resonant energy transfer, (RET).

There are many different processes which can give a vibrational frequency shift. Changes in the force field, (force constants), and changes in atomic masses e.g. changing from H₂O to D₂O, are intermolecular processes. If the conformation of a molecule is altered, (an inter- and intra molecular process), this will cause a frequency shift. For example changing from gauche to trans conformers in an alkyl chain will give a decrease in band position. Environmental changes, for example changing from gaseous to liquid carbon monoxide will give spectral peaks at different positions. Intermolecular forces e.g. hydrogen bonding and resonance energy transfer also cause a change in frequency.

Now the background to infrared spectroscopy has been summarised, it is necessary to explain how to obtain infrared spectra of molecular systems experimentally.

2.2. Fourier Transform Infrared, (FTIR), Spectroscopy.

Introduction.

In order to obtain an infrared spectrum of a particular sample, the variation of infrared absorbance with frequency needs to be determined. Infrared radiation sources are polychromatic, i.e. they emit radiation over a wide range of frequencies. Therefore a detection system is required which is capable of separating the infrared radiation frequencies with an acceptable resolution.

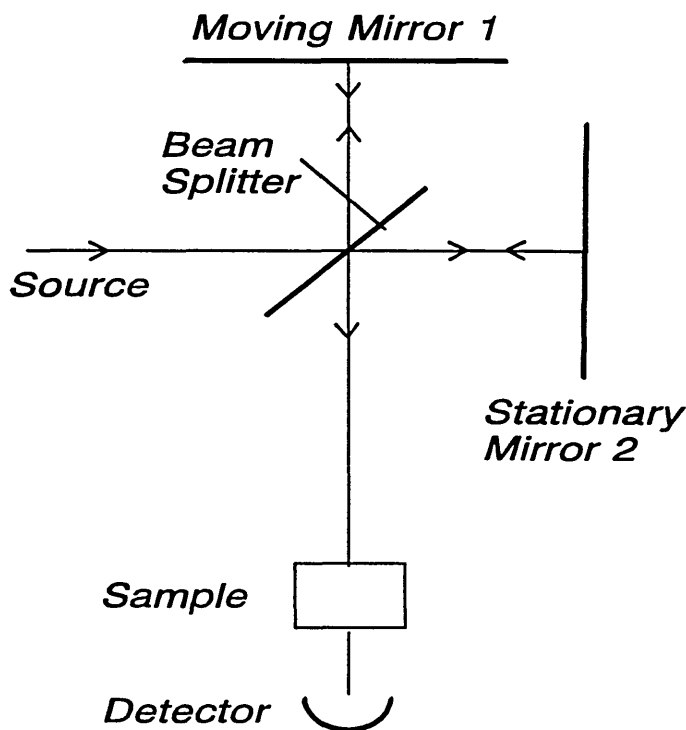
There are two types of spectrometer available for producing infrared spectra. These are the dispersive, diffraction grating or prism, spectrometer and the interferometer. An interferometer will initially produce an interferogram which needs to be transformed by a mathematical function, called a Fourier transform, before a recognisable infrared spectrum is produced. There are many excellent texts which detail the theory and background of Fourier transform infrared spectroscopy, [135-138], so only a brief summary of the theory will be given here. Interferometers have many advantages over dispersive instruments, which will be discussed here. The applications of these advantages to the research discussed in this thesis are also described.

2.2.1. The Michelson Interferometer.

A schematic of a Michelson interferometer can be seen in figure.2.4. Sometimes the interferometer is evacuated to less than 0.1 mm mercury pressure or with dry nitrogen gas, for example to prevent atmospheric water vapour entering the system. This could fog or destroy the beam splitter and also obscures weak infrared bands in the regions of the infrared spectrum where water vapour absorbs. The infrared source, e.g. a globar source, emits a polychromatic light beam which is collimated by mirrors. This beam then strikes the beam splitter, where 50% of the light is reflected onto moving mirror 1 and 50% is reflected onto stationary mirror 2. On reflection from mirrors 1 and 2, the beam is recombined and is focused onto the sample. After passing through the

sample, the unabsorbed radiation is then focused onto the detector. The recombining beams will have an optical path difference called retardation, x , dependent upon the displacement of the moving mirror from the zero path difference, (ZPD). If the two mirrors are equidistant from the beam splitter, the two beams will be in phase and constructive interference will occur. If the moveable mirror is displaced by $1/4 \lambda$, (where λ = wavelength of radiation), from the ZPD, with respect to the stationary mirror, then the retardation will be $1/2 \lambda$ and the recombining beams will be out of phase. Therefore destructive interference will occur, (for a monochromatic source). For polychromatic sources the measured interferogram will be a resultant of the interferograms corresponding to each wavenumber.

Figure.2.4. Schematic of Michelson Interferometer.



Mirror 1 moves about the ZPD at a constant rate. The interferometer produces an interferogram by combining all the interference patterns. (See figure.2.5). The intensity of the radiation at the detector can be written as follows:

$$I_{(x)} = 2 \int_0^{\infty} S(\bar{\nu}) \cos(2\pi\bar{\nu}x) d\bar{\nu} \quad (2.10)$$

$I_{(x)}$ = Intensity of signal at detector = Fourier transform of frequency distribution

$S(\bar{\nu})$ = Spectral density amplitude

$\bar{\nu}$ = Wave number

At the same time as the radiation is focused onto the detector, the signal is digitised at set distances of mirror movement, called the sampling interval, Δx . This is controlled by a laser in the instrument. The spectrum is produced by the Fourier transform of the interferogram, using the set sampling intervals, and the amplitude of each frequency element in the spectrum can be given by:

$$S_{(\bar{\nu})} = \sum_{x=0}^D I_{(x)} \cos(2\pi\bar{\nu}x) \Delta x \quad (2.11)$$

$I_{(x)}$ = Intensity of signal at detector

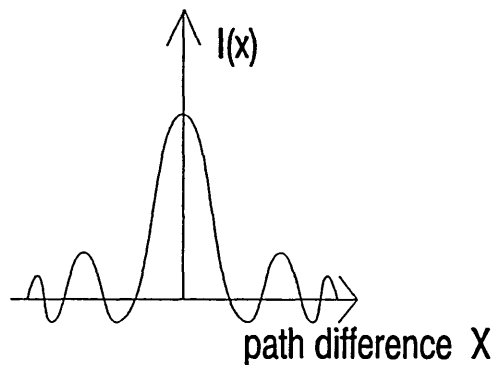
Δx = Sampling interval

x = Path difference, from 0 to D

N = Sampling number, usually 500 to 10 000

$x = N\Delta x$

Figure.2.5. Interferogram of Polychromatic Source.



Discrete sampling results in a limit to the frequency range over which the spectrum can be computed. Discrete sampling does not, however, give all the information from the interferogram. For each wavelength, two samples must be taken. Therefore the digitised sampling interval must be as follows:

$$\Delta x \leq \lambda_{\text{minimum}}/2 \quad (2.12)$$

λ_{minimum} = minimum wavelength in the range being studied. Therefore:

$$\Delta x = 1/(2 \bar{\nu}_{\text{maximum}}) \quad (2.13)$$

i.e. the highest frequency, cm^{-1} , attainable for a given sampling interval = $\bar{\nu}_{\text{maximum}}$, which equals $1/2 \Delta x$. This is called the aliasing frequency. If there are frequencies present that are greater than this, distortion of the spectrum occurs and filtering must be introduced.

For our Mattson interferometer, the laser wavelength is 632.8 nm. Sampling every two wavelengths, (1.2656 μm), gives an aliasing frequency of

$$\frac{10^4}{1.2656 \mu\text{m}} = 7960 \text{cm}^{-1}$$

In the Mattson Polaris interferometer the KBr beam splitter cuts out well before this frequency.

2.2.2. Advantages of Interferometry.

2.2.2.1. The Multiplex, (Fellgett), Advantage.

In an interferometer, the detector sees all the spectral elements 'at the same time'.

$$N = \frac{\bar{\nu}_H - \bar{\nu}_L}{\Delta \bar{\nu}_R} \quad (2.14)$$

N = Spectral elements

$\bar{\nu}_H$ = Highest wavenumber

$\bar{\nu}_L$ = Lowest wavenumber

$\Delta \bar{\nu}_R$ = Resolution

For thermal detectors, the signal to noise ratio, (S/N), is proportional to the square root of the time of observation of each element. (S/N) in a dispersive spectrometer is proportional to $T^{1/2}/N^{1/2}$ because a dispersive spectrometer looks at each element separately. (S/N) in a Fourier transform spectrometer is proportional to $T^{1/2}$. Where T is total time. Therefore the (S/N) gain for a Fourier transform spectrometer over a dispersive instrument is $N^{1/2}$. This is obviously advantageous when investigating very thin layers which have weak infrared absorbances, such as the monolayers being studied here. This advantage only applies if the major source of noise is from the detector. Other sources of noise can arise from the source or the spectrometer itself.

2.2.2.2. The Throughput, (Jacquinot), Advantage.

This arises because there are no slits in the spectrometer which means that the signal reaching the detector is much larger than for a grating spectrometer. The relative "Etendue", ($A\Omega$), for the two types of instrument has been shown to be, [138a], assuming equal collimator areas and focal lengths:

$$\frac{(A\Omega)_{FT}}{(A\Omega)_{DISP}} = 2\pi \left(\frac{F}{l'} \right) \quad (2.15)$$

A = Area of source

F = Focal length of collimator

Ω = Solid Angle subtended to source

l' = Slit height of grating

FT = Fourier transform

spectrometer

DISP = Dispersive

For a highly sensitive grating spectrometer, (e.g. PE580B), $F/l' \geq 30$. Therefore $A\Omega_{FT} / A\Omega_{DISP}$ is typically 180 - 200, [138a].

Detector noise, however, is proportional to the area of the detector so a small detector should be used, for a detector noise-limited system. Again this is of use for investigating monolayer systems as very small absorbances can be measured more easily by using an interferometer rather than a dispersive instrument.

2.2.2.3. Connes Advantage.

This is important for subtracting spectra from one another, e.g. if we subtract one spectrum from another spectrum, both need to have been sampled at exactly the same cm^{-1} intervals. Therefore the spectrometer needs to have been calibrated so that the wavenumber scale is controlled. This can be done and is of great importance to the research carried out here as spectra with very weak absorbances need to be ratioed against background spectra. Without this advantage, infrared analysis of the monolayers and submonolayers discussed in this thesis would not be possible.

2.2.2.4. Mirror Movement Averaging.

The signal to noise ratio is proportional to the square root of the number of scans taken. Therefore increasing the number of scans increases the signal to noise.

2.2.3. Disadvantages of Interferometry.

1. In a detector noise-limited system, (usual in mid-infrared instruments), the Fellgett advantage applies. However some instruments, e.g. far infrared, are source noise-limited. Therefore the detector will see all the noise all of the time, since the detector integrates over all frequencies. In a detector noise-limited system, the signal to noise ratio will be inversely proportional to the square root of the number of scans and also proportional to $T^{1/2}$, for both fast and slow-scanning instruments, therefore fast scanning is not an advantage. However, in mid infrared, fast scanning is necessary for successful measurement of low to medium resolution infrared spectra, where the interferogram has a high signal to noise ratio. Efficient measurement of high signal to noise, low to medium resolution spectra is not possible with a slow scanning instrument.

2. Single beam instruments have the inherent problem of bands due to water and carbon dioxide vapour, from the air, being present in the infrared spectra. This can be avoided by purging the instrument with dry nitrogen before use.

2.2.4. Instrument parameters.

2.2.4.1. Resolution.

The Rayleigh criterion states that two adjacent spectral lines of equal intensity, whose instrumental line shapes are defined by a function, sinc^2x , are considered to be just resolved when the centre of one line is at the same frequency as the first zero value of the instrument line shape of the other. In an interferometer resolution is determined by:

$$\Delta\bar{\nu}_R \propto 1/x \tag{2.16}$$

$$\Delta\bar{\nu}_R \propto 1/2d \tag{2.17}$$

$\Delta\bar{\nu}_R$ = resolution

x = maximum path difference = 2d

d = maximum mirror movement

There are several factors which affect resolution. These include the mirror travel distance and the number of points collected, the number of points transformed, the apodisation function used, the beam divergence, (only at 0.1 cm^{-1} level), and the sampling interval.

Resolution itself controls the following parameters: The spectral line width and the signal to noise ratio. For polychromatic interference, the signal decreases in amplitude as the path difference increases but the noise remains constant, so the signal to noise ratio depends on resolution employed.

2.2.4.2. Mirror Travel Rate.

In a mid infrared instrument, beam modulation is produced by the mirror. If the modulation rate = ν cms^{-1} , the path difference at time $t = 2\nu t$ cm.

$$I_{(x)} = \sum S_{\bar{\nu}} \cos(2\pi\bar{\nu}x)\Delta x \tag{2.18}$$

Therefore:

$$I_{(t)} = \sum S_{(f)} \cos(2\pi\bar{\nu}2vt) \quad (2.19)$$

$f = 2\bar{\nu}v = \text{modulation frequency}$

For the mid infrared range:

At 4000 cm^{-1} $f = 4000 \text{ cm}^{-1} / \text{cm s}^{-1} = 4 \text{ kHz}$

400 cm^{-1} $f = 400 \text{ cm}^{-1} / \text{cm s}^{-1} = 0.4 \text{ kHz}$

The mirror speed is controlled by the following parameters:

1. Detector response: Mercury Cadmium Telluride detectors are fast and are generally used in mid infrared spectrometers. Golay detectors are slow and are used in far infrared instruments.
2. Speed of a particular experiment.
3. Signal to noise ratio via number of scans.

2.2.4.3. Apodisation.

The word comes from the Greek 'α'πόδος' which means 'without feet'.

Apodisation functions are used to truncate the interferogram. Many apodisation functions are available and each one affects the interferogram to a different degree. The interferogram is effectively multiplied by the apodisation function, $D(x)$, which gradually reduces it to zero. For a 'box-car' apodisation function, the interferogram is cut off at ' x_{max} ' as follows, (see figure 2.6.(a)):

$$D(x) = +1 \quad \text{if } -x_{\text{max}} \leq x \leq +x_{\text{max}} \quad (2.20)$$

$$D(x) = 0 \quad \text{if } |x| > |x_{\text{max}}| \quad (2.21)$$

The spectrum produced is then:

$$S_{\bar{\nu}} = \int_{-\infty}^{\infty} I_{(x)} D_{(x)} \cos(2\pi\bar{\nu}x) dx \quad (2.22)$$

The Fourier transform of the apodisation function is then:

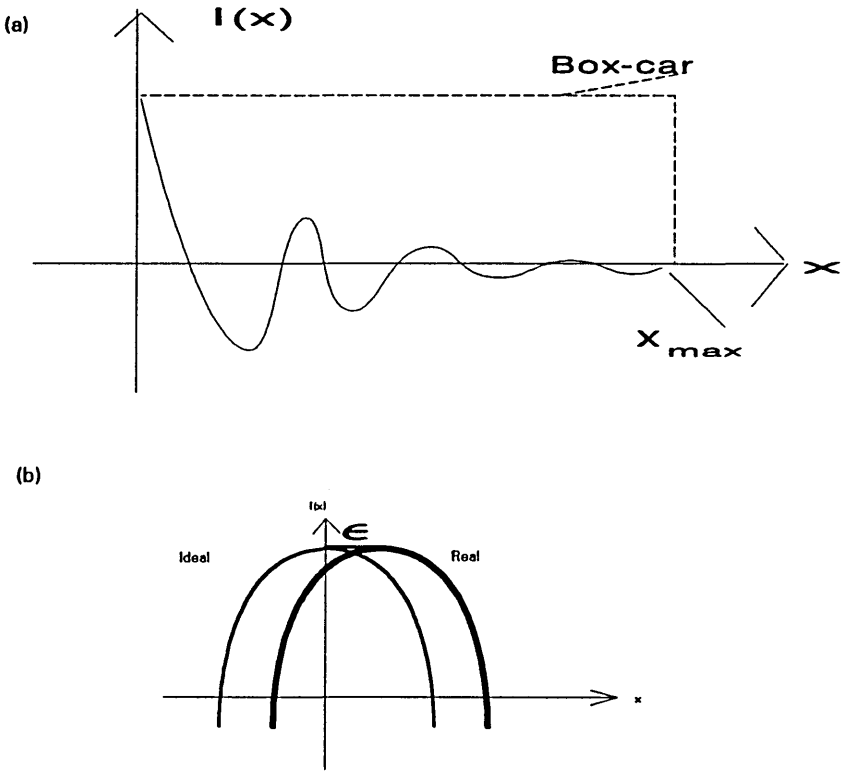
$$\text{FT}[D_{(x)}] = 2x_{\max} \text{sinc}(2\pi\bar{v}x_{\max}) \quad (2.23)$$

The box-car apodisation function produces a spectrum with large side-lobes and therefore is not of much use. There are other apodisation functions such as the 'triangular' or 'triangular squared' which remove these side-lobes. The Fourier transform of an interferogram, which has an apodisation function applied to it, gives a broader band in the resulting spectrum than an interferogram which is unaltered. Therefore resolution is lost. The 'stronger' the apodisation function, the poorer the resolution.

2.2.4.4. Phase Corrections.

Experimentally, optical and electronic effects cause interferograms to be asymmetric, (see figure.2.6.(b)). To produce a symmetric interferogram, a phase correction needs to be made, which the Mattson instrument does automatically.

Figure.2.6.(a). 'Box-Car' Apodisation. 2.6(b). Asymmetric Interferogram.



ϵ = Phase correction.

2.3. Attenuated Total Reflection, (ATR), Spectroscopy.

Introduction.

The production of an evanescent field in an optically rarer medium in contact with an optically denser medium, was first observed nearly two hundred years ago by Newton, [139]. Harrick, [140-141], and Fahrenfort, [142], made use of this effect to produce absorption spectra in the sixties when Harrick also published an excellent review on internal reflection, [143], from which, most of the theory in this section is derived. Some reasons why the ATR technique is valuable to spectroscopists include the facts that high sensitivity is obtained, (very thin films such as monolayers can be measured), sample preparation is simple, there are no spectral fringes, (except from the beamsplitter), which are seen in transmission infrared spectra, and a variety of different samples can be studied.

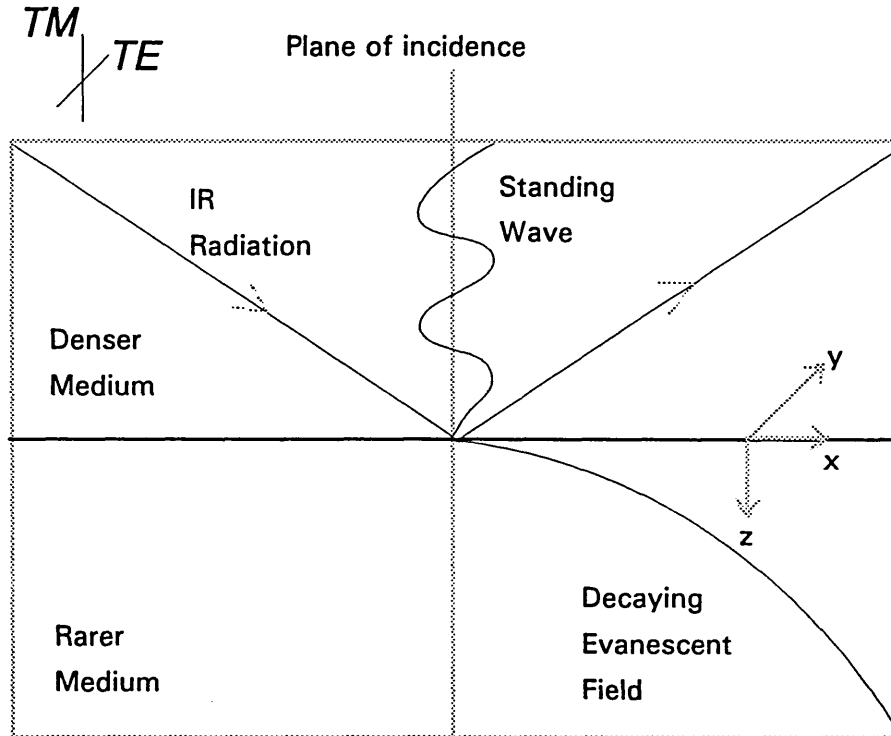
2.3.1. Total Internal Reflection.

If an optically dense material is in contact with an optically less dense material and if an electromagnetic wave is incident on the interface, at an angle greater than the critical angle, then total internal reflection will occur at the interface between the two media. A standing wave is present in the denser medium and an evanescent wave is produced in the rarer medium. The denser medium is the internal reflection element, IRE, and the less dense medium is the sample under investigation. (See figure.2.7). The electromagnetic wave has components in the x, y and z directions; E_x , E_y and E_z respectively.

There are two polarisations of the electromagnetic wave that need to be defined, (see figure.2.7). When the electromagnetic wave is polarised in a direction parallel to the plane of incidence only the E_x and E_z components of the light are present. These constitute the TM, Transverse Magnetic, p or parallel polarisation. When the electromagnetic wave is polarised in a direction

perpendicular to the plane of incidence, only the E_y component is present. This constitutes the TE, Transverse Electric, s or senkrecht polarisation.

Figure.2.7. Total Internal Reflection.



For unit incoming intensity, the reflected amplitudes, r_{TE} and r_{TM} are given by Fresnel's equations as follows:

$$r_{\text{perpendicular}} = r_{TE} = -\frac{\sin(\phi - \theta)}{\sin(\phi + \theta)} \quad (2.24)$$

$$r_{\text{parallel}} = r_{TM} = \frac{\tan(\phi - \theta)}{\tan(\phi + \theta)} \quad (2.25)$$

Where ϕ = angle of refraction, θ = angle of incidence and the reflected radiation intensity, R is equal to the reflected amplitude squared, i.e. $R = r^2$.

At the critical angle, i.e. when $\theta = \theta_c$ and $\phi = \pi/2$, R_{TE} and R_{TM} become exactly 100%, i.e. total reflection of the incident radiation occurs.

$$\theta_c = \sin^{-1} n_{21} \quad (2.26)$$

$$n_{21} = n_2/n_1$$

n_2 = Refractive index of the rarer medium

n_1 = Refractive index of the denser medium

For $\theta > \theta_c$, ϕ becomes imaginary. This was interpreted by Fresnel to mean that all the incident radiation is reflected and none is transmitted into the rarer medium.

Therefore the ideal situation is where the rarer medium is non-absorbing and the reflected rays will be of the same intensity as the incident rays. However, in practice, the rarer medium is absorbing and hence the reflection is said to be attenuated.

The materials used for the denser medium should ideally be transparent in the mid infrared region. e.g. KRS-5, (ThI₂.ThBr₂), or ZnSe. However materials such as silicon which are transparent over part of the mid infrared region are sometimes used as internal reflection elements.

The evanescent field produced in the rarer medium has the following properties, [143]:

(i) The field intensity in the rarer medium is not zero but there is an instantaneous normal component of energy flow into the medium with a time average equal to zero. i.e. there is no loss of energy at the interface between the rarer and denser media and total internal reflection occurs.

(ii) The evanescent field in the rarer medium is not transverse and has components in all directions which can interact with dipoles in a molecule in all orientations.

(iii) There is a non zero energy flow parallel to the surface, (along the x axis), resulting in a displacement of the incident and reflected waves. This is called the Goos-Hanchen shift.

The evanescent field is confined to the surface of the rarer medium and decreases in intensity with increasing distance into the rarer medium normal to

the surface, (along the z axis). The decay in evanescent field is exponential and can be written as follows:

$$E = E_0 \exp \left[\frac{-2\pi}{\lambda_1} \left(\sin^2 \theta_{\text{inc}} - n_{21}^2 \right)^{1/2} Z \right] \quad (2.27)$$

E_0 = Electric field amplitude at surface of rarer medium

E = The value the electric field amplitude decays to, at a distance Z into the rarer medium

θ_{inc} = angle of incidence

$\lambda_1 = \lambda/n_1$ = wavelength in free space/refractive index of denser medium
= wavelength of radiation in denser medium

The electric field amplitude decay coefficient, γ , is used to replace the exponential constant in equation (2.27) as follows:

$$E = E_0 \exp[-\gamma Z] \quad (2.28)$$

$$\gamma = \frac{2\pi \left(\sin^2 \theta_{\text{inc}} - n_{21}^2 \right)^{1/2}}{\lambda_1} \quad (2.29)$$

2.3.2. Depth of Penetration and the Effective Thickness.

The depth of penetration, d_p , of the evanescent wave into the rarer medium occurs when E decays to a value of $E_0 \exp[-1]$. This occurs when:

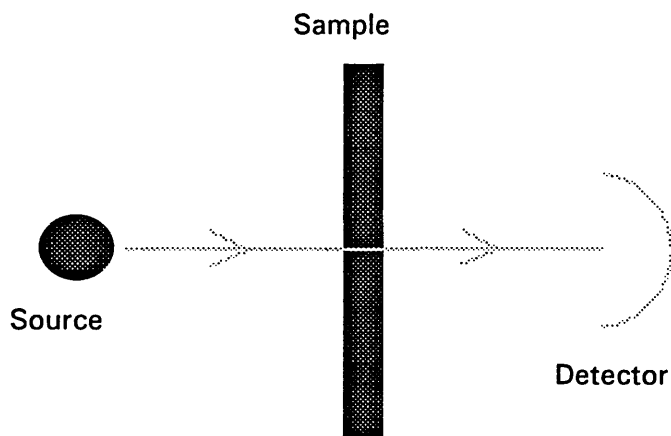
$$Z = d_p = \frac{1}{\gamma} \quad (2.30)$$

d_p is defined as the depth sampled in the internal reflection experiment. The real sampling depth, d_s , is actually larger than d_p , since the electric field amplitude at d_p is 37% of its value at the interface. d_s is approximately three times the size of d_p .

The effective thickness, d_e , is a measurement of the coupling of the evanescent field with the absorbing rarer medium. It is the thickness of a film of the sample that will give the same absorbance for transmission at normal incidence as that

obtained in an internal reflection experiment. (See figure 2.8. for the transmission experiment).

Figure.2.8. The Transmission Experiment.



The absorbing rarer medium can be treated in terms of intensity loss per reflection. If I_0 is incident intensity and I_R is reflected intensity then the reflectivity, R , is given by:

$$R = I_R/I_0 \quad (2.31)$$

For total reflection $I_R = I_0$ and $R=1$. This is analogous to transmission where:

$$T = \exp(-\alpha d) \quad (2.32)$$

T = transmittance

α = absorption coefficient of medium / cm^{-1}

d = sample thickness

For weak absorbers in the internal reflection spectroscopy experiment:

$$R = \exp(-\alpha d_e) \approx (1-a) \quad (2.33)$$

a = absorption parameter = αd_e for one reflection

α is the same as for transmission

For strong absorbers, there is a much more complicated equation for determining d_e . For a lossy dielectric, (one in an ATR experiment), with a complex refractive index, $\hat{n}_{\bar{\nu}} = n_{\bar{\nu}} + ik_{\bar{\nu}}$, the absorption coefficient is related to the attenuation index, κ , as follows:

$$\alpha = 4\pi n\kappa/\lambda \quad (2.34)$$

$$\hat{n}_{\bar{\nu}} = n_{\bar{\nu}} + ik_{\bar{\nu}} \quad n_{\bar{\nu}} = \text{real} , \quad ik_{\bar{\nu}} = \text{imaginary}$$

The electromagnetic wave interferes with the electron cloud of molecules and changes the polarisability of the molecule. This is proportional to the real part of the refractive index. Absorption of energy by the molecules produces the imaginary part of the complex refractive index, $ik(\bar{\nu})$. This is seen as absorption.

The effective thickness is useful for weak absorbers since internal reflection spectroscopy and transmission experiments can be compared and also because it can be used to calculate the theoretical upper limit of absorbance.

In order to calculate d_e , the electric field components, (E_x , E_y , and E_z), first need to be calculated. As previously stated there are two polarisations of the electromagnetic wave, TE and TM.

There are also two cases for the rarer medium:

1. The semi- infinite bulk case where the electric field amplitude falls to a very low value within the thickness of the film, t .

$$\text{i.e. } t \gg 1/\gamma \quad \text{or} \quad t \gg d_p$$

2. The thin film case where the electric field amplitude remains virtually constant over the film thickness. $\text{i.e. } t \ll 1/\gamma \quad \text{or} \quad t \ll d_p$

1. Semi- Infinite Bulk case.

TE wave

$$E_y = E_{\text{perpendicular}} = \frac{2 \cos \theta_{\text{inc}}}{(1 - n_{21}^2)^{1/2}} \quad (2.35)$$

TM wave

$$E_x = \frac{2(\sin^2 \theta_{\text{inc}} - n_{21}^2)^{1/2} \cos \theta_{\text{inc}}}{(1 - n_{21}^2)^{1/2} \left[(1 + n_{21}^2) \sin^2 \theta_{\text{inc}} - n_{21}^2 \right]^{1/2}} \quad (2.36, 2.37)$$
$$E_z = \frac{2 \sin \theta_{\text{inc}} \cos \theta_{\text{inc}}}{(1 - n_{21}^2)^{1/2} \left[(1 + n_{21}^2) \sin^2 \theta_{\text{inc}} - n_{21}^2 \right]^{1/2}}$$

2. Thin film case.

TE wave

$$E_y = E_{\text{perpendicular}} = \frac{2 \cos \theta_{\text{inc}}}{(1 - n_{31}^2)^{1/2}} \quad (2.38)$$

TM wave

$$E_x = \frac{2 \cos \theta_{\text{inc}} \left[\sin^2 \theta_{\text{inc}} - n_{31}^2 \right]^{1/2}}{(1 - n_{31}^2)^{1/2} \left[(1 + n_{31}^2) \sin^2 \theta_{\text{inc}} - n_{31}^2 \right]^{1/2}} \quad (2.39, 2.40)$$
$$E_z = \frac{2 \cos \theta_{\text{inc}} \sin \theta_{\text{inc}} n_{32}^2}{(1 - n_{31}^2)^{1/2} \left[(1 + n_{31}^2) \sin^2 \theta_{\text{inc}} - n_{31}^2 \right]^{1/2}}$$

$$n_{31} = n_3/n_1$$

E_y and E_z reach maxima at the critical angle whereas E_x decreases drastically near the critical angle and falls to zero at the critical angle. E_z becomes very large near the critical angle due to boundary conditions at the interface of the denser and rarer media. This produces intense fields normal to the surface.

The relation between the absorption parameter, a , and the electric field for a weak absorber, E , can be written as follows:

$$a = \frac{n_{21}\alpha}{\cos\theta_{inc}} \int_0^t E^2 dz \quad \text{or} \quad a = \frac{A}{N} = \frac{n_{21}\alpha c}{\cos\theta} \int_0^\infty E^2 dz \quad (2.41, 2.42)$$

A = Absorbance

N = Number of reflections

α = Molar absorption coefficient

c = Concentration

Solving this gives:

1. Semi- Infinite Bulk case. t goes to infinity:

$$a = \frac{n_{21} \alpha E_0^2}{2\gamma \cos\theta_{inc}} \quad (2.43)$$

2. Thin Film case. $t = d$, d = film thickness.

$$a = \frac{n_{21} \alpha d E_0^2}{\cos\theta_{inc}} \quad (2.44)$$

Because $a = \alpha d_e$, the values of d_e for TM and for TE polarisations can be calculated as follows:

1. Semi- Infinite Bulk case

TE wave

$$d_{e \text{ perpendicular}} = \frac{n_{21} \lambda_1 \cos\theta_{inc}}{\pi (1 - n_{21}^2) (\sin^2 \theta_{inc} - n_{21}^2)^{1/2}} \quad (2.45)$$

TM wave

$$d_{e \text{ parallel}} = \frac{n_{21} \lambda_1 \left(2 \sin^2 \theta_{inc} - n_{21}^2 \right) \cos \theta_{inc}}{\pi \left(1 - n_{21}^2 \right) \left[\left(1 + n_{21}^2 \right) \sin^2 \theta_{inc} - n_{21}^2 \right] \left(\sin^2 \theta_{inc} - n_{21}^2 \right)^{1/2}} \quad (2.46)$$

2. Thin Film case

TE wave

$$d_{e \text{ perpendicular}} = \frac{4n_{21} d \cos \theta_{inc}}{\left(1 - n_{31}^2 \right)} \quad (2.47)$$

TM wave

$$d_{e \text{ parallel}} = \frac{4n_{21} d \cos \theta_{inc} \left[\left(1 + n_{32}^4 \right) \sin^2 \theta_{inc} - n_{31}^2 \right]}{\left(1 - n_{31}^2 \right) \left[\left(1 + n_{31}^2 \right) \sin^2 \theta_{inc} - n_{31}^2 \right]} \quad (2.48)$$

For unpolarised radiation for both cases:

$$d_{eu} = (d_{e \text{ parallel}} + d_{e \text{ perpendicular}})/2 \quad (2.49)$$

There are several factors which effect d_e :

The electric field decay constant, which is proportional to wavelength, the electric field intensity at the surface, E_0^2 , the sampling area, $1/\cos \theta_{inc}$ and the refractive index matching, $n_2/n_1 = n_{21}$.

The decay constant increases as θ_{inc} increases and is independent of polarisation. As γ increases, the rate of electric field amplitude decays. Therefore d_e decreases as γ increases. The electric field intensity is proportional to E_0^2 . E_0 decreases with increasing θ_{inc} . E_0 is greater for TM polarisation than for TE

polarisation. Therefore as E_0^2 increases, d_e increases. The sampling area increases as θ_{inc} increases. Therefore as θ_{inc} increases, d_e decreases.

From equation, (2.43), it can be seen that as n_{21} goes to 1, d_e increases. Therefore as index matching increases, less spectral contrast is obtained. As n_{21} goes to 1, γ decreases. Therefore d_e increases. Usually it is assumed that n_{21} is constant, which is not true. The refractive index varies with wavelength.

As the wavelength in free space increases, d_e increases. This effect is seen as increasing spectral contrast at higher wavelengths and broadening of the infrared peaks on their long wavelength side, compared to transmission spectra.

From equations, (2.44) and (2.45), it can be seen that at $\theta_{inc} = \theta_c$, d_e becomes very large and the spectra are distorted.

For thin films, γ does not effect d_e and therefore the wavelength does not affect d_e . This means that for thin films no distortion of the spectra is seen. E_0^2 and θ_{inc} have the same effect on d_e for thin films as they have on d_e for thick films.

Müller et al, [144], considered an absorbing rarer medium with a constant refractive index and infinite plane wave irradiation. They produced a more complicated definition for γ , which accounted for the fact that the refractive index is complex. Using this definition, for the range $\kappa = 0$ to $\kappa = 0.053$, (absorption coefficient = $\alpha = 0$ to 1000 cm^{-1} , $\kappa =$ attenuation index), it was seen that the evanescent field was only slightly changed.

Most materials have an absorption coefficient less than 1000 cm^{-1} . Some organic materials, however, have absorption coefficients greater than 1000 cm^{-1} , and therefore the evanescent field is distorted.

Müller et al also determined effective thicknesses for an absorbing medium. They showed that the incident radiation is attenuated by absorption in the rarer medium and by distortion of the evanescent wave by the complex refractive index. From their equations part of the radiation is decoupled and transmitted into the rarer medium. Therefore part of the evanescent field is lost in the rarer

medium by propagation and the calculated d_e is larger than for the non-absorbing case.

2.3.3. Advantages of ATR.

1. Total internal reflection in the internal reflection element will produce many reflections. Therefore the sampling number is large and this increases sensitivity of the technique.
2. The technique is sensitive, e.g. to 3 nm sample thickness on ATR prism.
3. Interference effects are eliminated.
4. 'Depth Profiling' is possible by use of the evanescent wave.
5. d_p (or d_e) can be changed by using different IRE materials or by varying θ_{inc} .
6. In situ experiments can be performed.
7. Dichroic ratios and therefore orientation of molecules on a surface can be calculated when the technique is combined with FTIR.

2.3.4. Disadvantages of ATR.

1. Very good optical contact is required between the sample and the IRE.
2. The distribution of electric fields is complicated.
3. The total internal reflection wave loses energy at each reflection.

2.3.5. Linear Dichroism Theory.

Linear dichroism has been employed, [2, 42], over a considerable period of time in order to deduce information about the orientational 'ordering' of molecules on the surface of an ATR crystal.

Although the linear dichroic ratio, (LDR),

$$\text{LDR} = A_{\text{perpendicular}} / A_{\text{parallel}} = A_{\text{TE}} / A_{\text{TM}} \quad (2.50)$$

is easily defined and measured using the two different orthogonal polarisation directions, the recovery of well-defined molecular orientational information is often fraught with difficulties. There are several reasons for this. For example, the distinction between values of LDR calculated for the extremes of perfect ordering, (all molecules oriented at 90° to the crystal surface), and random orientation are often very close together, especially for ultrathin films, (see

chapter 3). Furthermore, there may be ambiguity in the determination, (see below), due to the lack of discrimination between random orientations and uniaxial orientations at a given angle. Indeed for ultrathin films the determination of a particular average angle of orientation is not usually feasible due to lack of experimental precision.

Thus for a random array of axially oriented molecules, (where there is no external force which causes the sample molecules to orient preferentially in either x or y directions, the band intensities will depend on all the three electric field components. The LDR can then be written, [144a]:

$$A_{TE} / A_{TM} = \frac{|E_y|^2}{|E_x|^2 + |E_z|^2} \quad (2.51)$$

For such a uniaxial system the measured absorbance can be written, [144b]:

$$A = b |\langle m | \bar{\mu} \cdot \bar{E} | k \rangle|^2 \quad (2.52)$$

Where,

$\langle m |$ and $\langle k |$ are the states involved in the transition

$b = \text{constant}$

$\bar{\mu} = \text{absorption transition moment}$

$\bar{E} = \text{electric field vector}$

The measured absorbance can then also be written as:

$$A = cl (\mu_x E_x + \mu_y E_y + \mu_z E_z)^2 \quad (2.53)$$

Where,

$c = \text{constant}$

$l = \text{effective path length}$

$$E_x: \quad \cos \psi = \sin \theta \cos \phi$$

$$E_y: \quad \cos \psi = \sin \theta \sin \phi$$

$$E_z: \quad \cos \psi = \cos \theta$$

ψ = angle between electric field vector of interest and the transition moment vector. The transition moment vector is perpendicular to the chain director, for our case.

θ = angle between the transition moment axis and the z axis.

ϕ = the angle the transition moment vector projection into the x-y plane, makes with the x axis.

Thus for, TE radiation, (E_y component only):

$$A_{TE} = cl |E_y|^2 |\mu|^2 \sin^2 \theta \sin^2 \phi = \frac{cl |E_y|^2 |\mu|^2 \sin^2 \theta}{2} \quad (2.54)$$

and for TM radiation, (E_x and E_z components):

$$A_{TM,z} = \frac{cl |E_z|^2 |\mu|^2 \sin^2 \theta}{2} \quad (2.55)$$

$$A_{TM,x} = cl |E_x|^2 |\mu|^2 \cos^2 \theta \quad (2.56)$$

So the Linear Dichroic Ratio = A_{TE} / A_{TM}

$$= \frac{|E_y|^2}{|E_x|^2 + 2|E_z|^2 \cot^2 \theta} \quad (2.57)$$

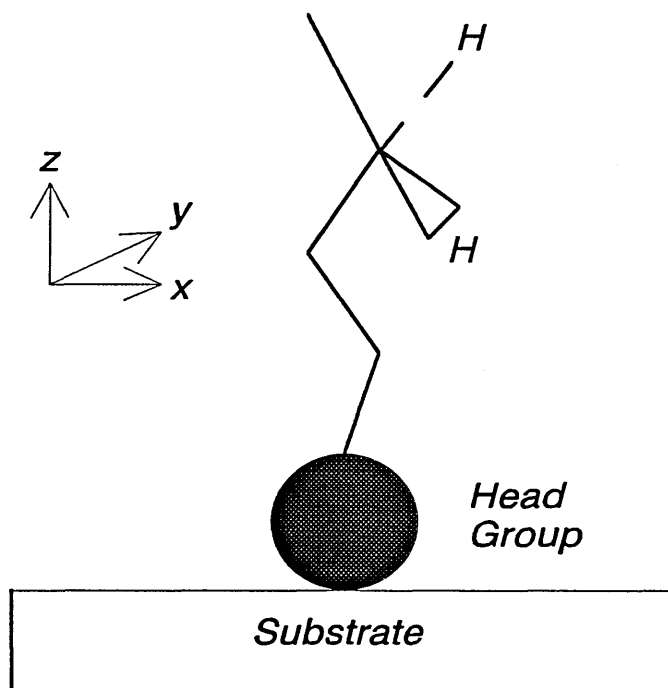
Equation (2.57) is relevant to a range of uniaxial samples from orientationally ordered, ('perfect'), to orientationally disordered, (random), systems. Taking one extreme of this, (see figure 2.9.), where all the molecular axes are parallel to the z axis, i.e. 'perfect' orientational order, angle θ is 90° . Equation (2.57) then reduces to:

$$\text{LDR} = A_{\text{TE}} / A_{\text{TM}} = \frac{|E_y|^2}{|E_x|^2} \quad (2.58)$$

It has already been mentioned that for an ordered system, with a certain angle of orientation, an LDR equivalent to that of a completely random system can arise. This will occur when equation (2.57) reduces to equation (2.51), i.e. when $\cot^2 \theta = 0.5$, i.e. when $\theta = 54.7^\circ$.

Therefore, when interpreting linear dichroic ratio results, great care must be taken and in general a determination of θ from equation (2.57) is problematical.

Figure.2.9. Long Alkyl-Chain Surfactant on Substrate.



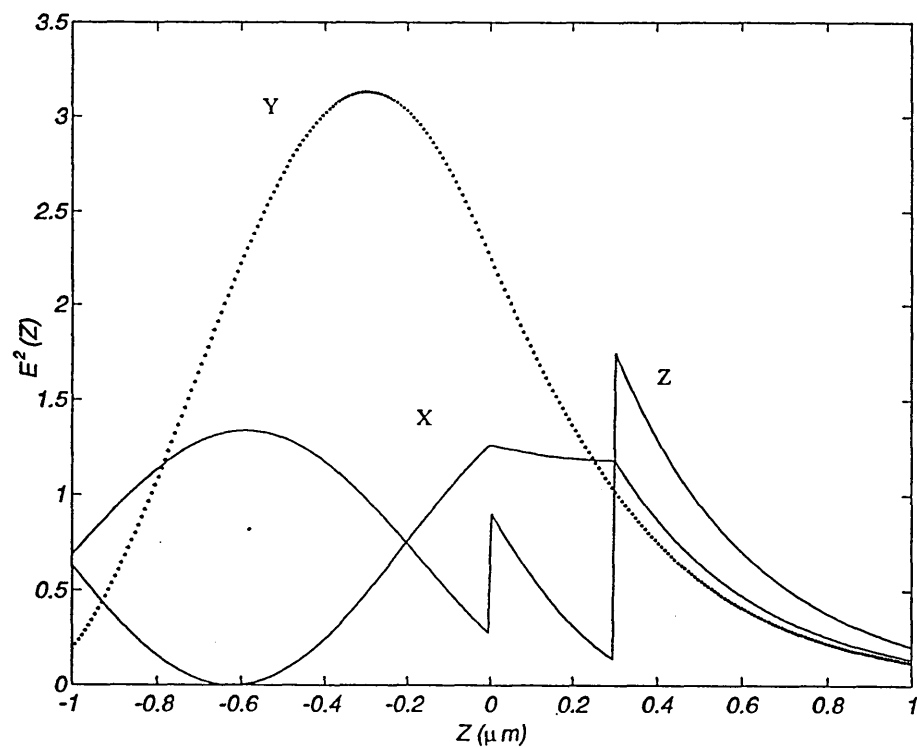
By substituting values of E_x , E_y and E_z into equations (2.51) and (2.58), the theoretical linear dichroic ratios for the orientationally ordered and the 'random' cases can be calculated. By measuring the values of A_{TE} and A_{TM} experimentally, the experimental dichroic ratio values can be calculated using equations (2.51) and (2.58). The experimental values can then be compared to the theoretical ones to determine the experimental degree of orientational order. Obviously, the more accurate the calculated theoretical dichroic ratio values are, the more reliable the comparison to experimental dichroic ratios will be. There are two methods of calculating the theoretical linear dichroic ratios which need to be defined. The first involves calculating the values of E_x , E_y and E_z from equations (2.35) to (2.37), for the semi-infinite bulk case, or from equations (2.38) to (2.40), for the thin film case, defined by Harrick, [143], and simply substituting

these values into equations (2.51) and (2.58) to give the 'perfect' and 'random' linear dichroic ratios. This method does not take account of the presence of intermediate layers between the sample and the substrate, e.g. an oxide layer. This is particularly important when considering thin films, e.g. a few monolayers or less, where the intermediate film thickness may be greater than the actual sample thickness or have optical properties which would effect the electric field components substantially. This method also does not show the variation of the electric field strengths over the thickness of the sample. Neither is it valid for intermediate film thickness, i.e. samples which are neither infinitely thin nor thicker than a few microns. All these factors can lead to discrepancies in the calculated theoretical dichroic ratios.

The second method involves using the actual calculated electric fields, based on particular solutions to Maxwell's equations with boundary conditions appropriate to the ATR experiment, [145]. These turn out to be extremely similar to those based on the Fresnel equation approximation. This can be used to calculate the change in the electric field components, E_x , E_y and E_z over film thickness and also takes into account any intermediate layers between the substrate and sample. The refractive index of each layer, the thickness of each layer, the wavelength of radiation and the angle of incidence are all taken into account. Other properties of each layer, such as whether the substrate is a dielectric or a metal are also taken into account. The output of the computer program is in the form of a plot of the electric field components squared, i.e. E_i^2 , (where $i=x,y$ or z), versus the depth penetrated through the sample. Figure 2.10. shows the variation in the electric field components for an ATR experiment with the following parameters: refractive index of substrate, $n_1 = 2.428$, attenuation index for substrate, $\kappa_1 = 0$, refractive index of sample, $n_2 = 1.64$, attenuation index of sample, $\kappa_2 = 0.4$, thickness of sample, $d_2 = 0.3 \mu\text{m}$, refractive index of surrounding atmosphere, $n_3 = 1$, attenuation index of surrounding atmosphere, $\kappa_3 = 0$. E_x , E_y and E_z are represented here as E_x^2 , E_y^2 and E_z^2 . $Z = 0$ represents the

interface between the substrate and the sample. The positive section of the z axis represents the rarer medium and the negative section of the z axis represents the denser medium. The variation of the electric field components through the sample can be clearly seen. The areas under each of the curves, E_x^2 , E_y^2 and E_z^2 , can also be integrated using the computer program. These integrated values can be substituted into equations (2.51) and (2.58) to give more accurate theoretical linear dichroic ratio values than by simply using E_x^2 , E_y^2 and E_z^2 values calculated from Harrick's equations.

Figure.2.10. Variation of Electric Field Components Through an ATR Sample.



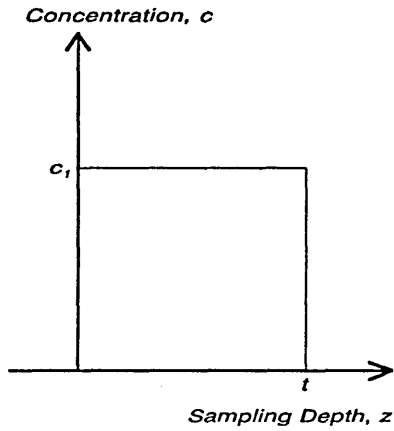
2.3.6. Surface Excess Concentrations in Inhomogeneous Systems.

Section 2.3.2. dealt with, amongst other issues, the equations relevant to one type of inhomogeneous system, i.e. one where the refractive index varies significantly with depth sampled, e.g. a few Langmuir-Blodgett layers on a substrate. As the evanescent field passes through the sample, it probes first the LB films with a refractive index value of approximately 1.4 - 1.5, then it passes into the air, with a refractive index of 1.0. For these systems, the thin film approximation is used. In this section, a different type of inhomogeneous system will be considered, namely one where the concentration is a function of sampling depth but the refractive index is, to a first approximation, constant, e.g. adsorption of a surfactant from bulk solution onto a substrate in the presence of the solution. The concentration will increase as the surface/bulk solution interface is approached. However the organic solvent will probably have a similar refractive index to that of the surfactant, so the refractive index will not vary greatly. Tompkins, [146], and Ohta and Iwamoto, [147], addressed the problem of varying concentration by using the equations for the semi- infinite bulk approximation as a starting point, giving:

$$\frac{A}{N} = a = \frac{n_2^2 E_0^2 \alpha}{\cos \theta} \int_0^{\infty} c(z) e^{-2z/d_p} dz \quad (2.59)$$

Tompkins considered a step profile, (see figure.2.11.), such that $c = c_1$ for $z \leq t$, and $c = 0$ for $z > t$.

Figure 2.11. Tompkins Step Concentration Profile.



By applying the step profile to equation (2.59) and integrating, Tompkins obtained:

$$\frac{A}{N} = a = \frac{n_{21} E_0^2}{\cos \theta} c_i \frac{d_p}{2} [1 - e^{-2t/d_p}] \quad (2.60)$$

Using Harrick's definition for d_e :

$$d_e = \frac{n_{21} E_0^2 d_p}{2 \cos \theta}$$

$$\frac{A}{N} = a = \alpha c_i d_e [1 - e^{-2t/d_p}] \quad (2.61)$$

The disadvantages of this approach include the facts that when $t > \lambda_1$, c_i can be determined but not t and that when $t < 0.05\lambda_1$, $c_i t$ can be determined but not the individual values of c_i and t .

Sperline et al, [148], considered a situation where there was both adsorbed surfactant on the substrate and free surfactant in the bulk solution. They used Tompkin's theory and a different concentration profile to study this system.

Sperline's concentration profile is as follows:

$$c(z) = c_i + c_b \text{ for } 0 < z < t \text{ and } c(z) = c_b \text{ for } t < z < \text{infinity.}$$

$c(z)$ = Concentration in M as a function of distance from the interface.

c_i = Interface concentration

c_b = Bulk concentration

t = Film thickness in cm

Because the concentration profile does not fall to zero, there will be both interface and bulk concentration terms in the absorbance equation. The integral

in equation (2.59) was evaluated by using the approximation $e^{(-2t/d_p)} = 1 - \frac{2t}{d_p}$

since $2t \ll d_p$. Substitution of d_p and d_e (unpolarised), into equation (2.61)

gave:

$$\frac{A}{N} = \alpha c_b d_e + \alpha (2d_e / d_p) (c_i t) \quad (2.62)$$

Both interface and bulk terms are present in this equation. This theory assumes that the molar absorption coefficient, α , of the surfactant is the same, when the surfactant is in bulk solution as when it is adsorbed onto the surface. This is not necessarily the case as the value of α for the part of the surfactant adsorbed onto the substrate may change on adsorption. In order to calculate c_b , it is also assumed that the bulk concentration changes very little as adsorption occurs. Therefore for highly concentrated solutions this is an accurate approximation.

Rewriting equation (2.62) gives:

$$\frac{A_s}{N} = \alpha_s c_s d_{es} + \alpha_s (2d_{es} / d_{ps}) (c_i t) \quad (2.63)$$

Where s denotes the sample surfactant. Substituting for N from the Beer-Lambert equation,

$$A_r = N \alpha_r c_r d_{er} \quad (2.64),$$

where r denotes the bulk solution, into equation (2.63), gives:

$$\Gamma = d_{ps} ((\alpha_r c_r d_{er} A_s / A_r) - \alpha_s c_s d_{es}) / (2000 \alpha_s d_{es}) \quad (2.65)$$

Where $\frac{c_i t}{1000} \text{ molcm} / \text{dm}^3 = \Gamma \text{ molcm}^{-2} = \text{Gibbs Surface Excess}$.

Sperline also calculated the percentage bulk contribution to the band intensity

as follows:
$$\% \text{ bulk} = 100 \frac{c_s d_s}{c_s d_{ps} + 2000 \Gamma} \quad (2.66)$$

Therefore if $c_i t$ and hence Γ can be determined from the ATR experiment, the percentage bulk contribution to the infrared band intensity can also be

determined. Before the experiment is carried out, however, the ATR crystal must first be carefully calibrated to determine the value of N , the number of reflections. Sperline et al have developed a method for doing this, which is outlined below:

2.3.7. Calibration of the Internal Reflection Element.

In the previous section, a method was described for determining the surface excess of a surfactant on a substrate, in the presence of the bulk solution. This is dependent upon the ability to separate the bulk and surface components which in turn depends on obtaining accurate values of d_e and d_p .

d_e is dependent upon (i) the refractive indices of the sample and the IRE, (ii) the wavelength of radiation, (iii) the polarisation, (iv) the angle of incidence, θ_{inc} , and (v) the number of reflections, N . (i) to (iii) are known and (iv) and (v) can be calculated by one of two methods: (a) by geometrical measurements of the ATR crystal, which tend not to be very accurate or (b) by Sperline's iterative procedure which is described below:

Sperline's procedure uses a species which will not adsorb onto the IRE. This is necessary as adsorbing species would lead to enhanced intensities in the ATR spectra. A solution of concentration, c_r , is prepared and the molar adsorption coefficient, α_r , of this solution is determined from a transmission measurement using the following equation: $A = -c_r l \alpha_r$ (2.67)

Where A = absorbance, c_r = concentration and l = solution path length.

The ATR spectrum of the solution is then obtained and the integrated absorption of a reference band in the spectrum is measured. d_{er} is calculated for the unpolarised case, using equations (2.45), (2.46) and (2.49), by assuming a value for θ . (Usually 45° is used as this is the manufacturer's specification). N is then calculated from equation (2.64). Using the following equation:

$$N = \frac{L}{d \tan \theta} \quad (2.68)$$

where L = sample contact length and d = sample thickness, a new value for $\theta = \theta_{\text{calc}}$ is determined. The original value of θ is now θ_{old} . The new value of θ is

$$\text{calculated as follows: } \theta_{\text{new}} = \frac{2\theta_{\text{old}} + \theta_{\text{calc}}}{3} \quad (2.69)$$

θ_{new} is then used to calculate a new value of d_e , which in turn is used in equation (2.64) to calculate a new value of N , which is then used in equation (2.68) to calculate a new value of θ_{calc} . The previous value of θ_{calc} now becomes

$$\theta_{\text{old}}. \text{ The cycle continues until: } \frac{|\theta_{\text{new}} - \theta_{\text{calc}}|}{\theta_{\text{new}}} < 0.0002 \quad (2.70)$$

The convergence of this process usually requires less than 10 cycles and the resulting values of N and θ can be used in the determination of surface excess concentrations, [149].

The thin film or semi- infinite bulk approximations for electric field components can be calculated from equations (2.35) to (2.40), dependent upon sample thickness. Electric field components can also be calculated from the program based on Maxwell's equations for a plane wave. For surfactant adsorption in the presence of bulk solution, the semi-infinite bulk approximations should be used and the surface and bulk components should be separated in order to determine the contribution of the adsorbed surfactant to the integrated intensity. This is done in chapter 4. When a thin film, such as a monolayer, is considered, both the thin film approximations and the theory based on Maxwell's equations should be applied to determine the electric field components and therefore the linear dichroic ratios. This is done in chapter 3.

Raman spectroscopy is a well- known complimentary technique to infrared spectroscopy and has been used here to provide more information on the systems being studied. The following section will detail the background theory of Raman spectroscopy.

2.4. Raman Spectroscopy.

Introduction.

The 'Raman' effect was predicted in 1923, [150], but was first observed by Raman in 1928. The early experiments used focused sunlight as the source but later Raman obtained spectra of benzene and carbon tetrachloride using a spectrograph with a mercury lamp source. The Raman scattered light is very weak, typically 10^{-8} times the intensity of the incident radiation. Therefore for many years source stability and low intensity were problems. Nowadays, highly monochromatic, narrow beam, coherent sources are available such as Argon ion and Helium- Neon lasers. Also facilities such as high resolution Raman microscopy and imaging have been developed which make the technique much more versatile. The theory of Raman spectroscopy has been well covered by a variety of authors, [150-152], so only a summary will be given here.

The Raman effect is simply the inelastic scattering of light by matter. When a photon of light interacts with a system, it can be scattered in one of three ways:

- i) Elastic scattering can occur where the photon retains its initial energy.
- ii) Inelastic scattering can occur where the photon can either:
 - a) Give its energy up to the molecule or
 - b) Remove energy from the molecule.

When the photon gives energy to the molecule the scattering is defined as Stokes scattering and when energy is removed from the molecule, the scattering is defined as anti- Stokes scattering. Rayleigh scattering arises when the photon retains its initial energy. The scattering range, over which most molecular vibrations and rotations occur, that is generally used is 2 to 5000 cm^{-1} .

2.4.1. Classical Theory.

When a molecule is placed in an electric field, a dipole moment, μ_{ind} , is induced, which for small fields is proportional to the field strength, E as follows:

$$\mu_{ind} = \alpha E + \beta E^2 + \gamma E^3 + \dots \quad (2.71)$$

Where α is the polarisability of the molecule, i.e. the ease with which the electron cloud of the molecule can be distorted. If the applied electric field is alternating the induced dipole will also alternate at the same frequency. The alternating electric field is expressed as follows:

$$E = E^0 \cos 2\pi \nu_0 t \quad (2.72)$$

E^0 = electric field at time t

ν_0 = angular frequency of radiation

The induced dipole emits or scatters radiation of frequency, ν_0 , which is Rayleigh scattering. If a diatomic molecule vibrates with frequency, ν_v , and performs simple harmonic vibrations, then q_v , the displacement, along the axis of vibration at time, t , is given by:

$$q_v = q_0 \cos 2\pi \nu_v t \quad (2.73)$$

If there is a change in polarisability during the vibration, for small displacements it becomes:

$$\alpha = \alpha^0 + \left(\frac{\partial \alpha}{\partial q_v} \right)_0 q_v \quad (2.74)$$

Substituting (2.73) into (2.74) gives:

$$\alpha = \alpha^0 + \left(\frac{\partial \alpha}{\partial q_v} \right)_0 \cos 2\pi \nu_v t \quad (2.75)$$

If radiation of frequency, ν_0 , interacts with the molecule then:

$$\mu_{ind} = \alpha E = \alpha E^0 \cos 2\pi \nu_0 t \quad (2.76)$$

Substituting (2.75) into (2.76) gives:

$$\mu_{ind} = \alpha^0 E^0 \cos 2\pi \nu_0 t + \left(\frac{\partial \alpha}{\partial q_v} \right)_0 E^0 q_0 \cos 2\pi \nu_v t \cos 2\pi \nu_0 t \quad (2.77)$$

$$= \alpha^0 E^0 \cos 2\pi\nu_0 t + \left(\frac{\partial \alpha}{\partial q_\nu} \right)_0 \frac{E^0 q_0}{2} [\cos 2\pi(\nu_0 + \nu_\nu)t + \cos 2\pi(\nu_0 - \nu_\nu)t]$$

Therefore ν_0 = Rayleigh scattering, $\nu_0 \pm \nu_\nu$ = Raman scattering.

For Raman scattering to occur the following must be true:

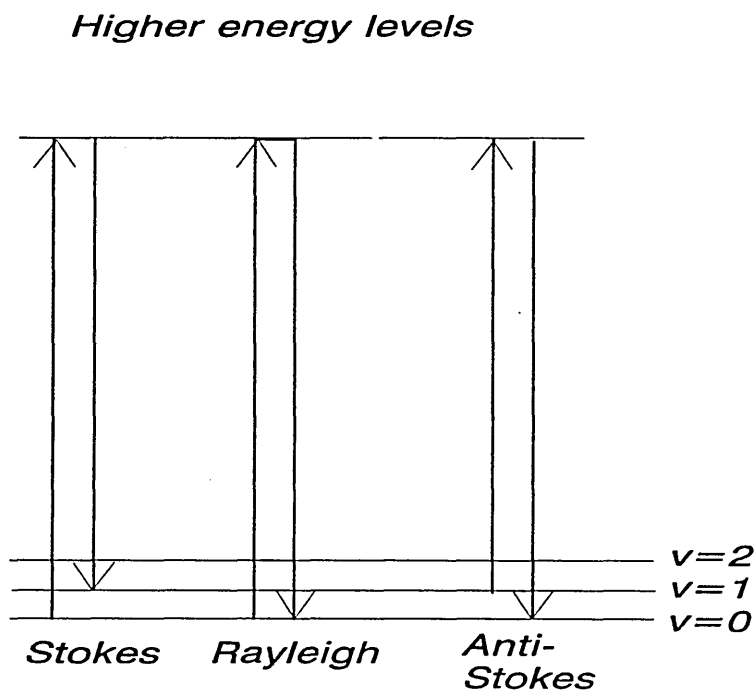
$$\left(\frac{\partial \alpha}{\partial q_\nu} \right)_0 \neq 0 \quad (2.78)$$

i.e. the polarisability of the molecule must change during the vibration.

2.4.2. Quantum Theory.

The quantum theory approach to Raman spectroscopy recognises that vibrational energy in a molecule is quantised. Rayleigh and Raman scattering are portrayed schematically in figure.2.12.

Figure.2.12. Rayleigh and Raman Scattering.



Where v are the vibrational levels in a lower energy electronic state.

At room temperature most vibrations are in the ground state, i.e. $v=0$.

Therefore Stokes transitions are more likely to occur than anti- Stokes transitions.

2.4.3. Polarisability.

This was defined in section 2.4.1. It is a tensor quantity and has x, y and z components. Therefore an electric field component can induce a dipole in the x, y and z directions as follows:

$$\begin{aligned}\mu_{\text{ind } x} &= \alpha_{xx} \epsilon_x + \alpha_{xy} \epsilon_y + \alpha_{xz} \epsilon_z \\ \mu_{\text{ind } y} &= \alpha_{yx} \epsilon_x + \alpha_{yy} \epsilon_y + \alpha_{yz} \epsilon_z \\ \mu_{\text{ind } z} &= \alpha_{zx} \epsilon_x + \alpha_{zy} \epsilon_y + \alpha_{zz} \epsilon_z\end{aligned}\tag{2.79}$$

2.4.4. Intensities.

The intensity of a Stokes Raman band of frequency, ν , scattered over a solid angle of 4π , by a randomly oriented molecule, moved from initial vibrational state, m , to final state, n , by an electric field is as follows:

$$I_{mn} = c I_o (\nu_o - \nu)^4 \sum_{ij} \left| \frac{\partial \alpha}{\partial q} \right|^2\tag{2.80}$$

I_o = Incident intensity

c = constant

Now that some of the background theory has been described, it is necessary to explain how to obtain Raman spectra experimentally.

2.4.5. Raman Instrumentation.

There are a number of instruments available for obtaining Raman spectra. These include dispersive spectrometers and spectrographs, Fourier transform Raman spectrometers and Raman microscopes. The grating, (or gratings), of a spectrometer disperses the light entering the monochromator and passes it

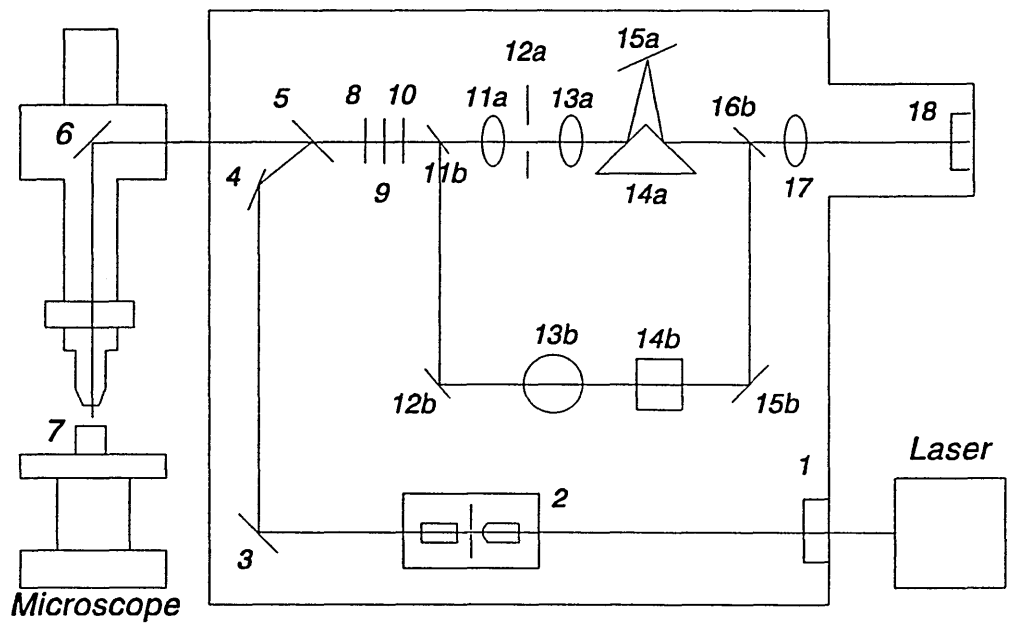
through one or more very narrow slits. This results in a well resolved, monochromatic beam. The spectrum, however is produced by rotating the grating, so that different wavelengths are focused onto the detector, which produces dispersion of the light. The spectrograph, on the other hand, uses much wider slits and a grating which produces less dispersion. Therefore a relatively broad band of light reaches the detector. The main advantage of the spectrograph is its high throughput and the main disadvantages are the low resolution and poor stray light rejection. Raman spectroscopists require high resolution and good stray light rejection. Therefore the spectrometer, with a double or triple monochromator and a photomultiplier tube detector, was more widely used than the spectrograph, before the introduction of CCD detectors. Fourier transform Raman spectroscopy has only recently been popular. In 1986, Hirschfield and Chase, [152], developed the basis of a method for converting FTIR instruments so that they could be used for Raman spectroscopy.

The Raman microscope was originally developed in the 1970's. The details of a Raman microscope, which has been developed recently, will be described here. It comprises a single stigmatic spectrograph, an integral optical microscope and a Peltier- cooled, multi- channel charged coupled device, (CCD), detector. The advantages of this system include the fact that surfaces can be imaged on a μm scale and that laminates can be 'depth profiled', also on a μm scale.

2.4.5.1. The Renishaw Raman Imaging Microscope.

A schematic of the microscope, system 2000, can be seen in figure.2.13.

Figure.2.13. A schematic of the Renishaw Raman Imaging Microscope.



Key:

- | | | |
|------|------------------------------------|---------------------------------|
| 1. | Plasma line rejection filter | |
| 2. | Spatial filter, (includes pinhole) | |
| 3. | Adjustable mirror | |
| 4. | Adjustable mirror | |
| 5. | Holographic notch filter | |
| 6. | Moveable mirror | |
| 7. | Sample | |
| 8. | Second holographic notch filter | |
| 9. | Polariser | |
| 10. | Half wave plate | |
| 11a. | Lens before slit | 11b. Moveable mirror |
| 12a. | Adjustable slit | 12b. Mirror |
| 13a. | Lens | 13b. Thin film filters |
| 14a. | Reflecting prism | 14b. Fabry Perot Interferometer |
| 15a. | Diffraction grating | 15b. Mirror |
| 16b. | Moveable mirror | |
| 17. | CCD focusing lens | |
| 18. | CCD | |

This instrument has been developed over the past few years by Prof. David Batchelder, University of Leeds and by Prof. David Pitt, Raman Transducer Systems, and has many advantages over a conventional Raman spectrometer. It can provide a high spectral resolution, (1 cm^{-1}), over a broad wavenumber range, (100 cm^{-1} to 7000 cm^{-1}), with a relatively high optical throughput, (25%). (Multiple grating spectrographs have a much lower light throughput). Therefore lower powered lasers can be used, (e.g. 25mW), as opposed to the expensive 5W water-cooled laser used with conventional Raman instruments. There is the possibility of obtaining depth resolution, via a confocal experiment, of $2\text{ }\mu\text{m}$ and the detection system, the Peltier-cooled, charged coupled device, (CCD), has very high quantum efficiency and very low noise. Two-dimensional photograph-like images can also be obtained.

The system can be operated in a variety of modes including Raman microprobe, confocal and imaging modes.

In the Raman microprobe mode, light from a small area of the sample is collected to give a Raman spectrum. Laser light, with a power of 25mW, can be first attenuated by the attenuation wheel, (before the plasma rejection filter), down to 5mW, if necessary, and then passes through the plasma line rejection filter, (1). This spectrally filters the laser to give a more 'monochromatic' beam. It blocks all emissions from the laser beam except the main lasing line. These unwanted emissions arise mainly from non-lasing transitions in the laser plasma. The filtered laser beam then passes through the spatial filter, (2), where the spatial distribution of the light intensity is improved. The spatial filter consists of a microscope objective, of X20 magnification, which focuses the beam onto a $10\mu\text{m}$ pinhole and then onto a second microscope objective, magnification X4. The position of the second objective is controlled by the computer and in the microprobe method it is positioned so that it is focused on the pinhole to produce a collimated, spatially clean beam. This collimated beam is then reflected by adjustable mirrors (3) and (4) onto a holographic notch filter, (5),

which reflects light of the laser wavelength and transmits all other wavelengths. Therefore the laser beam is reflected into the microscope and onto the sample, via mirror (6), which may be moved out of the beam path for normal use of the microscope. The microscope has short- working distance lenses of magnification X10, X20, X50 and X100. In the microprobe method, the X20 or X50 magnification lenses are used for studying liquids or solids and the laser beam is focused onto a small spot on the sample. The resulting Rayleigh and Raman scattering pass back up the microscope and onto the holographic notch filter, via mirror (6). The holographic notch filter then reflects the Rayleigh scatter, (laser line), back down into the lower half of the system and transmits the useful Raman scatter. Therefore the Rayleigh scatter is filtered out. The Raman light then hits another holographic notch filter, (8), which further reduces the Rayleigh scatter. At this point a polariser, (9), and a half wave plate, (10), can be used. In the microprobe method the beam then passes through a lens, (11a), which focuses the light onto the adjustable slits, (12a), which block unwanted stray light from the sample or spectrometer. This is where the main control of resolution and light throughput occurs. The light then passes to the lens, (13a), where it is recollimated, before it is reflected from the reflection prism, (14a), onto the diffraction grating, (15a). The diffraction grating is mounted on a rotary stage whose position can be altered by the computer. Therefore the angle of incidence and the central wavelength of the beam can be controlled. The grating has 1800 grooves/mm which gives a spectral range of 500 cm^{-1} when using a helium- neon, 632.8 nm, laser source and a spectral resolution of less than 2 cm^{-1} . The reflection prism then deflects the dispersed light through the CCD focusing lens, (17), and onto the surface of the CCD. The CCD is comprised of 600 vertical by 400 horizontal pixels. The long axis of the CCD describes spectral dimension while the shorter axis describes image height. Only a narrow vertical strip of the spectrum is used and the horizontal pixels are added together, (binned), to improve the signal to noise ratio of the system.

In the confocal mode the instrument is used as above, with the entrance slits closed to 10 μ m slit width, the X100 magnification lens and the CCD closed to 600 vertical x 4 horizontal pixels. This provides a depth resolution of the order of 2 μ m. The depth resolution can be monitored by using a silicon wafer as an internal calibration standard. The size of the CCD selected can be controlled by the software. The confocal mode produces a spectrum obtained from a very small volume of the sample.

The Raman imaging, or microscope, mode produces a photograph- like image of the sample using light scattered from one particular Raman peak. The beam passes through optics (1) to (10) as for the microprobe method. However the beam spot size on the sample is much larger than for the microprobe method. This is obtained by the computer-controlled movement of the second objective in the spatial filter, (2), being moved so that it is no longer focused on the pinhole. This means that the beam is no longer collimated when it hits the sample and therefore illuminates a larger sample area than for the microprobe method. After passing through the second holographic notch filter,(8), the Raman scatter is reflected by moveable mirror, (11b), onto mirror (12b). Mirror (11b) is automatically moved into the light path when the image function is selected by the software. Mirror (12b) then reflects the light onto the thin film filters, (13b). These have a narrow pass band and isolate the light from the chosen Raman band. They are tuned to a particular frequency by adjusting their angle of incidence with respect to the incoming beam. This again is controlled by the software and there is a choice of 9 different filters. The imaging beam then proceeds via mirror, (15b), and moveable mirror, (16b), to the CCD imaging lens, (17). This focuses the light onto the CCD to produce a photograph- like image which represents the two- dimensional distribution of the material, characterised by the chosen Raman peak. The imaging experiment can be used to determine the spatial distribution of a particular compound For example, in a

blended polymer, if one of the polymers has a Raman peak different from the other polymers this can be used to determine its distribution in the blend.

The confocal experiment can be used to probe laminates of different materials for example a laminate consisting of a thin layer, 2 μm , of polyethylene on top of a thick polypropylene layer has been depth profiled by Renishaw, [154]. As the laser beam is moved down 2 μm through the laminate, the bands due exclusively to the polyethylene disappear and the bands due exclusively to the polypropylene appear in the Raman spectra. This method can also be used for determining if inter-diffusion occurs within a particular laminate system. The confocal method has been utilised to produce some of the results presented in this thesis and described in chapter 6.

Now vibrational spectroscopy has been dealt with, a non- vibrational technique, atomic force microscopy, which is primarily used for obtaining topographic information from insulating samples, will be described in the next section.

2.5. Atomic Force Microscopy.

Introduction.

In 1986 Gerd Binnig and Heinrich Rohrer won the Nobel Prize in Physics for the invention of the Scanning Tunneling Microscope. They discovered that this could image individual atoms with excellent resolution. The success of this instrument led to the invention of other scanning probe microscopes, including the atomic force microscope, [155]. In scanning tunneling microscopy, (STM), a sharp metal tip is brought close enough to a metal sample so that electrons can tunnel, quantum mechanically, through the vacuum barrier separating the tip and sample. This tunneling current is extremely sensitive to the height of the tip above the surface. The surface topography of samples on a metal substrate can be easily analysed using STM, [156]. However, for insulating samples the method is of no use. This is where atomic force microscopy, (AFM), comes in. It was developed especially to image insulating samples and records the interatomic forces between a cantilever tip and atoms in a sample as the tip is scanned over the sample surface.

In this section a summary of the theory of AFM will be given, along with its advantages and disadvantages. The theory presented here has been derived from a variety of reviews and books on the subject, [155-158].

2.5.1. Atomic Force Microscopy Theory.

As previously stated, atomic force microscopy was initially developed in order that insulating surfaces could be imaged. G.Binnig, C.Gerber and C.Quate developed the first atomic force microscope in the late eighties, [155]. They discovered that it was possible to make a cantilever with a spring constant weaker than the equivalent spring constant between atoms. For example, the vibrational frequencies, ω , of atoms bound in a molecule are typically 10^{13} Hz. The mass of these atoms, m , is of the order of 10^{-25} kg. These values can be combined to give the interatomic spring constant, k , where

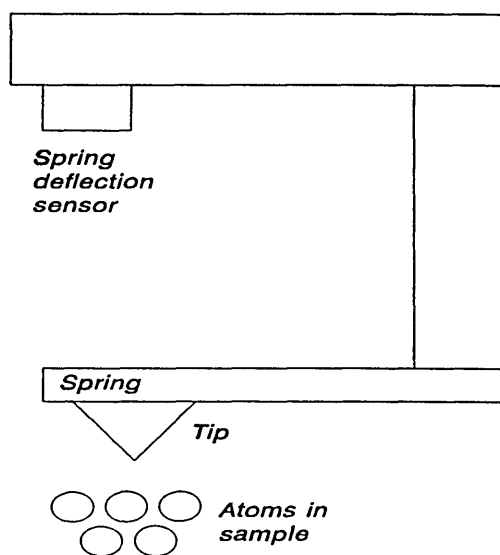
$$k = \omega^2 m \quad (2.81),$$

of the order of 10 Nm^{-1} . For comparison, the spring constant for a piece of aluminium foil, 4 mm long, is 1 Nm^{-1} . They believed that by sensing angstrom-sized displacements of a cantilever spring with a k value of the order of 10 Nm^{-1} , one could image atomic-scale topography. Also the force applied would not be strong enough to displace atoms from their atomic sites.

2.5.2. Components of the Atomic Force Microscope.

There are several necessary components required by all force microscopes. These are a sharp tip mounted on a 'soft' cantilever spring, a method of sensing cantilever deflection, a system to monitor and control the tip deflection, (and hence the interaction force), a mechanical system, which is usually piezoelectric, that can move the sample in a raster pattern with respect to the tip, and a display system which converts the measured data into an image. A schematic of the force sensor of an atomic force microscope is given in figure.2.14.

Figure.2.14. AFM Force Sensor.



The spring deflection sensor can be based on electron tunneling to the back of the spring, on optical interference between the back of the spring and a reference plate or by deflection of a laser light beam reflected off the back of the spring. The sensor should have sub-angstrom sensitivity and exert negligible force on the cantilever. The electron tunneling method, which was used by Binnig, is very sensitive. The tunneling current between two conducting surfaces varies exponentially with distance, (a factor of 10 per angstrom displacement). However contamination of the conducting surfaces leads to degradation of the instrument performance. Therefore most modern atomic force microscopes use the optical detection systems, interferometry or laser-beam deflection. Both are capable of measuring cantilever displacements of 0.01 nm. In the laser-beam deflection method, light from a diode laser is reflected off a mirror-like cantilever and is sensed by a two-element detector. The advantage of the interferometric sensing system is that mirror-like cantilevers are not required. This is advantageous for magnetic imaging where fine wire cantilevers are used. Original atomic force microscopes used a handmade cantilever spring, made from a piece of gold foil, approximately 1 mm long. The stylus used in conjunction with this was a small diamond glued to the foil. Nowadays, cantilever tips are microfabricated from silicon, silicon oxide or silicon nitride, using photolithographic techniques. Spring constants in the range of 0.1 to 1 Nm^{-1} and resonant frequencies of 10 to 100 KHz can be obtained. The cantilevers can be made with integrated tips.

The atomic force microscope can be operated in a variety of modes, including the contact and non-contact modes. Contact mode, as it suggests, scans over the sample surface, with the tip in contact with the sample. The forces involved here are the short-range interatomic forces. In the non-contact mode, the tip is moved away from the sample by 10 to 100 nm and longer range forces such as magnetic, electrostatic and attractive van der Waals forces become involved. The non-contact mode uses a different force detection system from the contact mode.

The cantilever is made to vibrate near its resonant frequency by the piezoelectric system. The spring constant of the cantilever, c_0 , is modified by the gradient of the force, $(\delta F_z / \delta z)$, thus:

$$c = c_0 + \delta F_z / \delta z \quad (2.82)$$

c = Effective spring constant .

For example, if the sample exerts an attractive force on the cantilever, the spring constant will decrease. Therefore the resonant frequency will decrease and this reduction in resonant frequency is detected by measuring the frequency change of the vibration. The major source of noise in the non-contact mode results from thermal vibrations of the cantilever. Since atomic force microscopy is such a sensitive technique, it is very important to eliminate external vibrations, e.g. building vibrations. These could cause unwanted vibration of the tip on the surface and generate false information about the sample. Cantilevers of very high resonant frequencies are required to reduce this effect. The frequency of vibration, e.g. of a building, is ν . The resonant frequency of the atomic force microscopy system is ν_0 . The amplitude of the tip motion is attenuated by a factor of $(\nu/\nu_0)^2$ in the limit $\nu \ll \nu_0$. Therefore if $\nu_0 = 20$ KHz and $\nu = 20$ Hz, a building vibration of amplitude $1 \mu\text{m}$ would result in a tip attenuation of less than 0.001 nm, which is very low. Other methods of reducing tip vibration include mounting the atomic force microscope on a vibration-table and obviously using the microscope on the ground floor or basement of a building, as opposed to higher floors.

2.5.3. Atomic Resolution.

Atomic resolution of surfaces is obtained by using a very small loading force on the tip, of the order of 10^{-7} to 10^{-11} N. The earlier stylus profilers used loading forces of approximately 10^{-4} N, which clearly would not be able to produce atomically resolved images. Ideally the tip-sample interaction would be via a

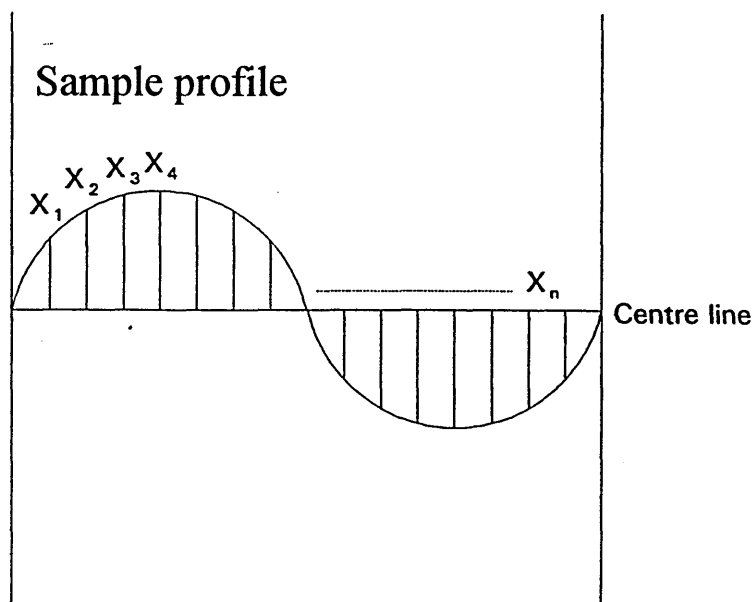
single atom at the end of the tip. Realistically the force is actually transmitted through irregularities in the tip, a few angstroms in size.

In order to image organic molecules, such as proteins, on a sample surface, the tip force must be less than 10^{-8} N to prevent the molecules being damaged. In air this is difficult to achieve due to thin water and hydrocarbon film formation on the sample surface, giving rise to meniscus forces. This can be overcome by imaging the surface under a liquid such as water or ethanol.

2.5.4. Roughness Average.

The roughness average, R_a , also known as the centre-line-average or the mean roughness, is depicted mathematically in figure.2.15, [159]. The roughness average can be calculated using the Nanoscope III atomic force microscope software.

Figure.2.15. Mathematical Derivation of R_a .



$$R_a = \frac{|X_1| + |X_2| + \dots + |X_n|}{n} \quad (2.83)$$

R_a is the arithmetic average value of the distance of the sample profile from the centre line along the whole sample length. The centre line is drawn by the software so that the sum of the areas of the profile above the centre line is equal to the sum of the areas below the centre line.

The R_a value is representative of the average roughness and therefore spurious peaks or valleys are averaged out and do not contribute greatly to the final R_a value. The R_a value is calculated over more than one sample length, e.g. over the whole AFM image area, to ensure that the value produced is typical of the surface. No information on the shape of the irregularities in a sample is given by the R_a value.

In this thesis the R_a values for different submono- and monolayer surfaces are given as an indication of the varying roughness of these samples.

2.5.5. Advantages and Disadvantages of Atomic Force Microscopy.

Although AFM can be applied more generally than STM, (i.e. both conductors and insulating samples can be imaged), there are several disadvantages of using AFM. For conductors, STM can provide tunneling spectra, but the AFM technique does not provide any spectroscopic data. Also when imaging certain organic molecules, the surface has to be imaged under a liquid. On the positive side, the fact that molecules in a liquid can be imaged is an advantage when looking at biological systems. Also atomic resolution is possible with AFM, provided a tip with a negligible force, i.e. less than 10^{-8} N, is used. This means that many biological and other organic molecules which could not be previously imaged by STM, can now be studied. Another advantage of AFM is that the sample preparation is relatively easy, i.e. the sample is not excessively small, as for TEM.

Atomic force microscopy is an ideal technique for imaging organic monomolecular films on semiconductors, such as silicon, and on insulators such as glass. This has been done and the results are reported in chapter 5.

CHAPTER.3. ATTENUATED TOTAL REFLECTION

SPECTROSCOPY OF THE *EX SITU* ADSORPTION OF LONG-CHAIN SILANES ONTO SILICON.

Introduction.

This chapter describes studies of the *ex situ* adsorption of two long-chain silanes onto silicon. The silanes are n-octadecyltrichlorosilane, OTS, and perfluorodecyl(ethyl)trichlorosilane, F8. The main objectives of the work described in this chapter are to determine the dipping time for formation of monolayers of OTS and F8 on silicon and to determine the degree of orientational order of these silane films as a function of surface coverage. Fourier transform infrared attenuated total reflection, FTIR-ATR, spectra, plots of dipping time versus absorbance and linear dichroic ratios are presented.

3.1. Experimental.

3.1.1. Chemicals.

N-octadecyltrichlorosilane, 99%, toluene, 99.9%, methanol, 99.9%, 2-propanol, 99.9%, chloroform, 99.9%, and acetone, 99.9%, were obtained from Aldrich Chemical Co.

Perfluorodecyl(ethyl)trichlorosilane, 99.5%, and freon 113, 99%, were obtained from Fluorochem Ltd.

The fluorinated compounds were dried over molecular sieve prior to use. The silanes were stored at 5°C, in a refrigerator. All other chemicals were used as received.

3.1.2. Substrates.

The substrates used for the ATR measurements were silicon ATR crystals with 45 to 50 internal reflections. These were cut from single-crystal, p-doped, silicon wafers and had angles of 30 to 60°. For the *ex situ* work the crystals did not

require calibrating. The calibration of the ATR crystals was performed prior to use for *in situ* experiments.

The silicon crystals were pre-cleaned by washing with acetone and methanol and then by refluxing in hot 2-propanol for at least 4 hours. They were then stored in a dessicator. After silane deposition, the crystals were cleaned by polishing with diamond paste, then washed with solvent and refluxed in 2-propanol, as above. All crystals were examined for contamination by FTIR-ATR prior to use.

All the glassware was pre-silanised with a 1mM OTS solution in toluene to ensure that all the silanol sites on the glass were coated with silane before use. The glassware was then washed thoroughly with solvent, (chloroform), to remove any excess OTS deposits. Once prepared, the silane solutions were transferred into, and stored in PTFE containers for the duration of the experiment.

3.1.3. Preparation of Solutions.

Solutions of OTS in toluene, at concentrations of 0.1 M and 1 mM, were prepared in OTS-coated volumetric flasks, and used immediately. Fresh solutions were prepared for each experiment.

Solutions of F8 in freon 113, at concentrations of 0.05 M and 0.5 mM, were prepared in OTS-coated volumetric flasks, and used immediately. Fresh solutions were prepared for each experiment.

The OTS solutions were prepared and used in a fume cupboard at 33% humidity and the F8 solutions were prepared and used within a dry nitrogen atmosphere. Both OTS and F8 solutions were prepared and used at room temperature and atmospheric pressure.

3.1.4. Preparation of Samples.

The OTS was deposited onto the silicon ATR crystal, by self-assembly, from the silane solution, in 5 minute dipping stages. After each dip, the sample was washed with chloroform, with methanol, and then with chloroform again, to remove any excess silane. The crystal was then examined using FTIR-ATR spectroscopy. The crystal was dipped in the silane solution for a further 5 minutes, solvent washed and examined by FTIR-ATR again. This process was repeated up to a maximum dipping time of 120 minutes, at which point it was determined, (from the integration of the bands due to the $\nu(\text{CH}_3)$ and $\nu(\text{CH}_2)$ stretching vibrations), that monolayer coverage had been achieved. This was said to be the point at which the integrated area under the bands due to the $\nu(\text{CH}_3)$ and $\nu(\text{CH}_2)$ stretching vibrations reached a constant value.

The F8 was deposited onto the silicon ATR crystal, by self-assembly, from the F8 silane solution, in stages. After each dipping stage, the sample was washed with freon to remove any excess silane. In some cases the sample was gently 'buffed' with a lens tissue to remove excess silane deposits. The prism was then examined by FTIR-ATR spectroscopy. The maximum dipping time was determined from the integration of the bands due to the CF_2 rocking and antisymmetric stretching vibrations. When the integrated intensity of the bands reached a constant value the dipping was ceased.

The studies have been described as *ex situ* since the samples are removed from solution for measurement at various stages of submono- or monolayer formation.

Cast films of OTS, from a 0.1 M solution in toluene, and of F8, from a 0.05 M solution in freon, were prepared on silicon and examined in ATR mode. These

spectra provided reference data against which to assess the self-assembled silane thin film spectra.

3.1.5. Spectroscopic Measurements.

A Mattson Polaris Fourier transform infrared spectrometer, fitted with a liquid nitrogen-cooled bullseye mercury-cadmium-telluride detector, was used in conjunction with a micro-ATR accessory to examine the ATR samples.

The instrument parameters used were as follows: A resolution of 4 cm^{-1} , zero-filling, 98% iris, a signal gain of 4, triangular apodisation and 256 scans. The large iris and signal gain were necessary to obtain a throughput signal with the required sensitivity.

The samples were scanned three times; unpolarized, TE polarized and TM polarized, for each dipping stage. Plots of the cumulative dipping time versus the integrated intensities of the chosen bands, ($\nu(\text{CH}_3)$ and $\nu(\text{CH}_2)$ stretching vibrations for OTS and CF_2 rocking and antisymmetric stretching vibrations for F8), of the unpolarized spectra were produced, to determine the time of monolayer formation for each silane.

The polarized spectra were used to obtain linear dichroic ratio values.

All spectra have been manipulated using a software package called FIRST. A sample spectrum is produced by ratioing a spectrum of the substrate with a spectrum of the sample and substrate. Integration of infrared bands and curve-fitting techniques are also possible using FIRST.

3.1.6. Linear Dichroic Ratio Calculations.

These were calculated from the equations described in chapter 2, (2.51,2.58), in three ways as follows:

1. Using Harrick's thin film approximations, [143], to calculate E_x , E_y and E_z , (2.38-2.40).
2. Using Y.P.Song's computer programs to calculate E_x^2 , E_y^2 and E_z^2 , [145], from first principles.
3. Using experimental values of A_{TE} and A_{TM} .

Calculations of the linear dichroic ratios were made for both OTS and for F8.

3.2. Results and Discussion.

3.2.1. N-octadecyltrichlorosilane.

The results of the studies on cast and self-assembled films of n-octadecyltrichlorosilane, OTS, $\text{CH}_3(\text{CH}_2)_{17}\text{SiCl}_3$, on silicon are given in this section.

3.2.1.1. Cast Films of OTS on Silicon.

The overlaid TE and TM polarized FTIR-ATR spectra, ($4000 - 1000 \text{ cm}^{-1}$), of a cast film of OTS on a silicon ATR prism can be seen in figure.3.1. By the nature of its preparation, this film would be expected to be orientationally and conformationally disordered. The assignments of the main infrared bands in the spectrum are given in table.3.1.

Figure.3.1. FTIR-ATR Spectrum of Cast OTS Film on Silicon.

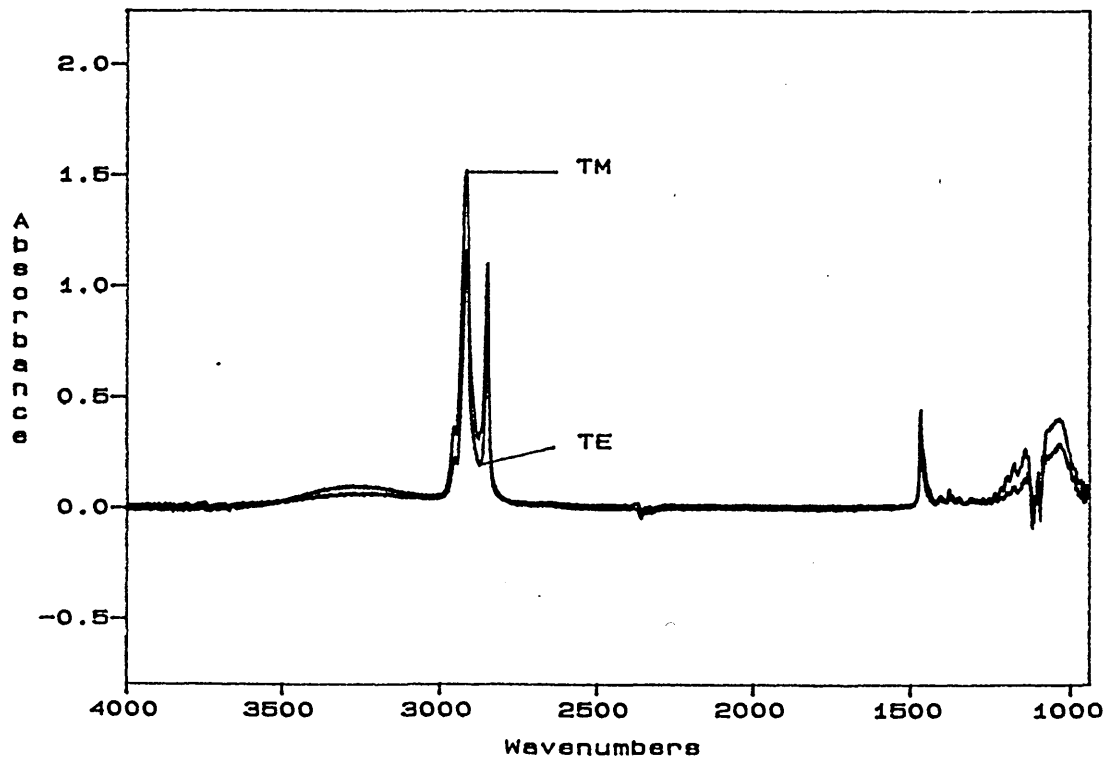


Table.3.1. Assignments of Bands in Infrared Spectrum of Cast Film of OTS on Silicon.

Band Position / cm ⁻¹	Infrared Assignment
3600-3000	$\nu(\text{OH})$ of H ₂ O
2955	$\nu(\text{CH}_3)$
2925	$\nu_{\text{as}}(\text{CH}_2)$
2854	$\nu_{\text{s}}(\text{CH}_2)$
1125	$\nu(\text{Si-O-Si})$ of silicon

The most prominent bands in the spectrum are those at 2955-2854 cm⁻¹ due to the $\nu(\text{CH}_3)$ and $\nu(\text{CH}_2)$ stretching vibrations, and therefore these were used for analysis of the OTS spectrum. The areas under the bands due to the $\nu(\text{CH}_3)$ and $\nu(\text{CH}_2)$ stretching vibrations for the TE and TM polarized spectra were integrated using the software. The integrated values were then used to calculate the linear dichroic ratio, (L.D.R), for the system, from equation (2.49), as follows:

Integrated area under bands due to $\nu(\text{CH}_3)$ and $\nu(\text{CH}_2)$ stretching vibrations for TE spectrum = A_{TE} .

Integrated area under bands due to $\nu(\text{CH}_3)$ and $\nu(\text{CH}_2)$ stretching vibrations for TM spectrum = A_{TM} .

$$\frac{A_{\text{TE}}}{A_{\text{TM}}} = \text{L.D.R.} = \frac{54.475}{83.641} = 0.65$$

Using Harrick's approximations for a thick film, (2.55-2.56), the linear dichroic ratios for the system above were calculated and are given in table.3.2.

Table.3.2. Calculated, (Harrick), Linear Dichroic Ratio Values for a Cast OTS Film on Silicon.

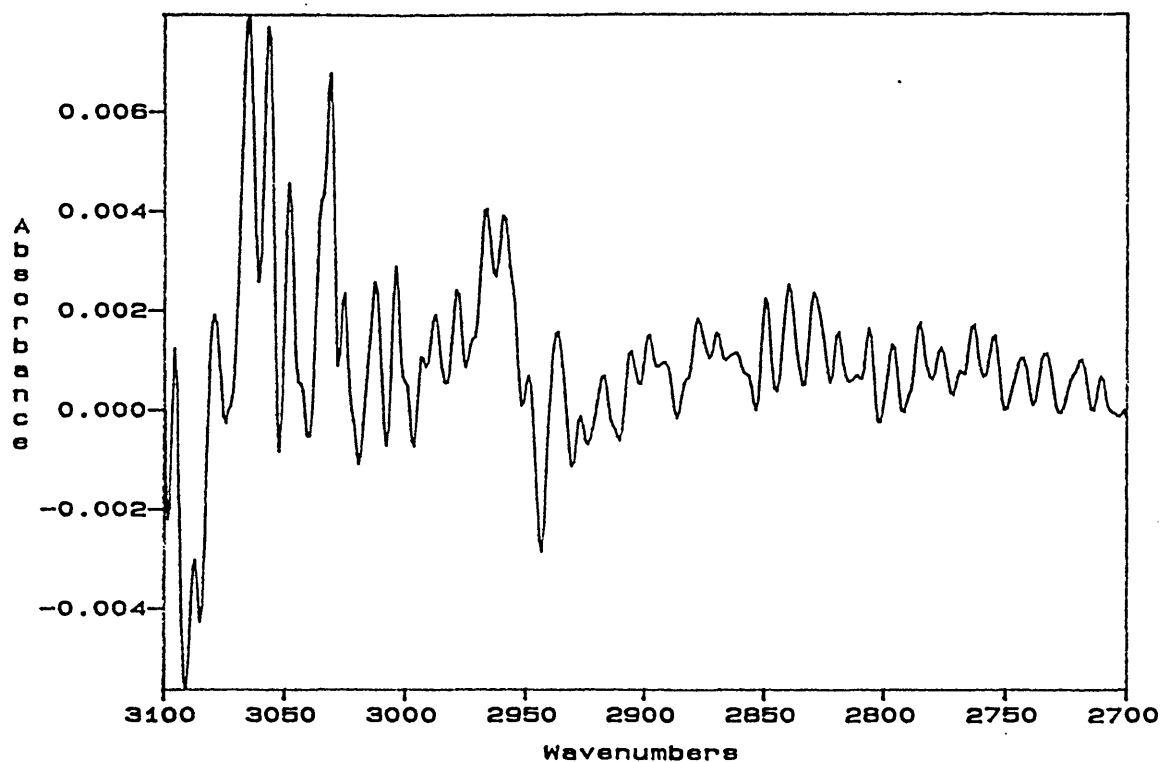
Orientational Order	Linear dichroic ratio
Random	0.5001
Perfect	1.2863

By comparing the experimental dichroic ratio value to the calculated values and looking at the band position of the $\nu_{as}(\text{CH}_2)$ stretching mode, it can be said that the cast film is disordered, as expected. An ordered film of OTS would be expected to have a $\nu_{as}(\text{CH}_2)$ band position at 2917 cm^{-1} , [28], and a perfect orientational L.D.R. value approaching 1.2863.

3.2.1.2. Self-Assembled Films of OTS on Silicon.

The FTIR-ATR spectrum of a pre-cleaned silicon ATR prism, can be seen in figure.3.2. The section of the spectrum in the $3100 - 2700 \text{ cm}^{-1}$ region is expanded to show that there is no hydrocarbon contamination in the sample. The observed fringes in the spectrum are due to the beam-splitter, (see later).

Figure.3.2. FTIR-ATR Spectrum of Pre-cleaned Silicon.



The FTIR-ATR spectrum, (4000 - 1000 cm^{-1}), of an OTS self-assembled film on a silicon ATR prism can be seen in figure.3.3. The silicon has been dipped in the OTS solution for the maximum dipping time for the experiment, 120 minutes. The assignments of the main bands in the infrared spectrum are given in table.3.3.

Figure.3.3. FTIR-ATR Spectrum of Self-assembled Film of OTS on Silicon.

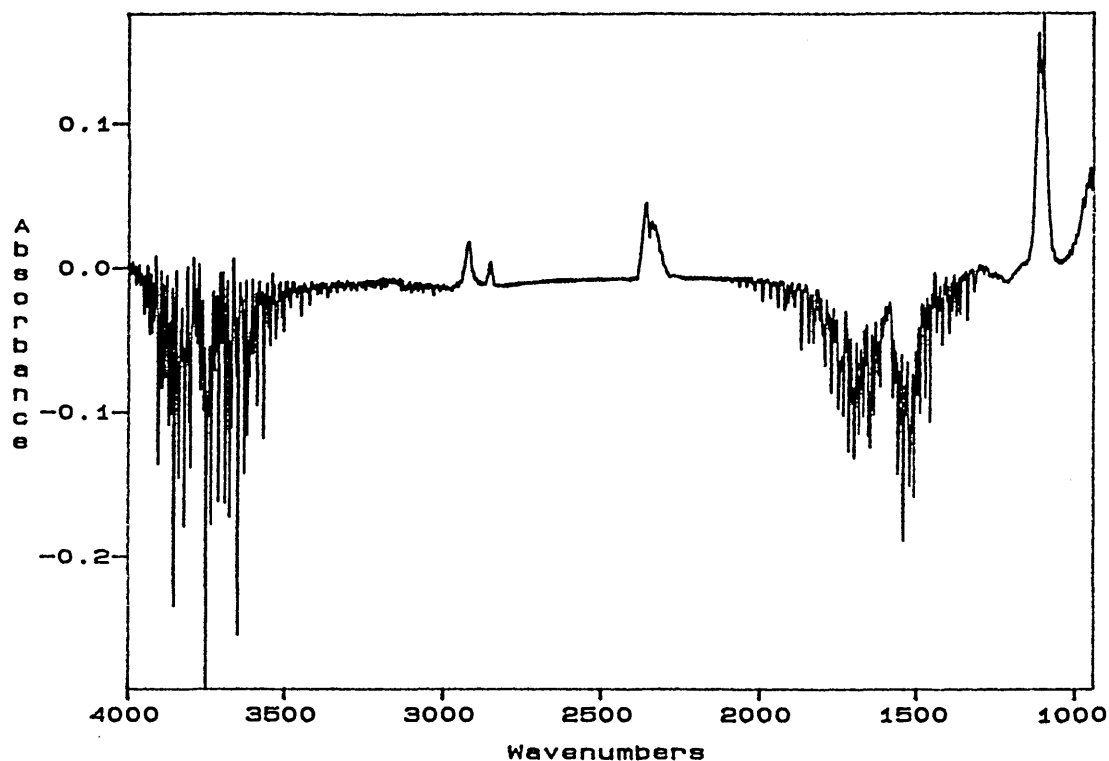


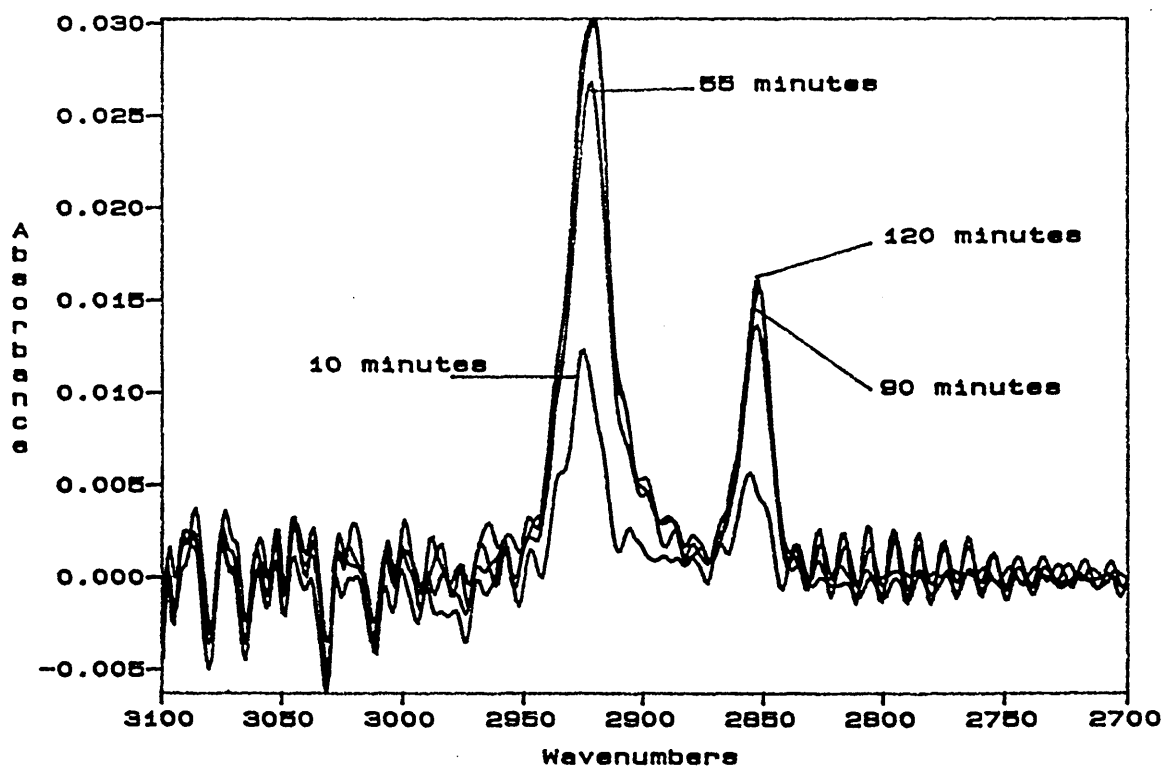
Table.3.3. Assignments of Bands in Infrared Spectrum of Self-Assembled OTS on Silicon.

Band Position / cm^{-1}	Infrared Assignment
2921	$\nu_{\text{as}}(\text{CH}_2)$
2852	$\nu_{\text{s}}(\text{CH}_2)$
1115	$\nu(\text{Si-O-Si})$ of silicon

The most intense bands in the spectrum, (corresponding to OTS), are those due to the $\nu(\text{CH}_2)$ stretching vibrations.

The unpolarized bands of the self-assembled OTS on silicon after 10, 55, 90 and 120 minutes dipping time, in the 1 mM toluene solution, can be seen in figure 3.4. The region 3100 - 2700 cm^{-1} is shown. The fringes in the wings of the spectra arise from the beam-splitter and are due to alignment problems of the micro-ATR crystal.

Figure.3.4. Overlaid Spectra of OTS on Silicon at 10, 55, 90 and 120 minutes dipping times.



The positions of the bands due to the antisymmetric CH_2 stretching vibrations for the unpolarized spectra are given in table.3.4.

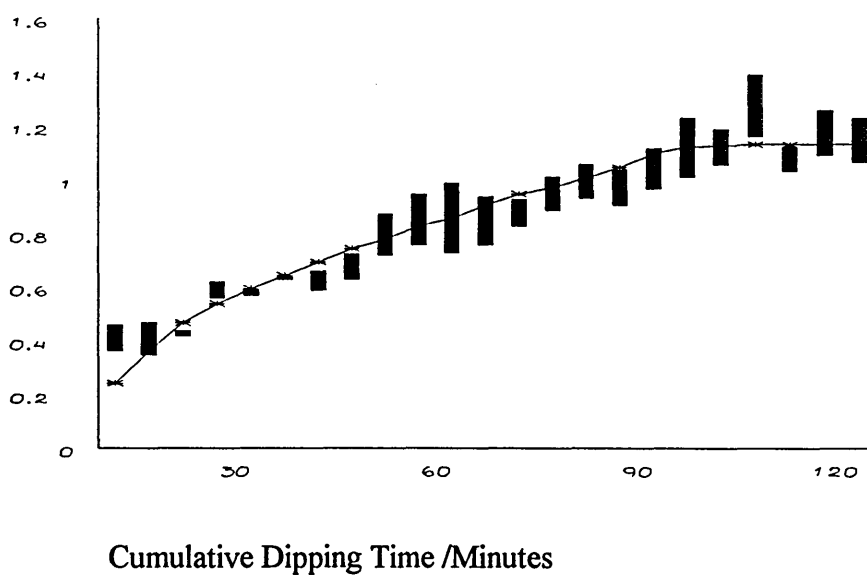
Table.3.4. Band Positions of the Antisymmetric CH₂ Stretching Vibrations of OTS on Silicon.

Cumulative Dipping Time / minutes	Band Position / cm ⁻¹
5	2927
10	2925
15	2926
20	2924
25	2925
30	2924
35	2924
40	2923
45	2924
50	2923
55	2922
60	2922
65	2923
70	2923
75	2922
80	2922
85	2922
90	2921
95	2921
100	2921
105	2921
110	2921
115	2921
120	2921

From figure.3.4. it can be seen that the intensity of the bands due to the $\nu(\text{CH}_2)$ stretching vibrations increases up to 90 minutes dipping time and then remains constant. This is depicted more clearly in a plot of the cumulative dipping time of the silicon in the OTS solution versus integrated intensity of the bands due to the $\nu(\text{CH}_2)$ stretching vibrations, (figure.3.5.).

Figure.3.5. Integrated Intensity under bands due to the $\nu(\text{CH}_3)$ and $\nu(\text{CH}_2)$ stretching vibrations, for a Self-Assembled Film of OTS on Silicon, Versus Cumulative Dipping Time.

Integrated Intensity of CH_2 Bands / cm^{-1}



The plot reaches a constant maximum at about 90 minutes dipping time, which corresponds to monolayer formation. These results agree with Kallury et al, [38]. All integrals are between 3000 and 2800 cm^{-1} .

By measuring the integrated areas under the peaks due to the $\nu(\text{CH}_2)$ stretching vibrations, in the polarized spectra of OTS, self-assembled onto silicon, the linear dichroic ratios for the system were calculated using equation (2.50). The error in these values is approximately 5%. These are given in table.3.5.

Table.3.5. Linear Dichroic Ratio Values for OTS-Coated Silicon.

Cumulative Dipping Time / minutes	Linear dichroic ratio
10	0.72
15	1.40
20	0.80
25	1.15
30	0.78
35	1.15
40	0.87
45	0.92
50	0.91
55	1.19
60	1.04
65	1.37
70	0.99
75	1.17
80	1.02
85	1.28
90	0.97
95	1.27
100	1.04
105	1.03
110	1.00
115	1.19
120	1.07

Spectra of TE and TM polarized samples at dipping times of 10, 55, 85, 120 minutes can be seen in figures.3.6 - 3.9.

Figure.3.6. Comparison of TE and TM Polarized Spectra: 10 Minutes Dipping Time.

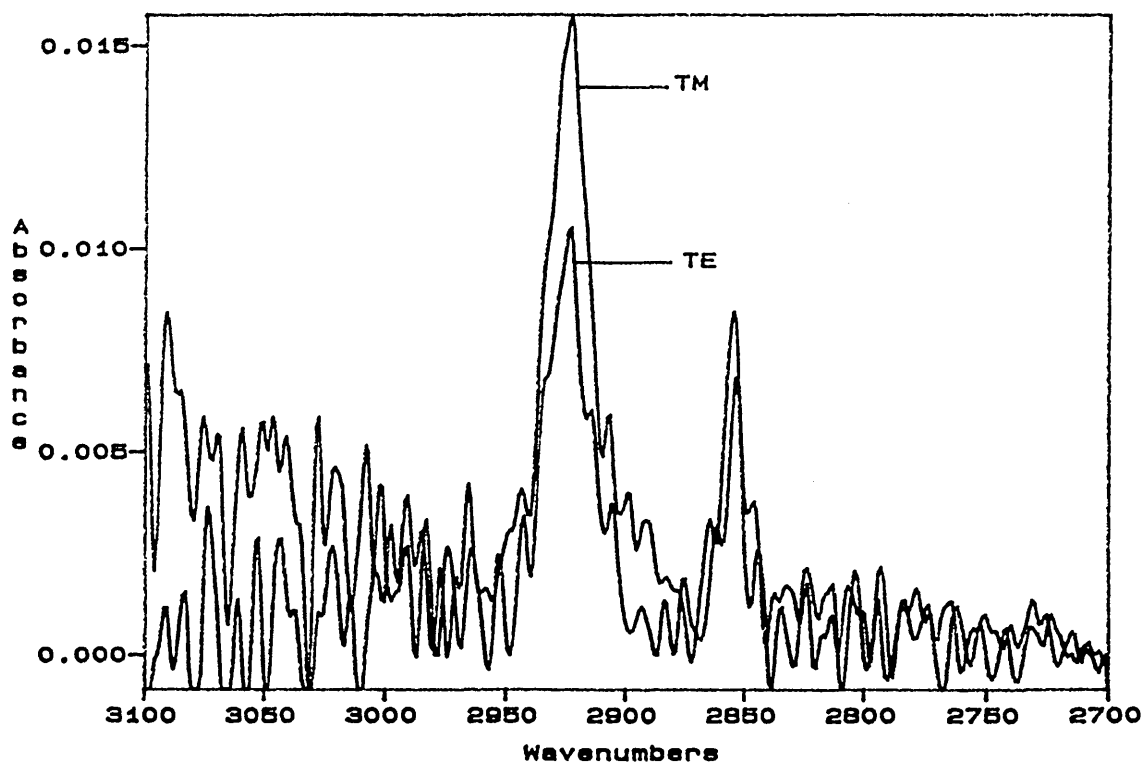


Figure.3.7. Comparison of TE and TM Polarized Spectra: 55 Minutes

Dipping Time.

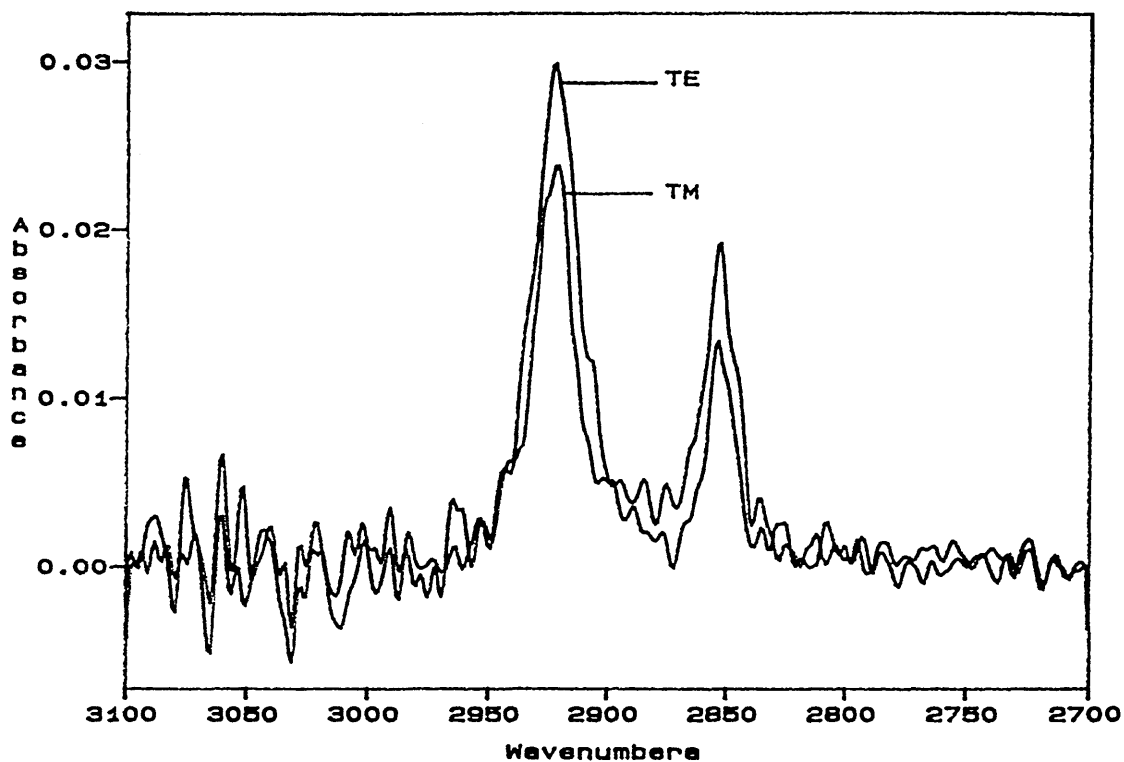


Figure.3.8. Comparison of TE and TM Polarized Spectra: 85 Minutes

Dipping Time.

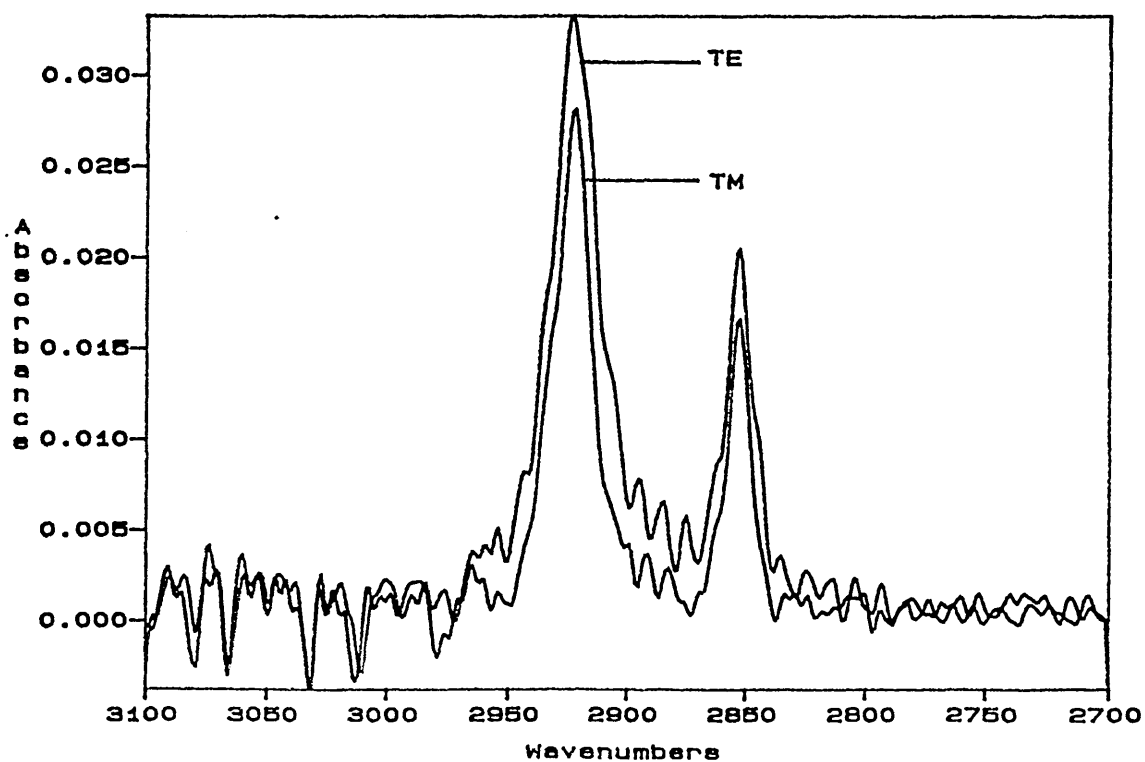
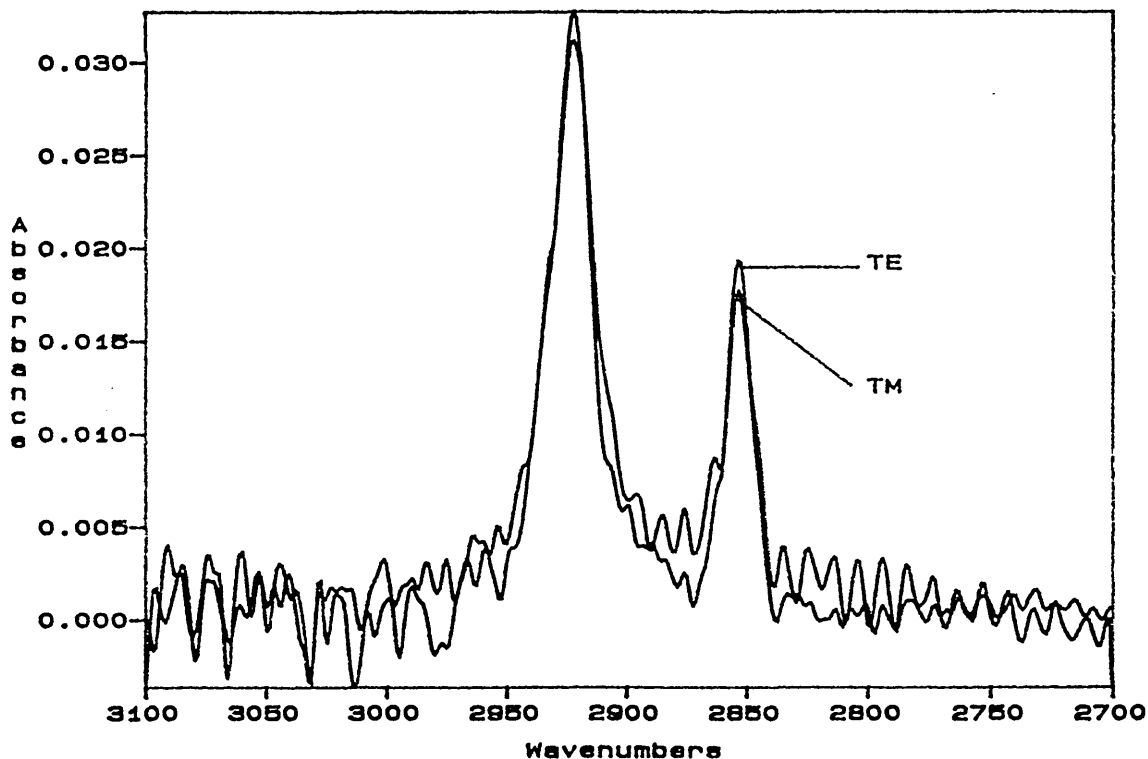


Figure.3.9. Comparison of TE and TM Polarized Spectra: 120 Minutes

Dipping Time.



The LDR values in table.3.5. oscillate and this may be due to the fact that the beam splitter fringes contribute to some of the spectra and not to others. It may also be a result of the actual dipping process itself. This may also explain why the measured LDR values are outside the calculated values.

These experimental values require a standard for comparison, in order to determine the variation in orientational order with increased coverage.

Harrick's approximations for thin films have always been used to determine the parameters required to calculate linear dichroic ratios for self-assembled layers, [28]. For this system, Sagiv et al, [28], determined the random and perfect orientational order linear dichroic ratio values, without accounting for the siliconoxide interlayer between the silicon substrate and the OTS film. These values are given in table.3.6.

siliconoxide interlayer between the silicon substrate and the OTS film. These values are given in table.3.6.

Table.3.6. Linear Dichroic Ratio Values for a Monolayer of OTS on Silicon, [28].

Orientational Order	Linear dichroic ratio.
Random	0.897
Perfect	1.094

Using Song's computer programs, the values for E_x^2 , E_y^2 and E_z^2 were obtained from first principles, as described in chapter 2. The parameters outlined in table.3.7. were used in the calculations.

Table.3.7. Parameters used in Linear Dichroic Ratio Calculations.

Medium	Parameter	Value
Silicon substrate	Refractive index, n	3.42
	Attenuation coefficient, κ	0
	Thickness	5 nm
Silicon oxide interlayer	Refractive index, n	1.46
	Attenuation coefficient, κ	0
	Thickness	2.6 nm
OTS film	Refractive index, n	1.5
	Attenuation coefficient, κ	0
	Thickness	2.6 nm
Air	Refractive index, n	1
	Attenuation coefficient, κ	0
	Wavelength	2885 cm^{-1}
	Angle of incidence	45°

Unlike Harrick's thin film approximations, this approach accounts for the effect of the silicon oxide interlayer. It also enables the calculation of the variation of the electric field components of the evanescent wave over the actual distance probed, which Harrick's equations do not, (see figure.3.10). In figure.3.10, the interface between the silicon substrate and the silicon oxide overlayer occurs at 0.0 μm on the z axis, the interface between the silicon oxide overlayer and the OTS monolayer occurs at 0.005 μm on the z axis and the interface between the OTS monolayer and the atmosphere, (air), occurs at 0.0076 μm on the z axis. It can be seen that the electric field components of the evanescent field, particularly the z component, vary as they pass through the various interfaces mentioned above.

The linear dichroic ratio values for perfect and random orientational order for the system whose optical properties are described in table.3.7, were calculated by substituting the values of E_x^2 , E_y^2 and E_z^2 into equations (2.51,2.58) and are given in table.3.8.

Table.3.8. Electric Field Squared Values and L.D.R. Values Calculated from Song's Programs.

Electric field squared values			Linear dichroic ratios	
$E_x^2 \times 10^{-2}$	$E_y^2 \times 10^{-2}$	$E_z^2 \times 10^{-3}$	Random	Perfect
1.3721	1.49562	3.81594	0.8528	1.0900

It can be seen that the linear dichroic ratios, calculated using electric field values, determined by Song's program, (which account for the silicon oxide interlayer), differ from those calculated using Harrick's thin film approximations, to determine the electric field components. Therefore the calculated values in table.3.8. will be used to compare to experimental values.

In order to compare the experimental and theoretical linear dichroic ratio values, a statistical analysis of the experimental values is required. The data are split into two sections, 0-50 minutes dipping time and 55-120 minutes dipping time, corresponding to 0-85% coverage and 85-100% coverage, respectively. This statistical analysis can be seen in table.3.9.

Figure.3.10. Plot of Variation of Evanescent Field Components Through the Silicon/ Silicon Oxide/ OTS Interlayer.

----- E^2_x
- - - - E^2_y
— — — E^2_z

E^2

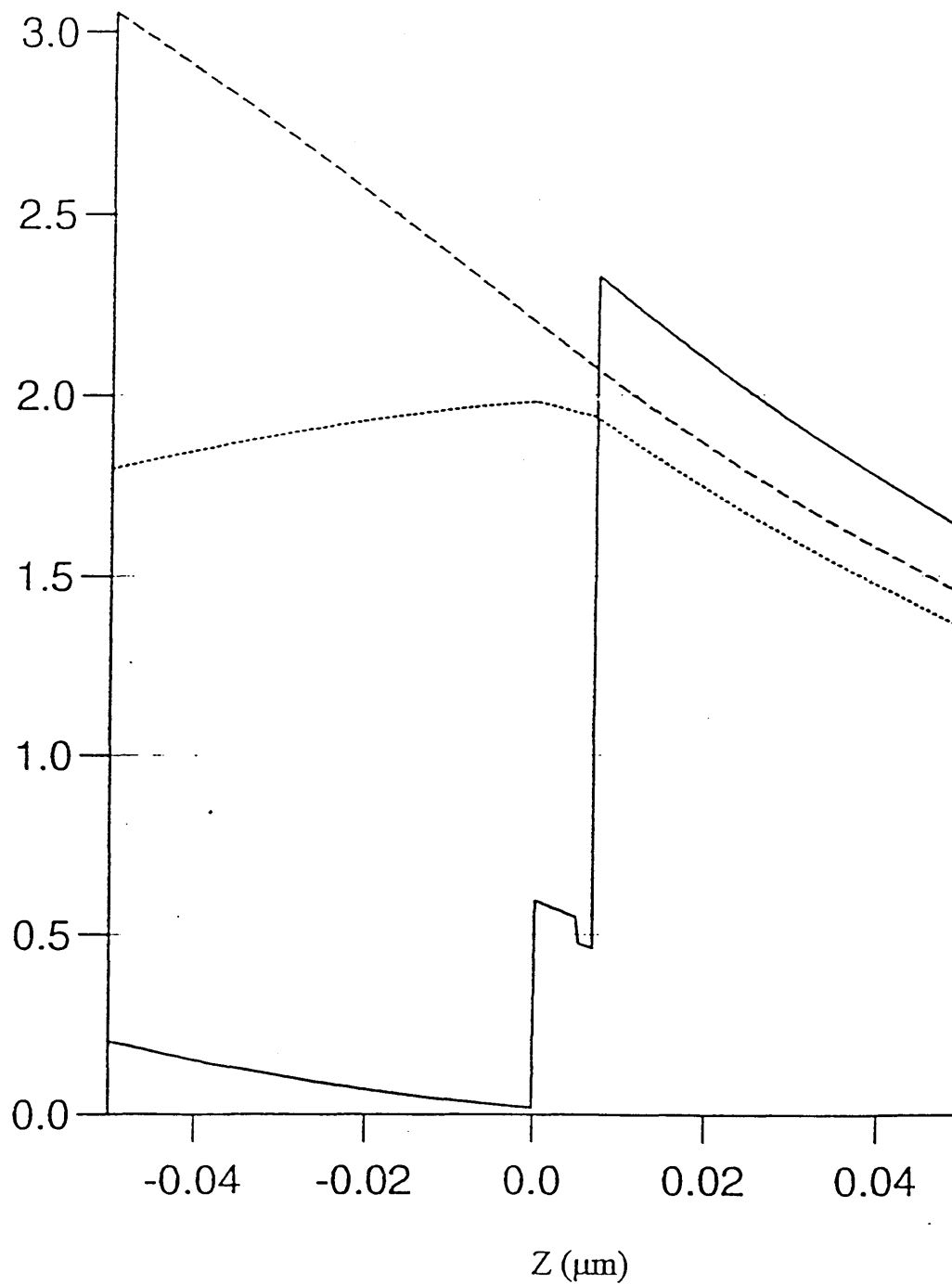


Table.3.9. Statistical Analysis of Experimental Linear Dichroic Ratios.

Dipping time / minutes	n = number of samples	\bar{x} = mean	s = standard deviation	Variation from mean
0-50	9	0.97	0.21	0.76-1.18
55-120	14	1.12	0.02	1.10-1.14

Comparison of these values to the calculated linear dichroic ratio values in table.3.8, shows that at higher coverage, there is statistical evidence that the OTS layer is approaching 'perfect' orientational order. There is obviously going to be a contribution from random error included in the experimental data. One source of systematic error is caused by the beam splitter- induced 'fringes'. Because of this a linear dichroic ratio value greater than 1.09 is not physically significant. However, it is still clear that the orientational order increases with degree of coverage.

Another indication of increased order is the shift of the $\nu_{as}(\text{CH}_2)$ band, (see table 3.4). This can be seen to have decreased from 2927 cm^{-1} , at low coverage to 2921 cm^{-1} , at higher, (monolayer), coverage. This shift is indicative, (considering the resolution of 2 cm^{-1} used in the experiment), of decreasing fluidity of the hydrocarbon chains, (decreasing gauche conformer population, increasing trans conformer population). However, it is also clear that the bandwidth of the $\nu_{as}(\text{CH}_2)$ band in the monolayer spectrum, (20 cm^{-1}), is larger than that of an all-trans OTS chain, (13-17 cm^{-1}), so although there is an increase in orientational order and a decrease in gauche conformers with increasing surface coverage, the monolayer is not 'perfectly' organised. This agrees with Gun and Sagiv, [26], who believed that a perfectly organised monolayer of OTS is produced by a single dipping stage, rather than by several dipping steps, as in the experiment here.

Another important issue that has been addressed here, is the possibility of the determination of tilt angle of the molecular chain axis to the surface normal. In order to see if this can be calculated, from equation (2.57), using experimental values of A_{TE} and A_{TM} and calculated values of E_x^2 , E_y^2 and E_z^2 , Song's computer programs were first used to calculate the L.D.R values which would arise from set angles, which were input into the program. The results can be seen in table.3.10.

Table.3.10. Calculated Linear Dichroic Ratio Values for Set Tilt-Angles.

Tilt Angle / Degree	Linear Dichroic Ratio
2	1.0893
3	1.0884
4	1.0871
5	1.0854
8	1.0782
10	1.0715
15	1.0482
20	1.0152
25	0.9724
35	0.8565

As previously stated a randomly ordered system may give the same LDR value as an ordered system with a tilt angle of 35°, (see table.3.10. above).

It can be seen from the results in table.3.10. that in order to calculate the tilt angle of the chain director to the surface normal from experimental dichroic ratio values, the experimental values need to be very accurate, since a large change in tilt angle only corresponds to a small change in the linear dichroic ratio. The

reason for this is because the z component of the evanescent field is an order of magnitude less than the x and y components of the evanescent field, (see table.3.8). Therefore large changes in the tilt angle only induce small changes in the linear dichroic ratio.

3.2.2. Perfluorodecyl(ethyl)trichlorosilane.

The results of the studies on cast and self-assembled films of perfluorodecyl(ethyl)trichlorosilane, F8, $\text{CF}_3(\text{CF}_2)_7\text{SiCl}_3$, on silicon are given in this section.

3.2.2.1. Cast Films of F8 on Silicon.

The TE and TM polarized FTIR-ATR spectra, ($4000\text{-}1000\text{ cm}^{-1}$), of a cast film of F8 on a silicon ATR prism can be seen in figure.3.11. By the nature of its preparation, this film would be expected to be disordered. The assignments of the main bands in the infrared spectrum can be seen in table.3.11.

Figure.3.11. FTIR-ATR Spectrum of Cast F8 Film on Silicon.

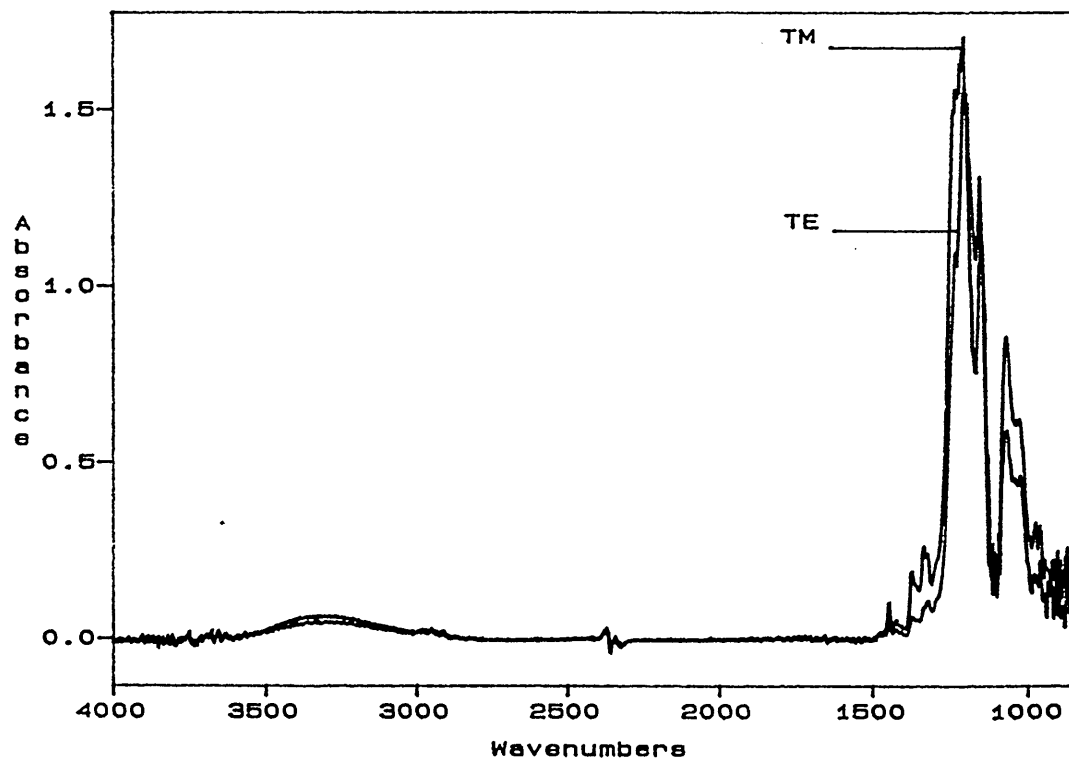


Table.3.11. Assignments of Bands in the Infrared Spectrum of a Cast Film of F8 on Silicon.

Band Position / cm ⁻¹	Infrared Assignment
1230	$\nu_{as}(\text{CF}_2)$ and $r(\text{CF}_2)$
1203	
1150	$\nu_s(\text{CF}_2)$
2980	$\nu_{as}(\text{CH}_3)$
2952	$\nu_{as}(\text{CH}_2)$
2914	$\nu_s(\text{CH}_3)$
2870	$\nu_s(\text{CH}_2)$

The most prominent bands in the spectrum, (due to F8 vibrations), are those at 1230-1150 cm⁻¹, due to the CF₂ rocking and stretching vibrations. Therefore these were used when analysing F8 spectra. If the CF vibrations are the same as CH vibrations then they will occur in a plane perpendicular to the carbon backbone.

The areas under the peaks, due to the CF₂ rocking and stretching vibrations, for the TE and TM polarized spectra were integrated using the software. These were then used to calculate the linear dichroic ratio value, (L.D.R.), for the system, from equation (2.50) as follows:

Integrated area under bands due to CF₂ rocking and stretching vibrations for the TE spectrum = A_{TE}

Integrated area under bands due to CF₂ rocking and stretching vibrations for the TM spectrum = A_{TM}

$$\frac{A_{\text{TE}}}{A_{\text{TM}}} = \text{L.D.R} = \frac{124.295}{159.882} = 0.78$$

Using Harrick's approximations for a thin film, (2.38-2.40), to calculate the electric field components of the evanescent wave, and then by substituting these electric field values into equation (2.50), the theoretical linear dichroic ratios for the system above were calculated and are given in table.3.12.

Table.3.12. Calculated, (Harrick), Linear Dichroic Ratio Values for Cast F8 Film on Silicon.

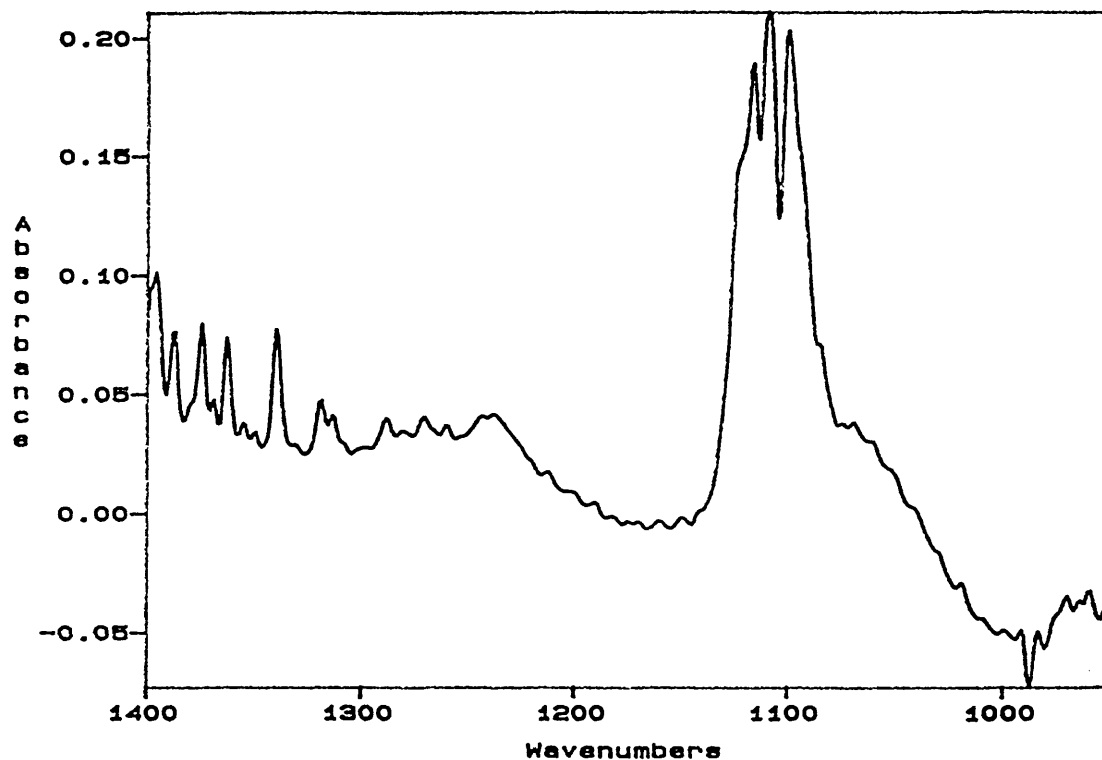
Orientational Order	Linear dichroic ratio
Random	0.49997
Perfect	1.3037

By comparing the experimental linear dichroic ratio value with the theoretical values, it can be said that the cast F8 film is disordered. An ordered film would be expected to have a linear dichroic ratio value close to 1.3037.

3.2.2.2. Self-assembled Films of F8 on Silicon.

The FTIR-ATR spectrum of a pre-cleaned silicon ATR prism can be seen in figure.3.12. The region 1400-950 cm^{-1} is expanded to show that there is no contamination in the area of interest of this experiment. The large peak at approximately 1100 cm^{-1} is due to the silicon absorption.

Figure.3.12. FTIR-ATR Spectrum of Pre-cleaned Silicon.



The FTIR-ATR spectrum of a self-assembled F8 film on a silicon ATR prism, after 60 minutes dipping time in the silane solution, can be seen in figure.3.13.

This sample was obtained by dipping the silicon prism in the F8 solution in 5 minute stages and then solvent washing to remove excess silane after each dipping stage. i.e. the sample was not subjected to 'buffing' to remove excess F8.

The assignment of the main bands in the spectrum are given in table.3.13.

Figure.3.13. FTIR-ATR Spectrum of Self-assembled Film of F8 on Silicon.

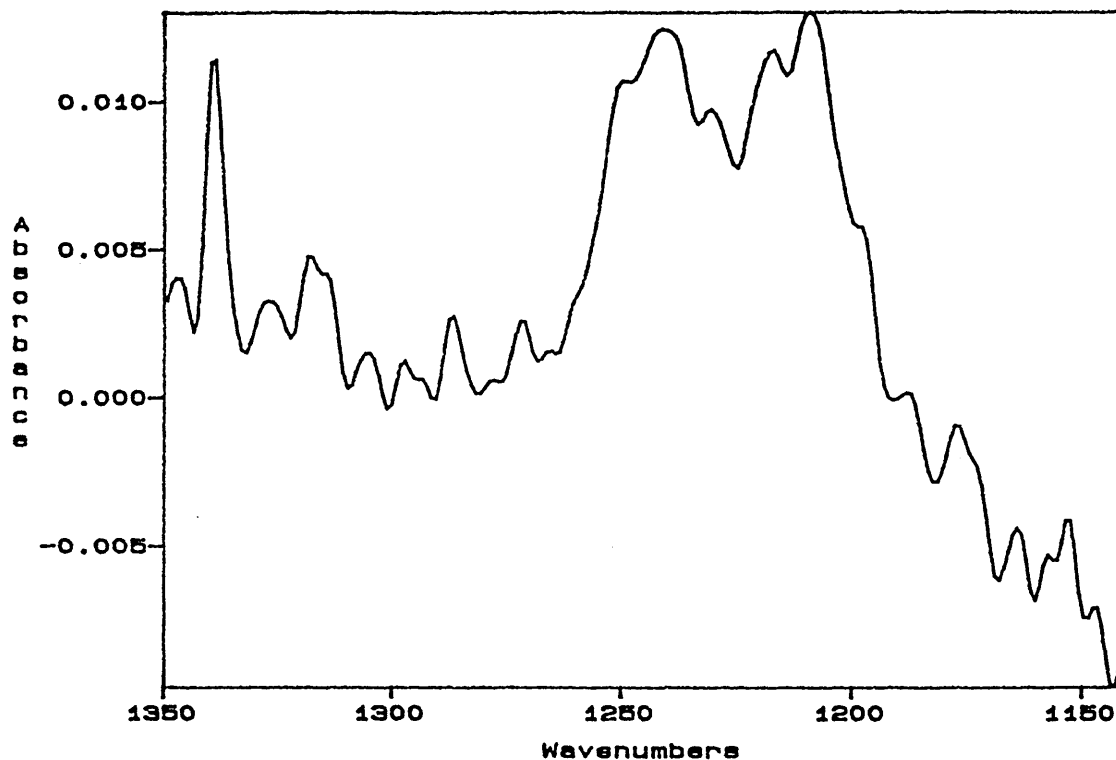


Table.3.13. Assignments of Bands in the Infrared Spectrum of Self-assembled F8 on Silicon.

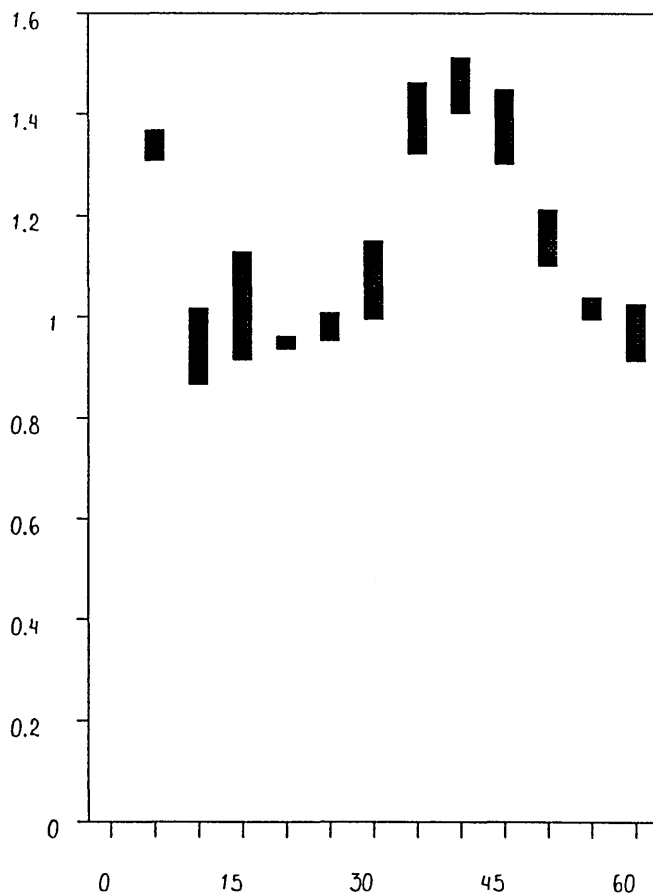
Band Position / cm ⁻¹	Infrared Assignment
1242	$\nu_{as}(\text{CF}_2)$ and $r(\text{CF}_2)$
1209	$\nu_{as}(\text{CF}_2)$ and $r(\text{CF}_2)$

The most intense bands in the spectrum, (due to F8 vibrations), are those corresponding to the CF₂ rocking and antisymmetric stretching vibrations. The band due to the CF₂ symmetric stretching vibration at approximately 1150 cm⁻¹ is very weak and is partly obscured by the absorption due to the silicon substrate, (not shown).

A plot of the cumulative dipping time versus the integrated intensity under the bands due to the CF_2 rocking and antisymmetric stretching vibrations can be seen in figure.3.14.

Figure.3.14. Integrated Intensity under bands due to $\nu_{\text{as}}(\text{CF}_2)$ and $r(\text{CF}_2)$ vibrations for a Self-assembled Film of F8 on Silicon, Vesus Cumulative Dipping Time, without Buffing.

Integrated intensity of $\nu_{\text{as}}(\text{CF}_2)$ and $r(\text{CF}_2)$ bands / cm^{-1}



Cumulative dipping time / Minutes

From figure.3.14, it can be seen that the intensity under the bands due to the CF_2 rocking and antisymmetric stretching vibrations, fluctuates with dipping time. This was suspected to be due to excess silane polymerising in solution and then depositing over the F8 film. It was believed that this excess silane could be removed by gently 'buffing' the sample to a constant integrated intensity, (of bands due to CF_2 rocking and antisymmetric stretching vibrations), for each dipping stage. Figure.3.15. shows the overlaid spectra at dipping times of 25 seconds, 1 minute, 5 minutes, 8 minutes and 60 minutes, in the region 1350-1150 cm^{-1} , with buffing. The assignments for the main infrared bands can be seen in table.3.14.

Figure.3.15. Overlaid Spectra of F8 on Silicon at Dipping Times of 25 seconds, 1, 5, 8 and 60 minutes.

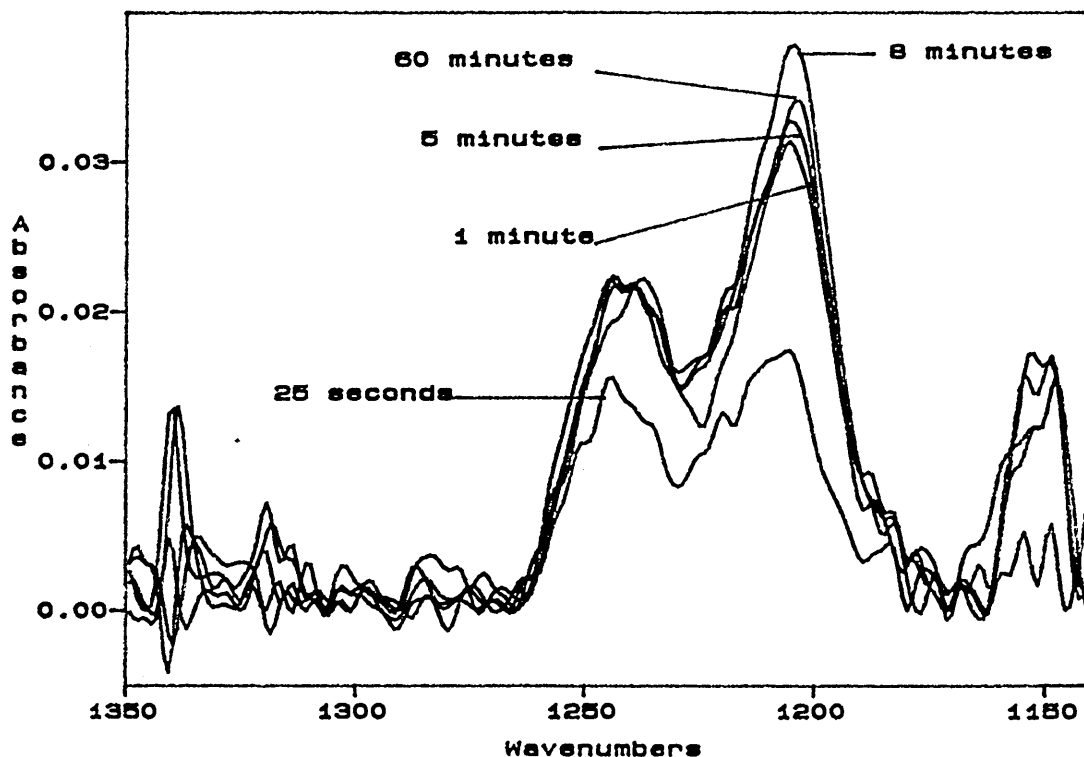


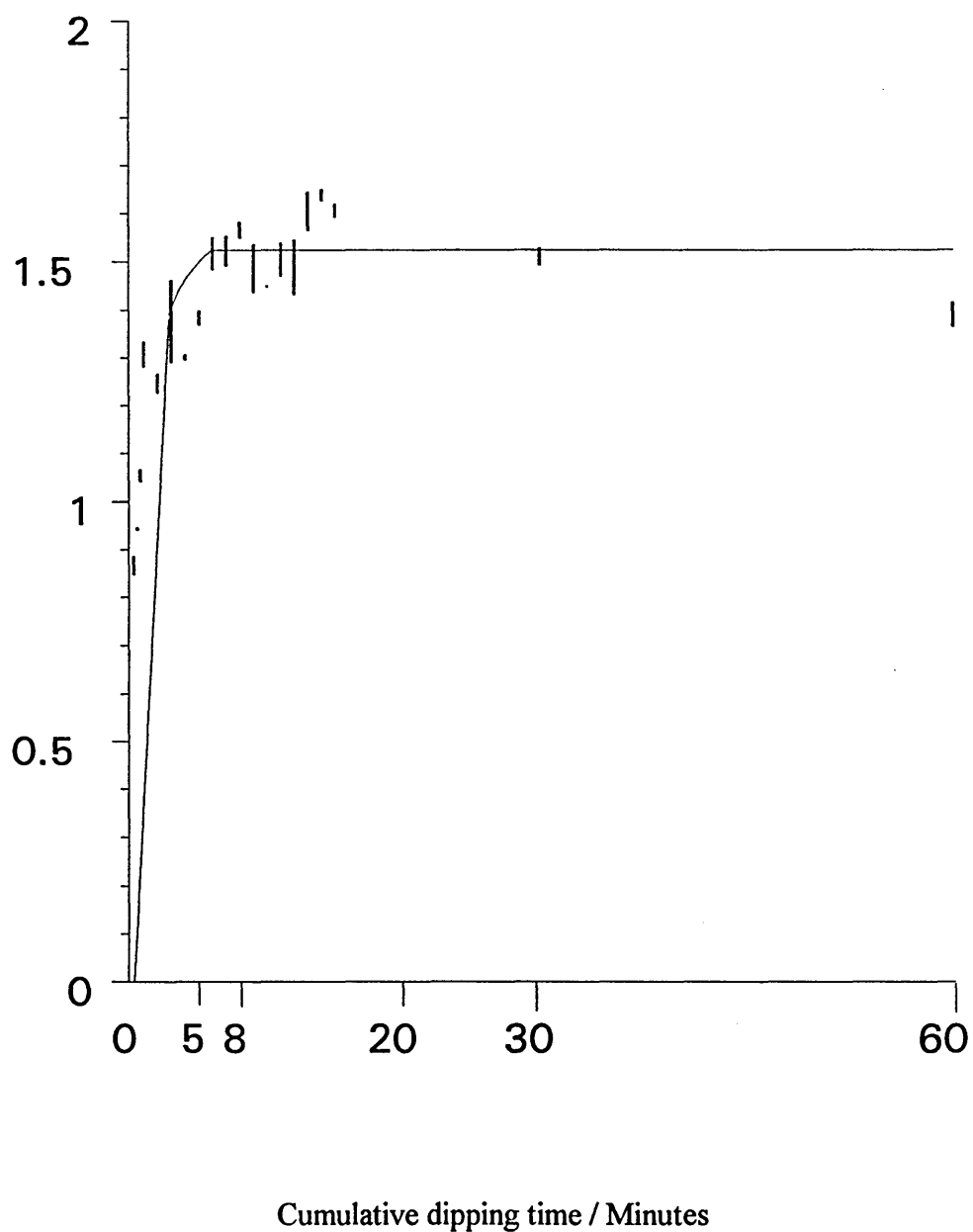
Table.3.14. Assignments of Bands in Infrared Spectrum of Self-assembled F8 on Silicon.

Band Position / cm^{-1}	Infrared Assignment
1239	$\nu_{\text{as}}(\text{CF}_2)$ and $r(\text{CF}_2)$
1203	$\nu_{\text{as}}(\text{CF}_2)$ and $r(\text{CF}_2)$
1146	$\nu_{\text{s}}(\text{CF}_2)$

It can be seen from figure.3.15. that the intensities of the bands, due to the CF_2 rocking and antisymmetric stretching vibrations, increase up to approximately 5 to 8 minutes dipping time and remain approximately constant up to a maximum dipping time of 60 minutes. This is shown more clearly in a plot of the cumulative dipping time, of the silicon in the F8 solution, versus integrated intensity under the bands, due to the CF_2 rocking and antisymmetric stretching vibrations, (figure.3.16).

Figure.3.16. Integrated Intensity under Bands due to the $\nu_{as}(\text{CF}_2)$ and $\nu_s(\text{CF}_2)$ Vibrations for a Self-assembled Film of F8 on Silicon, Versus Cumulative Dipping Time, with Buffing.

Integrated intensity of $\nu_{as}(\text{CF}_2)$ and $\nu_s(\text{CF}_2)$ bands / cm^{-1}



The plot in figure.3.16. reaches a constant maximum at about 5 to 8 minutes dipping time, which corresponds to monolayer formation. These results agree with Lindner and Arias, [46], who obtained their results using contact angle and surface free energy techniques.

Unfortunately the TE and TM spectra obtained in these experiments were very weak in the region of interest. Therefore no experimental linear dichroic ratio values could be calculated for this system. However, using Harrick's approximations for a thin film, [143], equations (2.38-2.40), and Song's computer programs, [145], to calculate the electric field components of the evanescent wave, the theoretical linear dichroic ratio values were calculated, from equations (2.51,2.58), (tables.3.15. and 3.16 respectively).

Table.3.15. Linear Dichroic Ratio Values for a Monolayer of F8 on Silicon, calculated from Harrick's equations for a thin film, [28].

Orientational Order	Linear dichroic ratio
Random	0.8897
Perfect	1.1010

Table.3.16. Linear Dichroic Ratio Values for a Monolayer of F8 on Silicon using Song's Computer Programs.

Orientational Order	Linear dichroic ratio
Random	0.8295
Perfect	1.096

As for OTS, differences between the linear dichroic ratio values calculated using the two methods, above, can be seen. These differences are partly due to

the fact that the results in table.3.16 account for the silicon oxide interlayer in the system, whereas those in table.3.15 do not.

3.3. Conclusions.

3.3.1. N-octadecyltrichlorosilane.

Cast and self-assembled submono- and monolayers of n-octadecyltrichlorosilane were produced on silicon ATR prisms and were studied using FTIR-ATR spectroscopy.

As expected, for the OTS cast film, a linear dichroic ratio value and $\nu_{as}(CH_2)$ band position indicative of an orientationally and conformationally disordered system, were obtained.

The monolayer of OTS was produced by self-assembly from a weak solution of the silane in toluene. The time for monolayer formation was determined to be approximately 90 minutes. From analysis of experimental linear dichroic ratio values, the submonolayer of OTS was found to be orientationally disordered, while the monolayer was found to be orientationally ordered. This increase in orientational order was seen to vary as a function of surface coverage.

The conformational order was also found to increase with surface coverage, (assumed from the decreasing band position of the $\nu_{as}(CH_2)$ peak with increased coverage), indicating a decrease in the number of gauche conformers. Although the final result was not a 'perfectly' well-ordered film, (assumed from the band width and band position of the $\nu_{as}(CH_2)$ peak in the final monolayer), the OTS monolayer was still relatively well-packed and ordered, as compared with cast OTS films.

An important issue that was covered here, was the fact that the intermediate silicon oxide layer was accounted for in the theoretical calculations of the linear dichroic ratio values, which has not been done before. This allowed a better standard to be used as a comparison for experimental linear dichroic ratio values. The theoretical approach also calculated the change in the electric field intensities of the evanescent wave with sample distance probed. An attempt to calculate the tilt angle of the chain director to the surface normal was made. It was first determined, from theoretical calculations, that very accurate

experimental linear dichroic ratio values are required to do this. In this case, it was found that the experimental data obtained were not precise enough to calculate linear dichroic ratio values, which could be used to determine the tilt angle of the molecular chain director to the surface normal.

3.3.2. Perfluorodecyl(ethyl)trichlorosilane.

Cast and self-assembled multi- and monolayer films of F8 were produced on silicon ATR prisms, and investigated using FTIR-ATR spectroscopy.

As expected, for the F8 cast film, a linear dichroic ratio value indicative of an orientationally and conformationally disordered film, was obtained.

The monolayer of F8 was produced by self-assembly, from a weak solution of the silane in freon 113. The time for monolayer formation was found to be approximately 5 to 8 minutes. This result was only obtained when the sample was buffed to constant intensity after each dipping stage. If the sample was not buffed, then the intensities under the bands, due to CF_2 rocking and antisymmetric stretching vibrations, were seen to fluctuate with dipping time.

Unfortunately the polarized spectra of these samples were very weak and therefore no experimental linear dichroic ratios could be calculated for the system. Harrick's approximations for a thin film and Song's computer programs were used to calculate the electric field components for the evanescent wave, which were then used to determine theoretical linear dichroic ratio values. As for OTS, the calculated values differed for the two different methods of calculation. These differences were attributed to the fact that in Song's computer programs, the effect of the silicon oxide interlayer was accounted for and that the variation in the electric field components of the evanescent wave were calculated, which were not accounted for using Harrick's equations.

This chapter has dealt with some aspects of these silane systems in an *ex situ* environment. The next chapter will detail similar systems in an *in situ* environment.

CHAPTER.4. ATTENUATED TOTAL REFLECTION SPECTROSCOPY OF THE *IN SITU* ADSORPTION OF LONG-CHAIN SILANES ONTO SILICON.

Introduction.

This chapter describes studies of the *in situ* adsorption of two long-chain silanes onto silicon oxide/silicon. The silanes are n-octadecyltrichlorosilane, OTS and perfluorodecyl(ethyl)trichlorosilane, F8. The main objectives of the work described in this chapter are to determine the time for formation of monolayers of OTS and F8 on silicon and to determine the area per molecule of these silanes on the substrate. Some Fourier transform infrared attenuated total reflection spectra, plots of absorbance versus time, (of exposure of silicon to silane solution), and Gibbs surface excess values are presented.

4.1. Experimental.

4.1.1. Chemicals.

N-octadecyltrichlorosilane, 99%, deuterated toluene, 99.9 D atom %, methanol, 99.9%, 2-propanol, 99.9%, acetone, 99.9%, were obtained from Aldrich Chemical Co.

Perfluorodecyl(ethyl)trichlorosilane, 99.5%, was obtained from Fluorochem Ltd.

The fluorinated silane and the deuterated toluene were dried over molecular sieve prior to use. The silanes were stored at 5°C in a refrigerator. All other chemicals were used as received.

4.1.2. Substrates.

The substrates used for the ATR measurements were silicon ATR crystals with 45-50 internal reflections. For the experiment only part of the surface of each crystal was exposed to the silane solution. Therefore the crystals required calibrating to determine the number of times the infrared beam probes the

solution, and to determine the angle of incidence for the experiment. The procedure for this calibration was outlined in section.2.3.7. and the experimental details will be given later.

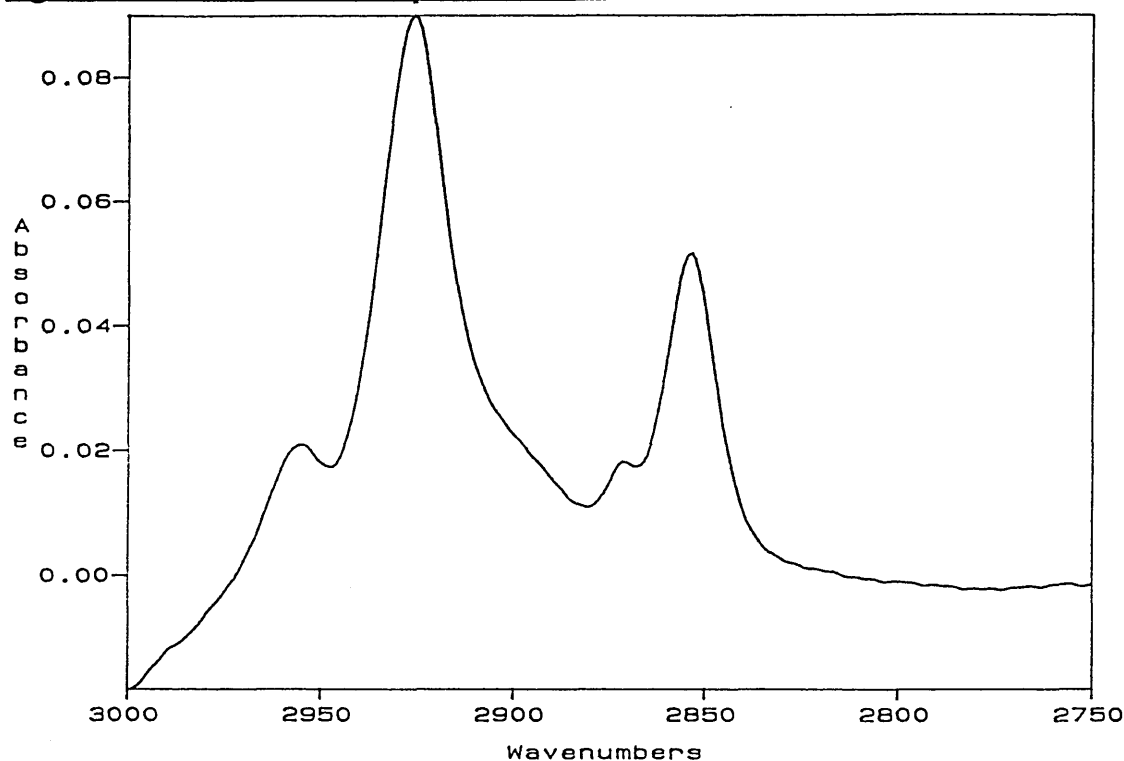
The silicon ATR prisms were cleaned by the method described in chapter.3.1.2. prior to use. All the glassware used was pre-treated with a weak OTS solution in toluene, as described in chapter.3.1.2.

4.1.3. Calibration of the Silicon ATR Prisms.

Several different silicon prisms were used in these experiments. Therefore each prism required calibrating. The calibration procedure was described in chapter.2.3.7.

A 5.56 mM hexadecane solution in deuterated toluene was prepared, and then analysed in a transmission cell, using KBr plates as the cell windows. The cell pathlength was determined from the fringes of a spectrum of the empty cell. The intensity under the bands due to the $\nu(\text{CH}_3)$ and $\nu(\text{CH}_2)$ stretching vibrations in the spectrum were integrated to give a value for the absorbance, (see figure.4.1.).

Figure.4.1. Transmission Spectrum of Hexadecane in a KBr Cell.



These values were then used to calculate the molar absorption coefficient of hexadecane using equation (2.67), as follows:

$$\alpha = \frac{A}{cl} = \frac{5.7619 \text{ cm}^{-1}}{0.00556 \text{ mol dm}^3 \times 0.02 \text{ cm}} = 51816 \text{ mol}^{-1} \text{ dm}^3 \text{ cm}^{-2}$$

A hexadecane solution of known concentration was injected into a liquid micro ATR cell, (see figure.4.2.), and the infrared spectrum was obtained. The integrated absorbance under the $\nu(\text{CH}_3)$ and $\nu(\text{CH}_2)$ stretching bands was measured. Using this absorbance value, the refractive indices of the sample and substrate, the substrate thickness, the inner diameter of the 'o' ring, (solution contact length), the calculated value of d_e , (2.45-2.46, 2.49), the wavelength of radiation, the molar absorption coefficient and the angle of incidence, (assume manufacturer's specification, 45°), the iterative program, described in section 2.3.7, was used to determine the values of N and θ , (N = number of reflections, θ = angle of incidence). The procedure was repeated for different concentrations of hexadecane and average values of N and θ were calculated.

4.1.4. Preparation of Solutions.

Solutions of OTS in deuterated toluene, at concentrations of 1, 5.8 and 11.6 mM were prepared in OTS-coated volumetric flasks and used immediately. Fresh solutions were prepared for each experiment.

Solutions of F8 in deuterated toluene, at concentrations of 0.25, 0.45 and 1 mM were prepared in OTS-coated volumetric flasks and used immediately. Fresh solutions were prepared for each experiment.

The OTS solutions were prepared and used in a fume cupboard at 33% humidity and the F8 solutions were prepared and used within a dry nitrogen atmosphere. Both silane solutions were prepared and used at room temperature and atmospheric pressure.

The molar absorption coefficients of both silanes were determined from equation (2.67). The absorbance value required for equation (2.67) was determined from a transmission cell experiment. An OTS solution of concentration 5.79 mM in deuterated toluene was injected into a transmission cell and the areas under the $\nu(\text{CH}_3)$ and $\nu(\text{CH}_2)$ stretching bands in the infrared spectrum were integrated to give an absorbance value for equation (2.67). For F8 a solution of concentration 0.162 M, in deuterated toluene, was injected into a transmission cell and the area under the $\nu_{\text{as}}(\text{CF}_2)$ stretching band was integrated. (The bands due to the stretching and rocking modes of CF_2 were curve-fitted using FIRST).

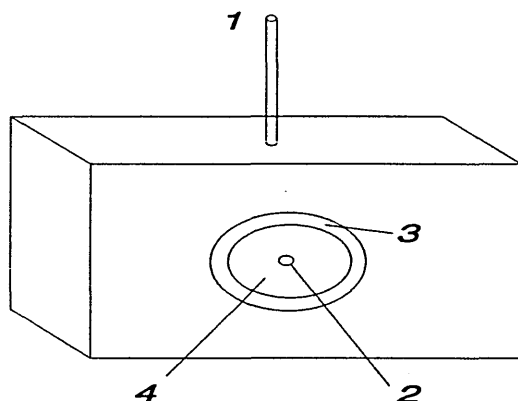
The pathlength of the cell was determined from the fringes in the spectrum of the empty cell.

4.1.5. Preparation of Samples.

The silicon prism was first checked to ensure that there was no contamination in the spectral regions of interest. The background for each sample was a spectrum of the liquid cell containing a silicon micro-ATR prism and pre-dried

deuterated toluene. A schematic of the liquid cell can be seen in figure.4.2. Once the background spectrum had been obtained, the liquid cell was disassembled, and both the cell and the silicon prism were dried to remove all the deuterated toluene.

Figure.4.2. Diagram of Liquid Micro ATR Cell, (Half of the cell is shown).



1. Capillary tube
2. Entrance of capillary tube into cell
3. Viton 'o'ring
4. Solution contact region

The silicon prism was held between the two identical halves of the cell. The solution was injected into the cell via the capillary tubes. Only the region enclosed by the 'o'rings contained solution and it was this region of the prism that required calibration.

The required silane solution was then injected into the cell and a series of spectra were acquired immediately. The length of each experiment was varied

until a plot of the integrated intensities of the infrared bands, ($\nu(\text{CH}_3)$ and $\nu(\text{CH}_2)$ stretching bands for OTS and $\nu_{\text{as}}(\text{CF}_2)$ stretching band for F8), versus exposure time reached a constant maximum. The CF_2 stretching and rocking bands were curve-fitted using FIRST.

The studies have been described as *in situ* since the samples are monitored during self-assembly of the silane onto the substrate.

4.1.6. Spectroscopic Measurements.

A Mattson Polaris Fourier transform infrared spectrometer, fitted with a liquid nitrogen-cooled bullseye mercury-cadmium-telluride detector, was used in conjunction with a micro-ATR accessory, (using the liquid cell), to examine the ATR samples.

The instrument parameters used were a resolution of 4 cm^{-1} , zero-filling, 98% iris, a signal gain of 4 and triangular apodisation. The iris and signal gain were required to obtain a signal throughput with high sensitivity.

Plots of the time of exposure of the silicon substrate to the silane solution versus the integrated intensity of the chosen infrared bands of the unpolarized spectra were produced, to determine the time of monolayer formation for each silane. The integrated intensity included contributions from both the surfactant in solution, (bulk liquid contribution), and from the surfactant adsorbed onto the silicon, (solid contribution). The intensity values used in the above-mentioned plots were those due to the adsorbed surfactant only. For the separation of the integrated intensity contributions, see sections 2.3.6 and 4.1.7. No polarized spectra were acquired because it was not possible to obtain TM and TE spectra at exactly the same point during adsorption. Therefore the polarized spectra would not be comparable.

The spectra were manipulated by the software package FIRST. A sample spectrum was obtained by ratioing the background spectrum, (liquid cell containing silicon prism and deuterated toluene), with a sample spectrum, (liquid

cell containing silicon prism and silane solution). Integration of the infrared bands and curve-fitting techniques were possible using FIRST.

4.1.7. Determination of the Gibbs Surface Excess and the Separation of Bulk and Solid Components in the System.

Using Sperline's equation, (2.62), [146]:

$$\frac{A}{N} = \alpha c_b d_e + \alpha \left(\frac{2d_e}{d_p} \right) (c_i t)$$

$c_i t$ can be calculated. c_b , the bulk concentration is known. α , the molar absorption coefficient and A , the integrated absorbance under the chosen infrared bands, can be measured experimentally. d_e and d_p can be calculated, using the value of θ determined from the iterative program, (section.2.3.7). N , the number of reflections, can be calculated from the iterative program, (section.2.3.7). The Gibbs surface excess is simply

$$\frac{c_i t}{1000} \text{ mol dm}^3 \text{ cm} = \Gamma \text{ mol cm}^{-2}.$$

Whitesides et al, [39] calculated for OTS that one molecule will occupy an area of $21 \pm 3 \text{ \AA}^2$. Using this range of values, the following calculation was performed:

In 1 cm^2 there are $\frac{1 \times 10^{16}}{24}$ to $\frac{1 \times 10^{16}}{18}$ molecules.

This is equivalent to $\frac{1 \times 10^{16} \text{ cm}^2}{24} \times \frac{1}{6.02217 \times 10^{23} \text{ mol}^{-1}}$ to $\frac{1 \times 10^{16} \text{ cm}^2}{18} \times \frac{1}{6.02217 \times 10^{23} \text{ mol}^{-1}}$.

Which gives a Gibbs surface excess of 6.919×10^{-10} to $9.225 \times 10^{-10} \text{ mol cm}^{-2}$. A Gibbs surface excess less than $6.919 \times 10^{-10} \text{ mol cm}^{-2}$ would indicate a larger surface area per molecule than 24 \AA^2 , or only partial monolayer formation. A Gibbs surface excess greater than $9.225 \times 10^{-10} \text{ mol cm}^{-2}$ would indicate a

surface area per molecule less than 18\AA^2 or, (more realistically), multilayer formation. Using the Gibbs surface excess values calculated from experimental data, it is possible to determine the surface areas per molecule for both OTS and F8, which will be demonstrated here.

The percentage contribution of the bulk liquid solution to the integrated intensity is given in equation (2.66) as follows: $\% \text{ bulk} = \frac{100c_s d_s}{c_s d_{ps} + 2000\Gamma}$

Once this has been calculated, it is a simple matter of subtracting the bulk contribution, to the integrated intensity, from the total integrated absorbance to give the value of the surface contribution. It is the values of the surface contribution that are used in the plots of integrated intensity versus exposure time, (4.1.6).

4.2. Results and Discussion.

4.2.1. Calibration of Silicon ATR Prisms.

Three silicon ATR prisms were calibrated for use in the *in situ* experiments, as described in sections 4.1.3. and 2.6.7, using hexadecane solutions at concentrations of 0.2, 0.06, 0.02 and 0.0011 M, in deuterated toluene. The resulting values of N and θ can be seen in table 4.1.

Table 4.1. Calculated Values of N and θ for Silicon ATR Prisms.

Prism number	N = number of reflections	θ = angle of incidence / °
1	16	42.423
2	25	31.241
3	22	34.460

From the variation in N and θ , (table.4.1.), it can be seen that it was necessary to calculate accurate values of N and θ . If an angle of 45° had been assumed for any of the silicon prisms above, it would have resulted in miscalculations of d_e and d_p and hence Γ .

The values of N in the table have been rounded up or down to the nearest integer.

4.2.2. N-octadecyltrichlorosilane.

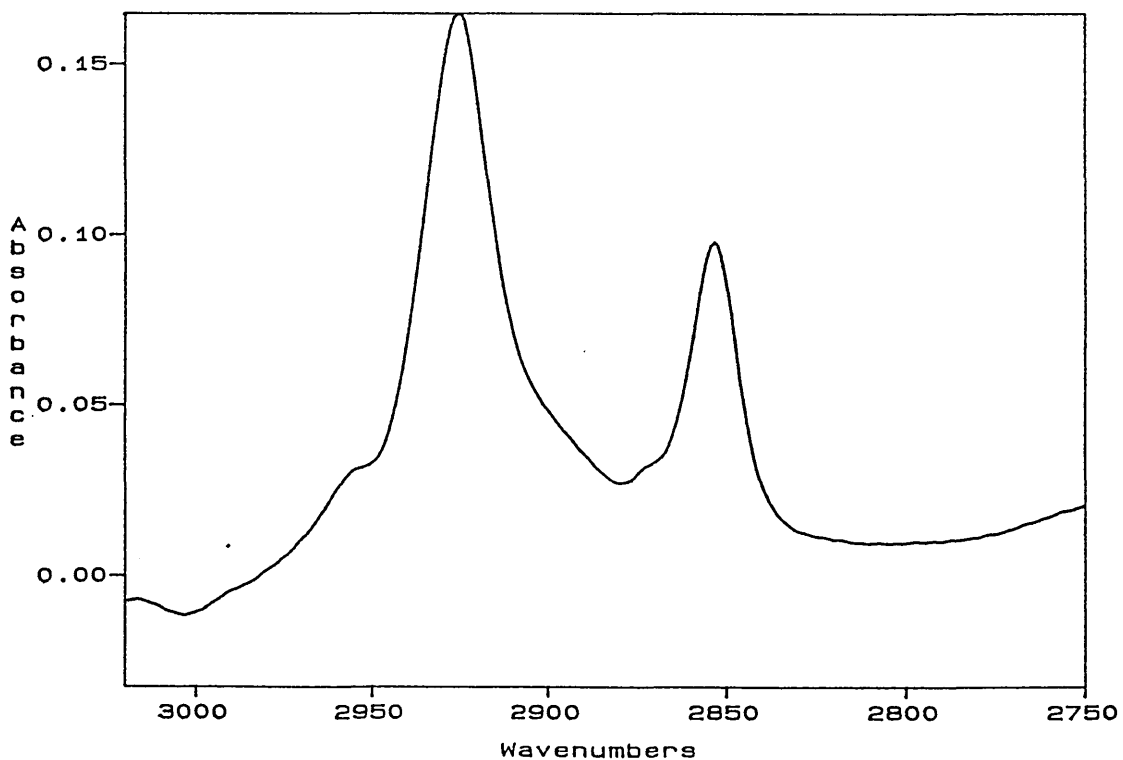
The results of the studies of self-assembled films of n-octadecyltrichlorosilane, OTS, $\text{CH}_3(\text{CH}_2)_{17}\text{SiCl}_3$, on silicon are given in this section.

4.2.2.1. Molar Absorption Coefficient.

This was calculated for OTS from equation (2.67), $A = \alpha cl$.

A, the absorbance was determined from the integration under the bands due to the $\nu(\text{CH}_3)$ and $\nu(\text{CH}_2)$ stretching bands in the transmission infrared spectrum to be 8.579 cm^{-1} , (see figure.4.3).

Figure.4.3. Transmission Spectrum of OTS in deuterated toluene.



The concentration of the OTS solution was 5.769 mM and the path length of the cell was 0.02 cm. Substituting these values into equation (2.67) gave the following results:

$$\alpha = \frac{A}{cl} = \frac{8.579 \text{ cm}^{-1}}{0.02 \text{ cm} \times 5.769 \times 10^{-3} \text{ mol dm}^{-3}} = 74354 \text{ mol}^{-1} \text{ dm}^3 \text{ cm}^{-2}$$

The molar absorption coefficient for OTS, ($\nu(\text{CH}_3)$ and $\nu(\text{CH}_2)$ stretching bands) = $74354 \text{ mol}^{-1} \text{ dm}^3 \text{ cm}^{-2}$.

4.2.2.2. Self-Assembled Films of OTS on Silicon.

Films of OTS were self-assembled onto silicon and monitored by FTIR-ATR spectroscopy during their formation. These films were prepared using three different concentrations of OTS in deuterated toluene: 1, 5.8 and 11.6 mM.

The unpolarized FTIR-ATR spectra, ($3150\text{-}2750 \text{ cm}^{-1}$), of the self-assembled film of OTS from a 1 mM solution in toluene, after 2.5, 52 and 107 minutes exposure time to the silane solution, can be seen in figures.4.4 to 4.6. The region, $3150 \text{ to } 2750 \text{ cm}^{-1}$, is shown since the most prominent bands in the OTS spectrum occur in this region, (those due to the $\nu(\text{CH}_3)$ and $\nu(\text{CH}_2)$ stretching bands). Spectra were acquired at 2.38 minutes and then every 7.14 minutes up to a maximum time of 166.6 minutes.

Figure.4.4. FTIR-ATR Spectrum of Self-Assembled OTS Film on Silicon after 2.5 minutes, (1 mM Solution).

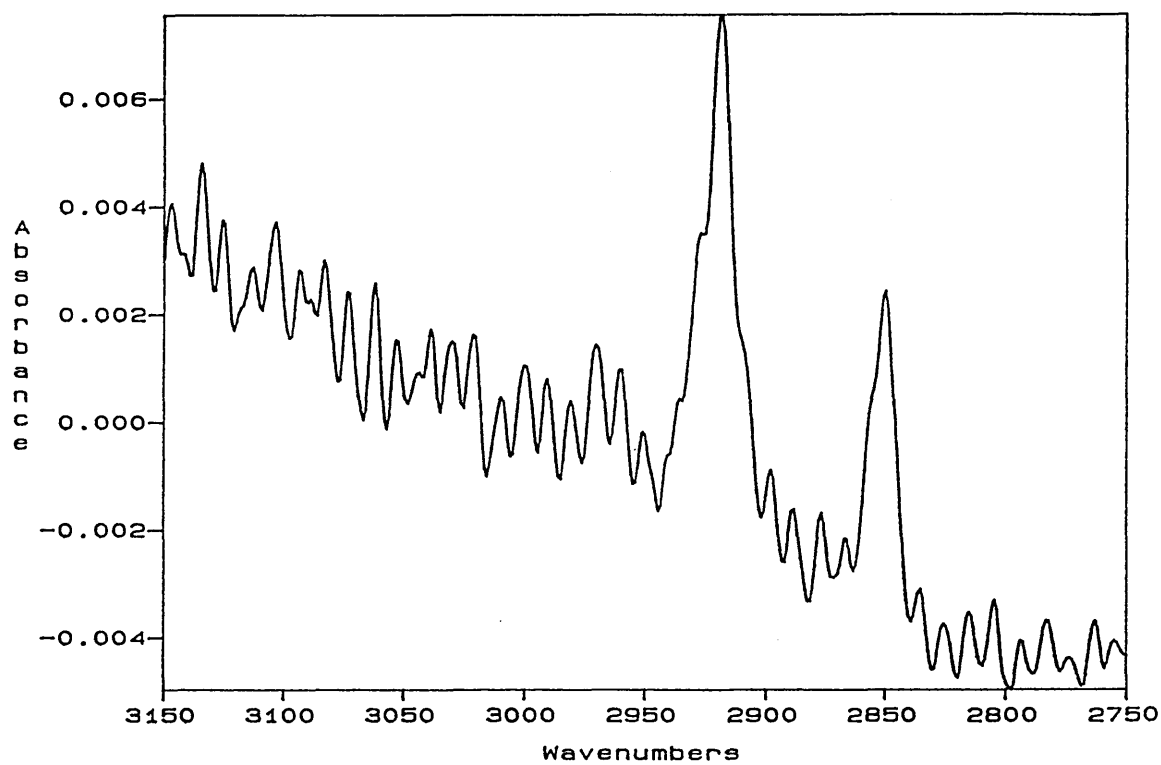


Figure.4.5. FTIR-ATR Spectrum of Self-Assembled OTS Film on Silicon after 52 minutes, (1 mM Solution).

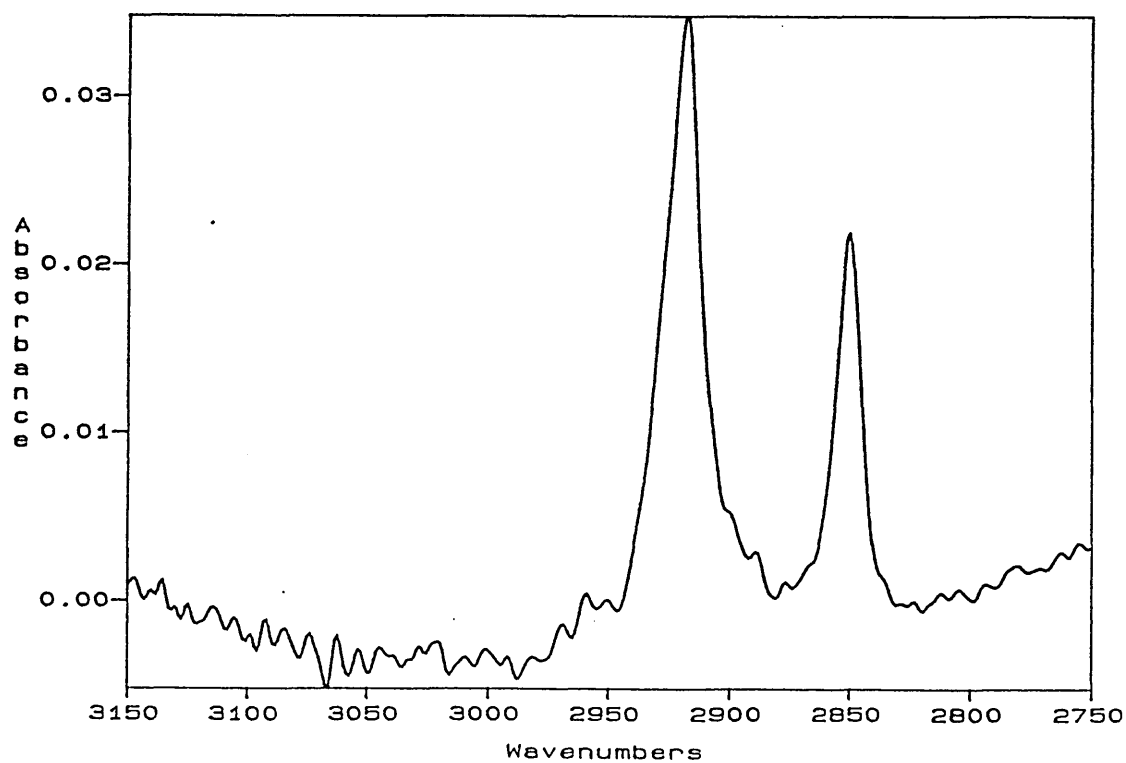
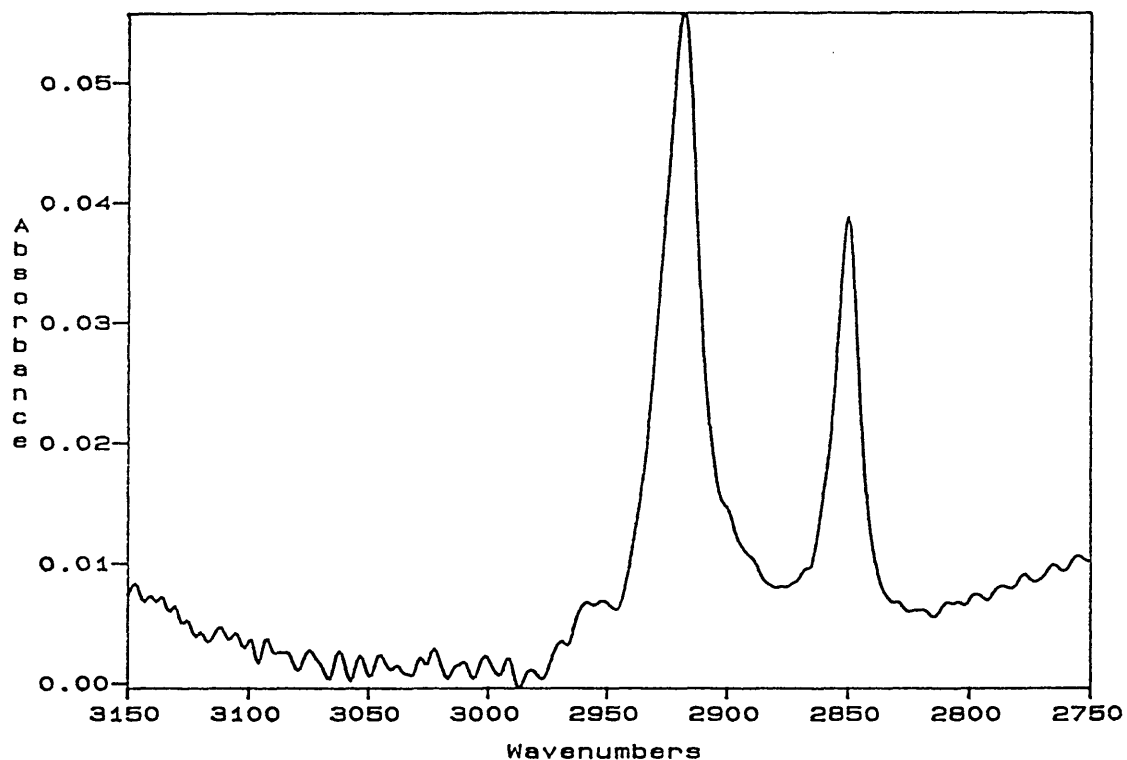


Figure.4.6. FTIR-ATR Spectrum of Self-Assembled OTS Film on Silicon after 107 minutes, (1 mM Solution).



The fringes in the spectra are due to the beam-splitter and arise from problems with aligning the micro ATR prism.

The areas under the bands due to the $\nu(\text{CH}_3)$ and $\nu(\text{CH}_2)$ stretching bands were integrated for all the spectra using FIRST, and are reported in table.4.2.

The areas were obtained by integrating between two different sets of wavenumbers, to estimate the error. This procedure of integration is used for all the measurements of integrated intensity presented in this chapter. All calculated values are quoted to three decimal places only.

The values for c_1t and for the Gibbs surface excess were calculated, (2.62) and the results are reported in table.4.3.

Table.4.2. Total Integrated Intensity Under FTIR-ATR Spectra of Self-Assembled OTS Films on Silicon, (1 mM Solution).

Time exposed to solution / minutes	Integrated Intensity / cm^{-1}
2.38	0.305-0.315
9.52	0.438-0.458
16.66	0.576-0.589
23.8	0.704-0.737
30.94	0.788-0.857
38.08	0.892-0.893
45.22	0.991-1.004
52.36	1.086-1.087
59.5	1.181-1.185
66.64	1.239-1.366
73.78	1.346-1.366
80.92	1.399-1.453
88.06	1.459-1.511
95.2	1.547-1.576
102.34	1.632-1.659
109.48	1.710-1.736
116.62	1.793-1.816
123.76	1.872-1.895
130.90	1.926-1.947
138.04	1.900-1.923
145.18	1.952-1.960
152.32	1.965-1.990
159.4	1.943-1.950
166.6	1.922-1.935

Table.4.3. Gibbs Surface Excess for a Self-Assembled OTS Film on Silicon, (1 mM Solution).

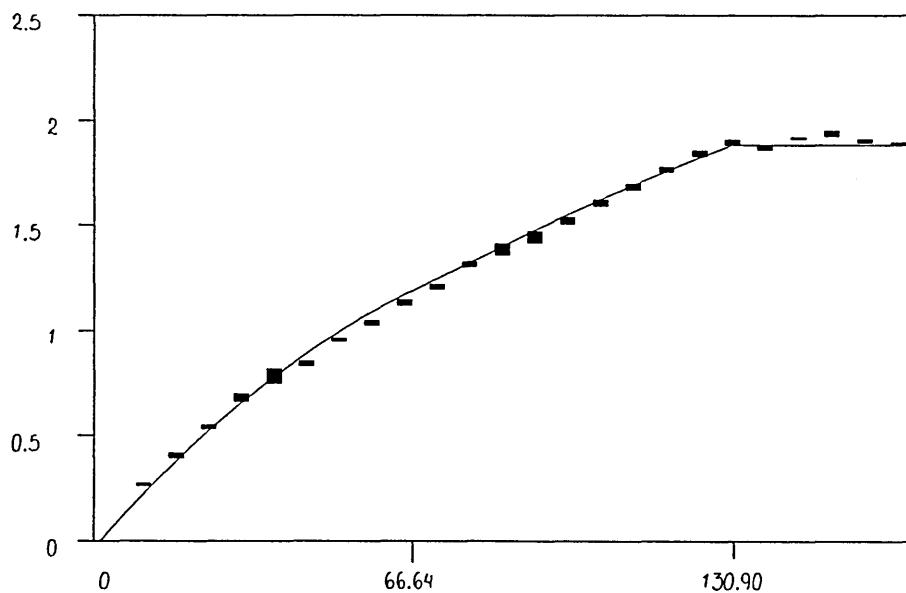
Time exposed to solution / minutes	10^{-10} Gibbs surface excess/ mol cm ⁻²
2.38	0.964-1.000
9.52	1.448-1.520
16.66	1.950-1.997
23.8	2.415-2.535
30.94	2.721-2.972
38.08	3.099-3.103
45.22	3.459-3.506
52.36	3.805-3.808
59.5	4.150-4.165
66.64	4.361-4.430
73.78	4.750-4.823
80.92	4.943-5.140
88.06	5.161-5.351
95.2	5.482-5.587
102.34	5.791-5.889
109.48	6.074-6.169
116.62	6.376-6.460
123.76	6.664-6.747
130.90	6.860-6.936
138.04	6.765-6.849
145.18	6.955-6.984
152.32	7.002-7.093
159.4	6.922-6.947
166.6	6.846-6.893

The percentage contribution of the bulk solution to the integrated intensity, (reported in table.4.2), and hence the bulk and surface contributions to the integrated intensity were calculated and the results are given in table.4.4.

A plot was then produced of the surface contribution to the intensity versus exposure time to solution. This can be seen in figure.4.7.

Figure.4.7. Plot of Integrated Intensity, (Surface Contribution), Versus Exposure Time to Solution, (1 mM Solution).

Integrated intensity of $\nu(\text{CH}_3)$ and $\nu(\text{CH}_2)$ stretching bands / cm^{-1}



Exposure time to silane solution / minutes

Table.4.4. Bulk and Surface Contributions to the Integrated Intensity, (1 mM).

Time of exposure to solution / minutes	Bulk Liquid Contribution / cm^{-1}	Surface Contribution / cm^{-1}
2.38	0.040	0.265-0.275
9.52	0.040	0.398-0.418
16.66	0.040	0.536-0.549
23.8	0.040	0.664-0.697
30.94	0.040	0.748-0.817
38.08	0.040	0.852-0.853
45.22	0.040	0.951-0.964
52.36	0.040	1.046-1.047
59.5	0.040	1.141-1.145
66.64	0.040	1.199-1.218
73.78	0.040	1.306-1.326
80.92	0.040	1.359-1.413
88.06	0.040	1.419-1.471
95.2	0.040	1.507-1.536
102.34	0.040	1.592-1.619
109.48	0.040	1.670-1.696
116.62	0.040	1.753-1.776
123.76	0.040	1.832-1.855
130.90	0.040	1.886-1.907
138.04	0.040	1.860-1.883
145.18	0.040	1.912-1.920
152.32	0.040	1.925-1.950
159.4	0.040	1.903-1.910
166.6	0.040	1.882-1.895

It can be seen from the plot in figure.4.7. that monolayer coverage for this system has been reached, since the plot reaches a constant maximum value at about 130 minutes exposure time to the silane solution. The Gibbs surface excess at this point is $6.860\text{-}6.936 \times 10^{-10} \text{ mol cm}^{-2}$. Therefore the area per molecule, a , is calculated as follows:

$$a, (1 \text{ mM}) = \frac{1 \times 10^{16}}{6.898 \pm 0.038 \times 10^{-10} \text{ mol cm}^{-2}} \times \frac{1}{6.02217 \times 10^{23} \text{ mol}^{-1}} = 24.05 \pm 0.17 \text{ \AA}^2$$

This agrees well with the area per molecule value reported in the literature, [39].

The unpolarized FTIR-ATR spectra, ($3150\text{-}2750 \text{ cm}^{-1}$), of the self-assembled film of OTS from a 5.8 mM solution in toluene, after 3, 81 and 180 minutes exposure time to the silane solution, can be seen in figures.4.8 to 4.10. The region, $3150 \text{ to } 2750 \text{ cm}^{-1}$, is shown since the most prominent bands in the OTS spectrum occur in this region, (those due to the $\nu(\text{CH}_3)$ and $\nu(\text{CH}_2)$ stretching bands). Spectra were obtained every 3 minutes up to a maximum of 180 minutes.

Figure.4.8. FTIR-ATR Spectrum of Self-Assembled OTS Film on Silicon

after 3 minutes, (5.8 mM Solution).

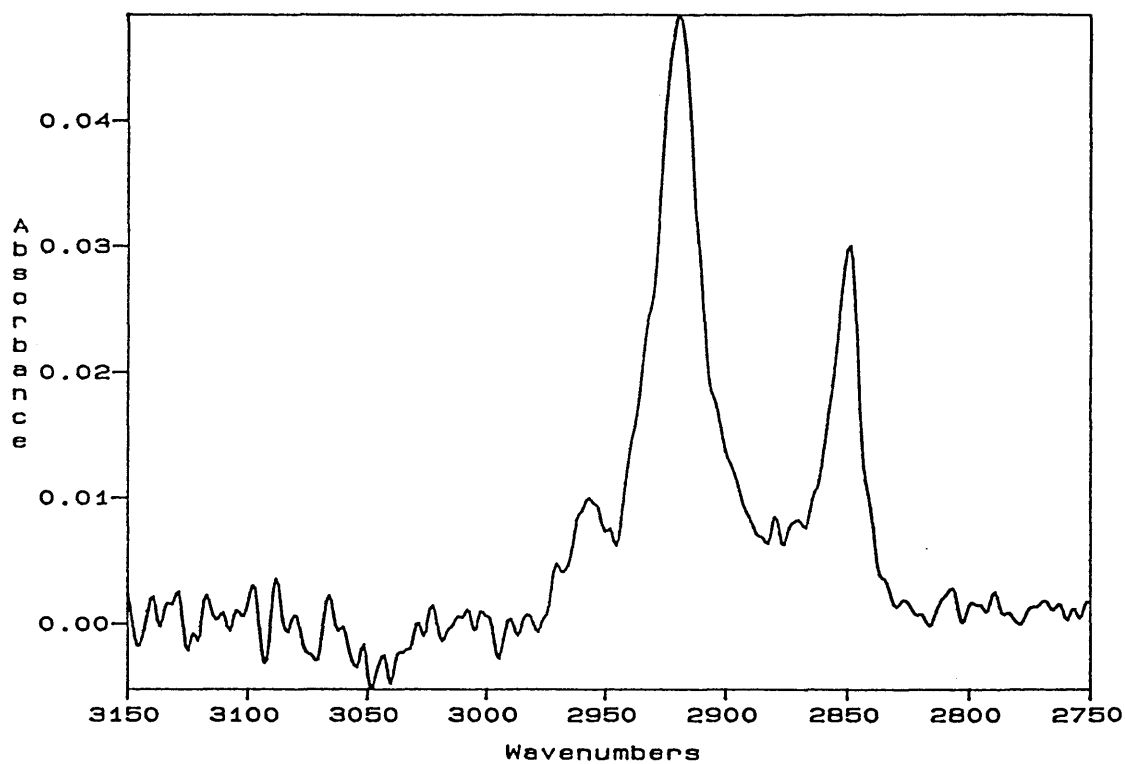


Figure.4.9. FTIR-ATR Spectrum of Self-Assembled OTS Film on Silicon

after 81 minutes, (5.8 mM Solution).

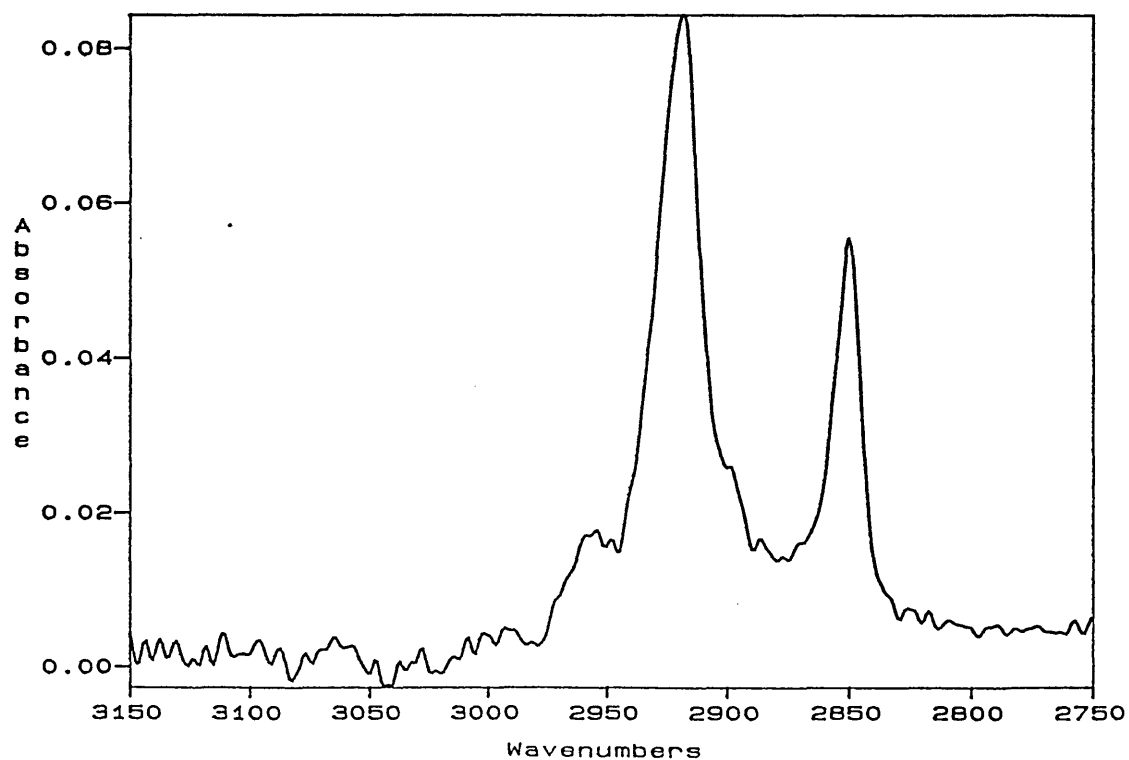
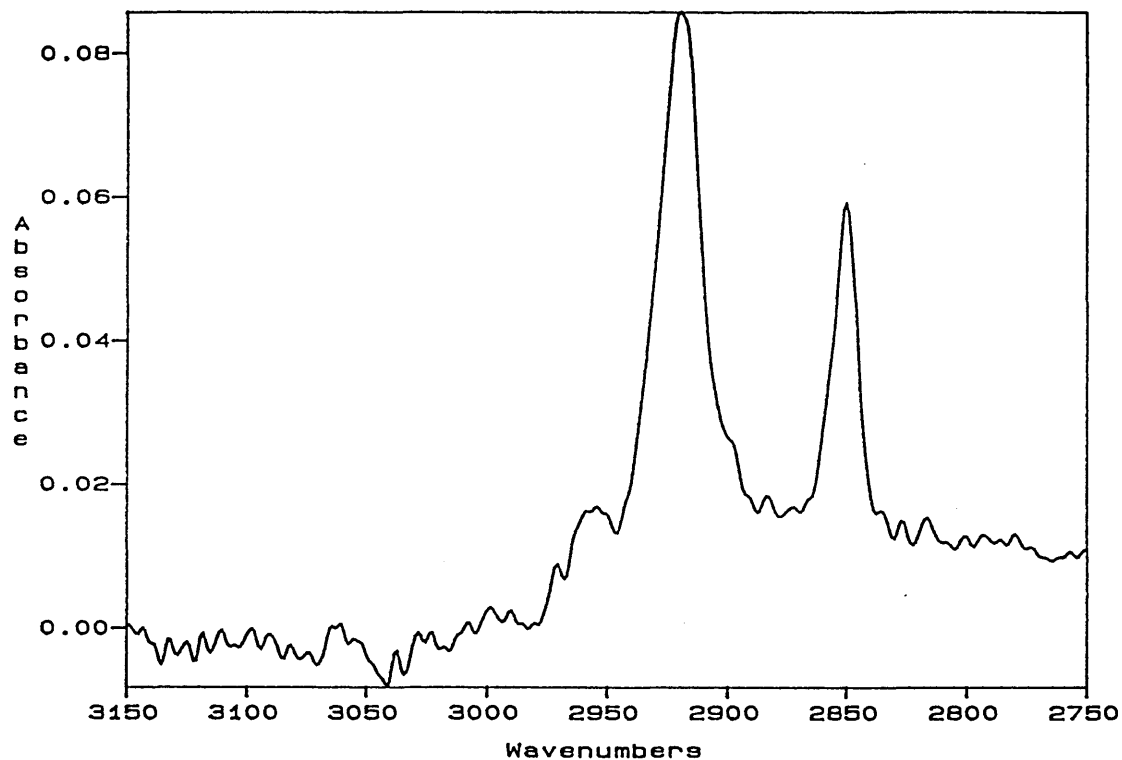


Figure.4.10. FTIR-ATR Spectrum of Self-Assembled OTS Film on Silicon after 180 minutes, (5.8 mM Solution).



The areas under the bands due to the $\nu(\text{CH}_3)$ and $\nu(\text{CH}_2)$ stretching vibrations were integrated for all the spectra using FIRST, and some of the results are reported in table.4.5.

Table.4.5. Total Integrated Intensity Under FTIR-ATR Spectra of Self-Assembled OTS Films on Silicon, (5.8 mM Solution).

Time exposed to solution / minutes	Integrated Intensity / cm^{-1}
3	2.498-2.528
15	3.212-3.233
30	3.456-3.485
45	3.632-3.653
60	3.666-3.679
69	4.001-4.026
75	3.898-3.919
90	4.066-4.088
105	3.965-3.987
120	3.781-3.802
135	3.660-3.681
150	4.075-4.095
165	3.556-3.578
180	3.855-3.878

The values for c_t and for the Gibbs surface excess were calculated, (2.62) and some of the results are reported in table.4.6.

Table.4.6. Gibbs Surface Excess for a Self-Assembled OTS Film on Silicon, (5.8 mM Solution).

Time exposed to solution / minutes	10^{-10} Gibbs surface excess / mol cm ²
3	3.726-3.767
15	5.139-5.181
30	5.628-5.687
45	5.981-6.024
60	6.050-6.076
69	6.722-6.772
75	6.515-6.557
90	6.852-6.896
105	6.649-6.694
120	6.280-6.322
135	6.038-6.080
150	6.870-6.910
165	5.829-5.873
180	6.429-6.475

The percentage contribution of the bulk solution to the integrated intensity, (reported in table.4.5), and hence the bulk and surface contributions to the integrated intensity were calculated and the results are given in table.4.7.

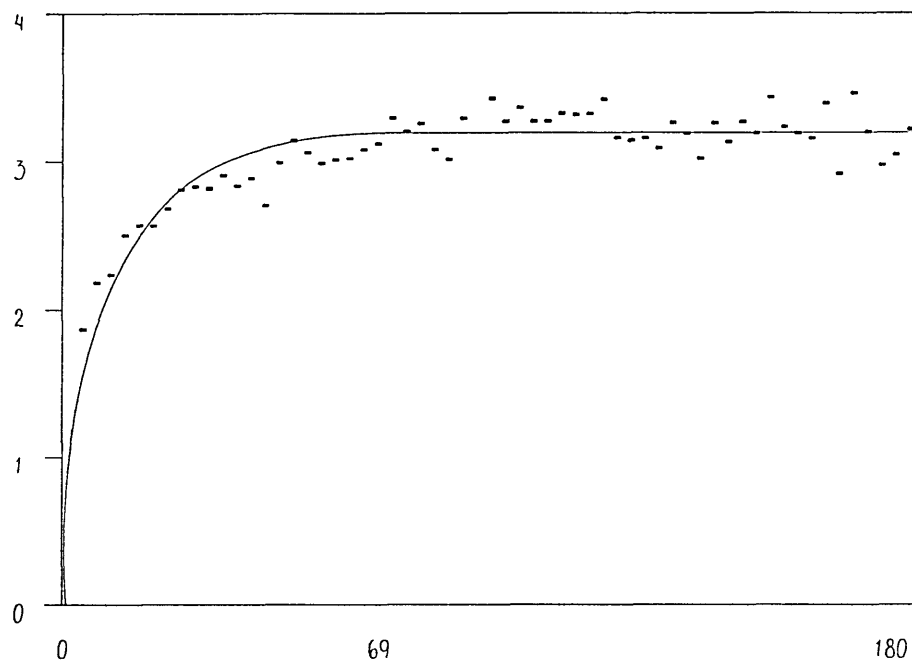
Table.4.7. Bulk and Surface Contributions to the Integrated Intensity, (5.8 mM Solution).

Time of exposure to solution / minutes	Bulk Liquid Contribution / cm ⁻¹	Surface Contribution / cm ⁻¹
3	0.6506	1.857-1.877
15	0.6506	2.561-2.582
30	0.6506	2.805-2.834
45	0.6506	2.981-3.002
60	0.6506	3.015-3.028
69	0.6506	3.350-3.375
75	0.6506	3.247-3.268-
90	0.6506	3.415-3.437
105	0.6506	3.314-3.336
120	0.6506	3.130-3.151
135	0.6506	3.009-3.030
150	0.6506	3.424-3.444
165	0.6506	2.905-2.927
180	0.6506	3.204-3.227

A plot was then produced of the surface contribution to the intensity versus exposure time to solution. This can be seen figure.4.11.

Figure.4.11. Plot of Integrated Intensity, (Surface Contribution), Versus Exposure Time to Solution, (5.8 mM Solution).

Integrated intensity of $\nu(\text{CH}_3)$ and $\nu(\text{CH}_2)$ stretching bands / cm^{-1}



Exposure time to silane solution / minutes

It can be seen from the plot in figure.4.11. that monolayer coverage is obtained after approximately 70 minutes exposure time of the silicon to the silane solution, (i.e. when the plot reaches a constant maximum). The Gibbs surface excess at this point is $6.722\text{-}6.772 \times 10^{-10} \text{ mol cm}^{-2}$. Therefore the area per molecule, a , is calculated as follows:

$$a, (5.8 \text{ mM}) = \frac{1 \times 10^{16}}{6.747 \pm 0.025 \times 10^{-10} \text{ mol cm}^{-2}} \times \frac{1}{6.02217 \times 10^{23} \text{ mol}^{-1}} = 24.6 \pm 0.10 \text{ \AA}^2$$

This agrees well with the literature value reported by Whitesides et al, [39].

The unpolarized FTIR-ATR spectra, (3150-2750 cm^{-1}), of the self-assembled film of OTS from an 11.6 mM solution in toluene, after 3, 30 and 120 minutes exposure time to the silane solution, can be seen in figures.4.12 to 4.14. The region, 3150 to 2750 cm^{-1} , is shown since the most prominent bands in the OTS spectrum occur in this region, (those due to the $\nu(\text{CH}_3)$ and $\nu(\text{CH}_2)$ stretching vibrations). Spectra were acquired every 3 minutes up to a maximum of 120 minutes.

Figure.4.12. FTIR-ATR Spectrum of Self-Assembled OTS Film on Silicon after 3 minutes, 11.6 mM Solution).

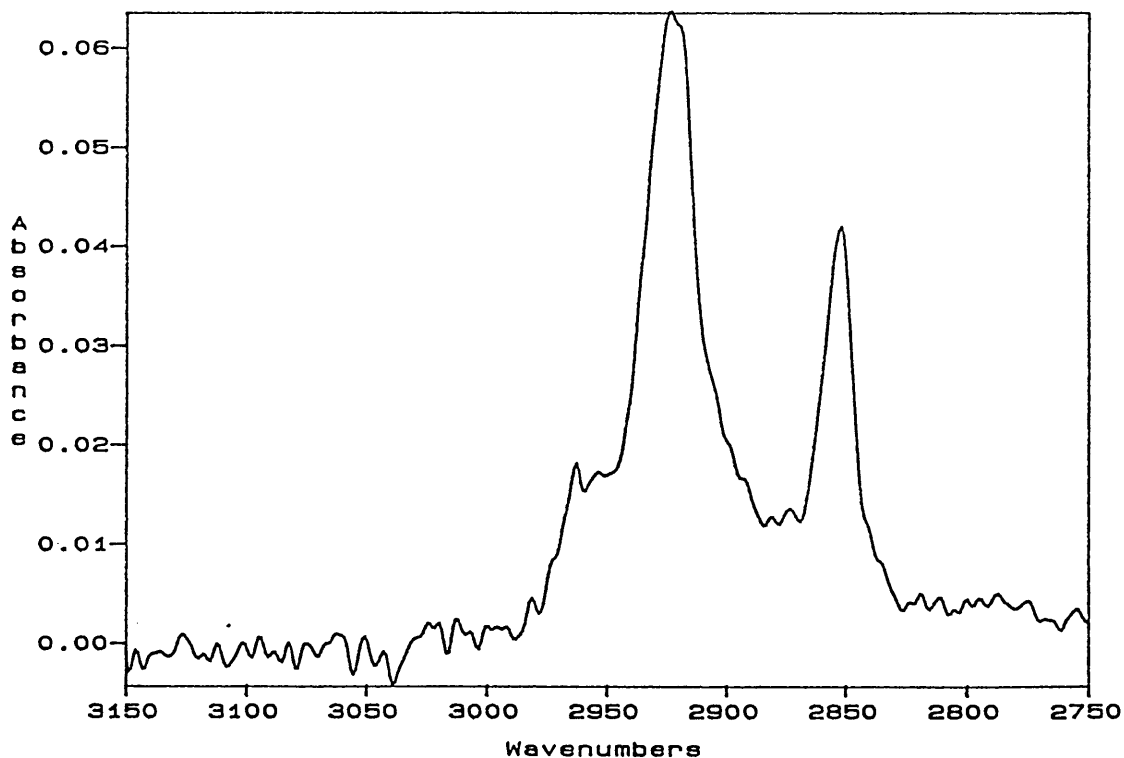


Figure.4.13. FTIR-ATR Spectrum of Self-Assembled OTS Film on Silicon after 30 minutes, (11.6 mM Solution).

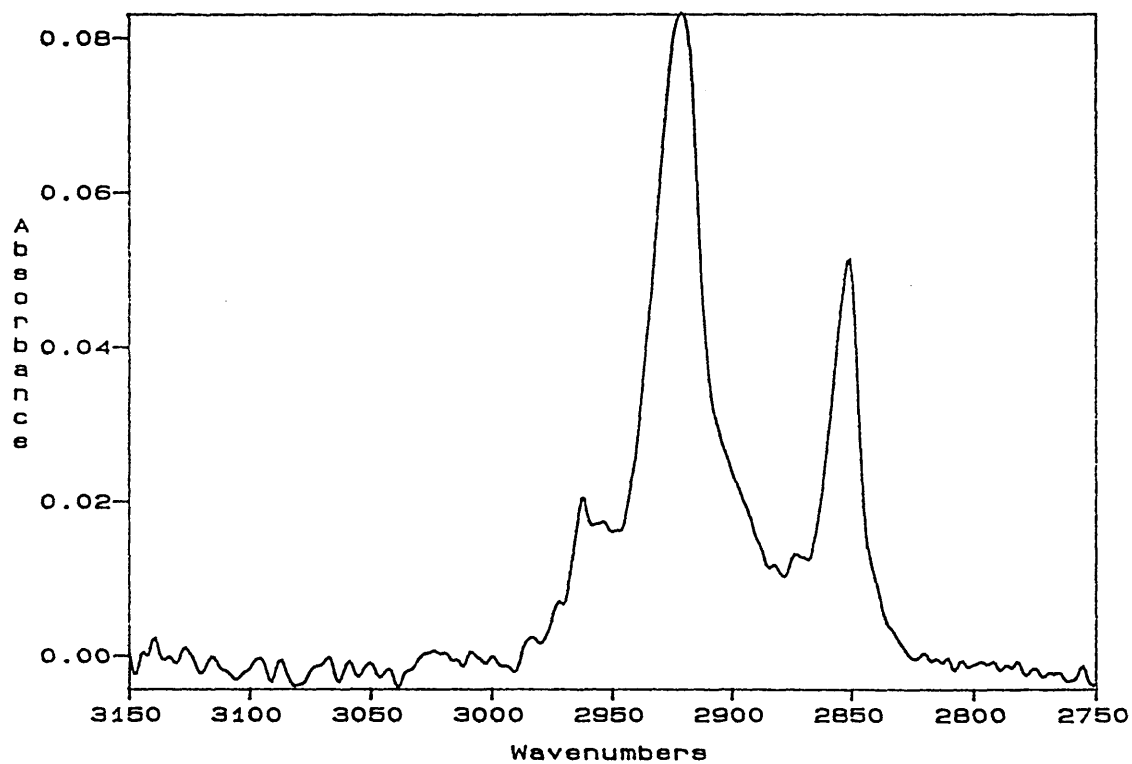
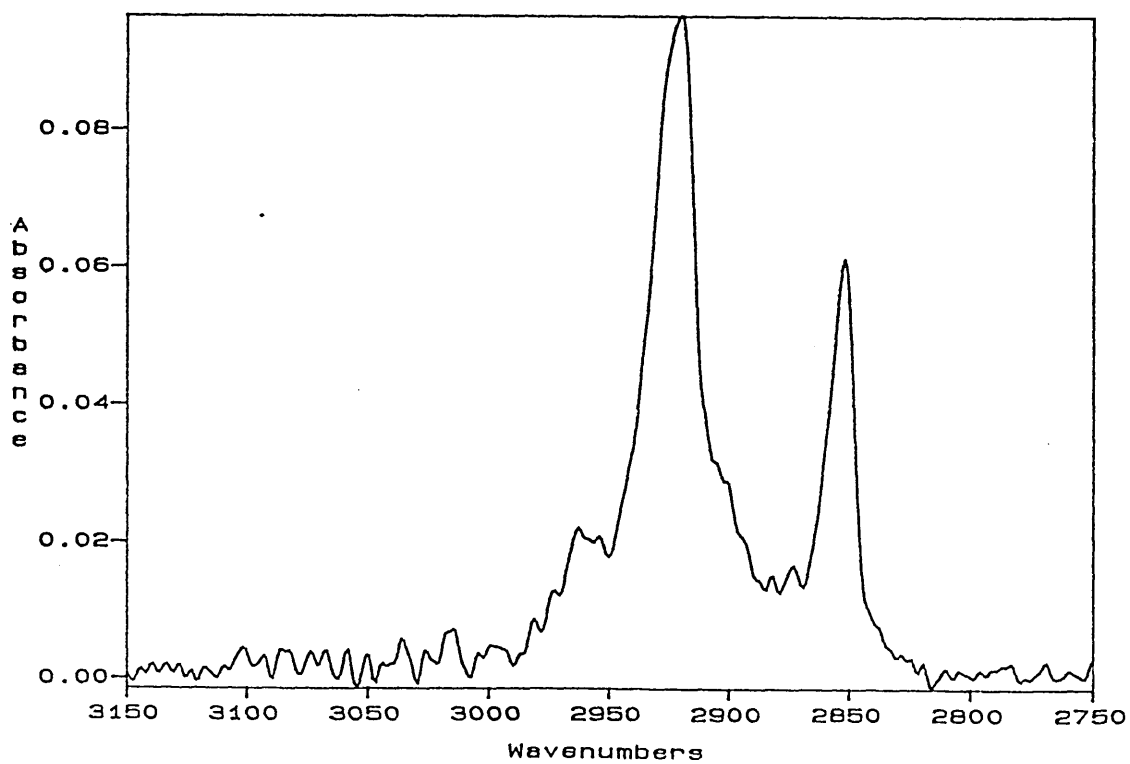


Figure.4.14. FTIR-ATR Spectrum of Self-Assembled OTS Film on Silicon after 120 minutes, (11.6 mM Solution).



The areas under the bands due to the $\nu(\text{CH}_3)$ and $\nu(\text{CH}_2)$ stretching vibrations were integrated for all the spectra using FIRST, and some of the results are reported in table.4.8.

Table.4.8. Total Integrated Intensity Under FTIR-ATR Spectra of Self-Assembled OTS Films on Silicon, (11.6 mM Solution).

Time exposed to solution / minutes	Integrated Intensity / cm^{-1}
3	3.445-3.469
15	4.356-4.380
30	4.588-4.600
45	4.539-4.551
60	4.648-4.668
75	4.799-4.819
90	4.822-4.846
105	4.878-4.890
120	4.873-4.890

The values for c_t and for the Gibbs surface excess were calculated, (2.62) and some of the results are reported in table.4.9.

Table.4.9. Gibbs Surface Excess for a Self-Assembled OTS Film on Silicon, (11.6 mM Solution).

Time exposed to solution / minutes	10^{-10} Gibbs surface excess / mol cm ⁻²
3	4.301-4.349
15	6.129-6.177
30	6.594-6.618
45	6.496-6.520
60	6.715-6.755
75	7.017-7.058
90	7.064-7.112
105	7.176-7.200
120	7.166-7.200

The percentage contribution of the bulk solution to the integrated intensity, (reported in table.4.8), and hence the bulk and surface contributions to the integrated intensity were calculated and the results are given in table.4.10.

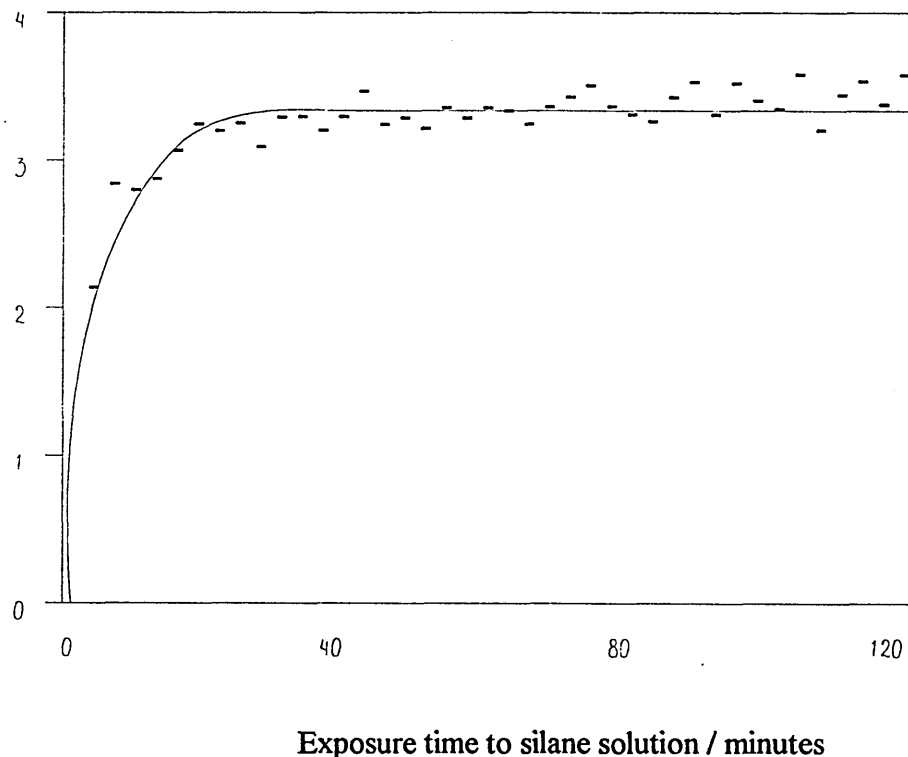
Table.4.10. Bulk and Surface Contributions to the Integrated Intensity,
(11.6 mM Solution).

Time of exposure to solution / minutes	Bulk Liquid Contribution / cm ⁻¹	Surface Contribution / cm ⁻¹
3	1.3012	2.144-2.168
15	1.3012	3.055-3.079
30	1.3012	3.287-3.299
45	1.3012	3.238-3.250
60	1.3012	3.347-3.367
75	1.3012	3.498-3.518
90	1.3012	3.521-3.545
105	1.3012	3.577-3.589
120	1.3012	3.572-3.589

A plot was then produced of the surface contribution to the intensity versus exposure time to solution. This can be seen figure.4.15.

Figure.4.15. Plot of Integrated Intensity, (Surface Contribution), Versus Exposure Time to Solution, (11.6 mM Solution).

Integrated intensity of $\nu(\text{CH}_3)$ and $\nu(\text{CH}_2)$ stretching bands / cm^{-1}



It can be seen from the plot in figure.4.14. that monolayer coverage is obtained after approximately 40 minutes exposure of the silicon to the silane solution, (i.e. when the plot reaches a constant maximum). The Gibbs surface excess at this point is $6.715\text{-}6.755 \times 10^{-10} \text{ mol cm}^{-2}$. Therefore the area per molecule, a , is calculated as follows:

$$a, (11.6 \text{ mM}) = \frac{1 \times 10^{16}}{6.735 \pm 0.020 \times 10^{-10} \text{ mol cm}^{-2}} \times \frac{1}{6.02217 \times 10^{23} \text{ mol}^{-1}} = 24.66 \pm 0.08 \text{ \AA}^2$$

This agrees with both the area per molecule obtained in the previous two experiments and with the literature value reported by Whitesides et al, [39].

From these results, the average area per molecule was obtained for OTS as follows:

$$a, (1 \text{ mM}) = 24.05 \pm 0.17 \text{ \AA}^2$$

$$a, (5.8 \text{ mM}) = 24.60 \pm 0.10 \text{ \AA}^2$$

$$a, (11.6 \text{ mM}) = 24.66 \pm 0.08 \text{ \AA}^2$$

$$\text{Average area per molecule} = \frac{(24.05 + 24.60 + 24.66)}{3} = 24.44 \text{ \AA}^2$$

$$\text{Error in average} = \left(\frac{\left(\frac{0.17}{24.05} + \frac{0.10}{24.60} + \frac{0.08}{24.66} \right)}{3} \right) 24.44 = 0.12 \text{ \AA}^2$$

$$\text{Average area per molecule for OTS} = 24.44 \pm 0.12 \text{ \AA}^2$$

The area per molecule values obtained for the three different concentrations of OTS solution were very similar. These values all agreed well with the value reported by Whitesides et al, [39], for a monolayer of OTS on silicon, obtained from XRD measurements, ($21 \pm 3 \text{ \AA}^2$). Also the area occupied by each silanol group on the silicon surface has been previously determined as approximately 25 \AA^2 , [18]. Therefore it is deduced that for all three concentrations of OTS used here, monolayer formation has occurred. As the concentration of the OTS solution was decreased, it was seen that the monolayer took longer to form. The values obtained for the areas per molecule, for the three different concentrations did not agree with the value, reported by Fujii et al, of an OTS monolayer on silicon obtained from atomic force microscopy measurements, ($43 \pm 7 \text{ \AA}^2$), [57]. Because the areas probed in FTIR-ATR spectroscopy and XRD are similar, these results may be compared. However, because the areas sampled by FTIR-ATR spectroscopy and AFM are very different, (mm^2 for ATR and nm^2 for AFM), the two sets of data would not necessarily be expected to be exactly the same. Also Fujii et al, [57], used a sample preparation technique that may have

produced a surface silanol group density less than 1 silanol group per 25 Å², [62]. Therefore, OTS molecules would not necessarily be closely packed and would possibly be tilted to the surface normal which would then give an area per molecule greater than that reported by Whitesides et al, [39].

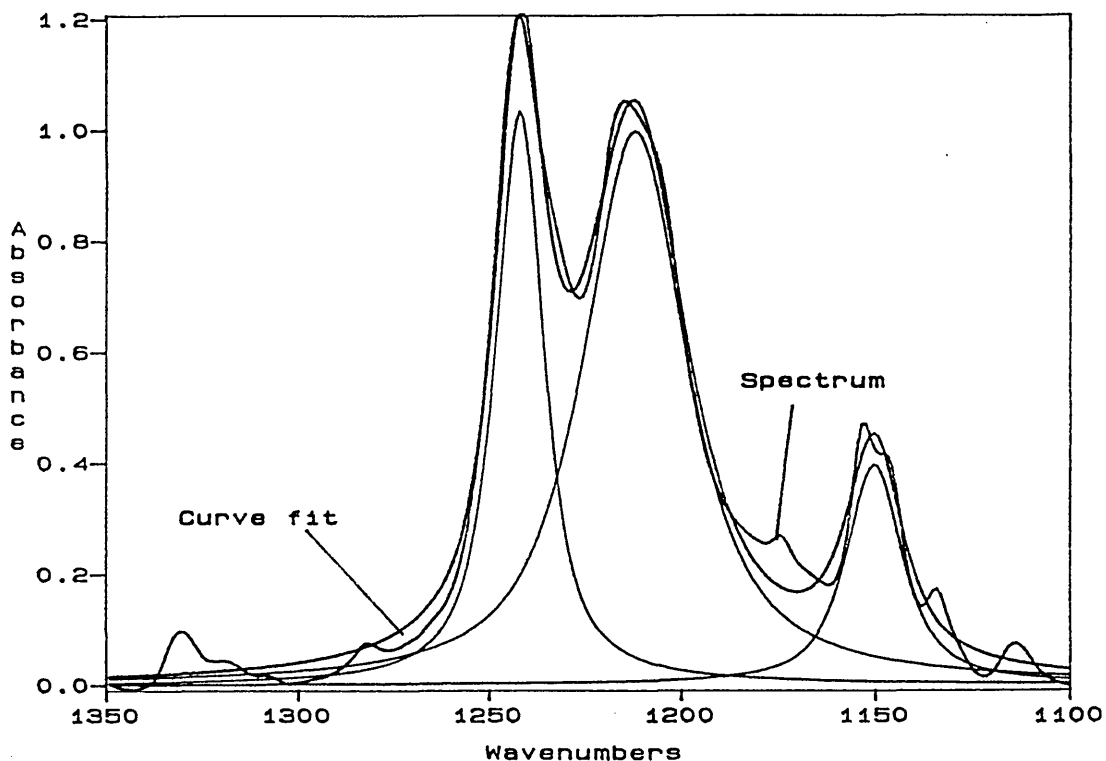
4.2.3. Perfluorodecyl(ethyl)trichlorosilane.

The results of the studies of self-assembled films of perfluorodecyl(ethyl)trichlorosilane, F8, CF₃(CF₂)₇(CH₂)₂SiCl₃, on silicon are given in this section. The bands due to the CF₂ stretching and rocking modes for all the spectra in this section were curve-fitted using the FIRST software. However only the first spectrum presented, (figure.4.16), is shown with the fitted curves.

4.2.3.1. Molar Absorption Coefficient.

This was calculated for F8 from equation (2.67), $A = \alpha cl$. A, the absorbance was determined from the integration under the bands due to the $\nu_{as}(\text{CF}_2)$ stretching vibration in the transmission infrared spectrum to be 53.9035 cm⁻¹, (see figure.4.16).

Figure.4.16. Transmission Spectrum of F8 in deuterated toluene.



The concentration of the F8 solution, c , was 0.162 M and the path length of the cell was 0.002 cm. Substituting these values into equation (2.67) gave the following results:

$$\alpha = \frac{A}{cl} = \frac{53.9035 \text{ cm}^{-1}}{0.002 \text{ cm} \times 0.162 \text{ mol dm}^{-3}} = 166369 \text{ mol}^{-1} \text{ dm}^3 \text{ cm}^{-2}$$

The molar absorption coefficient for F8, ($\nu_{\text{as}}(\text{CF}_2)$ stretching band),
 = 166369 $\text{mol}^{-1} \text{ dm}^3 \text{ cm}^{-2}$.

4.2.3.2. Self-Assembled Films of F8 on Silicon.

Films of F8 were self-assembled onto silicon and monitored by FTIR-ATR spectroscopy during formation. These films were prepared using three different concentrations of F8 in deuterated toluene: 0.25, 0.45 and 1 mM.

The unpolarized FTIR-ATR spectra, (1350-1150 cm^{-1}), of the self-assembled film of F8 from an 0.25 mM solution in toluene, after 10, 220 and 500 minutes

exposure time to the silane solution, can be seen in figures.4.17 to 4.19. The region, 1350 to 1150 cm^{-1} , is shown since the most prominent bands in the F8 spectrum occur in this region, (those due to the CF_2 stretching and rocking vibrations). The large absorbance peak at approximately 1150 cm^{-1} is due to the absorption of the silicon substrate. Spectra were acquired every 10 minutes up to a maximum of 500 minutes.

Figure.4.17. FTIR-ATR Spectrum of Self-Assembled F8 Film on Silicon after 10 minutes, 0.25 mM Solution).

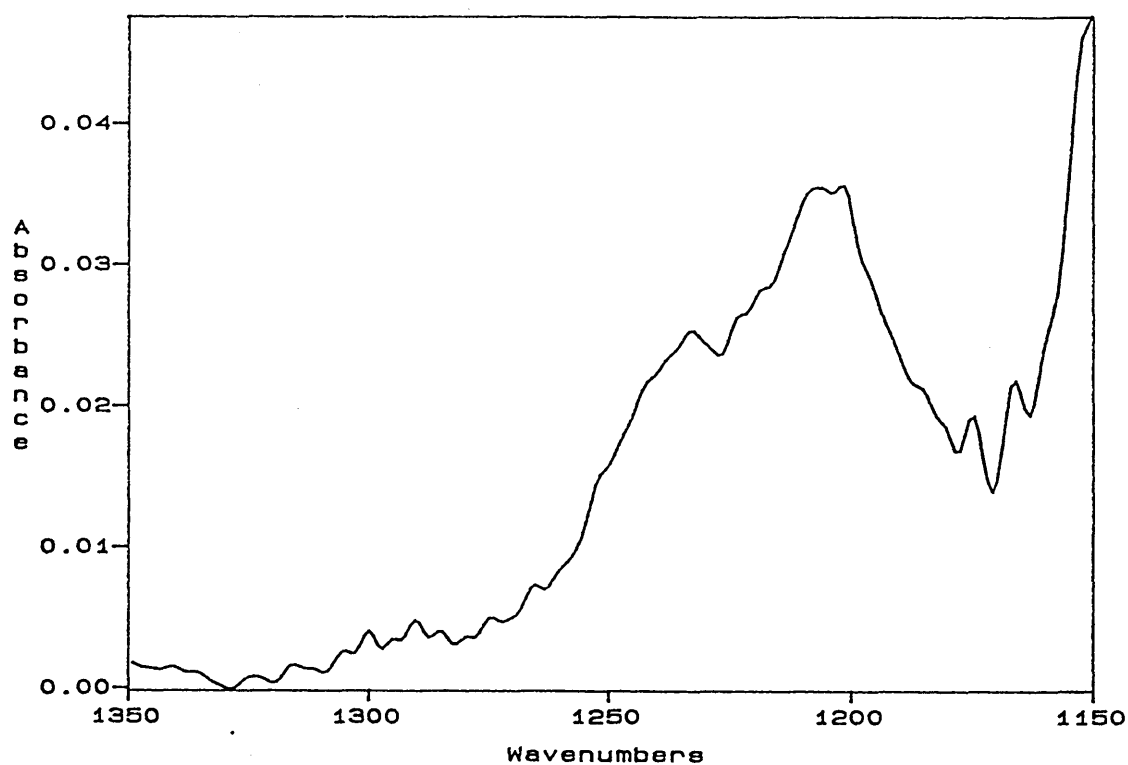


Figure.4.18. FTIR-ATR Spectrum of Self-Assembled F8 Film on Silicon

after 220 minutes, (0.25 mM Solution).

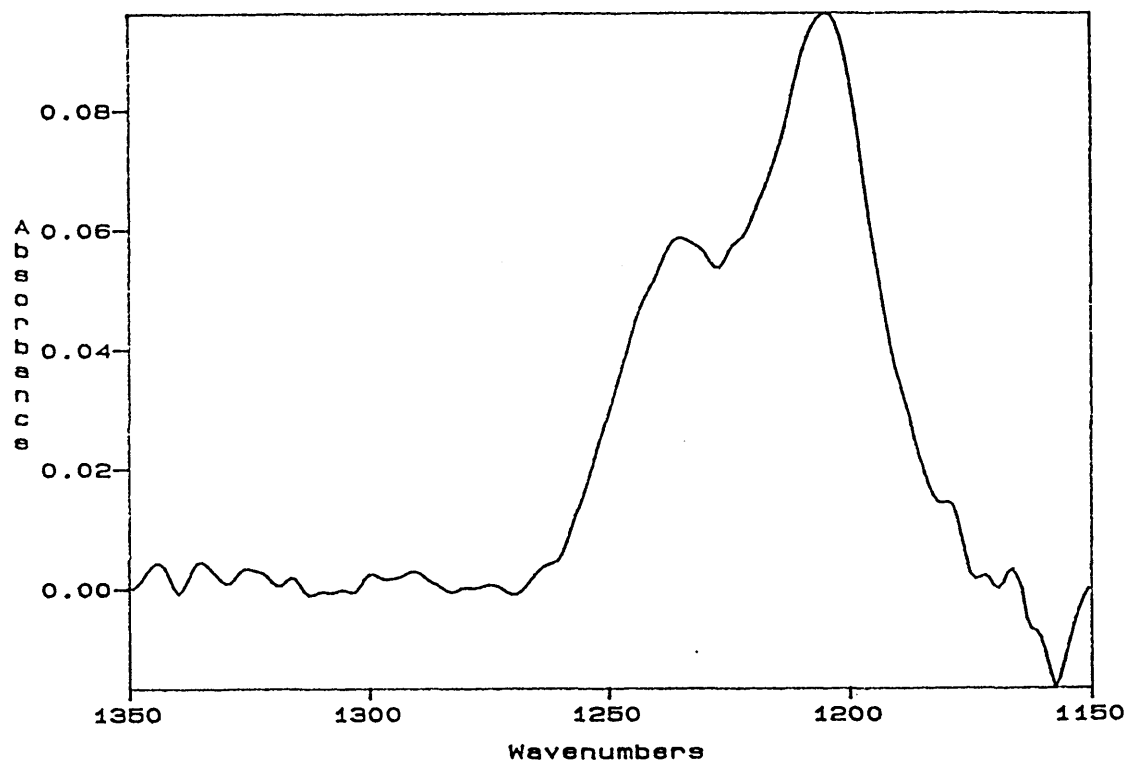
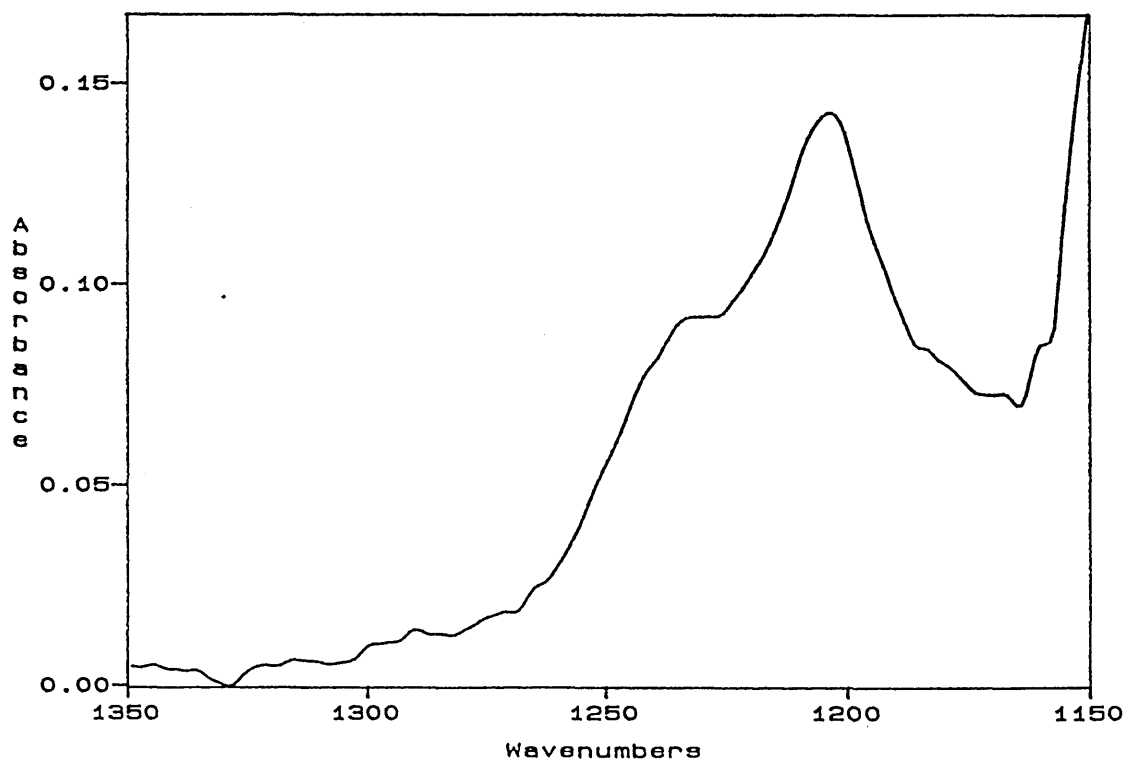


Figure.4.19. FTIR-ATR Spectrum of Self-Assembled F8 Film on Silicon

after 500 minutes, (0.25 mM Solution).



The areas under the bands due to the $\nu_{as}(\text{CF}_2)$ stretching vibrations were integrated for all the spectra using FIRST, and some of the results are reported in table.4.11.

Table.4.11. Total Integrated Intensity Under FTIR-ATR Spectra of Self-Assembled F8 Films on Silicon, (0.25 mM Solution).

Time exposed to solution / minutes	Integrated Intensity / cm^{-1}
10	0.881-0.883
60	2.172-2.193
120	2.766-2.789
180	3.175-3.213
220	3.442-3.462
240	3.201-3.226
300	3.378-3.407
360	3.538-3.544
420	3.539-3.576
480	3.647-3.632
500	3.510-3.512

The values for c_t and for the Gibbs surface excess were calculated, (2.62) and some of the results are reported in table.4.12.

Table.4.12. Gibbs Surface Excess for a Self-Assembled F8 Film on Silicon,
(0.25 mM Solution).

Time exposed to solution / minutes	10^{10} Gibbs surface excess / mol cm ⁻²
10	1.308-1.311
60	3.354-3.386
120	4.294-4.331
180	4.943-5.002
220	5.366-5.397
240	4.984-5.024
300	5.264-5.310
360	5.517-5.527
420	5.518-5.577
480	5.690-5.667
500	5.474-5.477

The percentage contribution of the bulk solution to the integrated intensity, (reported in table.4.11), and hence the bulk and surface contributions to the integrated intensity were calculated and the results are given in table.4.13.

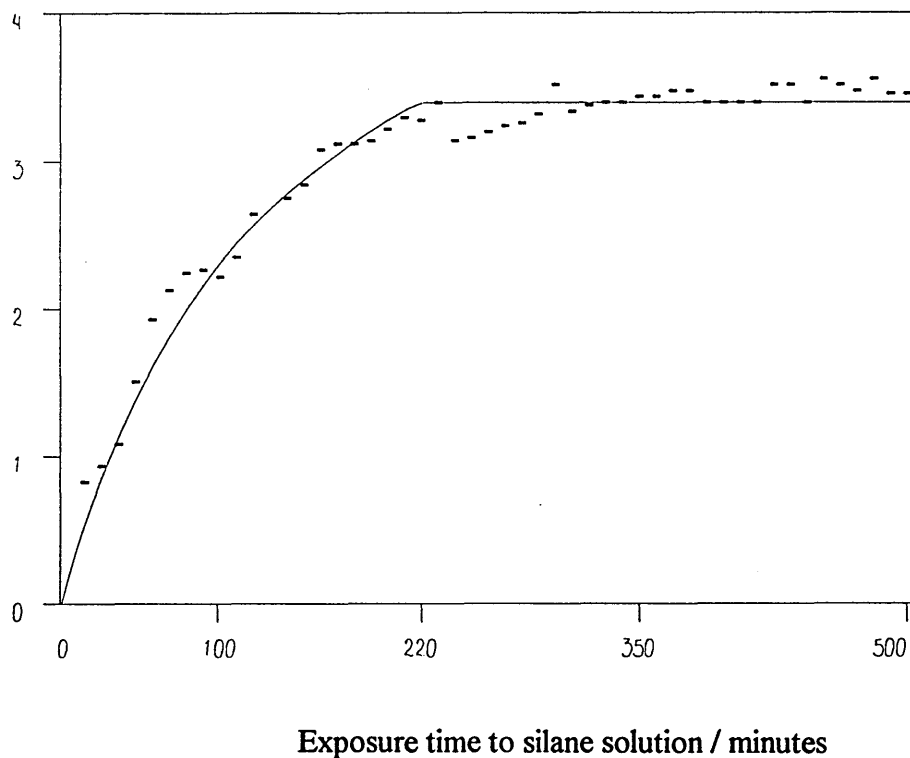
Table.4.13. Bulk and Surface Contributions to the Integrated Intensity,
(0.25 mM Solution).

Time of exposure to solution / minutes	Bulk Liquid Contribution / cm ⁻¹	Surface Contribution / cm ⁻¹
10	0.0550	0.826-0.827
60	0.0550	2.117-2.137
120	0.0550	2.711-2.734
180	0.0550	3.120-3.158
220	0.0550	3.387-3.407
240	0.0550	3.146-3.171
300	0.0550	3.323-3.352
360	0.0550	3.483-3.489
420	0.0550	3.483-3.520
480	0.0550	3.577-3.592
500	0.0550	3.455-3.457

A plot was then produced of the surface contribution to the intensity versus exposure time to solution. This can be seen figure.4.20.

Figure.4.20. Plot of Integrated Intensity, (Surface Contribution), Versus Exposure Time to Solution, (0.25 mM Solution).

Integrated intensity of $\nu_{as}(\text{CF}_2)$ stretching bands / cm^{-1}



It can be seen from the plot in figure.4.20. that monolayer coverage is obtained after approximately 220 minutes exposure of the silicon to the silane solution, (i.e. when the plot reaches a constant maximum). The Gibbs surface excess at this point is $5.366\text{-}5.397 \times 10^{-10} \text{ mol cm}^{-2}$. Therefore the area per molecule, a , is calculated as follows:

$$a, (0.25 \text{ mM}) = \frac{1 \times 10^{16}}{5.382 \pm 0.02 \times 10^{-10} \text{ mol cm}^{-2}} \times \frac{1}{6.02217 \times 10^{23} \text{ mol}^{-1}} = 30.86 \pm 0.1 \text{ \AA}^2$$

Fuji et al, [57], using atomic force microscopy, determined the area per molecule of OTS and of F8 adsorbed onto silicon. They discovered that the

fluorocarbon chain occupied an approximate area of 15% greater than the non-fluorinated chain.

The unpolarized FTIR-ATR spectra, ($1350-1150\text{ cm}^{-1}$), of the self-assembled film of F8 from a 0.45 mM solution in toluene, after 2.38, 52.36 and 66.64 minutes exposure time to the silane solution, can be seen in figures.4.21 to 4.23. The region, $1350\text{ to }1150\text{ cm}^{-1}$, is shown since the most prominent bands in the F8 spectrum occur in this region, (those due to the CF_2 stretching and rocking vibrations). Spectra were acquired at 2.38 minutes and then every 7.14 minutes up to a maximum of 66.64 minutes.

Figure.4.21. FTIR-ATR Spectrum of Self-Assembled F8 Film on Silicon after 2.38 minutes, (0.45 mM Solution).

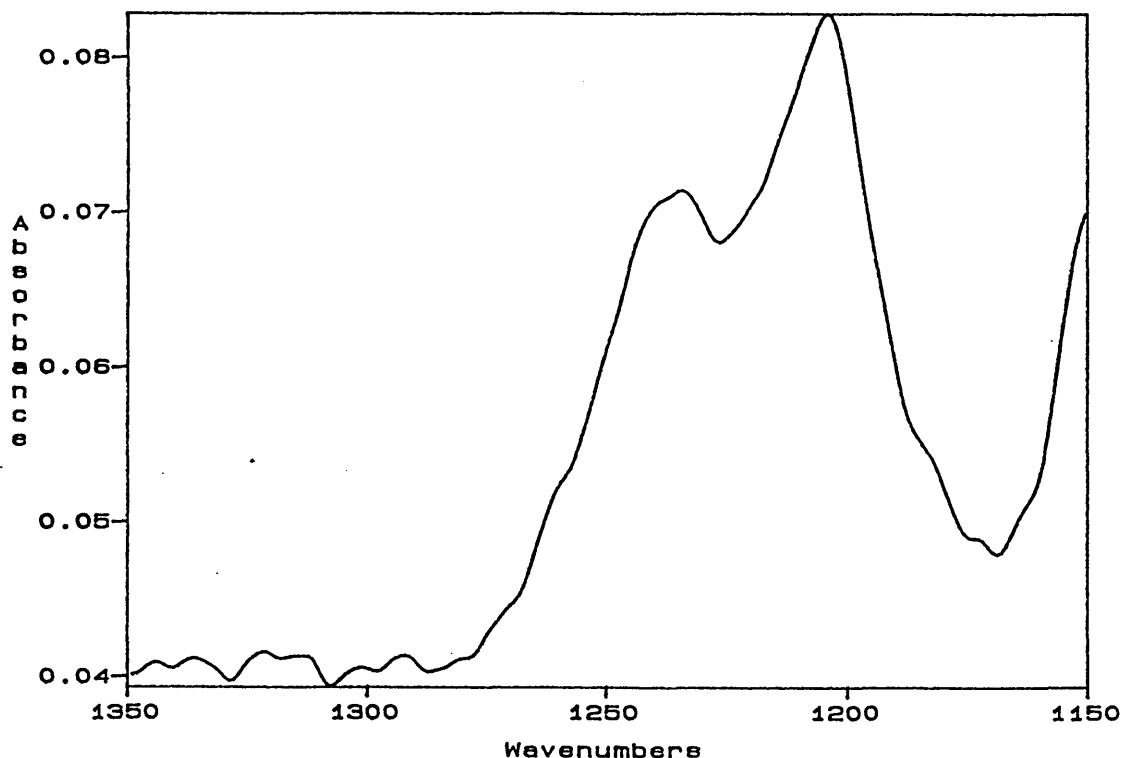


Figure.4.22. FTIR-ATR Spectrum of Self-Assembled F8 Film on Silicon

after 52.36 minutes, (0.45 mM Solution).

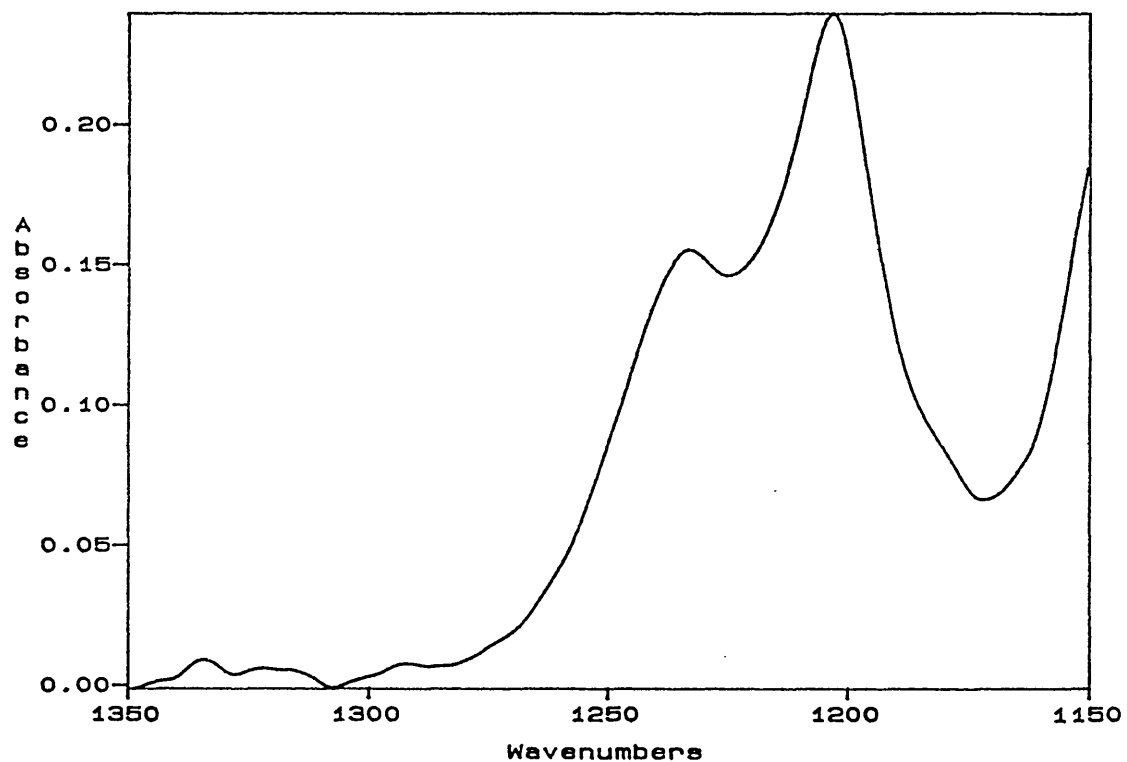
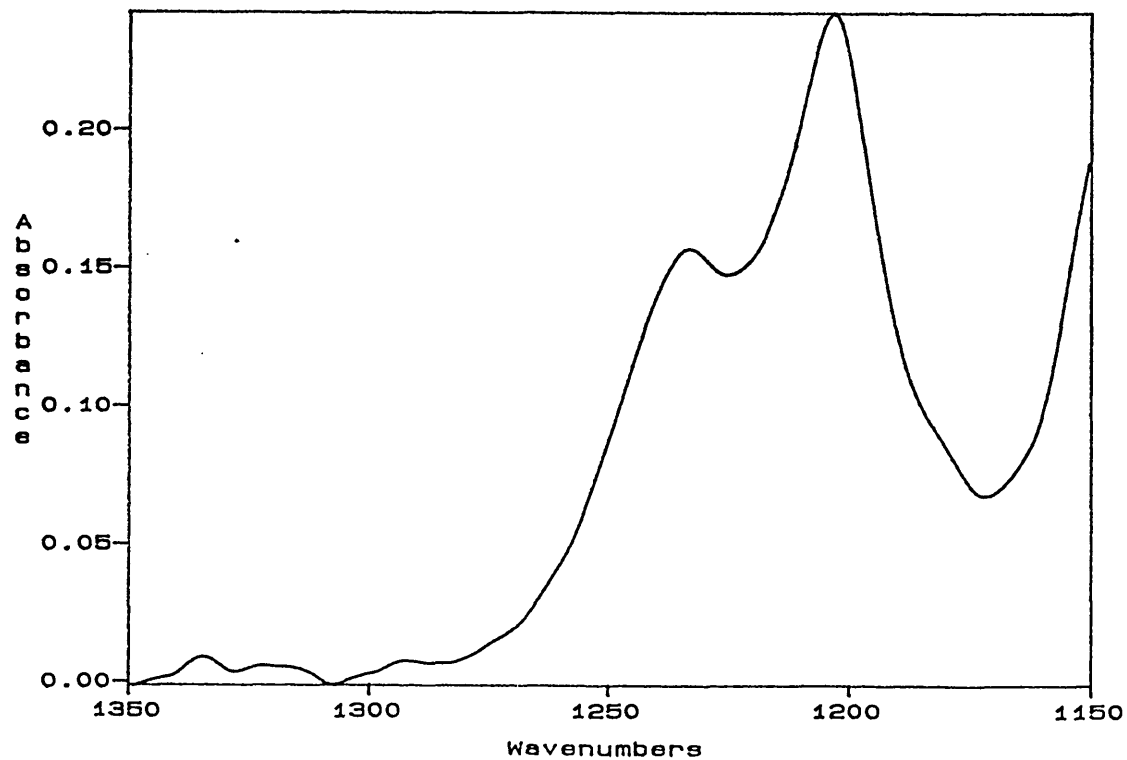


Figure.4.23. FTIR-ATR Spectrum of Self-Assembled F8 Film on Silicon

after 66.64 minutes, (0.45 mM Solution).



The areas under the bands due to the $\nu_{as}(\text{CF}_2)$ stretching vibrations were integrated for all the spectra using FIRST, and some of the results are reported in table.4.14.

Table.4.14. Total Integrated Intensity Under FTIR-ATR Spectra of Self-Assembled F8 Films on Silicon, (0.45 mM Solution).

Time exposed to solution / minutes	Integrated Intensity / cm^{-1}
2.38	1.501-1.502
9.52	4.104-4.136
16.66	6.368-6.382
23.8	7.518-7.540
30.94	8.219-8.239
38.08	8.631-8.651
45.22	8.754-8.774
52.36	8.919-8.949
59.5	8.919-8.939
66.64	8.937-8.957

The values for c_t and for the Gibbs surface excess were calculated, (2.62) and some of the results are reported in table.4.15.

Table.4.15. Gibbs Surface Excess for a Self-Assembled F8 Film on Silicon,
(0.45 mM Solution).

Time exposed to solution / minutes	10^{-10} Gibbs surface excess / mol cm ⁻²
2.38	0.628-0.630
9.52	2.347-2.368
16.66	3.842-3.852
23.8	4.602-4.616
30.94	5.065-5.078
38.08	5.337-5.350
45.22	5.418-5.431
52.36	5.527-5.540
59.5	5.527-5.540
66.64	5.539-5.552

The percentage contribution of the bulk solution to the integrated intensity, (reported in table.4.14), and hence the bulk and surface contributions to the integrated intensity were calculated and the results are given in table.4.16.

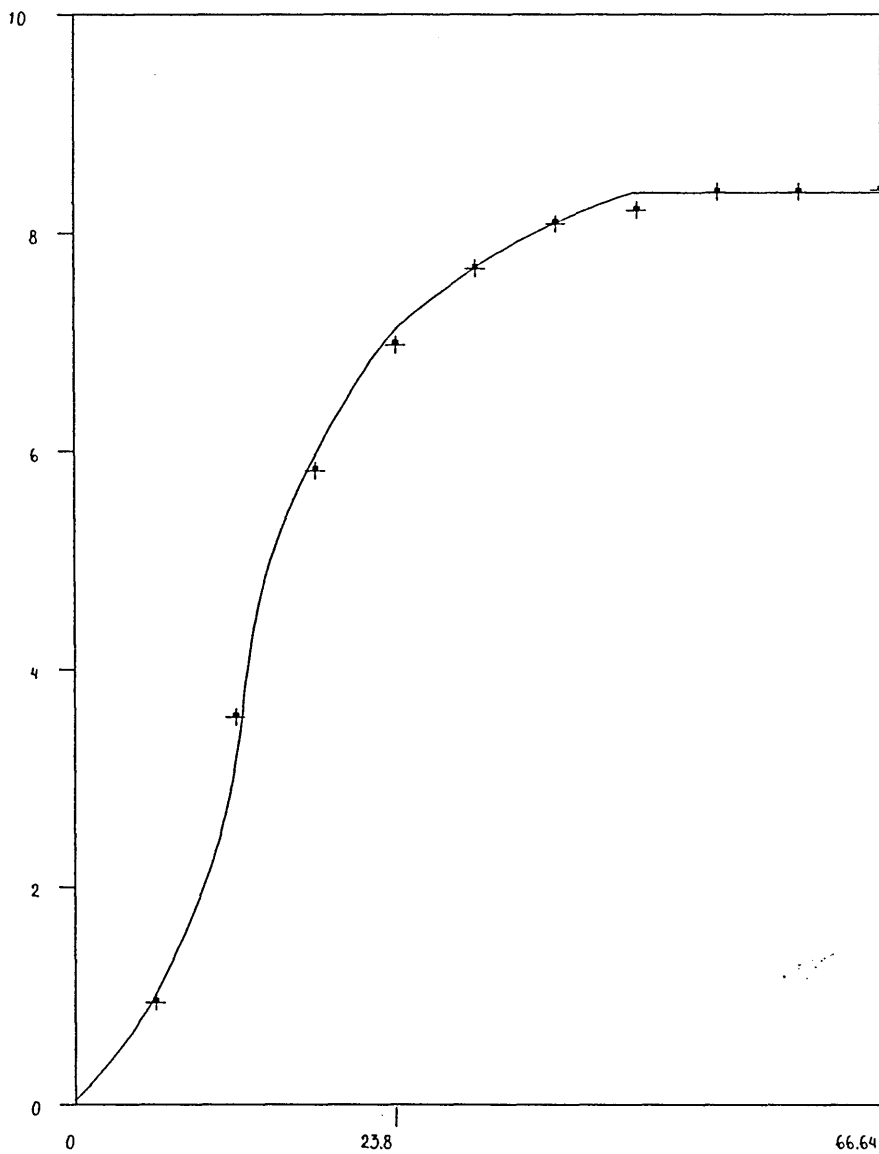
Table.4.16. Bulk and Surface Contributions to the Integrated Intensity,
(0.45 mM Solution).

Time of exposure to solution / minutes	Bulk Liquid Contribution / cm^{-1}	Surface Contribution / cm^{-1}
2.38	0.5491	0.951-0.954
9.52	0.5491	3.555-3.587
16.66	0.5491	5.819-5.833
23.8	0.5491	6.969-6.991
30.94	0.5491	7.670-7.690
38.08	0.5491	8.082-8.102
45.22	0.5491	8.205-8.225
52.36	0.5491	8.370-8.390
59.5	0.5491	8.370-8.390
66.64	0.5491	8.388-8.408

A plot was then produced of the surface contribution to the intensity versus exposure time to solution. This can be seen figure.4.24.

Figure.4.24. Plot of Integrated Intensity, (Surface Contribution), Versus Exposure Time to Solution, (0.45 mM Solution).

Integrated intensity of $\nu_{as}(\text{CF}_2)$ stretching bands / cm^{-1}



Exposure time in silane solution / minutes

It can be seen from the plot in figure.4.24. that monolayer coverage is obtained after approximately 52 minutes exposure of the silicon to the silane solution, (i.e. when the plot reaches a constant maximum). The Gibbs surface excess at this point is $5.527\text{-}5.540 \times 10^{-10} \text{ mol cm}^{-2}$. Therefore the area per molecule, a , is calculated as follows:

$$a, (0.45 \text{ mM}) = \frac{1 \times 10^{16}}{5.534 \pm 0.01 \times 10^{-10} \text{ mol cm}^{-2}} \times \frac{1}{6.02217 \times 10^{23} \text{ mol}^{-1}} = 30.0 \pm 0.04 \text{ \AA}^2$$

This result agrees with the result from the previous experiment.

The unpolarized FTIR-ATR spectra, ($1350\text{-}1150 \text{ cm}^{-1}$), of the self-assembled film of F8 from an 1 mM solution in toluene, after 2.38, 16.66 and 71.4 minutes exposure time to the silane solution, can be seen in figures.4.25 to 4.27. The region, $1350 \text{ to } 1150 \text{ cm}^{-1}$, is shown since the most prominent bands in the F8 spectrum occur in this region, (those due to the CF_2 stretching and rocking vibrations). Spectra were acquired every 2.38 minutes up to a maximum of 71.4 minutes.

Figure.4.25. FTIR-ATR Spectrum of Self-Assembled F8 Film on Silicon after 2.38 minutes, (1 mM Solution).

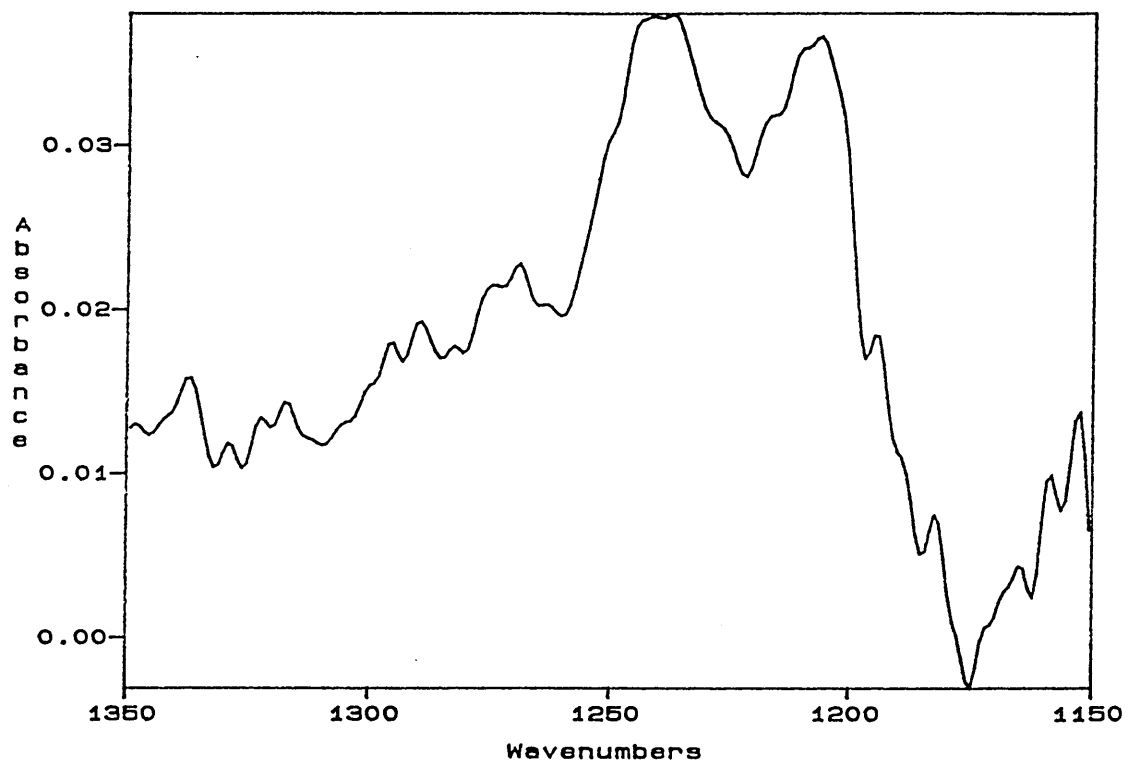


Figure.4.26. FTIR-ATR Spectrum of Self-Assembled F8 Film on Silicon after 16.66 minutes, (1 mM Solution).

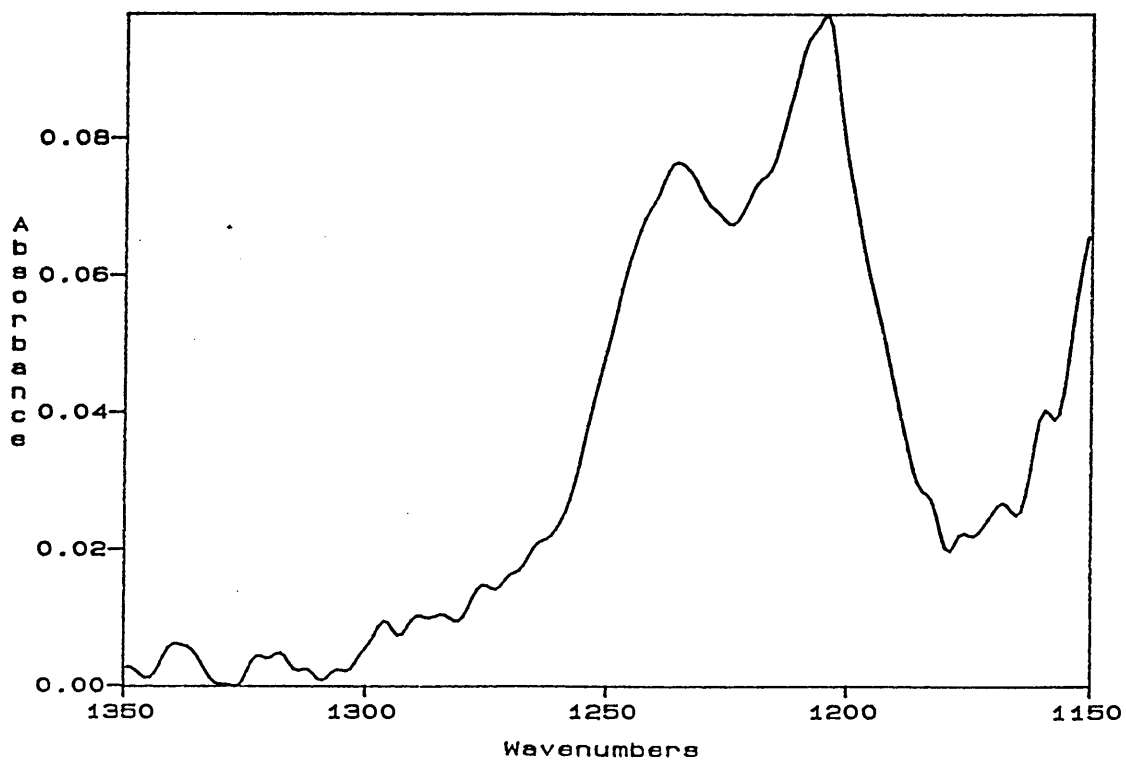
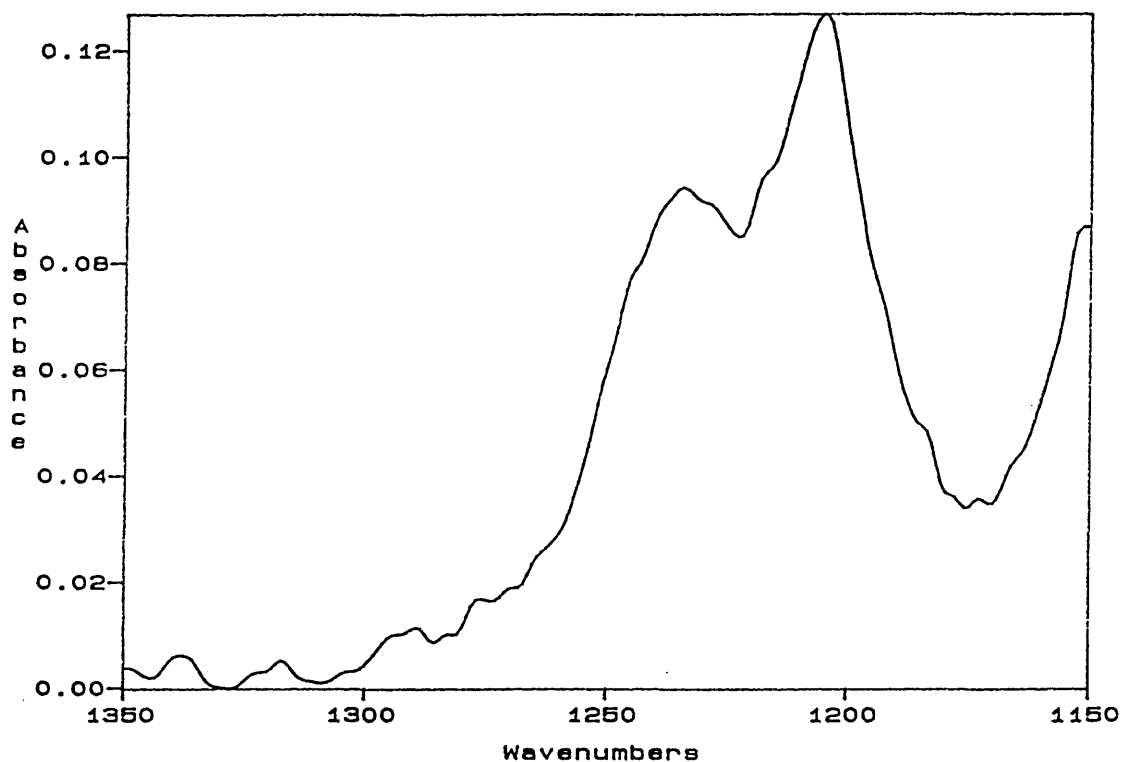


Figure.4.27. FTIR-ATR Spectrum of Self-Assembled F8 Film on Silicon after 71.4 minutes, (1 mM Solution).



The areas under the bands due to the $\nu_{as}(\text{CF}_2)$ stretching vibrations were integrated for all the spectra using FIRST, and some of the results are reported in table.4.17.

Table.4.17. Total Integrated Intensity Under FTIR-ATR Spectra of Self-Assembled F8 Films on Silicon, (1 mM Solution).

Time exposed to solution / minutes	Integrated Intensity / cm^{-1}
2.38	1.276-1.296
9.52	2.151-2.174
16.66	3.798-3.820
23.8	3.798-3.820
30.94	3.918-3.938
38.08	3.958-3.978
45.22	3.958-3.978
52.36	4.156-4.176
59.5	4.235-4.256
66.64	4.394-4.414
71.4	4.434-4.454

The values for $c;t$ and for the Gibbs surface excess were calculated, (2.62) and some of the results are reported in table.4.18.

Table.4.18. Gibbs Surface Excess for a Self-Assembled F8 Film on Silicon,
(1 mM Solution).

Time exposed to solution / minutes	10^{-10} Gibbs surface excess / mol cm ⁻²
2.38	1.672-1.704
9.52	3.059-3.096
16.66	5.668-5.703
23.8	5.668-5.703
30.94	5.859-5.889
38.08	5.921-5.953
45.22	5.921-5.953
52.36	6.235-6.267
59.5	6.360-6.393
66.64	6.612-6.644
71.4	6.675-6.707

The percentage contribution of the bulk solution to the integrated intensity, (reported in table.4.17), and hence the bulk and surface contributions to the integrated intensity were calculated and the results are given in table.4.19.

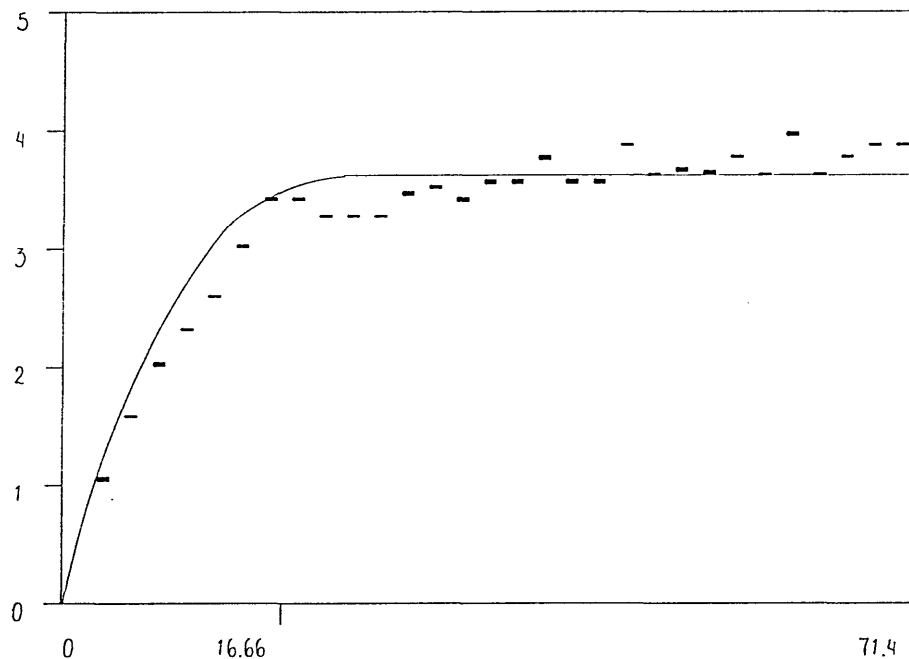
Table.4.19. Bulk and Surface Contributions to the Integrated Intensity, (1 mM Solution).

Time of exposure to solution / minutes	Bulk Liquid Contribution / cm ⁻¹	Surface Contribution / cm ⁻¹
2.38	0.2201	1.056-1.076
9.52	0.2201	1.931-1.954
16.66	0.2201	3.578-3.600
23.8	0.2201	3.578-3.600
30.94	0.2201	3.699-3.718
38.08	0.2201	3.737-3.758
45.22	0.2201	3.737-3.758
52.36	0.2201	3.936-3.956
59.5	0.2201	4.015-4.036
66.64	0.2201	4.174-4.194
71.4	0.2201	4.214-4.234

A plot was then produced of the surface contribution to the intensity versus exposure time to solution. This can be seen figure.4.28.

Figure.4.28. Plot of Integrated Intensity, (Surface Contribution), Versus Exposure Time to Solution, (1 mM Solution).

Integrated intensity of $\nu_{as}(\text{CF}_2)$ stretching bands / cm^{-1}



Exposure time in silane solution / minutes

It can be seen from the plot in figure.4.28. that monolayer coverage is obtained after approximately 17 minutes exposure of the silicon to the silane solution, (i.e. when the plot reaches a constant maximum). The Gibbs surface excess at this point is $5.667 \times 10^{-10} \text{ mol cm}^{-2}$. Therefore the area per molecule, a , is calculated as follows:

$$a, (1 \text{ mM}) = \frac{1 \times 10^{16}}{5.686 \pm 0.02 \times 10^{-10} \text{ mol cm}^{-2}} \times \frac{1}{6.02217 \times 10^{23} \text{ mol}^{-1}} = 29.21 \pm 0.09 \text{ \AA}^2$$

This value is again in good agreement with the values obtained from the experiments with 0.25 and 0.45 mM solutions. From these results, the average area per molecule is obtained for F8 as follows:

$$a, (0.25 \text{ mM}) = 30.86 \pm 0.10 \text{ \AA}^2$$

$$a, (0.45 \text{ mM}) = 30.00 \pm 0.04 \text{ \AA}^2$$

$$a, (1 \text{ mM}) = 29.21 \pm 0.09 \text{ \AA}^2$$

$$\text{Average area per molecule} = \frac{(30.86 + 30.00 + 29.21)}{3} = 30.02 \text{ \AA}^2$$

$$\text{Error in average} = \left(\frac{\left(\frac{0.10}{30.86} + \frac{0.04}{30.00} + \frac{0.09}{29.21} \right)}{3} \right) 30.02 = 0.08 \text{ \AA}^2$$

$$\text{Average area per molecule for F8} = 30.02 \pm 0.08 \text{ \AA}^2$$

The area per molecule values obtained for the three different concentrations of F8 were very similar. These values were larger than those observed for the OTS films. The average area per molecule obtained for F8 was 22.8% larger than the average area per molecule value obtained for OTS. This agrees with Fujii et al, who found an area per molecule for F8 greater than that for OTS, [57].

However, the exact value obtained for the average area per molecule for F8 disagreed with the value obtained by Fujii et al, ($50 \pm 8 \text{ \AA}^2$). As for the OTS samples, the ATR data would not be expected to agree exactly with the AFM data, due to the different sampling areas. For the monolayers of F8 formed here, as the concentration of the F8 increased, the time for monolayer formation decreased, as would be expected. The reason why the F8 molecules occupied a larger area than the OTS molecules can be explained by two factors. Firstly, the CF_3 end group has a larger van der Waals radius than the OTS, CH_3 end group and the F8 chain forms a helix, while the OTS adsorbs onto the substrate as a

extended chain. Both the CF_3 end group and the F8 helix would be expected to occupy a larger area than the OTS end group and straight chain, [57].

For the same concentration, the F8 monolayer was found to form much faster than the OTS monolayer. This was due to the relative rates of hydrolysis of the SiCl groups on the silane molecules, (an $\text{S}_{\text{N}}2$ reaction with OH^- as the nucleophile). In F8 the SiCl groups were hydrolysed faster than those on the OTS molecules. This was because CF_3 and CF_2 groups on F8 molecules are more electron withdrawing than CH_3 and CH_2 groups on OTS molecules. Therefore, because the F8 molecules were hydrolysed faster than the OTS molecules, F8 adsorbed onto the substrate more quickly than OTS.

4.3. Conclusions.

Self-assembled monolayers of OTS and F8 were produced on silicon ATR prisms. The formation of these monolayers was followed by Fourier transform infrared-attenuated total reflection spectroscopy in an *in situ* environment.

The silicon prisms first had to be calibrated to determine the exact number of reflections in the regions of the prism that were in contact with the solution, and also to determine the angle of incidence for the experiment. This was necessary so that accurate values of d_e and d_p could be calculated for each silicon prism used. The molar absorption coefficients for the bands due to the $\nu(\text{CH}_3)$ and $\nu(\text{CH}_2)$ stretching vibrations for OTS and for the band due to the $\nu_{\text{as}}(\text{CF}_2)$ stretching vibration for F8 were also determined.

For the 1 mM OTS solution, it was found that maximum coverage of the substrate was obtained, after 130 minutes exposure time to the silane solution. For the 5.8 mM solution, monolayer coverage was achieved after approximately 70 minutes exposure time of the silicon to the silane solution. The 11.6 mM solution produced monolayer coverage of the silicon prism after 40 minutes exposure time to the solution. All the area per molecule values obtained agreed well with those reported in the literature for a monolayer of OTS on silicon,

[39]. Therefore it can be concluded that monolayers of OTS were produced for all the concentrations described.

All three F8 solutions gave Gibbs surface excess values that were similar. It was reported that the area per molecule of a fluorinated alkyl-chain, (F8), was greater than the area per molecule of a non-fluorinated alkyl-chain, (OTS), (both molecules adsorbed onto silicon), [57]. The results produced here agree with this data. It is believed that the F8 chain occupies more space than the OTS chain, since the F8 chain forms a helix, while the OTS is an extended-chain molecule, and also because the CF_3 molecules in the F8 chain have a larger van der Waals radius than the CH_3 molecules in the OTS chain. The exposure times for maximum, (monolayer), coverage were approximately 220, 52 and 16 minutes for the F8 solutions at 0.25, 0.45 and 1 mM solutions respectively. The areas per molecule obtained for F8 and OTS on silicon, measured by *in situ* FTIR-ATR, disagreed with those produced by Fujii et al, measured by AFM, [57]. The FTIR-ATR spectroscopic results here would not be expected to agree completely with the AFM results reported by Fujii et al, [57], because of the different sampling areas probed by the two techniques, (mm^2 for ATR and nm^2 for AFM). Also Fujii et al, [57], used a sample preparation technique which may have produced a lower silanol group density on the silicon surface than that reported by Whitesides et al, [39]. This could cause the production of silane layers that were not close packed, with silane molecules possibly tilted. Therefore, the area occupied by these tilted silane molecules would be greater than that observed by Whitesides et al, [39].

For the same concentration solution, it was seen that the OTS monolayer formed more slowly than the F8 monolayer. This was because the F8 molecules were more easily hydrolysed than the OTS molecules, so the F8 adsorbed onto the silicon substrate faster than the OTS.

It can be seen that the dipping times for monolayer formation in the *ex situ* experiments, reported in chapter 3, do not agree with the exposure times for monolayer formation in the *in situ* experiments, reported in this chapter. The monolayers appear to take longer to form in the *in situ* experiment than in the *ex situ* experiment for the same concentration of silane, for both OTS and F8. This issue will be explained in chapter 7, where the results obtained from the *in situ* and *ex situ* experiments will be compared.

CHAPTER.5. ATOMIC FORCE MICROSCOPY OF THE *EX SITU* **ADSORPTION OF LONG-CHAIN SILANES ONTO SILICON.**

Introduction.

This chapter describes studies of the *ex situ* adsorption of two long-chain silanes onto silica. The silanes are n-octadecyltrichlorosilane, OTS and perfluorodecyl(ethyl)trichlorosilane, F8. The main objectives of this chapter are to determine the dipping time for formation of monolayers of OTS and F8 on silica and to see how the surface topography of these films varies with degree of coverage. Two- and three- dimensional atomic force microscopy, (AFM), images are presented.

5.1. Experimental.

5.1.1. Chemicals.

N-octadecyltrichlorosilane, 99.5%, toluene, 99.9%, methanol, 99.9%, 2-propanol, 99.9%, chloroform, 99.9%, and acetone, 99.9% were obtained from Aldrich Chemical Co.

Perfluorodecyl(ethyl)trichlorosilane, 99.5% and freon 113, 99% were obtained from Fluorchem Ltd.

The fluorinated compounds were dried over molecular sieve prior to use. The silanes were stored at 5°C, in a refrigerator. All other chemicals were used as received.

5.1.2. Substrates.

The substrates used for the atomic force microscopy measurements were Pilkington float glass slides. As suggested by the name, the glass is manufactured by floating on hot tin. The tin side of the float glass can be distinguished from the non-tin side by using a UV lamp. The tin side will fluoresce when the UV light is shone onto it.

The float glass substrates were pre-cleaned by washing with acetone and methanol and then by refluxing in hot 2-propanol for at least 4 hours. They were then stored in a dessicator until used. The reason why the non-tin side of the glass is examined as opposed to the tin side is because the non-tin side is atomically smoother than the tin side, and therefore is a better surface for AFM measurements.

5.1.3. Preparation of Solutions.

Two sets of solutions were prepared for each silane, one under class 100 clean room conditions and the other in the laboratory, (no clean room classification). For the samples prepared in the laboratory, the OTS solutions were prepared in a fume cupboard and the F8 solutions were prepared within a dry nitrogen environment. All the OTS and F8 solutions were prepared and used at room temperature and at atmospheric pressure.

The OTS solutions were made up in toluene, at a concentration of 1 mM, in OTS-coated volumetric flasks, and used immediately. (See chapter.3.12. for procedure of coating glassware with OTS).

The F8 solutions were made up in freon 113, at a concentration of 0.5 mM, in OTS-coated volumetric flasks, and used immediately.

Fresh solutions were prepared for each experiment.

5.1.4. Preparation of Samples.

The OTS was deposited onto the Pilkington float glass slides, by self-assembly, from the silane solutions, with dipping times of 20, 40, 90 and 120 minutes. After each dip, the slides were washed with chloroform, with methanol and then with chloroform again, to remove any excess silane deposits.

The F8 was deposited onto the Pilkington float glass slides, by self-assembly, from the F8 solutions, with dipping times of 15 seconds, 5, 8, and 30 minutes.

After each dipping stage, the samples were washed with freon 113 and gently 'buffed' with a lens tissue to remove any excess silane deposits.

The solutions and samples prepared in the clean room were used and stored there until required for analysis. After silane deposition, the slides were cut to approximately 1 cm² and the non-tin side of each sample was examined by atomic force microscopy.

Atomic force microscopy images of pre-cleaned float glass, on the non-tin side, were also obtained.

The studies are described as *ex situ* since the samples are removed from solution for measurement at various stages of mono- or multi-layer formation.

5.1.5. Atomic Force Microscopy Measurements.

A Nanoscope III, (Digital Instruments, Santa Barbara, California, U.S.A), atomic force microscope was used to obtain three-dimensional images of the samples. The 'D'-scanning head, (maximum scanning area of 15 x 15 μm²), and the 100 μm silicon nitride cantilever tip, with a spring constant of 0.38 Nm⁻¹, were used in normal scanning mode. The atomic force microscope was vibration table-mounted to eliminate external vibrational noise.

To ensure that the images were reproducible and that the tip was not dislodging material on the surface, several images in different areas and at various magnifications were obtained.

Once the images were obtained, the software was used to determine the roughness average, (R_a), value for each sample. This value was used as a measure of surface roughness for each sample. The root mean square roughness, (standard deviation from the mean roughness, RMS), values of each sample were also computed by the software.

The software was also used to obtain two-dimensional section analyses for each sample, giving information on the height and diameter of the features seen

in the three-dimensional images. In each of the section analyses presented in this chapter the image is in the bottom left-hand corner of each figure. The cross-section, along the white line in the image, is shown in the top left-hand corner of each figure. The height of the bright 'spots' in the cross-section of each image is shown in the box in the bottom right hand corner next to 'vert distance' and the diameter of each spot is shown next to 'horiz distance'. The brighter areas in each image represent 'peaks' on the sample and the darker areas represent 'troughs' on the sample.

5.2. Results and Discussion.

5.2.1. Pilkington Float Glass.

The results of the atomic force microscopy studies on the non-tin side of Pilkington float glass will be given in this section.

The float glass was imaged over several areas, and the resulting three-dimensional line plot of an image obtained over a $1 \times 1 \mu\text{m}^2$ area can be seen in figure.5.1. The roughness average value for the float glass was also calculated over several areas and the results are reported in table.5.1.

Table.5.1. R_a values for Pilkington Float Glass.

Area of Sample / μm^2	R_a / nm \pm 0.01 nm
10 x 10	0.256
1 x 1	0.254
0.5 x 0.5	0.252
0.005 x 0.005	0.031

For all the samples in table.5.1, (except the $5 \times 5 \text{ nm}^2$ sample), the R_a values quoted are greater than that of the usual AFM substrate, mica, but are still small enough for the investigation of the thin films described here, [61].

5.2.2. N-octadecyltrichlorosilane.

The results of the studies on self-assembled films of n-octadecyltrichlorosilane, OTS, $\text{CH}_3(\text{CH}_2)_{17}\text{SiCl}_3$, on Pilkington float glass will be given in this section. The samples, which were dipped in the OTS solutions for 20, 40, 90 and 120 minutes, either under class 100 clean room conditions or in the open laboratory, were examined using atomic force microscopy on the non-tin side of the glass only.

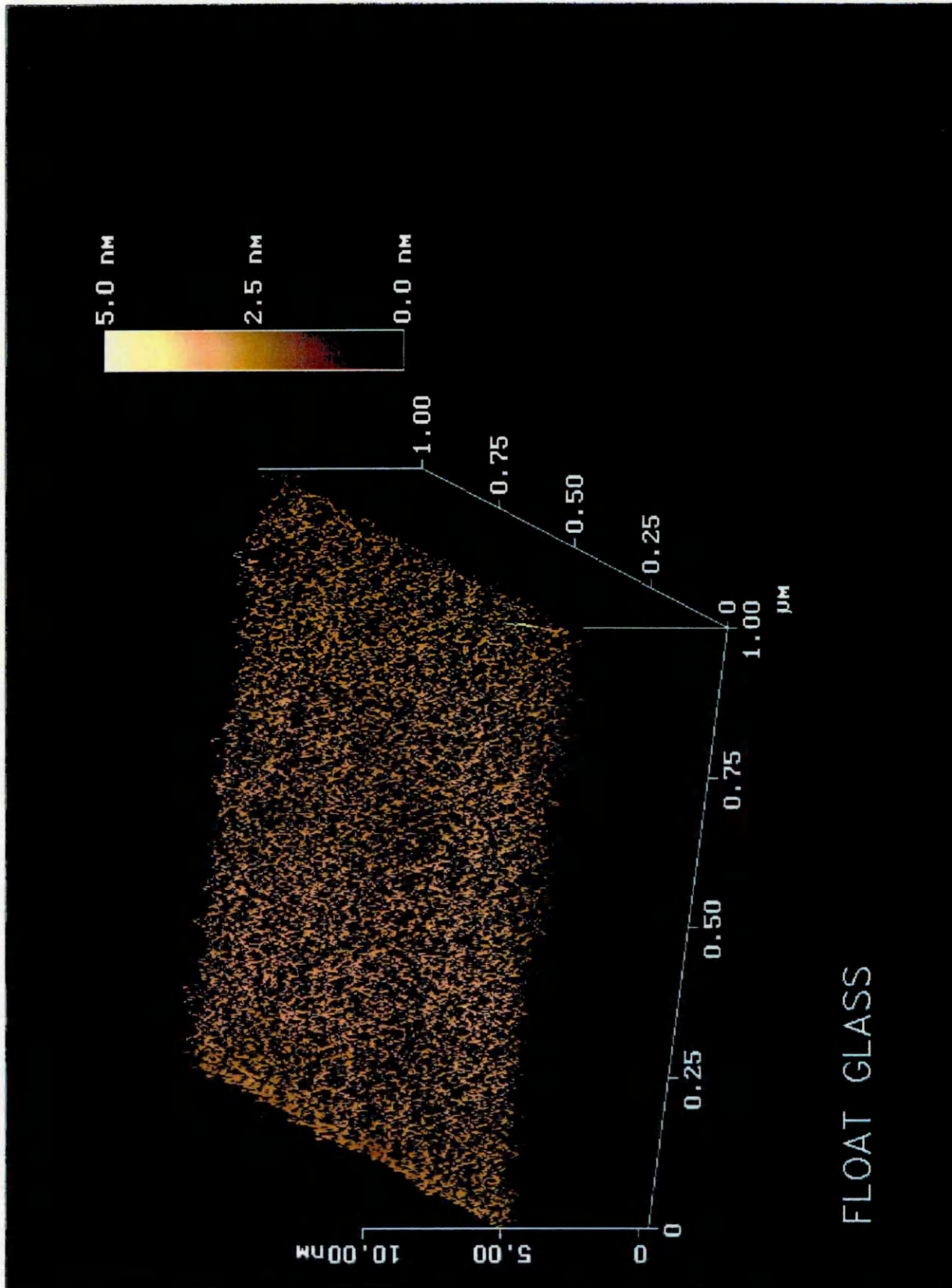


Figure 5.1.

Both three-dimensional line plots and two-dimensional section analyses are presented for each sample. The three-dimensional line images depict the surface features on each sample. The two-dimensional section analyses provide a measure of some of the features shown in the three-dimensional images. The roughness average and RMS values for each sample were calculated using the computer software and the results are reported in table.5.2.

Table.5.2. R_a and RMS values for OTS-coated Pilkington Float Glass.

Figure number	Description	R_a / nm \pm 0.01 nm	RMS /nm \pm 0.01 nm
5.2	OTS 20 minutes dipping time, clean room, 3-D	0.109	0.145
5.3	OTS 20 minutes dipping time, clean room, 2-D	0.109	0.145
5.4	OTS 20 minutes dipping time, open laboratory, 3-D	0.246	0.445
5.5	OTS 20 minutes dipping time, open laboratory, 2-D	0.246	0.445
5.6	OTS 40 minutes dipping time, clean room, 3-D	0.131	0.168
5.7	OTS 40 minutes dipping time, clean room, 2-D	0.131	0.168
5.8	OTS 40 minutes dipping time, open laboratory, 3-D	0.188	0.245
5.9	OTS 40 minutes dipping time, open laboratory, 2-D	0.188	0.245
5.10	OTS 90 minutes dipping time, clean room, 3-D	0.066	0.094
5.11	OTS 90 minutes dipping time, clean room, 2-D	0.066	0.094
5.12	OTS 90 minutes dipping time, open laboratory, 3-D	0.056	0.076
5.13	OTS 90 minutes dipping time, open laboratory, 2-D	0.056	0.076
5.14	OTS 120 minutes dipping time, clean room, 3-D	0.100	0.143
5.15	OTS 120 minutes dipping time, clean room, 2-D	0.100	0.143
5.16	OTS 120 minutes dipping time, open laboratory, 3-D	0.101	0.151
5.17	OTS 120 minutes dipping time, open laboratory, 2-D	0.101	0.151

The three-dimensional atomic force microscopy image of OTS on float glass, prepared under clean room conditions, and removed from the silane solution after 20 minutes dipping time, can be seen in figure.5.2. In the image islands can be seen. A section analysis through some of these islands is shown in figure.5.3. The heights of these islands are less than that of an OTS monolayer, i.e. less than 2.6 nm. The R_a value for this surface was computed to be 0.109 nm. This is less than the R_a value for the float glass substrate over this area.

The corresponding three-dimensional atomic force microscopy image of the sample prepared in the open laboratory is depicted in figure.5.4. Again, islands are observable in this image. The cross-sectional analysis of some of these islands is shown in figure.5.5. The islands in the cross-sectional analysis can be seen to be of monolayer height and less. The R_a value for this image is 0.246 nm, which is just less than the R_a value for the float glass substrate but larger than the R_a value for the corresponding sample prepared under clean room conditions.

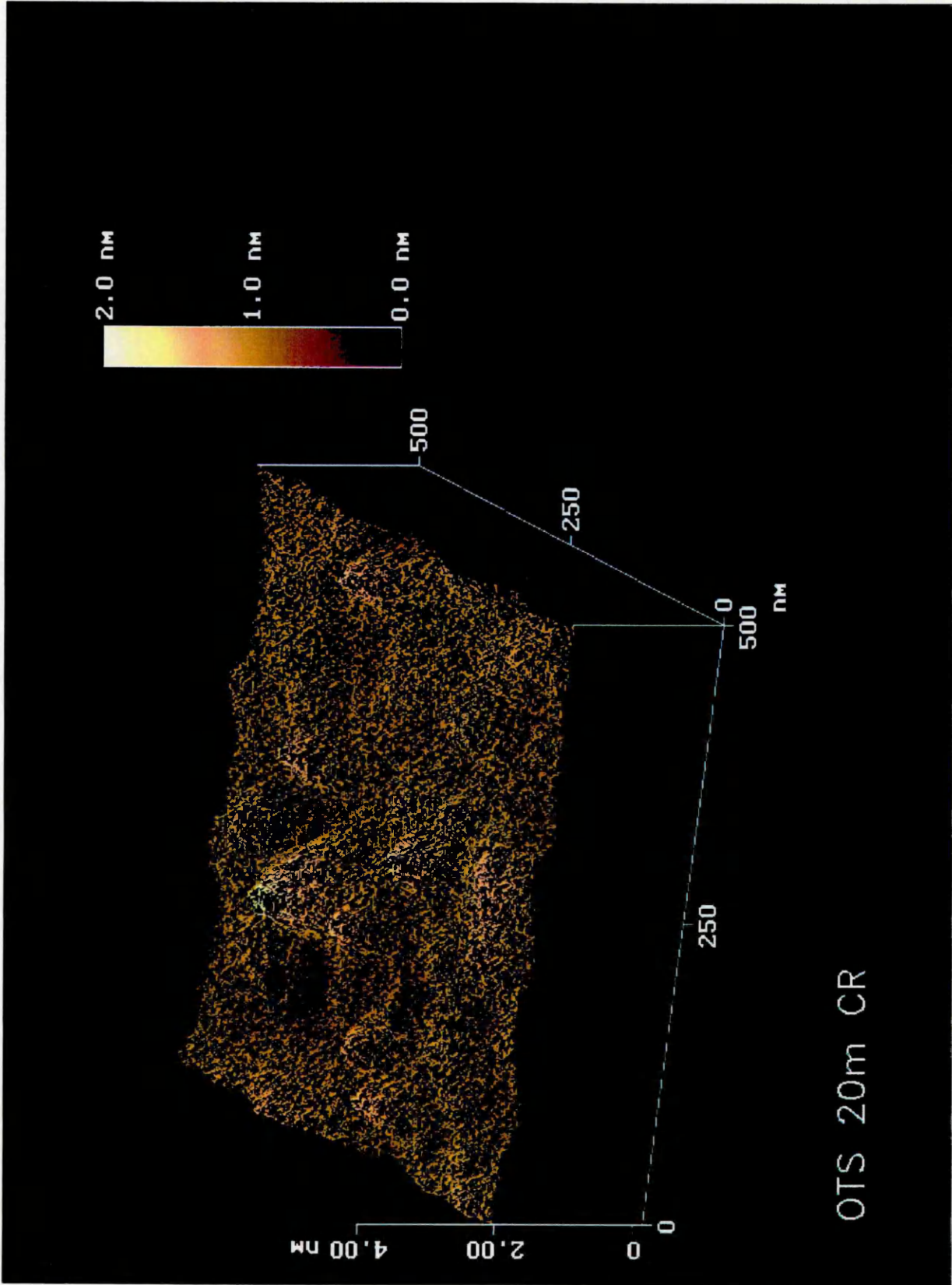
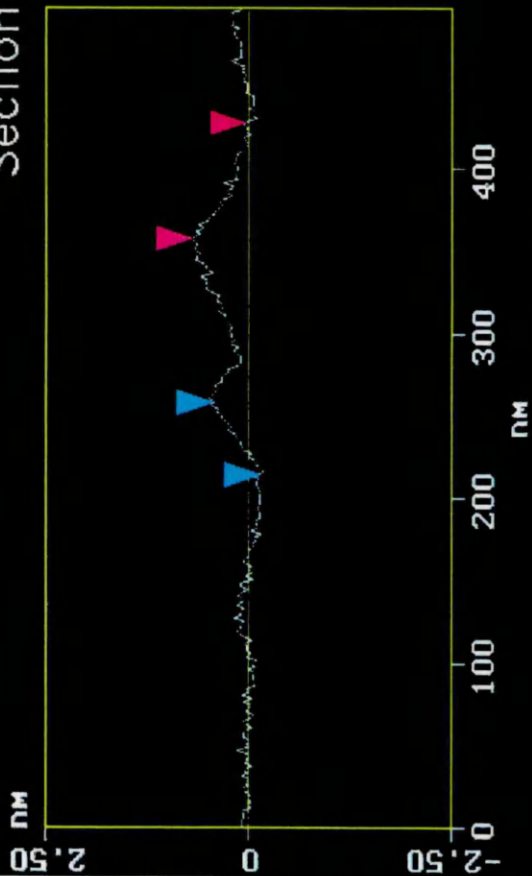


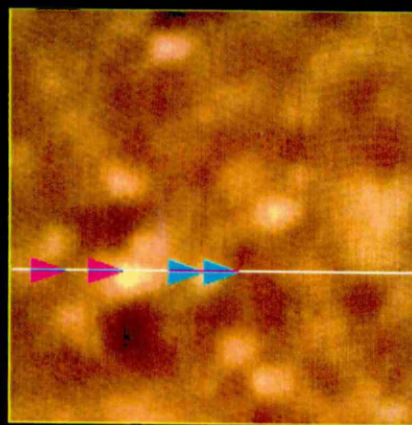
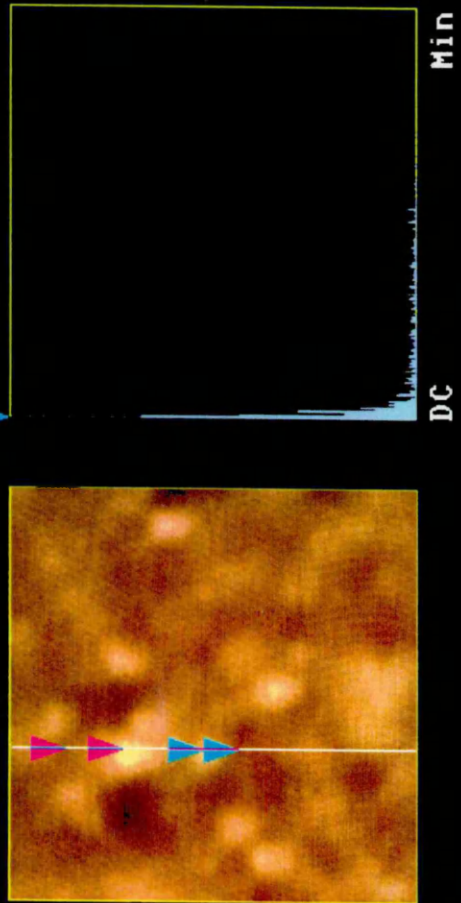
Figure.5.2.

Section Analysis



L	70.313 nm
RMS	0.205 nm
Ic	DC
Ra(Ic)	0.051 nm
Rmax	0.272 nm
Rz	0.165 nm
Rz Cnt	8

Horiz distance(L)	42.969 nm
Vert distance	0.588 nm
Angle	0.784 deg
Horiz distance	70.313 nm
Vert distance	0.685 nm
Angle	0.558 deg
Horiz distance	
Vert distance	
Angle	
Spectral period	DC
Spectral freq	0 Hz
Spectral amp	0.202 nm



OTS 20m CR

Figure.5.3.

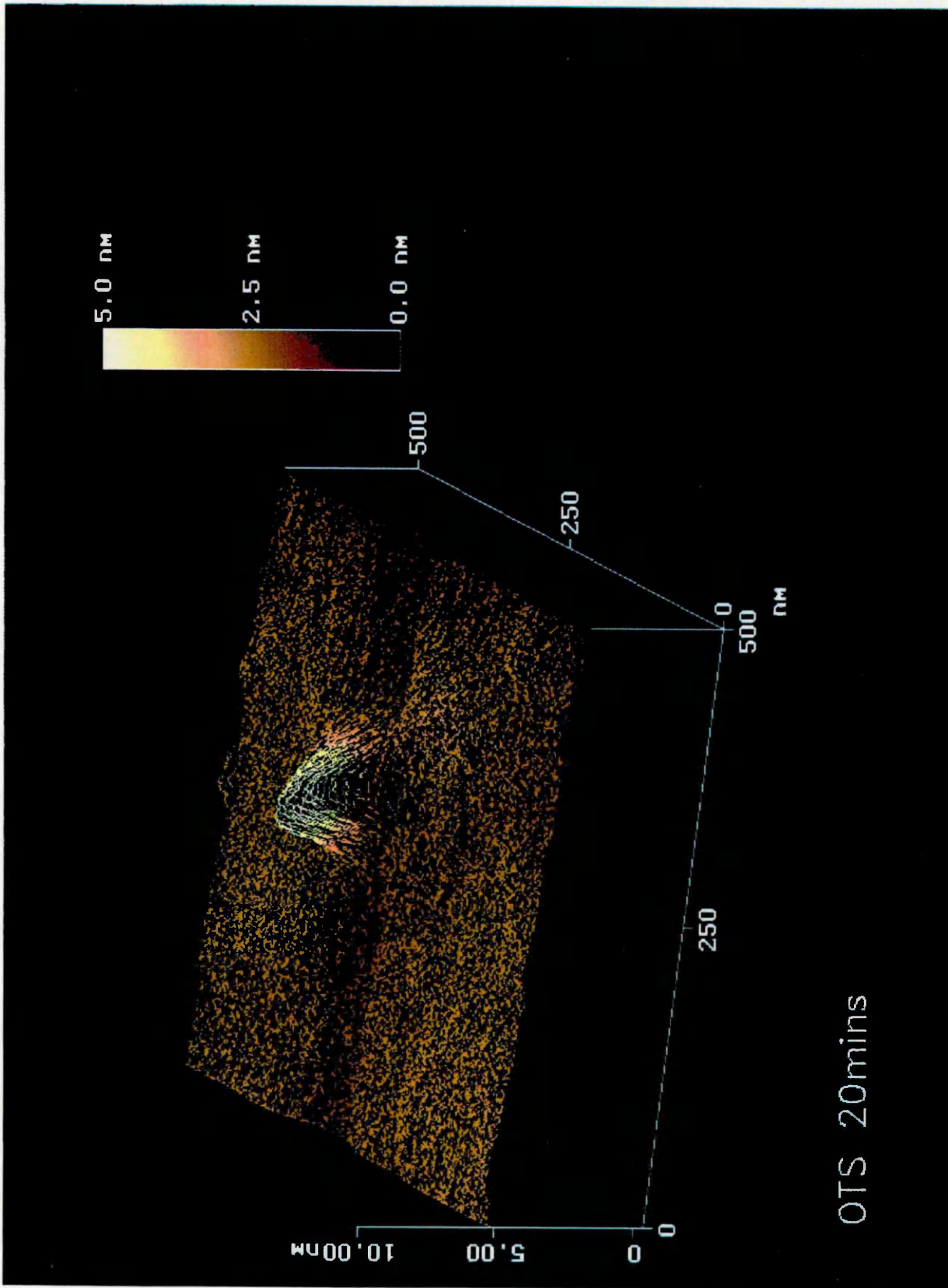
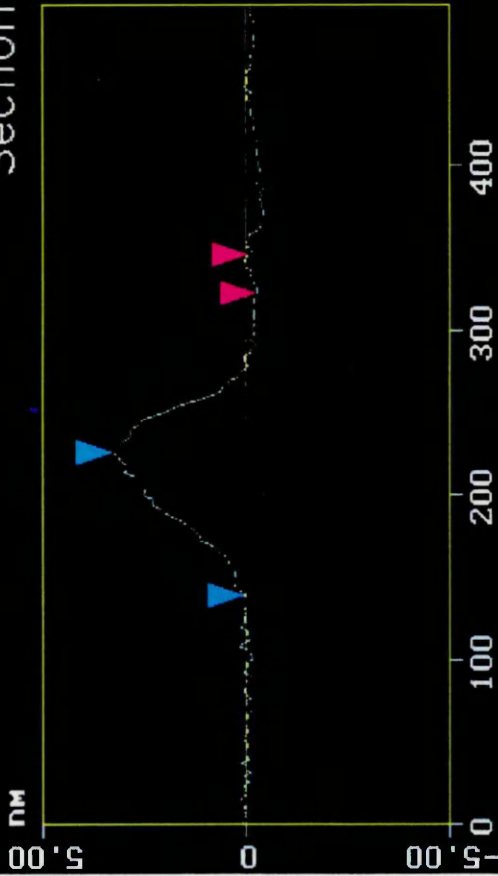


Figure 5.4.

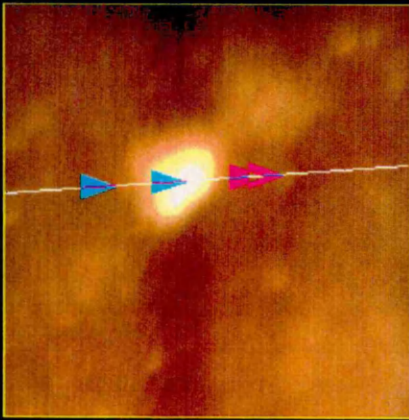
Cursor Marker Spectrum Zoom Center Line Offset Clear

Section Analysis



L	23.438 nm
RMS	0.105 nm
Ic	DC
Ra(Ic)	0.027 nm
Rmax	0.182 nm
Rz	0.081 nm
Rz Cnt	8

Spectrum



DC Min

Horiz distance(L)	87.891 nm
Vert distance	3.270 nm
Angle	2.131 deg
Horiz distance	23.438 nm
Vert distance	0.204 nm
Angle	0.500 deg
Horiz distance	
Vert distance	
Angle	
Spectral period	DC
Spectral freq	0 Hz
Spectral amp	0.553 nm

OTS 20mins

Cursor: fixed Zoom: 2:1 Cen line: Off Offset: Off

Figure 5.5.

The three-dimensional atomic force microscopy image of OTS on float glass, prepared under clean room conditions and removed from the silane solution after 40 minutes dipping time, can be seen in figure.5.6. Since poor resolution was obtained in the 4 nm x 500 nm x 500 nm image, the 4 nm x 10 μ m x 10 μ m image is shown. Islands can be seen in this image. A section analysis through some of these islands is depicted in figure.5.7. The islands can be seen to be of a height less than an OTS monolayer. The R_a value for this image is 0.131 nm, which is less than the R_a value for the float glass substrate, over this area, and also less than the R_a value obtained for the surface shown in figure.5.2. Therefore the surface is becoming smoother as compared with the sample shown in figure.5.2.

The corresponding three-dimensional atomic force microscopy image of the sample prepared in the open laboratory can be seen in figure.5.8. Some of the islands observed in this image have been analysed, using the section analysis software, and are shown in figure.5.9. The heights of these islands are less than the height of an OTS monolayer. The R_a value for this surface is 0.188 nm, which is less than the R_a value for the glass substrate and also less than the R_a value obtained for the sample shown in figure.5.4. Therefore the surface in figure.5.8. is smoother than the surface in figure.5.4. However the R_a value obtained for the sample shown in figure.5.8. is larger than that obtained for the corresponding sample prepared in the clean room.

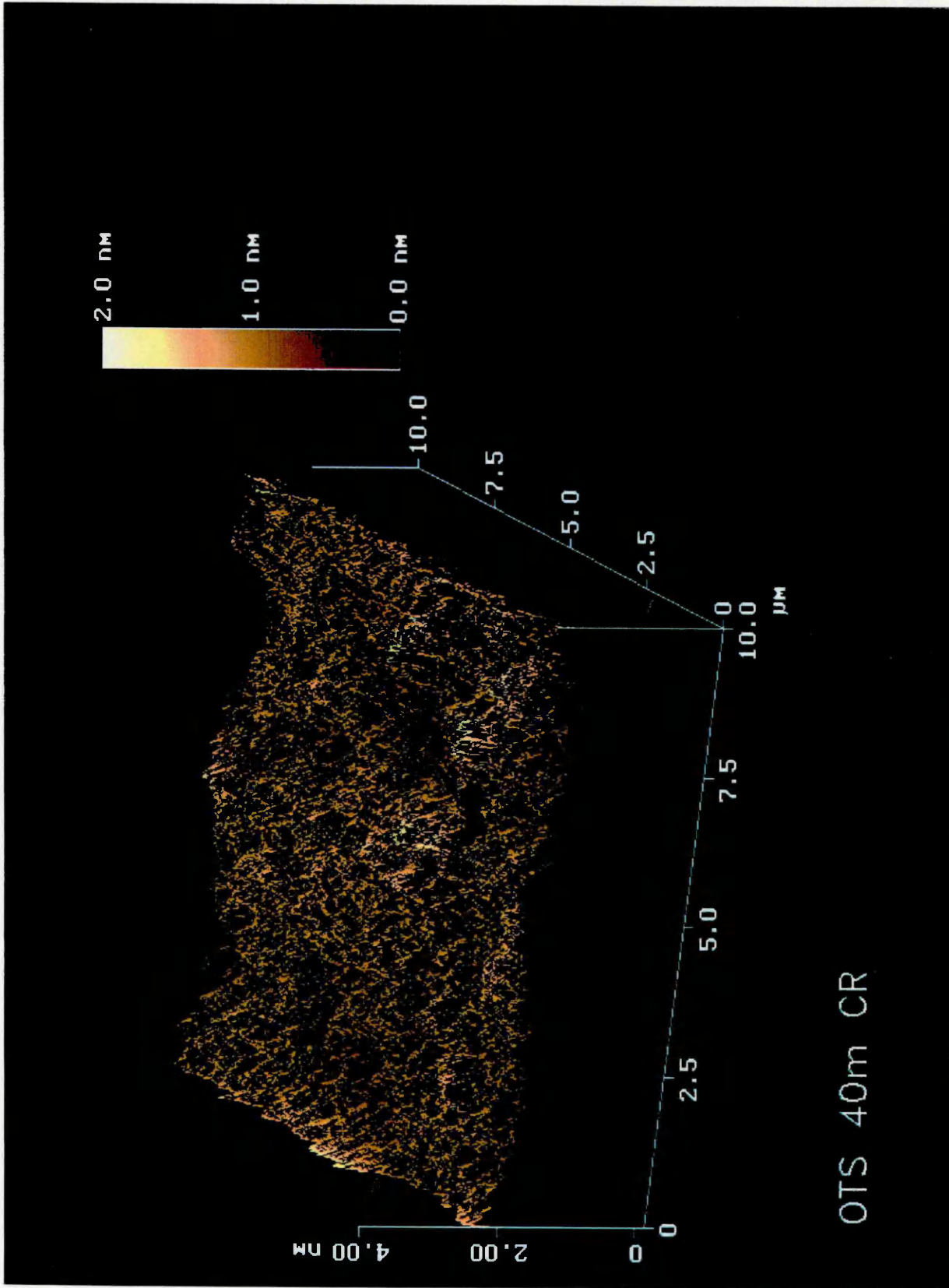
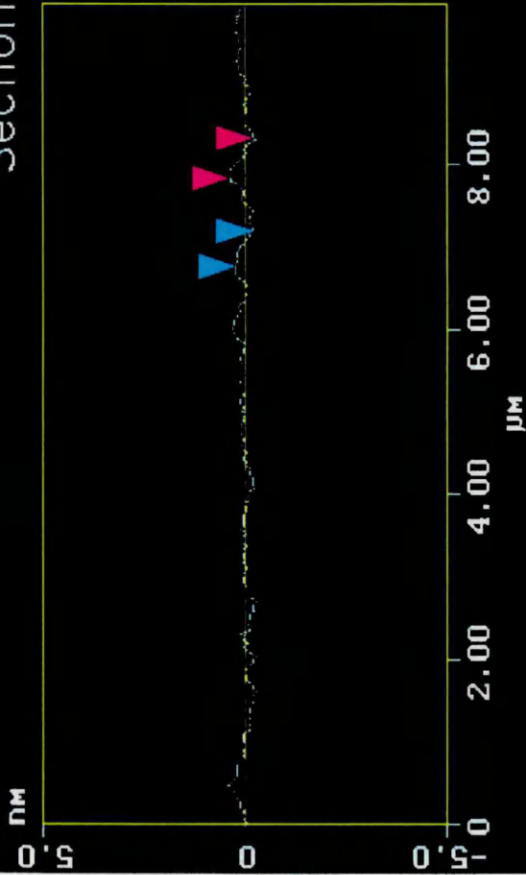


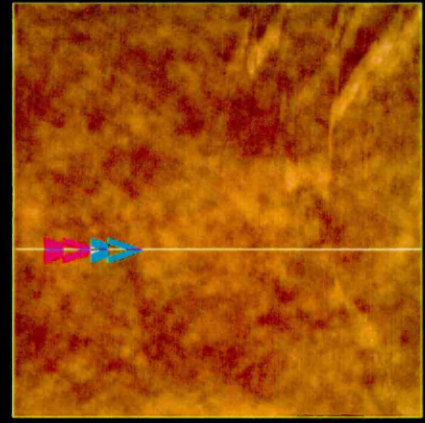
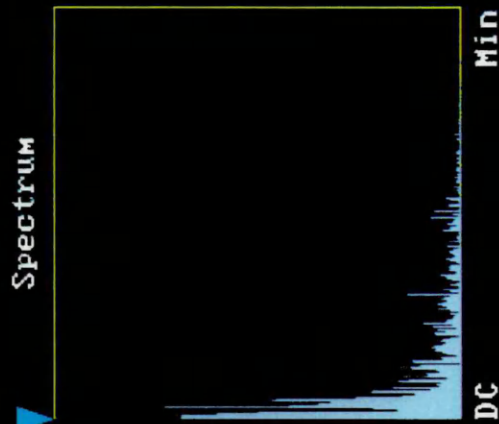
Figure 5.6.

Section Analysis



L	468.75 nm
RMS	0.199 nm
IG	DC
Ra(Ic)	0.039 nm
Rmax	0.159 nm
Rz	0.119 nm
Rz Cnt	6

Horiz distance(L)	429.69 nm
Vert distance	0.425 nm
Angle	0.057 deg
Horiz distance	468.75 nm
Vert distance	0.581 nm
Angle	0.071 deg
Horiz distance	
Vert distance	
Angle	
Spectral period	DC
Spectral freq	0 Hz
Spectral amp	0.072 nm



OTS 40M CR

Figure 5.7.

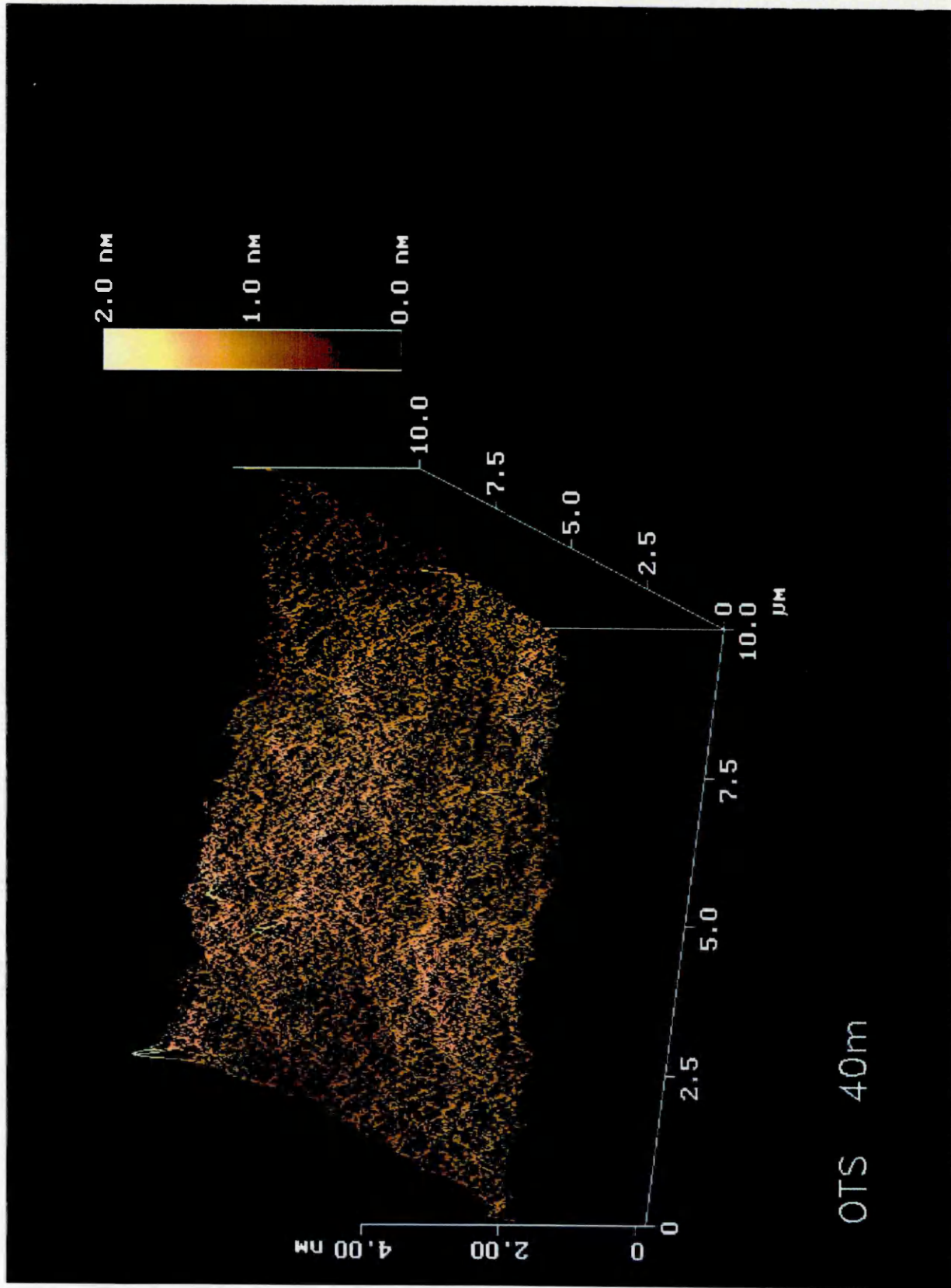
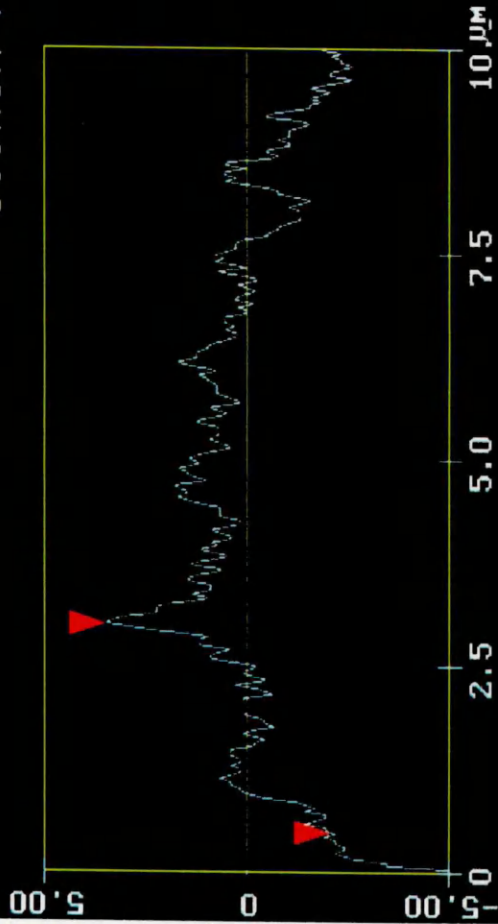


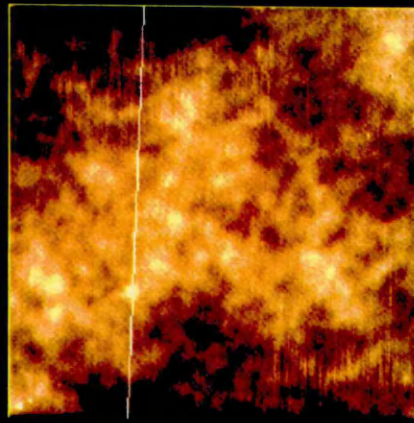
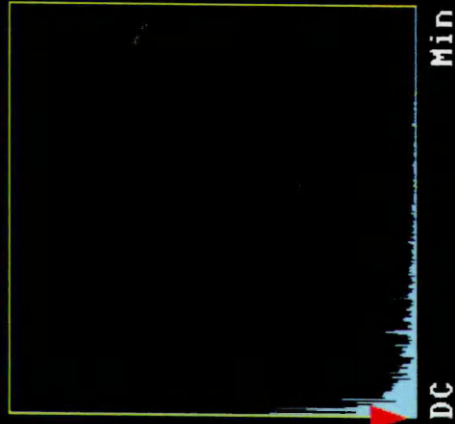
Figure.5.8.

Section Analysis



L	2.539	μm
RMS	0.215	nm
Ic	DC	
Ra(Ic)	0.114	nm
Rmax	0.671	nm
Rz	0.270	nm
Rz Cnt	valid	

Spectrum



Horiz distance(L)	2.539	μm
Vert distance	1.144	nm
Angle	0.026	deg
Horiz distance		
Vert distance		
Angle		
Horiz distance		
Vert distance		
Angle		
Spectral period	DC	
Spectral freq	0.000	Hz
Spectral amp	0.004	nm

Figure.5.9.

The three-dimensional atomic force microscopy image of OTS on float glass, prepared in the clean room and removed from the silane solution after 90 minutes dipping time, can be seen in figure.5.10. This surface appears to have very small islands compared to the surfaces shown in figures.5.2 and 5.6. The section analysis of the surface in figure.5.10. shows that the 'islands' seen are only 0.158 nm in height, (see figure.5.11). The R_a value obtained for this surface was 0.066 nm. This R_a value is much smaller than the R_a value of the float glass substrate over this area and also less than the R_a values obtained for the samples shown in figures.5.2 and 5.6, (also prepared under clean room conditions). Therefore, the surface dipped for 90 minutes is smoother than the surfaces dipped for 20 and 40 minutes, (all prepared in the clean room).

The corresponding three-dimensional atomic force microscopy image of the sample prepared in the open laboratory, is shown in figure.5.12. This again shows very small islands compared to the samples shown in figures.5.4. and 5.8., (also prepared in the open laboratory). The section analysis of the image in figure.5.12. can be seen in figure.5.13. The 'islands' in figure.5.13. are only 0.161 nm in height. The R_a value obtained for this surface was 0.056 nm. This is much smaller than the R_a value obtained for the float glass substrate and also smaller than the R_a values obtained for the samples shown in figures.5.4. and 5.8. Therefore the surface dipped for 90 minutes is smoother than the surfaces dipped for 20 and 40 minutes, (all prepared in the open laboratory).

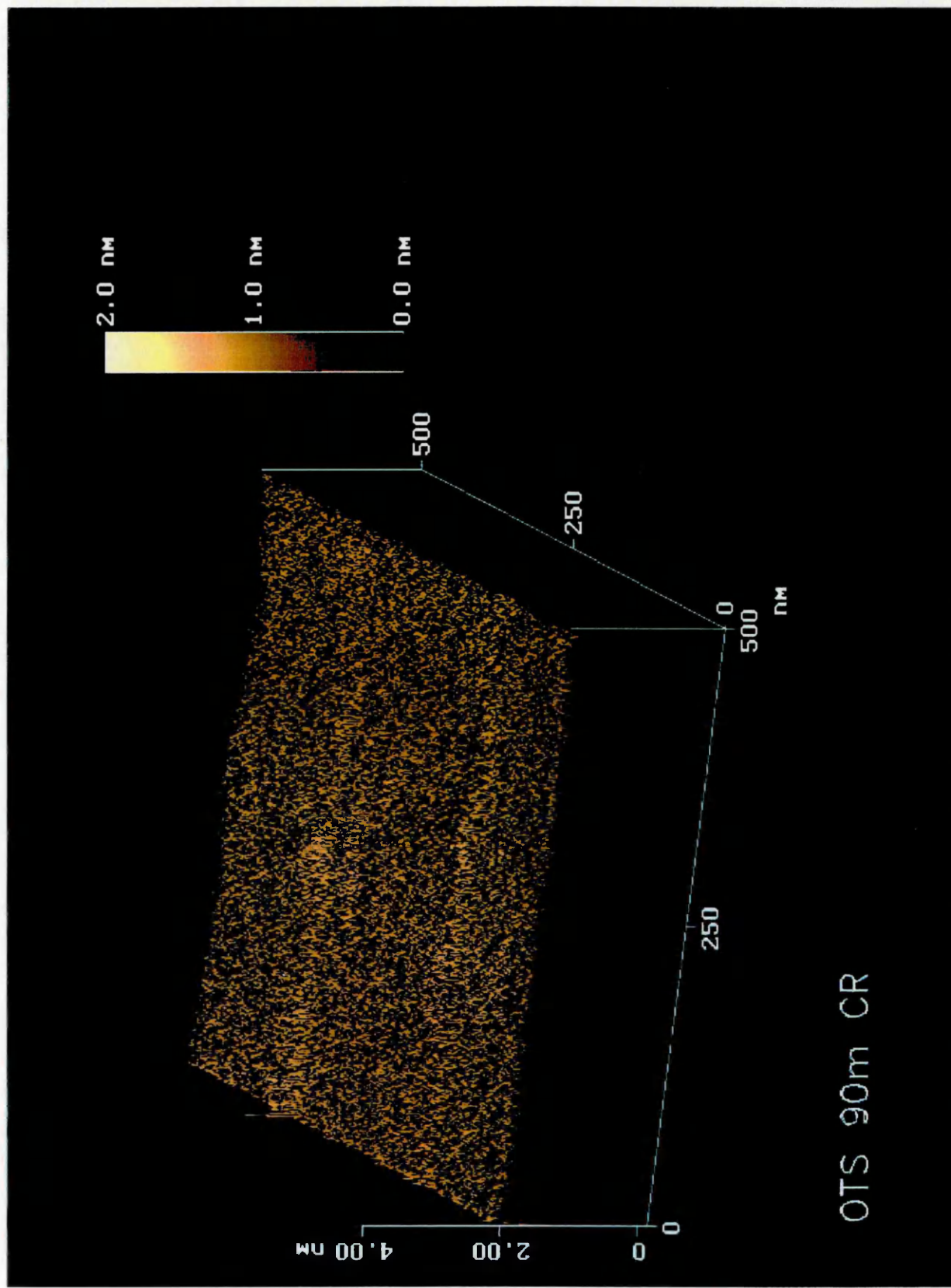
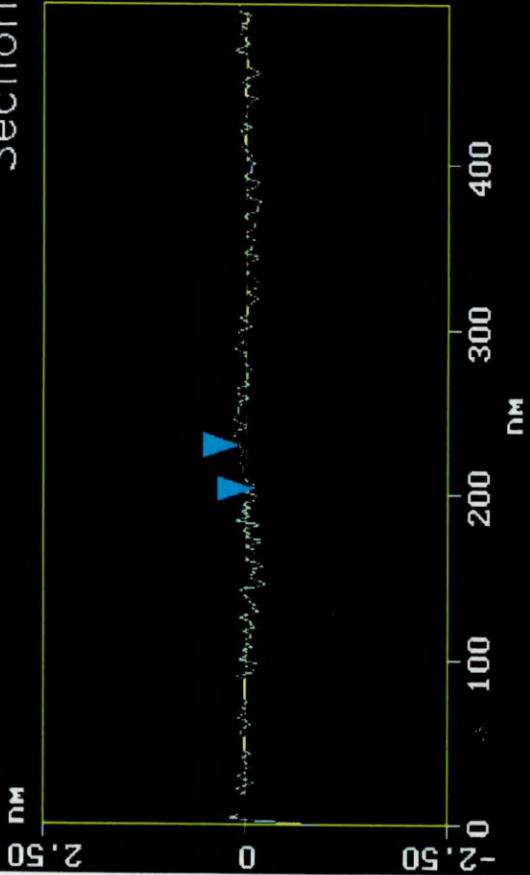


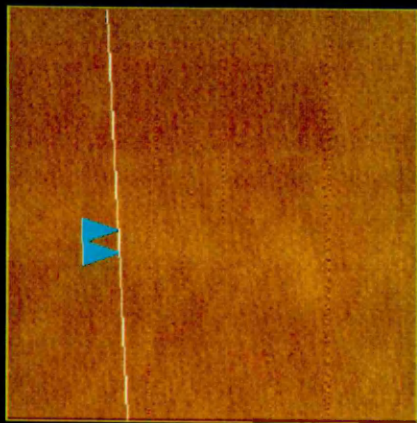
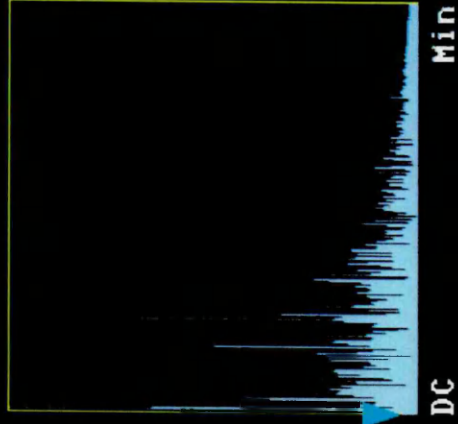
Figure 5.10.

Section Analysis



L	27.344 nm
RMS	0.059 nm
Ic	DC
Ra(Ic)	0.029 nm
Rmax	0.136 nm
Rz	0.136 nm
Rz Cnt	2

Horiz distance(L)	27.344 nm
Vert distance	0.158 nm
Angle	0.331 deg
Horiz distance	
Vert distance	
Angle	
Horiz distance	
Vert distance	
Angle	
Spectral period	DC
Spectral freq	0 Hz
Spectral amp	0.001 nm



OTS 90M CR

Figure 5.11.

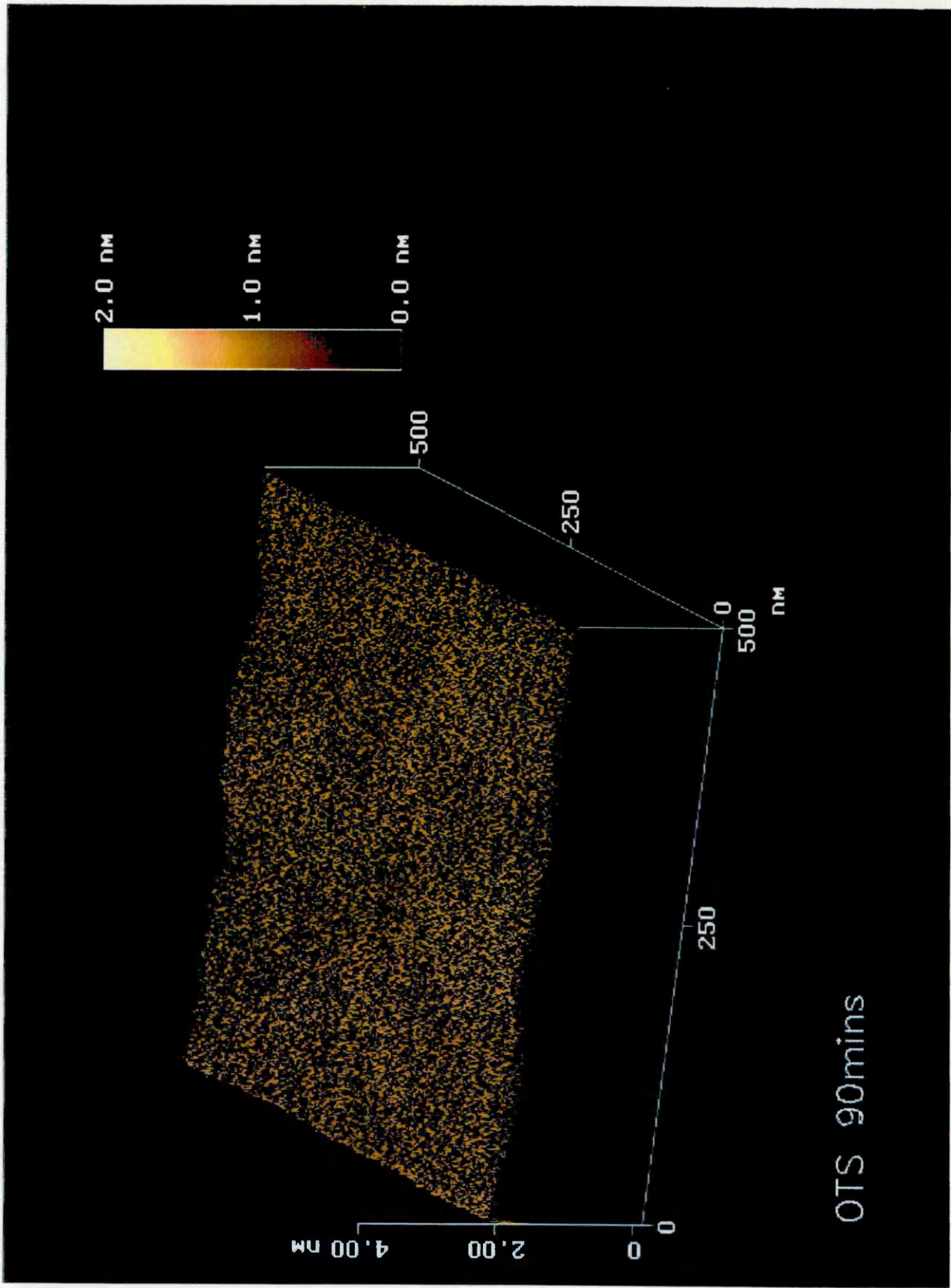
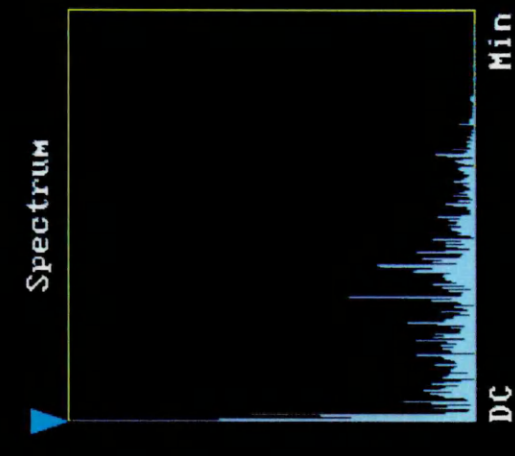


Figure 5.12.

Section Analysis



L	72.266 nm
RMS	0.069 nm
Ic	DC
Ra(Ic)	0.027 nm
Rmax	0.183 nm
Rz	0.132 nm
Rz Cnt	valid



Horiz distance(L)	72.266 nm
Vert distance	0.161 nm
Angle	0.128 deg
Horiz distance	
Vert distance	
Angle	
Horiz distance	
Vert distance	
Angle	
Spectral period	DC
Spectral freq	0 Hz
Spectral amp	0.044 nm

OTS 90mins

Figure.5.13.

Figure.5.14. depicts a three-dimensional atomic force microscopy image of OTS on float glass, prepared under clean room conditions and removed from the silane solution after 120 minutes dipping time. Islands are observable in this image. The section analysis through some of these islands can be seen in figure.5.15. The islands are of a height less than an OTS monolayer. The R_a value computed for this surface was 0.100 nm. This value is greater than the R_a value obtained for the sample shown in figure.5.10. Therefore the surface is becoming rougher.

The corresponding three-dimensional atomic force microscopy image of the sample prepared in the open laboratory is shown in figure.5.16. Islands can again be seen in this image. The section analysis through some of these islands is depicted in figure.5.17. The islands in figure.5.17. can be seen to be of monolayer height and less. The R_a value for this sample is 0.101 nm. This is less than the R_a value for the float glass substrate, approximately the same as the R_a value for the corresponding sample prepared under clean room conditions, but larger than the R_a value obtained for the sample dipped for 90 minutes in the open laboratory. Therefore the surface shown in figure.5.16 is rougher than the surface shown in figure.5.12.

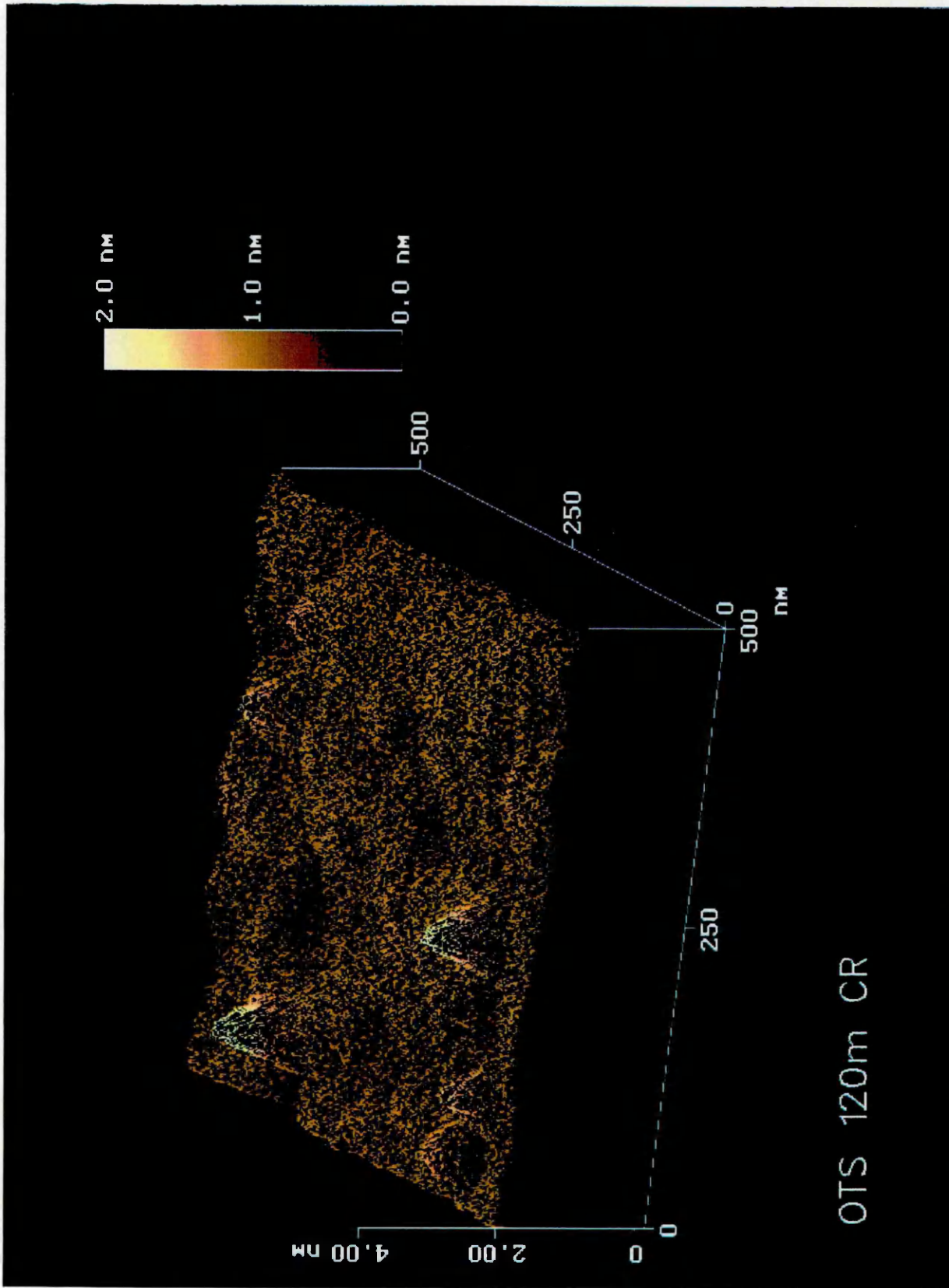
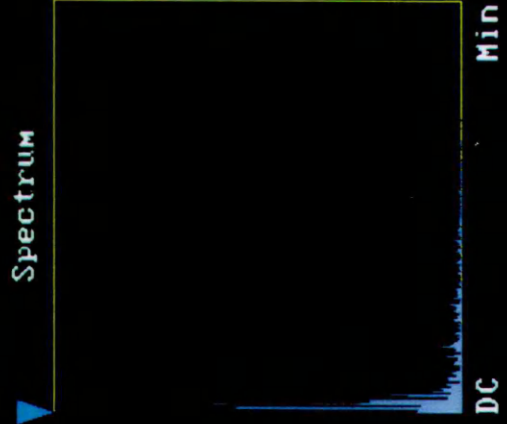
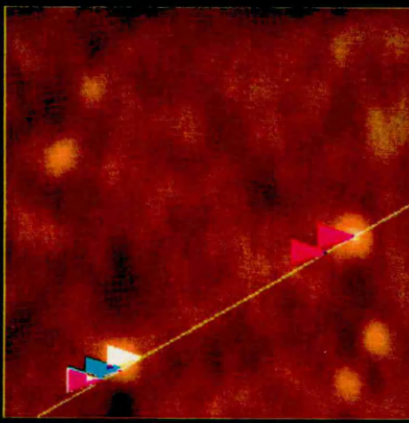


Figure 5.14.

Section Analysis



L	56.641	nm
RMS	0.267	nm
Ic	DC	
Ra(Ic)	0.231	nm
Rmax	0.813	nm
Rz	0.813	nm
Rz Cnt	2	



Horiz distance(L)	23.438	nm
Vert distance	0.718	nm
Angle	1.754	deg
Horiz distance	37.109	nm
Vert distance	0.810	nm
Angle	1.250	deg
Horiz distance	56.641	nm
Vert distance	0.078	nm
Angle	0.079	deg
Spectral period	DC	
Spectral freq	0	Hz
Spectral amp	0.212	nm

OTS 120m CR

Figure.5.15.

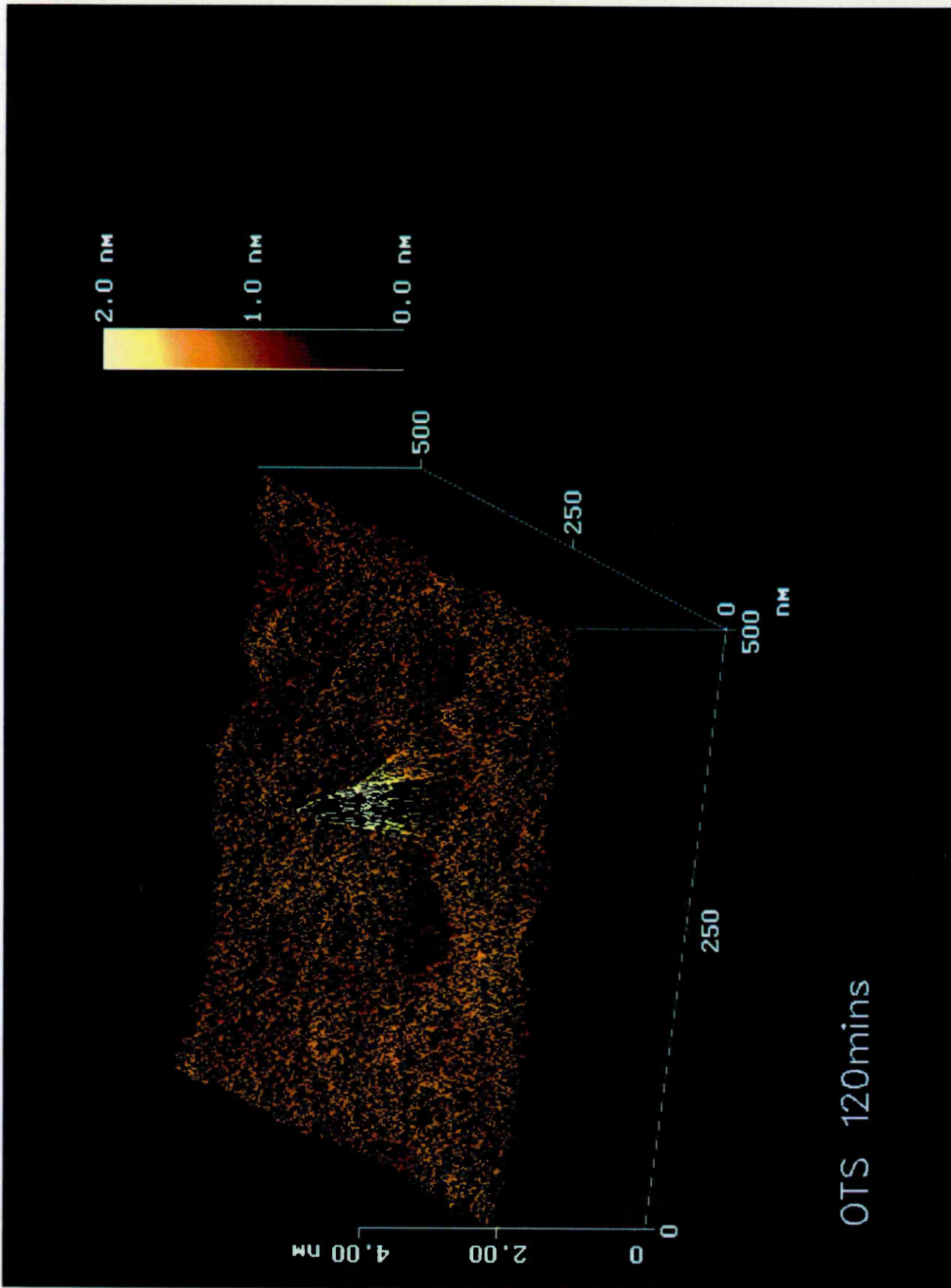
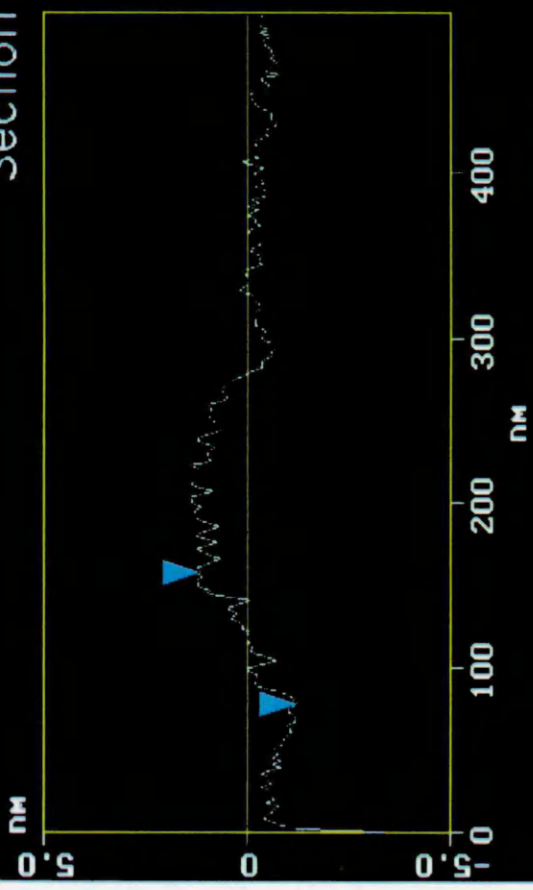


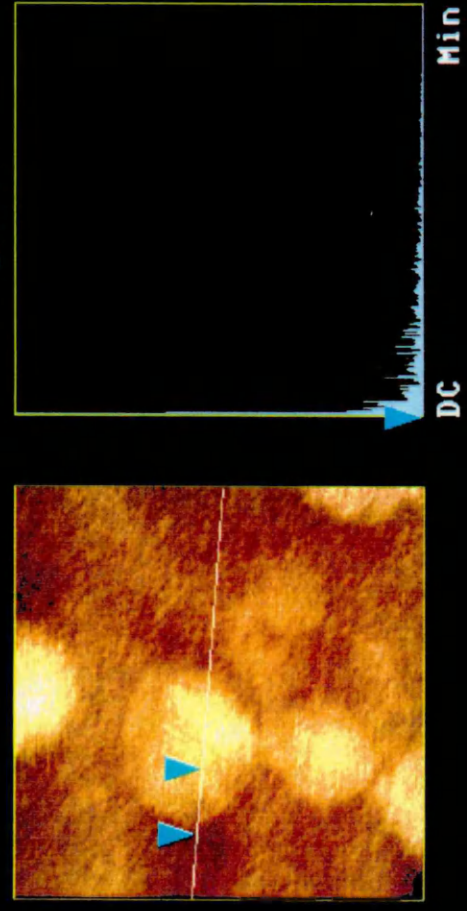
Figure 5.16.

Section Analysis



L	80.078 nm
RMS	0.649 nm
Ic	DC
Ra(Ic)	0.208 nm
Rmax	1.219 nm
Rz	0.592 nm
Rz Cnt	valid

Horiz distance(L)	80.078 nm
Vert distance	2.387 nm
Angle	1.708 deg
Horiz distance	
Vert distance	
Angle	
Horiz distance	
Vert distance	
Angle	
Spectral period	DC
Spectral freq	0 Hz
Spectral amp	0 nm



OTS 120mins

Figure 5.17.

For all the samples, except those dipped for 90 minutes, the samples prepared under clean room conditions have smaller R_a values than those prepared in the open laboratory. These differences in the R_a values are not likely to be due to dust, since dust would be observed in all the samples prepared in the open laboratory and also dust particles would be expected to be of the order of microns in size. No explanation why this difference occurs is given here.

However, previous researchers have found that reproducibility of atomic force microscopy images on OTS-coated silicon, were only produced when the samples were prepared under class 100 clean room conditions, [60]. Therefore when interpreting the results obtained here, in terms of the formation of OTS films, only the samples prepared under class 100 clean room conditions should be considered. However, an interpretation is given for all the results obtained.

All the images obtained had R_a values less than the R_a value obtained for the glass substrate. Previous researchers, [61], have noted this effect, (see section 1.3.2.), and have attributed it to OTS molecules cross-linking to form a smooth surface so that not all the OTS molecules are adsorbed to the surface.

For the samples prepared under class 100 clean room conditions, it was observed that the R_a value decreased as the dipping time increased from 20 to 40 to 90 minutes. The RMS value obtained for the sample dipped for 90 minutes, (0.094 nm), was less than that observed for a monolayer of OTS on a glass cover slip, (0.18 nm), [61]. When the dipping time was increased to 120 minutes, the R_a value was seen to increase. Therefore as the dipping time increased up to 90 minutes, the surface became gradually smoother and as the dipping time increased from 90 to 120 minutes, the surface became rougher. These results were interpreted in the following way: The samples at 20 and 40 minutes dipping time represent submonolayer coverage, the sample at 90 minutes dipping time represents monolayer coverage and the sample at 120 minutes dipping time represents above-monolayer coverage. Further evidence for this is the presence of the islands observed in the samples dipped for 20, 40 and 120 minutes in the

silane solutions. These islands are not observed for the sample dipped for 90 minutes. The islands seen in the samples dipped for 20 and 40 minutes are attributed to orientationally disordered molecules distributed over the glass surface. The islands seen in the sample dipped for 120 minutes are attributed to orientationally disordered molecules distributed over the monolayer. The reason the islands are termed disordered is because their heights are less than that of an OTS monolayer. Orientationally ordered molecules would be expected to have a height approximately equal to that of an OTS monolayer, i.e. 2.6 nm.

Even though the R_a values of the samples prepared in the open laboratory differ from those prepared in the clean room, both sets of results show the same trend. That is, they decrease up to a dipping time of 90 minutes, then increase up to a dipping time of 120 minutes.

Further evidence for the dipping time for formation of the OTS monolayer was given from the FTIR spectroscopy data reported in Chapter.3. The comparison of the FTIR-ATR results from chapter 3. with the AFM results obtained here, is given in chapter 7.

5.2.3. Perfluorodecyl(ethyl)trichlorosilane.

The results of the studies on self-assembled films of perfluorodecyl(ethyl)trichlorosilane, F8, $\text{CF}_3(\text{CF}_2)_7(\text{CH}_2)_2\text{SiCl}_3$, on Pilkington float glass will be given in this section. The samples, which were dipped for 15 seconds, 5, 8 and 30 minutes, either under class 100 clean room conditions or in the open laboratory, were examined using atomic force microscopy, on the non-tin side of the glass only. In this context, the 'open laboratory' refers to a dry nitrogen atmosphere, with no clean room classification.

As for the OTS-coated samples, both three-dimensional images and two-dimensional section analyses are presented for each sample. The roughness average, (R_a), and root mean square roughness, (RMS), values for each sample were obtained using the computer software, and are reported in table.5.3.

The three-dimensional atomic force microscopy image of F8 on float glass, prepared under clean room conditions, and removed from the silane solution after 15 seconds dipping time, is shown in figure.5.18. Islands are observed in this image. The cross-sectional analysis of some of the islands in this image is given in figure.5.19. It can be seen from figure.5.19. that the islands are of a height less than that of an F8 monolayer, i.e. less than 1.6 nm. The R_a value obtained for this sample was 0.176 nm. This value is less than the R_a value obtained for the float glass substrate.

The corresponding three-dimensional atomic force microscopy image of the sample prepared in the open laboratory can be seen in figure.5.20. Many islands are clearly observable in this image. The cross-sectional analysis through some of these islands is given in figure.5.21. The heights of the islands in figure.5.21. are much larger than an F8 monolayer. In fact some of the islands are several monolayers in height. The R_a value obtained for this surface was 0.968 nm. This is much larger than both the R_a value of the float glass and the R_a value of the corresponding sample prepared in the clean room.

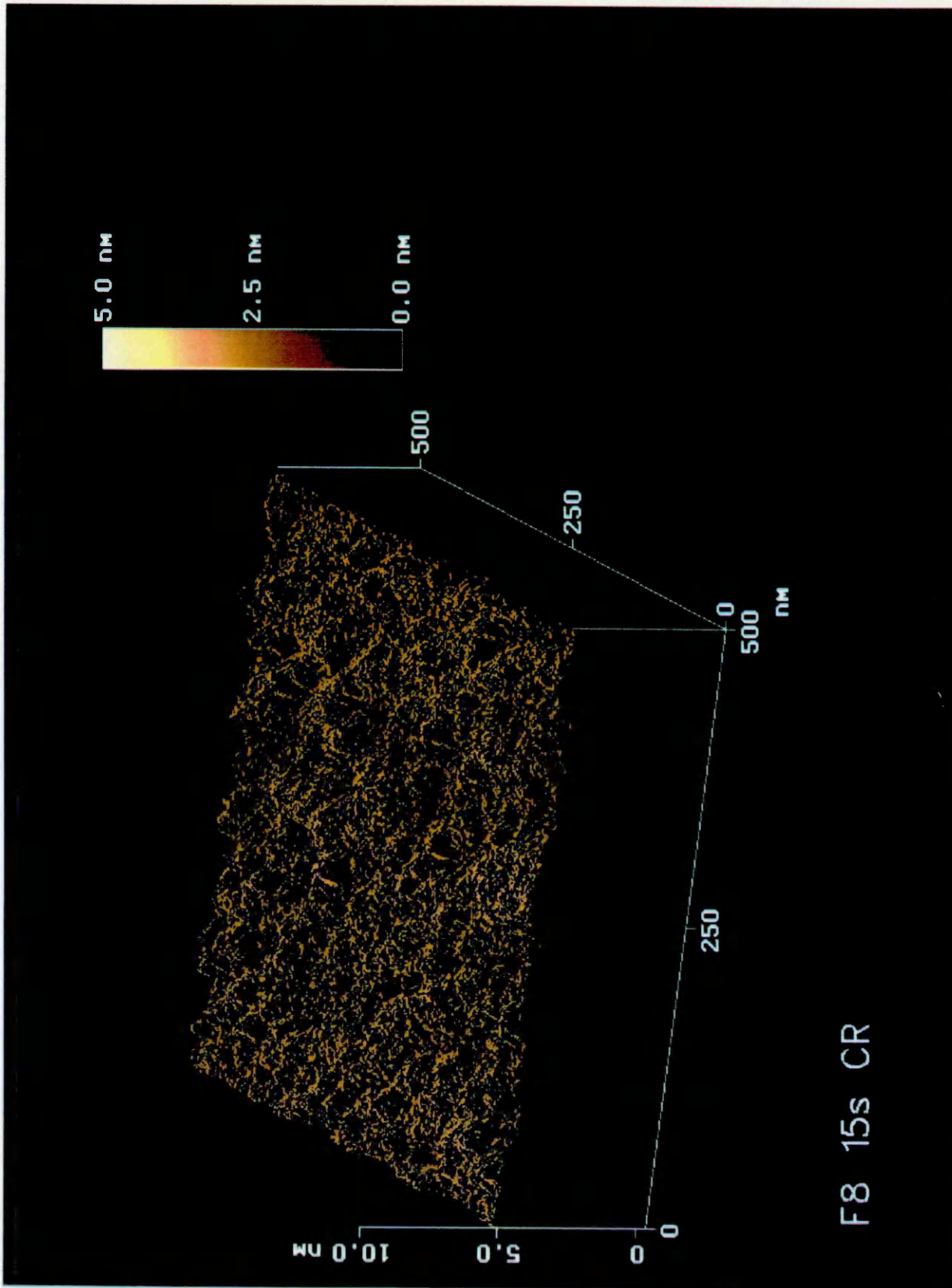
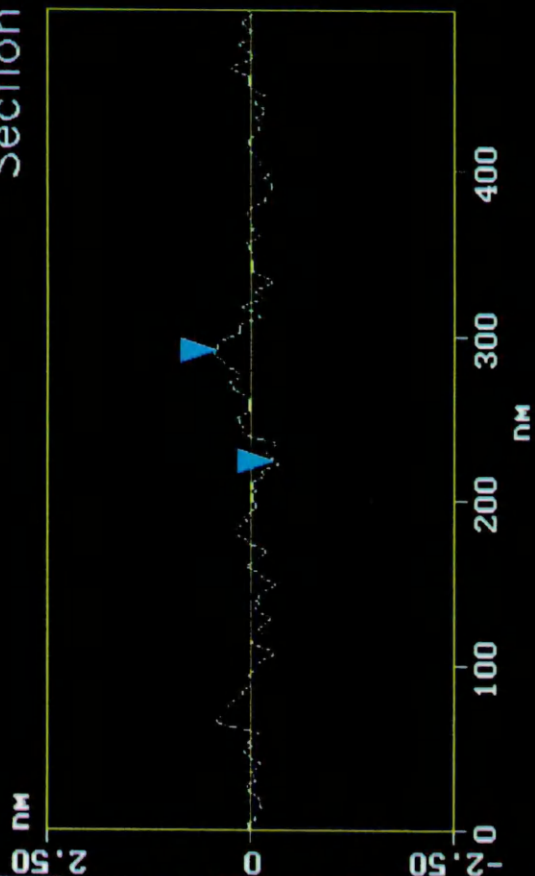


Figure 5.18.

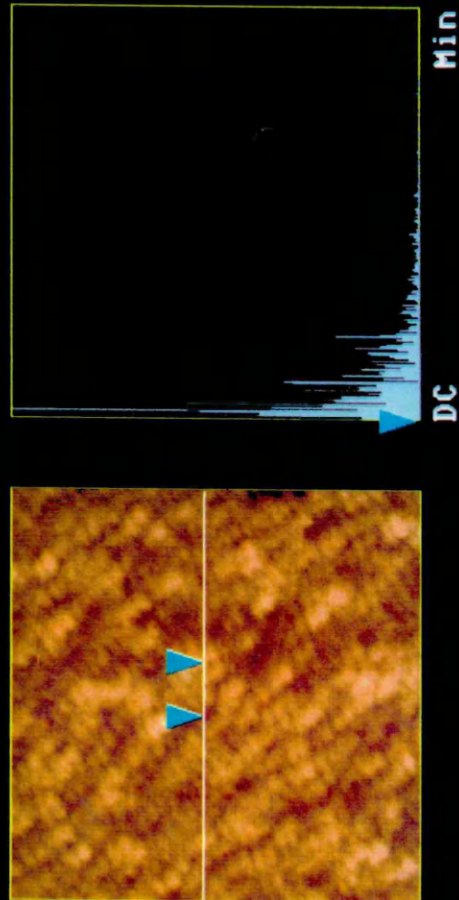
Cursor Marker Spectrum Zoom Center Line Offset Clear

Section Analysis



L	66.406 nm
RMS	0.204 nm
Ic	DC
Ra(Ic)	0.078 nm
Rmax	0.391 nm
Rz	0.201 nm
Rz Cnt	8

Horiz distance(L)	66.406 nm
Vert distance	0.688 nm
Angle	0.594 deg
Horiz distance	
Vert distance	
Angle	
Horiz distance	
Vert distance	
Angle	
Spectral period	DC
Spectral freq	0 Hz
Spectral amp	0.0003 nm



F8 15s CR

Cursor: fixed Zoom: 2:1 Cen line: off Offset: off

Figure.5.19.

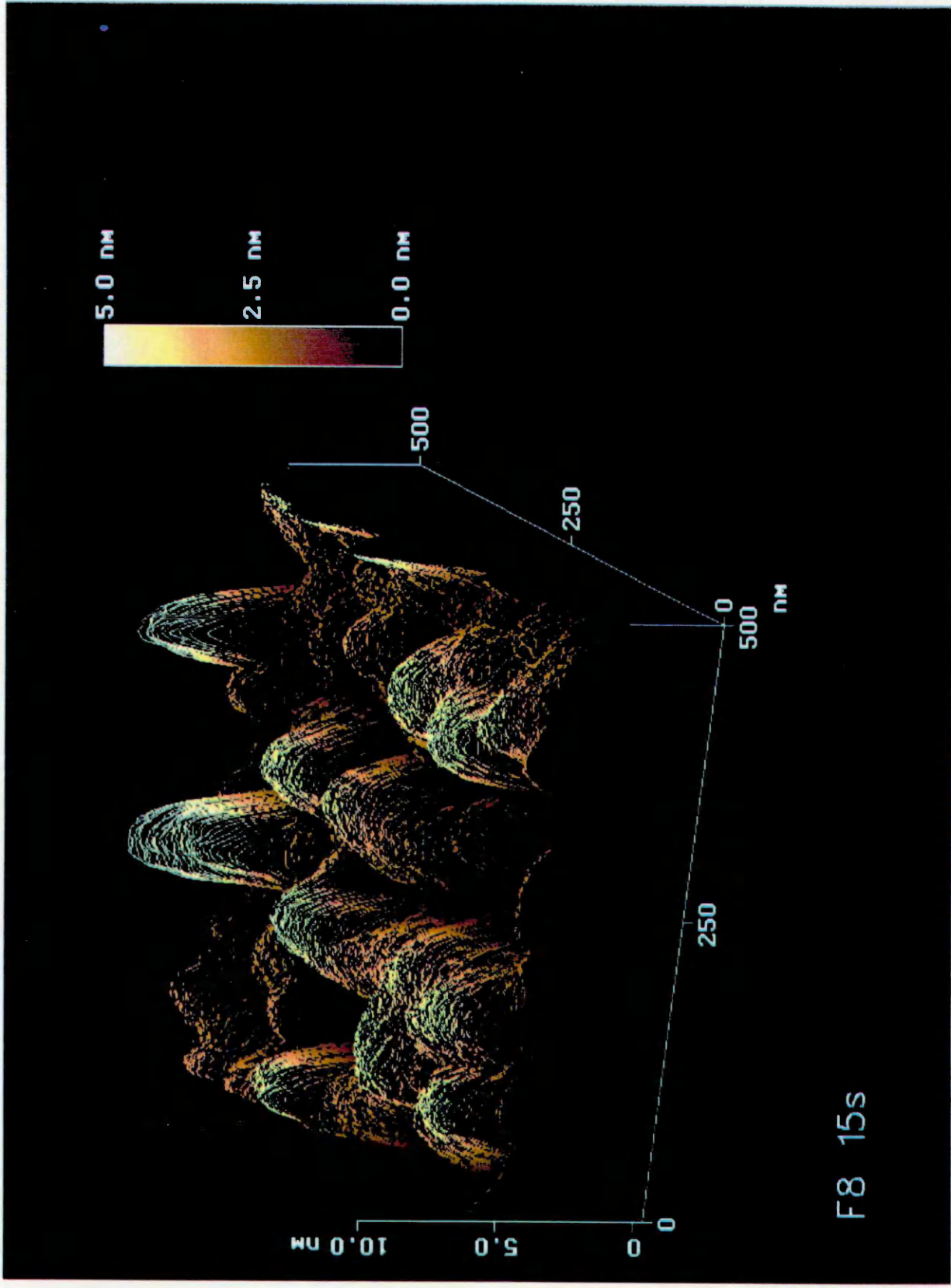
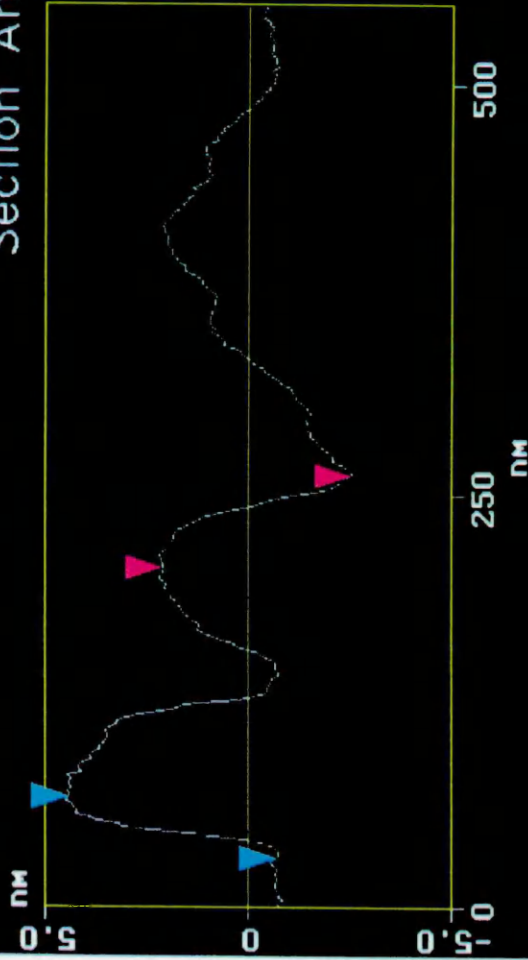


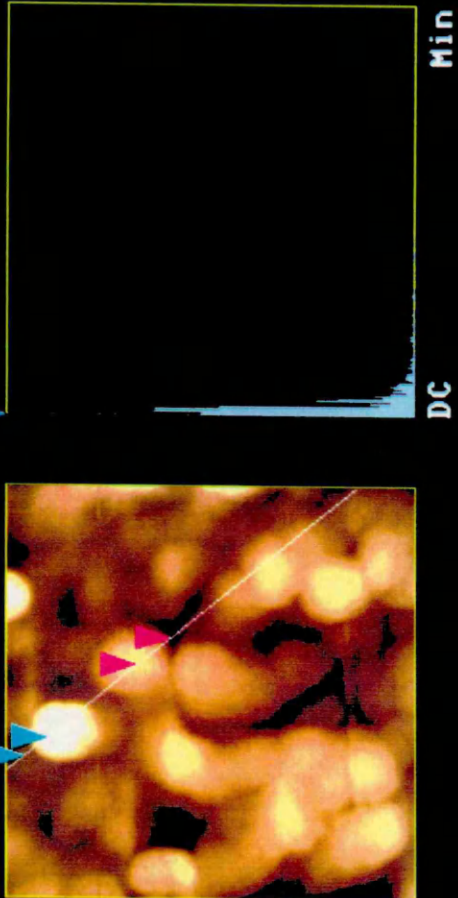
Figure 5.20.

Section Analysis



L	54.688 nm
RMS	1.662 nm
Ic	DC
Ra(Ic)	0.449 nm
Rmax	1.884 nm
Rz	1.884 nm
Rz Cnt	2

Horiz distance(L)	37.109 nm
Vert distance	5.123 nm
Angle	7.860 deg
Horiz distance	54.688 nm
Vert distance	4.609 nm
Angle	4.818 deg
Horiz distance	
Vert distance	
Angle	
Spectral period	DC
Spectral freq	0 Hz
Spectral amp	1.069 nm



F8 15s

Figure 5.21.

Table.5.3. R_a and RMS values for F8-coated Pilkington Float Glass.

Figure number	Description	R_a / nm \pm 0.01 nm	RMS /nm \pm 0.01 nm
5.18	F8 15 seconds dipping time, clean room, 3-D	0.176	0.220
5.19	F8 15 seconds dipping time, clean room, 2-D	0.176	0.220
5.20	F8 15 seconds dipping time, open laboratory, 3-D	0.968	1.223
5.21	F8 15 seconds dipping time, open laboratory, 2-D	0.968	1.223
5.22	F8 5 minutes dipping time, clean room, 3-D	0.096	0.122
5.23	F8 5 minutes dipping time, clean room, 2-D	0.096	0.122
5.24	F8 5 minutes dipping time, open laboratory, 3-D	0.174	0.242
5.25	F8 5 minutes dipping time, open laboratory, 2-D	0.174	0.242
5.26	F8 8 minutes dipping time, clean room, 3-D	0.070	0.094
5.27	F8 8 minutes dipping time, clean room, 2-D	0.070	0.094
5.28	F8 8 minutes dipping time, open laboratory, 3-D	0.088	0.110
5.29	F8 8 minutes dipping time, open laboratory, 2-D	0.088	0.110
5.30	F8 30 minutes dipping time, clean room, 3-D	0.124	0.175
5.31	F8 30 minutes dipping time, clean room, 2-D	0.124	0.175
5.32	F8 30 minutes dipping time, open laboratory, 3-D	0.175	0.225
5.33	F8 30 minutes dipping time, open laboratory, 2-D	0.175	0.225

The three-dimensional atomic force microscopy image of F8 on float glass, prepared in the clean room, and removed from the silane solution, after 5 minutes dipping time can be seen in figure.5.22. Some of the islands observable in this image have been measured using the section analysis software and the resulting image can be seen in figure.5.23. The heights of these islands are less than monolayer height. The R_a value obtained for this surface was 0.096 nm. This is less than the R_a value obtained for the float glass substrate and less than the R_a value obtained for the sample dipped for 15 seconds, in the clean room. This indicates an increased smoothness in the sample dipped for 5 minutes compared to the sample dipped for 15 seconds, (both prepared in the clean room).

The corresponding three-dimensional atomic force microscopy image of the sample prepared in the open laboratory, is shown in figure.5.24. Some of the islands observed in this image have been analysed using the software and the results can be seen in figure.5.25. The islands seen in figure.5.25. are of a height less than a monolayer. The R_a value computed for this surface was 0.174 nm. This is less than the R_a value obtained for the float glass substrate, and much smaller than the R_a value obtained for the sample dipped for 15 seconds in the open laboratory. Therefore it appears that the surface of the sample dipped for 5 minutes is smoother than the surface of the sample dipped for 15 seconds, (both in the open laboratory).

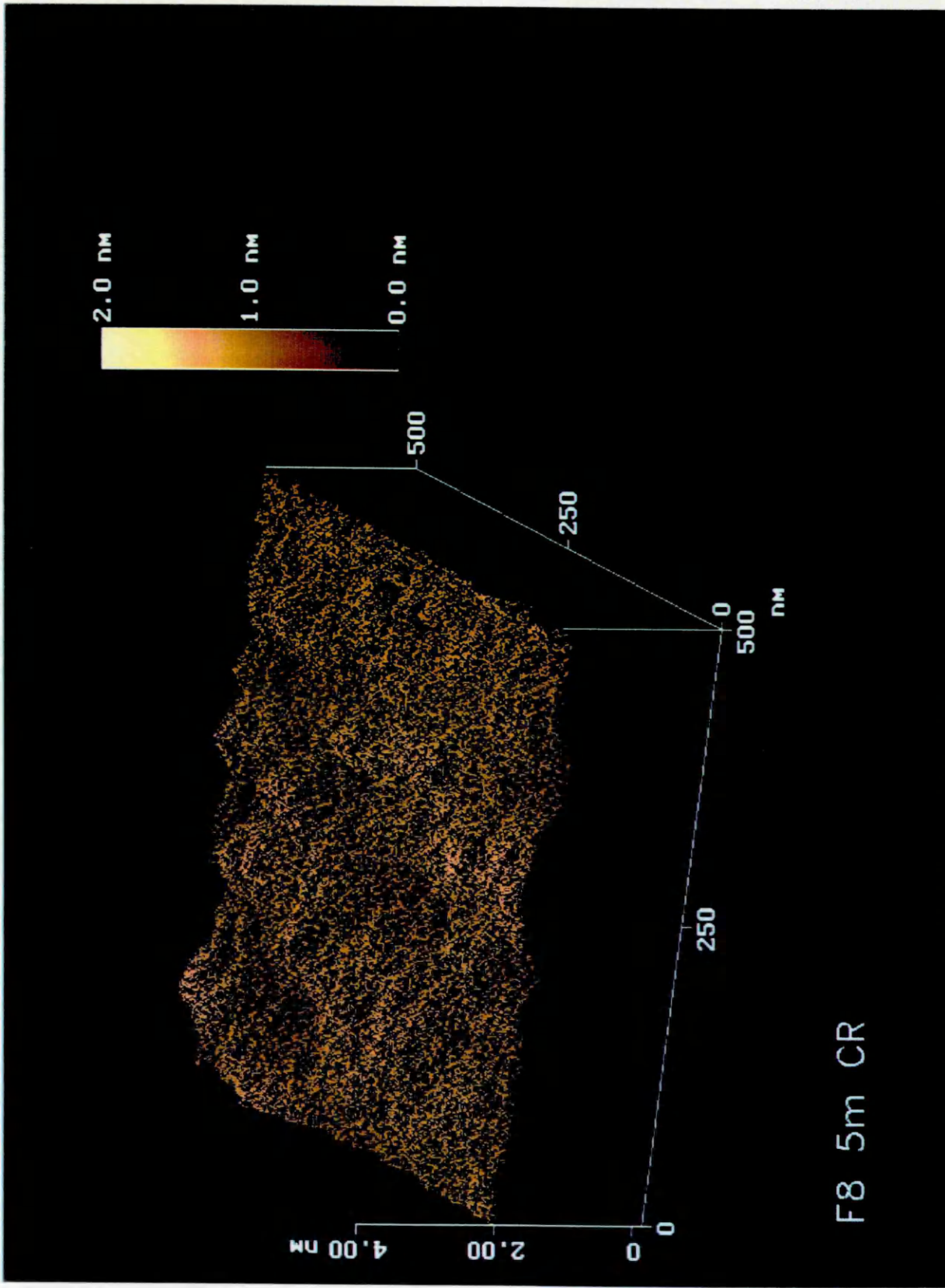
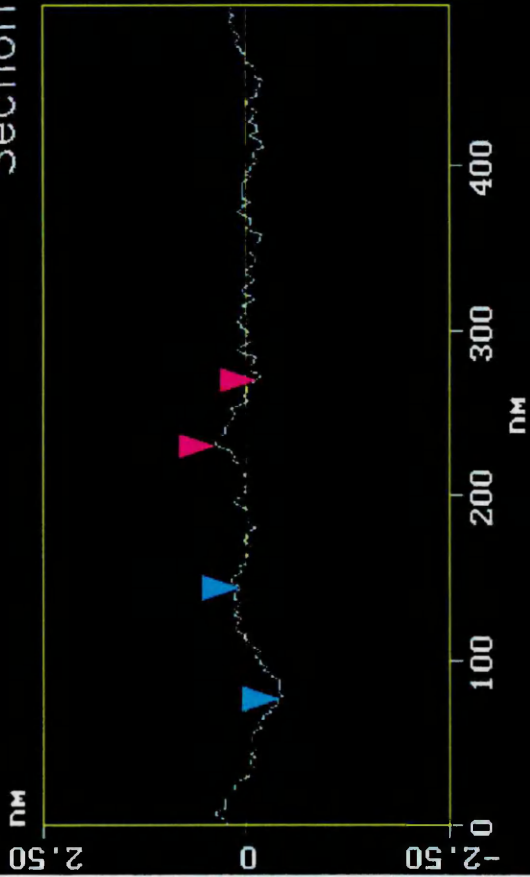


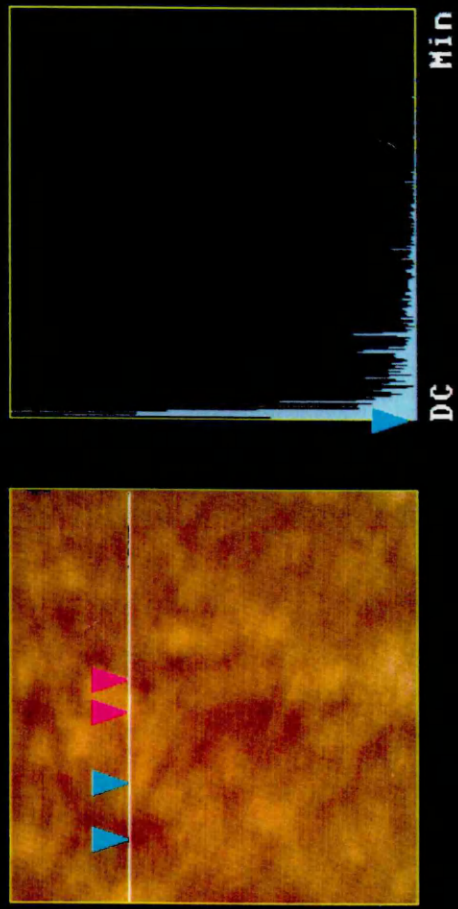
Figure.5.22.

Section Analysis



L	39.063	nm
RMS	0.149	nm
Ic	DC	
Ra(Ic)	0.021	nm
Rmax	0.164	nm
Rz	0.072	nm
Rz Cnt	valid	

Horiz distance(L)	68.359	nm
Vert distance	0.460	nm
Angle	0.386	deg
Horiz distance	39.063	nm
Vert distance	0.509	nm
Angle	0.746	deg
Horiz distance		
Vert distance		
Angle		
Spectral period	DC	
Spectral freq	0	Hz
Spectral amp	0.001	nm



F8 5m CR

Figure.5.23.

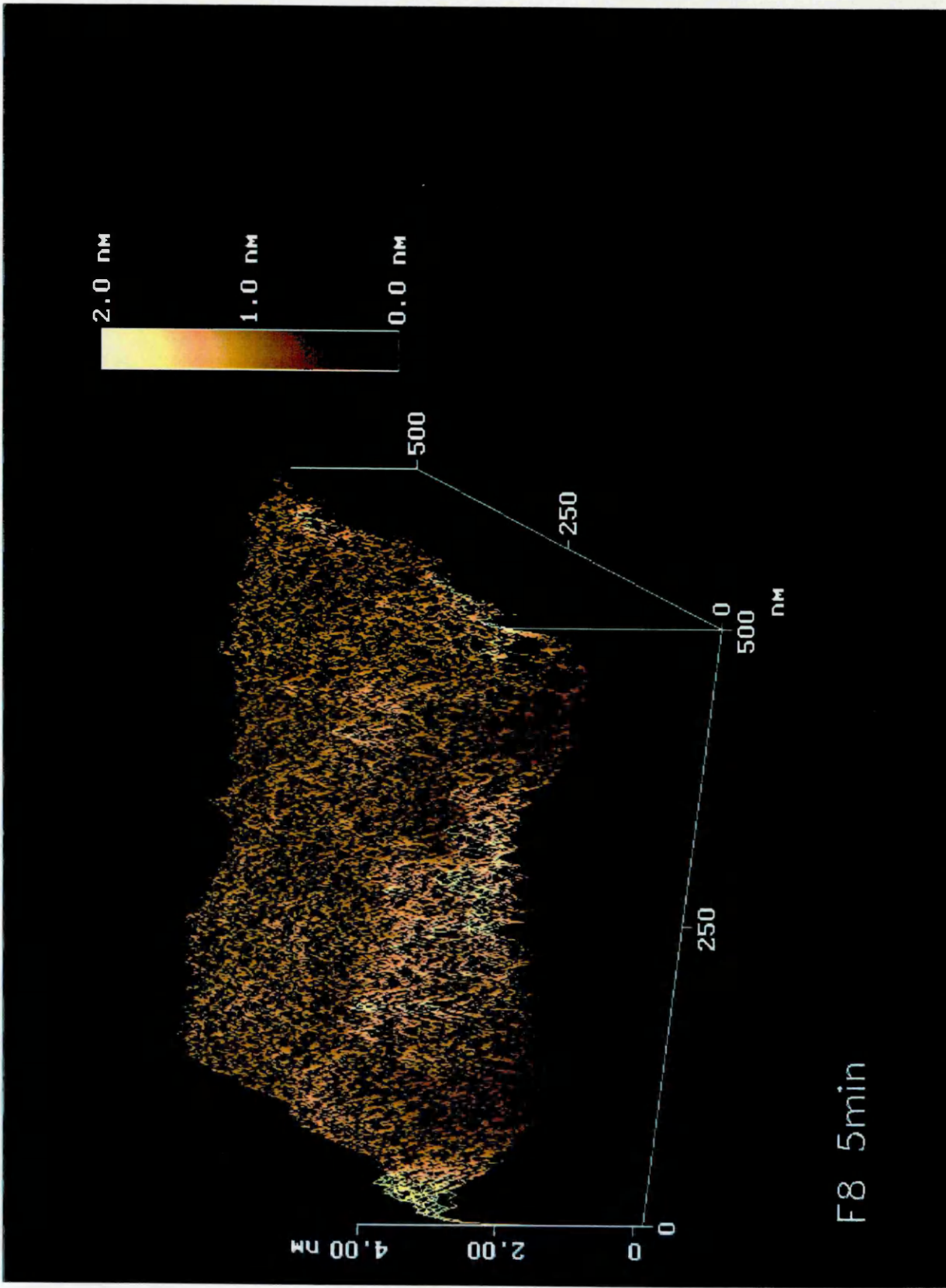
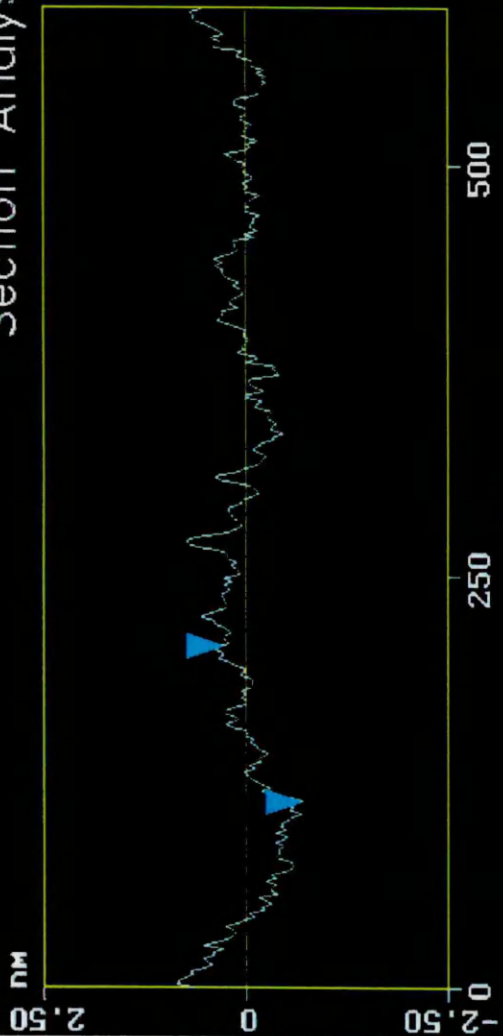


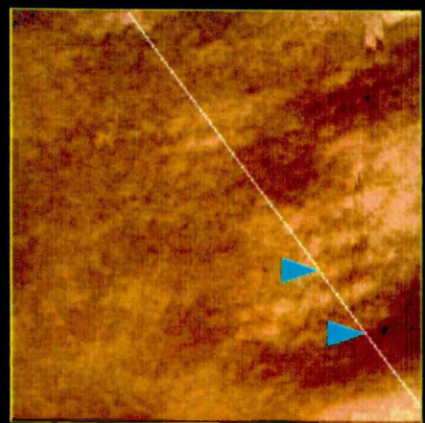
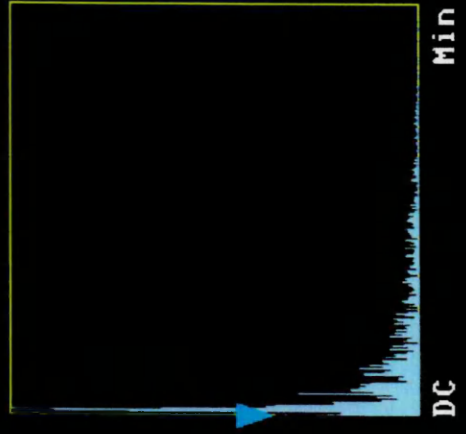
Figure 5.24.

Section Analysis



L	93.750 nm
RMS	0.215 nm
Ic	DC
Ra(Ic)	0.108 nm
Rmax	0.714 nm
Rz	0.326 nm
Rz Cnt	valid

Horiz distance(L)	93.750 nm
Vert distance	1.015 nm
Angle	0.620 deg
Horiz distance	
Vert distance	
Angle	
Spectral period	DC
Spectral freq	0 Hz
Spectral amp	0.058 nm



F8 5min

Figure.5.25.

The three-dimensional atomic force microscopy image of an F8-coated float glass sample, prepared in the clean room and removed from the silane solution after 8 minutes dipping time, can be seen in figure.5.26. A few small islands are observable in this image. The cross-sectional analysis of some of the islands in this image can be seen in figure.5.27. The islands in figure.5.27. are of a height much smaller than a monolayer of F8. The R_a value obtained for this surface was 0.070 nm. This is much smaller than the R_a value obtained for the glass substrate and also smaller than the R_a values obtained for the samples dipped for 15 seconds and 5 minutes, (in the clean room). Therefore this surface is smoother than the surfaces of the samples dipped for 15 seconds and 5 minutes.

The three-dimensional atomic force microscopy image of an F8-coated glass sample, prepared in the open laboratory, and removed from the silane solution after 8 minutes dipping time, is shown in figure.5.28. The islands observed in this image have been analysed using the software and the results can be seen in figure.5.29. The islands seen in figure.5.29. are of a height much less than an F8 monolayer. The R_a value obtained for this surface was 0.088 nm. This is much smaller than the R_a value obtained for the glass substrate and also smaller than the R_a values obtained for the samples dipped for 15 seconds and 5 minutes, (in the open laboratory). Therefore this sample appears to be smoother than those dipped for 15 seconds and 5 minutes. The R_a value for the sample prepared in the open laboratory is slightly larger than that obtained for the sample prepared in the clean room, (both dipped for 8 minutes).

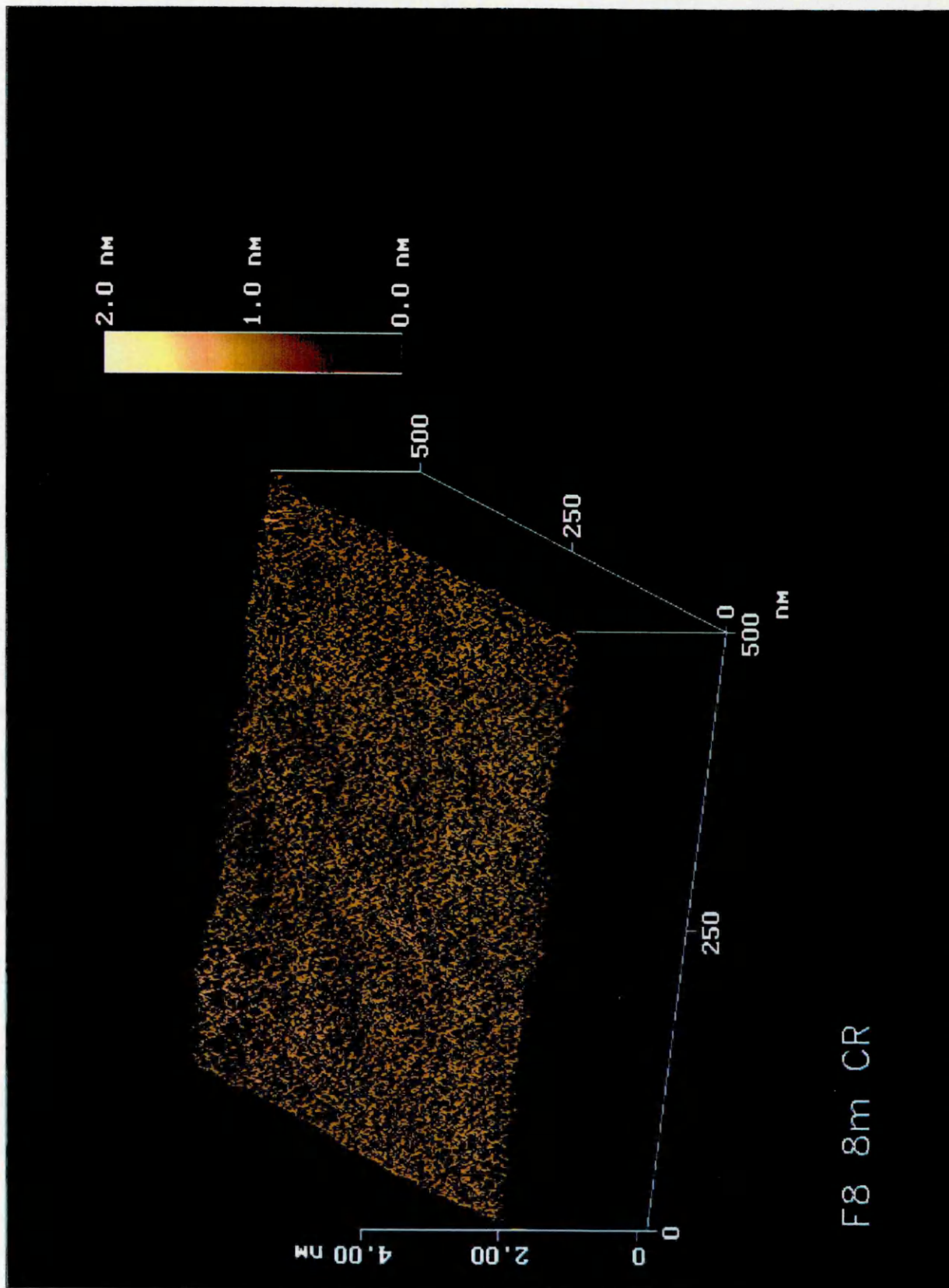
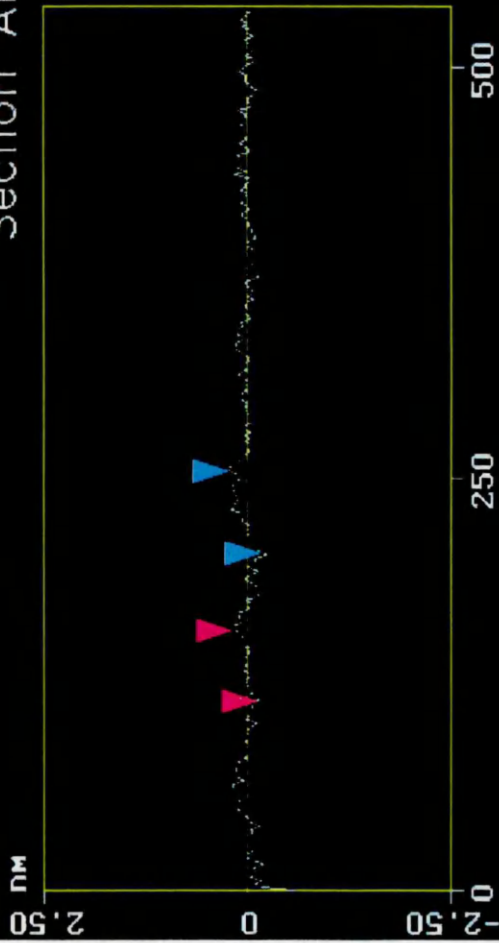
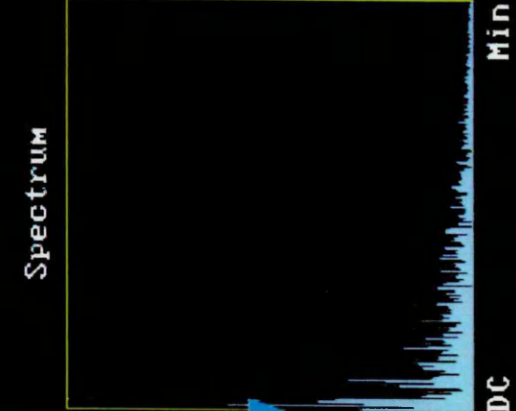


Figure 5.26.

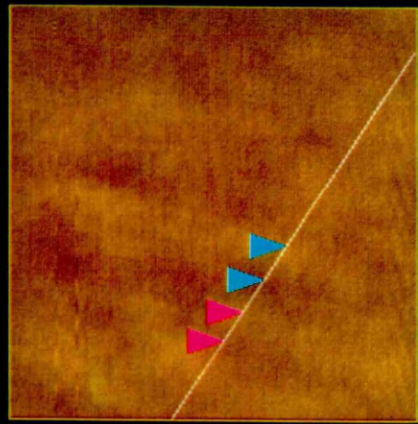
Section Analysis



L	42.969	nm
RMS	0.074	nm
Ic	DC	
Ra(Ic)	0.029	nm
Rmax	0.181	nm
Rz	0.096	nm
Rz Cnt	valid	



Horiz distance(L)	48.828	nm
Vert distance	0.354	nm
Angle	0.415	deg
Horiz distance	42.969	nm
Vert distance	0.351	nm
Angle	0.468	deg
Horiz distance		
Vert distance		
Angle		
Spectral period	DC	
Spectral freq	0	Hz
Spectral amp	0.023	nm



F8 8M CR

Figure 5.27.

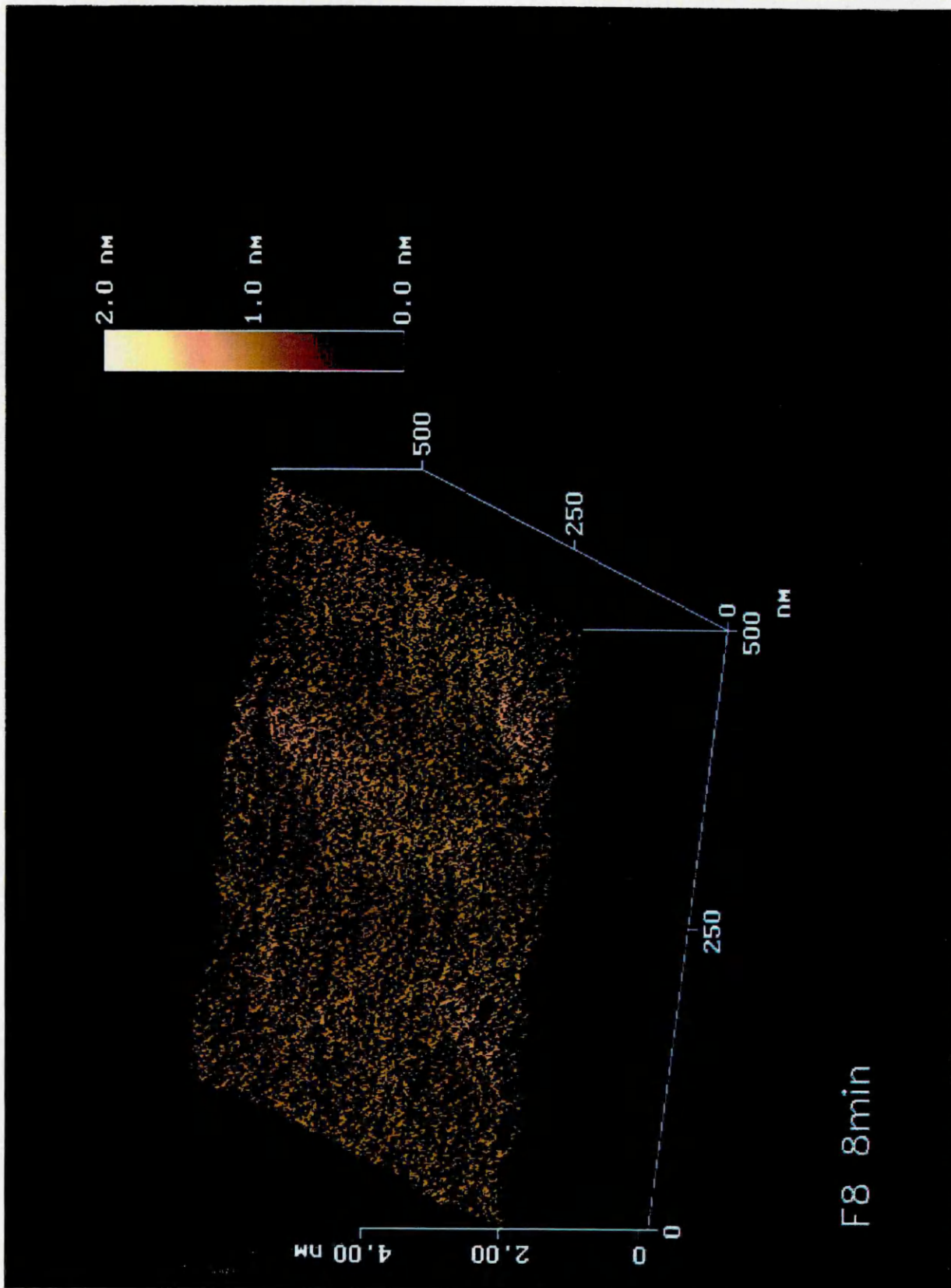
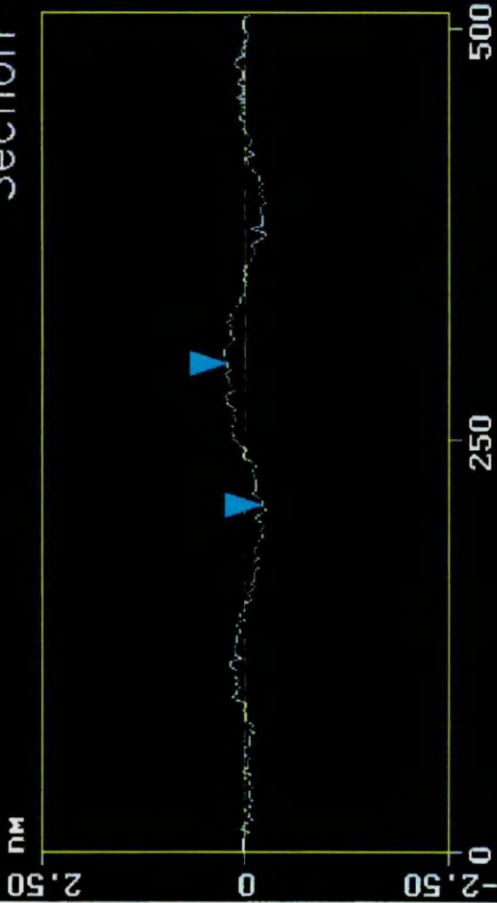


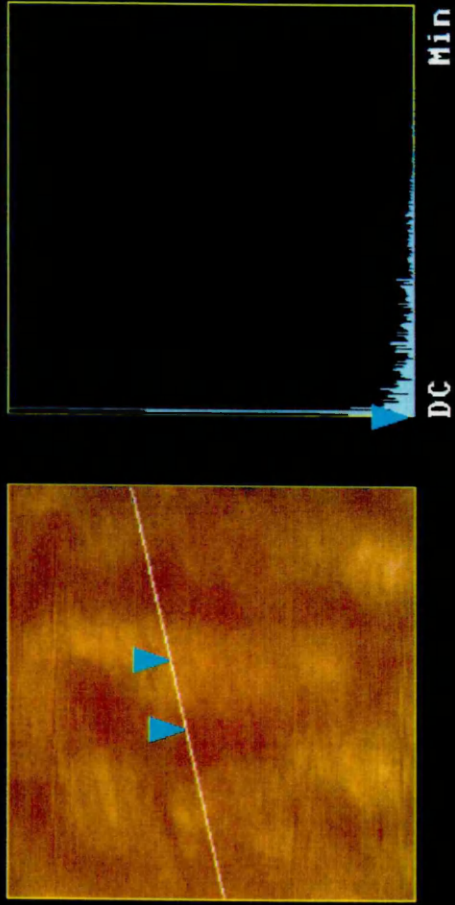
Figure 5.28.

Section Analysis



L	85.938 nm
RMS	0.143 nm
IC	DC
Ra(1c)	0.044 nm
Rmax	0.221 nm
Rz	0.129 nm
Rz Cnt	valid

Horiz distance(L)	85.938 nm
Vert distance	0.431 nm
Angle	0.287 deg
Horiz distance	
Vert distance	
Angle	
Horiz distance	
Vert distance	
Angle	
Spectral period	DC
Spectral freq	0 Hz
Spectral amp	0.001 nm



F8 8min

Figure.5.29.

The three-dimensional atomic force microscopy image of F8 on float glass, prepared in the clean room and removed from the silane solution after 30 minutes dipping time is shown in figure.5.30. Again, islands can be seen in this image. The section analysis of some of the islands in figure.5.30. is depicted in figure.5.31. The heights of these islands can be seen to be of monolayer height and less. The R_a value obtained for this surface was 0.124 nm. This is smaller than the R_a value of the float glass substrate but larger than the R_a value of the sample dipped for 8 minutes, (in the clean room). Therefore the surface is becoming rougher again.

The three-dimensional atomic force microscopy image of F8-coated float glass, prepared in the open laboratory, and removed from the silane solution after 30 minutes dipping time, can be seen in figure.5.32. There are many islands observable in this image. The section analysis of this image is given in figure.5.33. The heights of some of the islands in this image, can be seen, from figure.5.33. to be of monolayer height and less. The R_a value obtained for this surface was 0.175nm. This is less than the R_a value obtained for the float glass substrate. However, it is greater than the R_a value obtained for the sample dipped for 8 minutes, (in the open laboratory). Therefore, this indicates that the surface is becoming rougher. The R_a value obtained for the sample in figure.5.32. is also larger than the R_a value obtained for the corresponding sample prepared in the clean room.

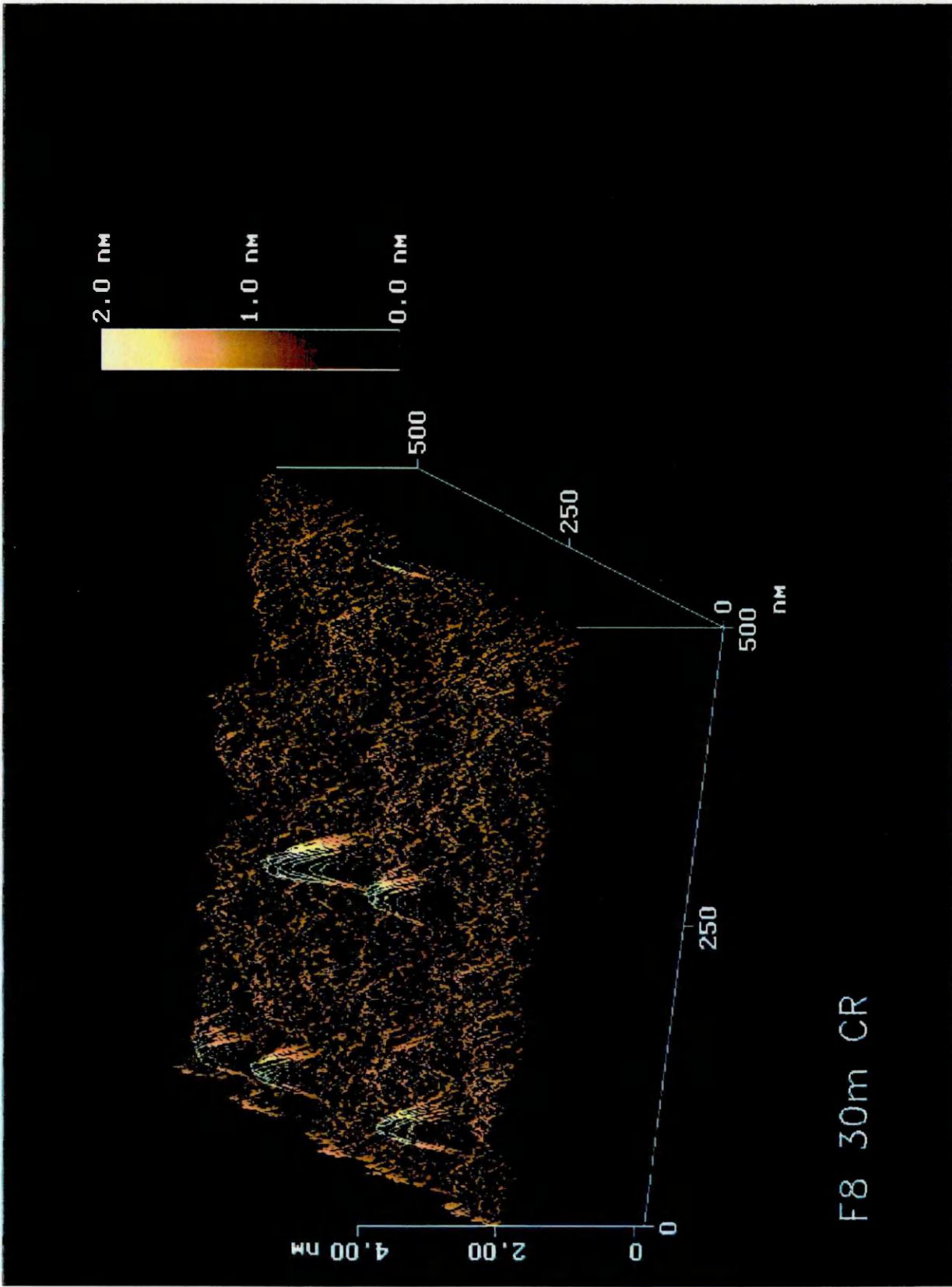


Figure 5.30.

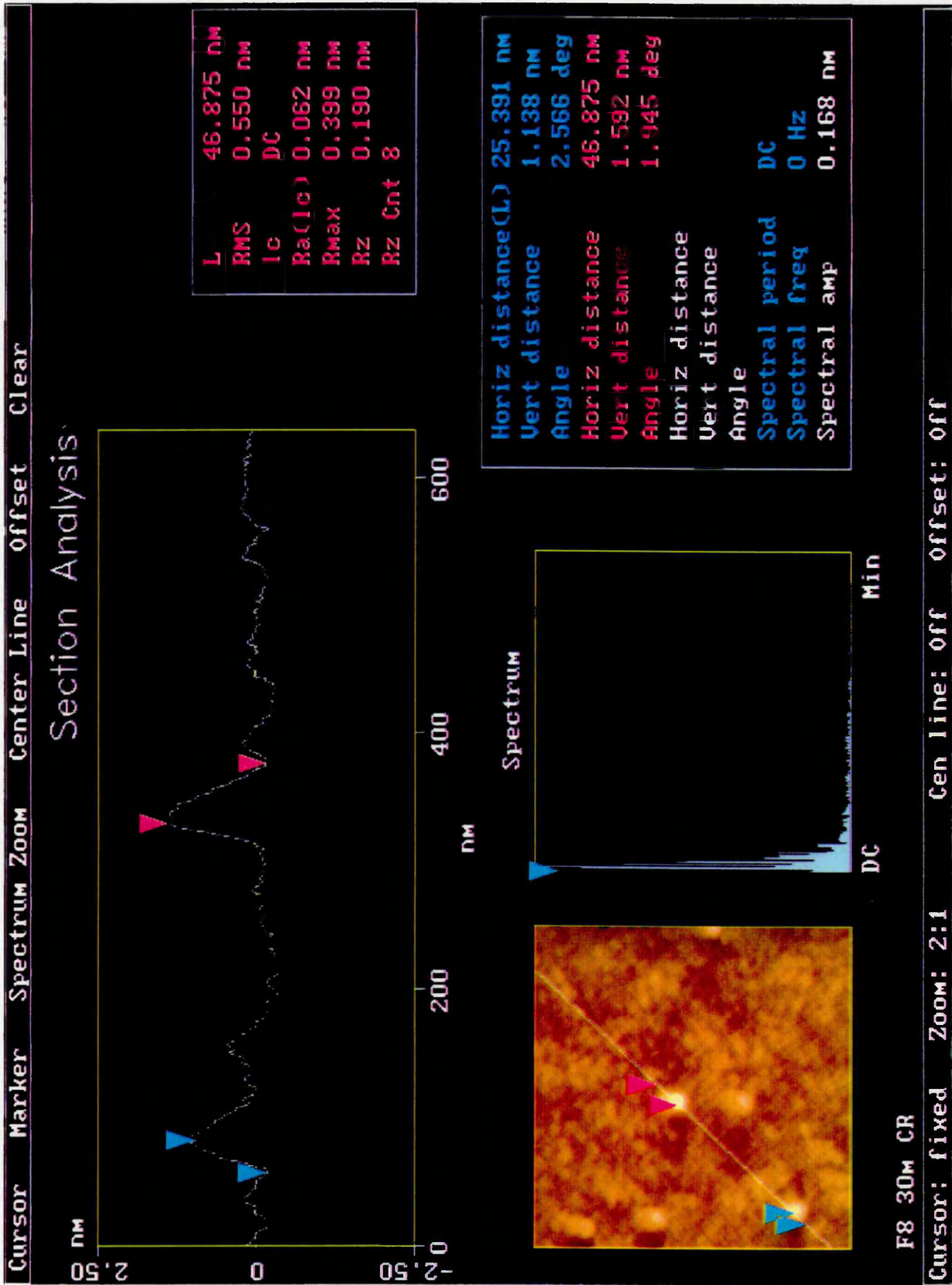


Figure.5.31.

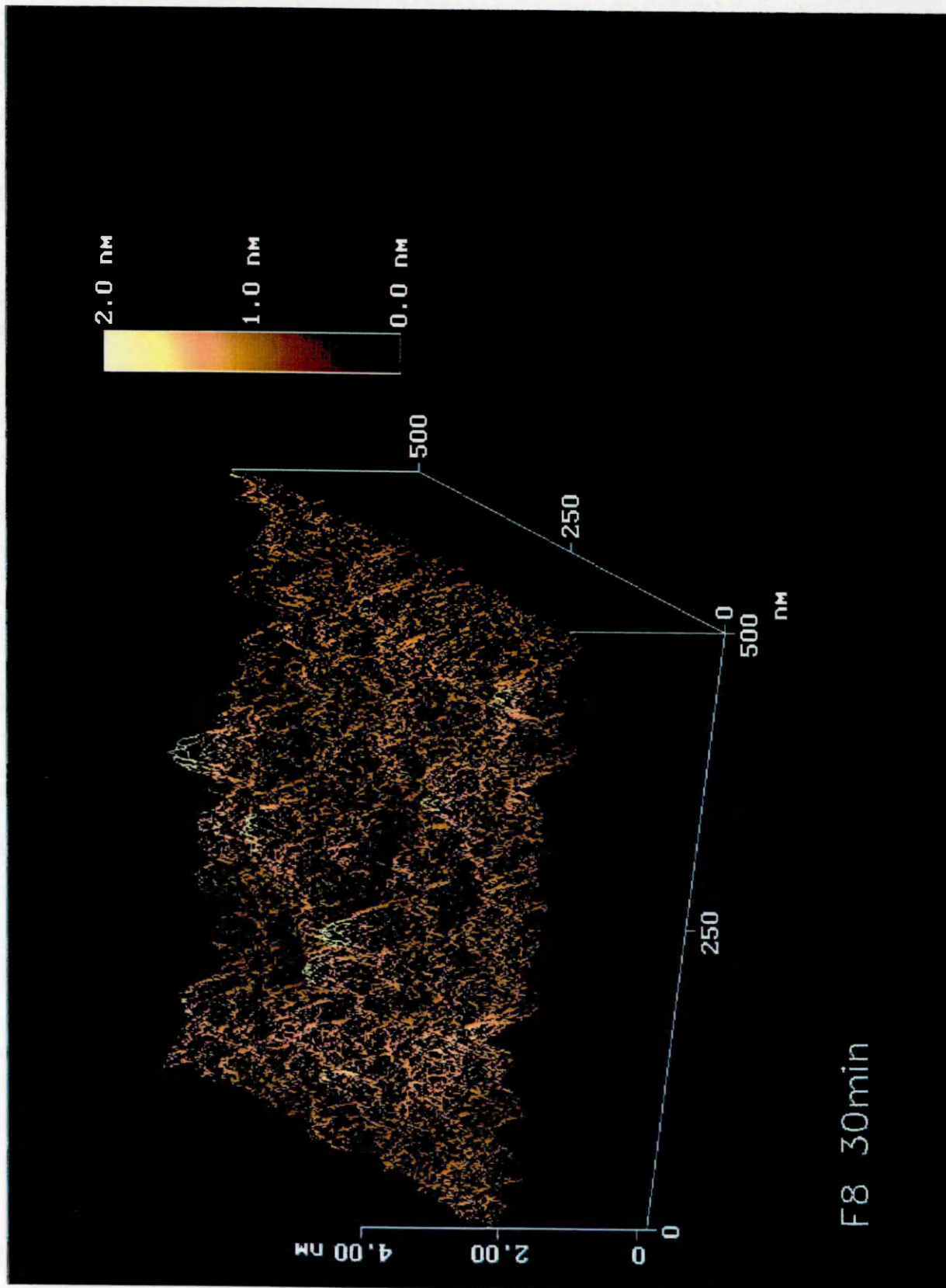
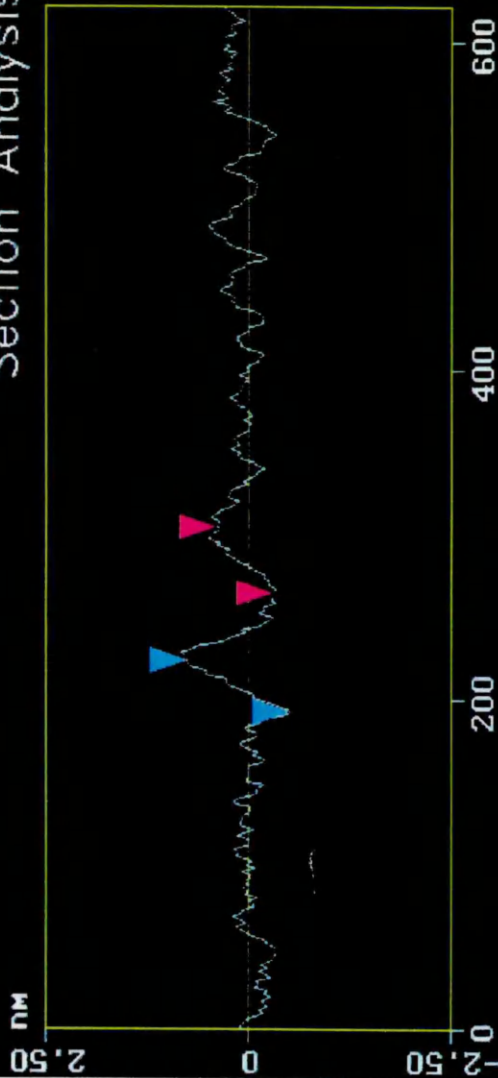


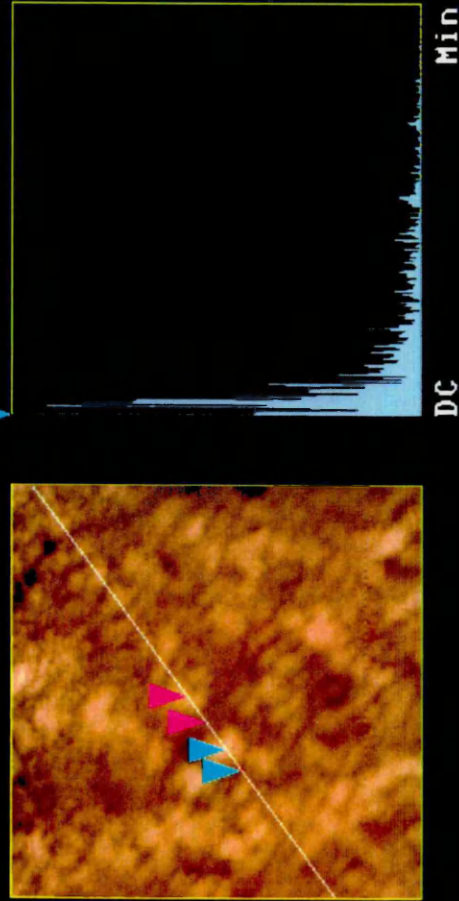
Figure. 5.32.

Section Analysis



L	39.063	nm
RMS	0.282	nm
IC	DC	
Ra(1c)	0.055	nm
Rmax	0.287	nm
Rz	0.155	nm
Rz Cnt	8	

Horiz distance(L)	31.250	nm
Vert distance	1.293	nm
Angle	2.369	deg
Horiz distance	39.063	nm
Vert distance	0.714	nm
Angle	1.047	deg
Horiz distance		
Vert distance		
Angle		
Spectral period	DC	
Spectral freq	0	Hz
Spectral amp	0.105	nm



F8 30min

Figure 5.33.

For all the F8-coated samples, those prepared in the clean room had R_a values smaller than those prepared in the open laboratory. As explained for the OTS-coated samples, the reasons for this are not clear.

For the samples prepared under class 100 clean room conditions, it was observed that the R_a value decreased as dipping time increased up to 8 minutes. When the dipping time was increased from 8 to 30 minutes, the R_a value was seen to increase. Therefore as the dipping time increased up to 8 minutes, the surface became gradually smoother. Then, as the dipping time was increased from 8 minutes to 30 minutes, the surface became rougher. These results were interpreted in the following way: The sample at 15 seconds dipping time represents submonolayer coverage, the sample at 5 minutes dipping time represents almost monolayer coverage, the sample at 8 minutes coverage represents monolayer coverage and the sample at 30 minutes dipping time represents above-monolayer coverage. Further evidence for the time for formation of the monolayer is the presence of the larger islands at 15 seconds and 30 minutes dipping time and much smaller islands at 5 and 8 minutes dipping time. The islands observed at 15 seconds dipping time are attributed to orientationally disordered F8 molecules distributing over the glass substrate. The islands at 30 minutes dipping time are attributed to orientationally disordered F8 molecules distributing over the F8 monolayer. These molecules are said to be disordered, since an orientationally ordered F8 layer would be expected to have a height similar to that of an F8 monolayer, i.e. 1.6 nm.

Even though the R_a values of the samples prepared in the open laboratory differed from the R_a values of the samples prepared in the clean room, the same trend was observed for both sets of values. That is, a decrease in R_a value up to 8 minutes dipping time and then an increase in R_a value up to 30 minutes dipping time.

For all the samples, features in the images were probed at different magnifications. These features did not change shape but varied in size according to the magnification. Therefore the images were reproducible.

The rates of adsorption of the two silanes onto glass were expected to be dependent upon many conditions, including water content in solvent and atmospheric humidity. The rate of adsorption of F8 onto the glass was faster than that of OTS because the SiCl groups on the F8 molecules were hydrolysed faster than those on the OTS molecules. This was because the CF₃ and CF₂ groups on the F8 molecules were more electron withdrawing than the CH₃ and CH₂ groups on the OTS molecules. Therefore, the nucleophilic substitution of Cl in SiCl with OH⁻ was easier for F8 than for OTS.

Further evidence for the time of formation of the monolayer was given by the FTIR spectroscopy data reported in chapter 3. The comparison of the FTIR-ATR results from chapter 3 and the AFM data presented here, will be given in chapter 7.

5.3. Conclusions.

5.3.1. Float Glass.

The R_a values obtained from the atomic force microscopy images of float glass, measured over the same areas as the sample images, were obtained using the software. Although these R_a values were larger than the usual AFM substrate, mica, they were still small enough for the investigation of the thin films, described here.

In this chapter, two- and three-dimensional images of silane-coated Pilkington float glass were presented. These images were compared to float glass images and to each other, in order to determine the dipping time for formation of the monolayers and the variation of the surface topography with degree of coverage. Two sets of samples were prepared for each of the silanes used, one set under class 100 clean room conditions and the other in the open laboratory, (see section.5.1. for details).

Reproducibility of the AFM images was checked by imaging each sample in several areas at several magnifications. The images were found to be reproducible.

The R_a values obtained for all the silane-coated samples, (except the F8-coated sample dipped in the open laboratory for 15 seconds), were smaller than the R_a value obtained for the float glass substrate. This 'smoothing' effect was interpreted in the literature, [61], to be due to the entropy-driven cross-linkage of silane, (OTS), chains to form siloxane links, Si-O-Si, so that not all the silane, (OTS), molecules were adsorbed onto the glass substrate. Therefore the silane, (OTS), film 'smooths' the substrate surface. Similar silane film formation appears to have occurred with the samples here.

The R_a values obtained for all the samples prepared in the clean room, (except the OTS-coated sample dipped for 90 minutes), were smaller than for the corresponding samples dipped in the open laboratory. No reason for this

difference in R_a value has yet been established, although some researchers, [60], did find that only samples, (of OTS on silicon), prepared under class 100 clean room conditions gave reproducible atomic force microscopy results.

5.3.2. N-octadecyltrichlorosilane.

Submono-, mono- and above-monolayers of OTS were formed on Pilkington float glass substrates, using the self-assembling monolayer technique. These films were characterised by atomic force microscopy. The roughness average, (R_a), values obtained for the OTS-coated samples, prepared in the clean room were seen to decrease up to 90 minutes dipping time and then to increase up to 120 minutes dipping time. The RMS, (and R_a), value obtained for the sample dipped for 90 minutes in the silane solution, was very small, (smaller than the RMS value quoted for an OTS monolayer on a glass coverslip, [61]). Therefore the OTS monolayer formation occurred at approximately 90 minutes dipping time. Island formation was observed in the images of the samples dipped for 20, 40 and 120 minutes in the silane solution. The islands at 20 and 40 minutes dipping time were attributed to orientationally disordered OTS molecules adsorbing onto the glass substrate and the islands at 120 minutes dipping time were attributed to orientationally disordered OTS molecules distributing over the OTS monolayer. The molecules in the islands were disordered since, the island heights were less than the height of an OTS monolayer.

Even though the R_a values for the OTS-coated float glass prepared in the open laboratory, differed from the R_a values of the samples prepared in the clean room, the two sets of values showed the same trend. That is, a decrease in R_a value was observed up to a dipping time of 90 minutes and then an increase in R_a value from 90 to 120 minutes dipping time.

Further evidence for the dipping time for monolayer formation and orientational order was given in chapter 3.

5.3.3. Perfluorodecyl(ethyl)trichlorosilane.

Submono-, mono- and above-monolayers of F8 were formed on Pilkington float glass. These films were characterised by atomic force microscopy. The roughness average, (R_a), values obtained for the F8-coated samples, prepared in the clean room were seen to decrease up to 8 minutes dipping time and then to increase again up to 30 minutes dipping time. The RMS, (and R_a), value obtained for the sample dipped for 8 minutes in the F8 solution was very small, (smaller than the RMS value obtained for a monolayer of OTS on a glass coverslip, [61]). Therefore monolayer formation occurred at approximately 8 minutes dipping time in the F8 solution. Island formation was seen in the samples dipped for 15 seconds, 5 and 30 minutes. The islands at 15 seconds and 30 minutes were much larger than those at 5 minutes dipping time and were attributed to orientationally disordered F8 molecules adsorbing onto the glass, (15 seconds) and onto the F8 monolayer, (30 minutes). The islands were said to be disordered because some of their heights were less than monolayer height, i.e. less than 1.6 nm. Orientationally ordered molecules would be expected to be of a height similar to an F8 monolayer. At 5 minutes it was believed that the monolayer was nearly complete.

Even though the R_a values for the F8-coated float glass samples prepared in the open laboratory differed from the R_a values of the samples prepared in the clean room, the same trend was observed for both sets of values. That is, a decrease in R_a value was observed up to 8 minutes dipping time and then an increase in R_a value from 8 to 30 minutes dipping time.

Further evidence for the dipping time for formation of the F8 monolayer was given in chapter 3.

The F8 monolayers were seen to form faster than the OTS monolayers. This can be explained by the fact that the F8 SiCl groups were hydrolysed faster than the OTS SiCl groups and therefore the F8 molecules adsorbed onto the glass faster than the OTS molecules.

A comparison of the *ex situ* FTIR-ATR results from chapter 3 and the AFM results described in this chapter will be given in chapter 7.

The next chapter deals with a completely different system from the one described in the last three chapters. Infrared and Raman spectroscopy and microscopy data of the 'coupling agent' reactions of shorter-chain silanes, (with amino- and mercapto-substituted end groups), with silicon or glass and poly(vinyl)chloride, will be presented.

CHAPTER.6. VIBRATIONAL SPECTROSCOPY AND MICROSCOPY OF THE CHEMICAL INTERACTIONS IN POLYMER/SILANE/SiO₂ LAMINATES.

Introduction.

This chapter describes studies of the adsorption of two short-chain silanes onto silicon and quartz. The interactions of these adsorbed silanes with a polymer overlayer were also investigated. The two short-chain silanes in question were (3-aminopropyl)trimethoxysilane, $\text{NH}_2(\text{CH}_2)_3\text{Si}(\text{OCH}_3)_3$, A1100, and (3-mercaptopropyl)triethoxysilane, $\text{SH}(\text{CH}_2)_3\text{Si}(\text{OCH}_2\text{CH}_3)_3$, A1891. The main objectives of the work described in this chapter are to determine whether inter-diffusion between the silane and polymer layers occurs and also to determine the distribution of the silane molecules in the polymer overlayer.

6.1. Experimental.

6.1.1. Chemicals.

(3-aminopropyl)trimethoxysilane, 97%, n-octadecyltrichlorosilane, 99.5%, toluene, 99.9%, N, N-dimethylformamide, (DMF), 99.9%, poly (vinylchloride), (PVC), molecular weight, 80 000, secondary standard, were obtained from Aldrich Chemical Co.

(3-mercaptopropyl)triethoxysilane, 97%, was provided by Pilkington plc.

All chemicals were used as received. The silanes were stored in a refrigerator at 5°C.

6.1.2. Substrates.

The substrates used for Raman measurements were polished quartz slides, obtained from Multi-Lab, Newcastle.

For infrared measurements, silicon micro ATR prisms, with approximately 45 to 50 internal reflections were used.

All the substrates were precleaned by washing with acetone and methanol and then by refluxing in hot 2-propanol for at least 4 hours. The substrates were stored in a dessicator prior to use. After silane and polymer deposition, the silicon ATR crystals were cleaned by polishing with diamond paste, then by washing with solvent as above. The quartz slides were not re-used.

All the glassware was pre-silanised with OTS, as described in section.3.1.2, to prevent adsorption of the short-chain silanes to the glass surfaces.

6.1.3. Preparation of Solutions.

Poly(vinylchloride) solutions were prepared at 5% and 10% w/w concentrations, by dissolving the PVC powder in N, N-dimethylformamide with aggressive stirring. No heat stabilisers or other additives were introduced into the solutions.

The aminosilane, A1100, was prehydrolysed in a 9:1, 2-propanol:water, mixture for at least an hour before use. The mercaptosilane, A1891, was prehydrolysed in the same way, but was left for at least 24 hours before use. Silane solutions were prepared at 4% and 20% w/w concentration and each contained 3% acetic acid. If condensation of the silanes in the solutions was observed, the solutions were discarded and fresh ones were prepared.

6.1.4. Preparation of Silane Films.

Cast silane films were produced by pipetting a known volume of 20% w/w silane solution onto a known area of substrate. These films were then heated at 80°C for 5 minutes to drive off any solvent present. The thickness of silane produced by this method was approximately 5 to 7 μm .

Dipped silane films were produced by dipping the substrate into the silane solution for a set time. Films of approximately 5 nm in thickness were produced by dipping the substrate into a 20% w/w silane solution for 6 minutes, washing with methanol and then drying in an oven at 80°C for 5 minutes, [83-85].

Thinner silane films, approximately 1 nm in thickness, were produced by dipping the substrate into a 4% w/w silane solution for 6 minutes, washing with methanol and then drying in an oven at 80°C for 5 minutes, [83-85].

It was observed that the aminosilane formed smooth layers on the substrates whereas the mercaptosilane tended to form 'globules'.

6.1.5. Preparation of Polymer Films.

The PVC films were prepared, (from solution in DMF), on the bare substrates and also on top of the silane-coated substrates, by using either a dipping or a casting method. The dipped films were produced by using a dip motor to control the speed of withdrawal of the substrate from the 10% w/w PVC solution. The cast films were prepared by pipetting a known volume of PVC solution, (5 or 10% w/w), onto the required substrate. The films for Raman investigation were vacuum dessicated for 30 minutes and then heated in an oven at 150-170°C for 5 minutes. The purpose of the vacuum dessication was to remove solvent from the PVC films slowly, so that a smooth polymer surface was produced. The samples for infrared investigation were only heated at 150-170°C, (for varying times), so that the laminates could be studied as soon after PVC deposition as possible.

The thickness of the PVC films was measured using a Rank-Taylor Hobson Talysurf Profiler, to an accuracy of $\pm 0.02 \mu\text{m}$.

6.1.6. Spectroscopic Measurements.

All the samples were analysed before and after PVC deposition. Pure PVC films on silicon and quartz were also studied. Some of the PVC films could be

removed after deposition, by peeling, and these were also analysed by Raman Confocal microscopy.

A Renishaw System 2000 spectrometer, with a 5mW helium-neon laser was used in either the confocal or microprobe modes to obtain spectra of the samples on quartz. The confocal microscopy method was used to determine the distribution of the silane molecules on the polymer layers and also to depth profile the laminates. The parameters used were a resolution of 1 cm^{-1} , a magnification of 100 and a spatial resolution of $1 \times 1 \times 2\ \mu\text{m}^3$. The microprobe method was used to obtain spectra from the pure PVC and pure silane films on quartz and also to look at the surfaces of the laminates. The parameters used for the microprobe method were a resolution of 4 cm^{-1} and a magnification of 50.

A Mattson Polaris FTIR spectrometer, with a resolution of 4 cm^{-1} , zero-filling, 98% iris, a signal gain of 4, triangular apodisation and 1024 scans, was used to obtain infrared spectra of the samples on silicon ATR prisms. Any FTIR transmission measurements used the same parameters but a signal gain of 1 and 25% iris.

6.2. Results and Discussion.

6.2.1. Raman Spectroscopy Results.

The Raman spectrum, ($400\text{ to }4000\text{ cm}^{-1}$), of a cast PVC film, deposited from a 5% w/w solution in DMF, onto a quartz slide is shown in figure.6.1.

The Raman spectrum, ($600\text{ to }3400\text{ cm}^{-1}$), of a cast A1891 film, deposited from a 20% w/w solution in a 2-propanol/water solvent mixture, onto a quartz slide is shown in figure.6.2.

The Raman spectrum, ($400\text{ to }4000\text{ cm}^{-1}$), of a cast A1100 film, deposited from a 20% w/w solution in a 2-propanol/water solvent mixture, onto a quartz slide is shown in figure.6.3.

Figure.6.1. Raman Spectrum of Pure PVC Film on Quartz.

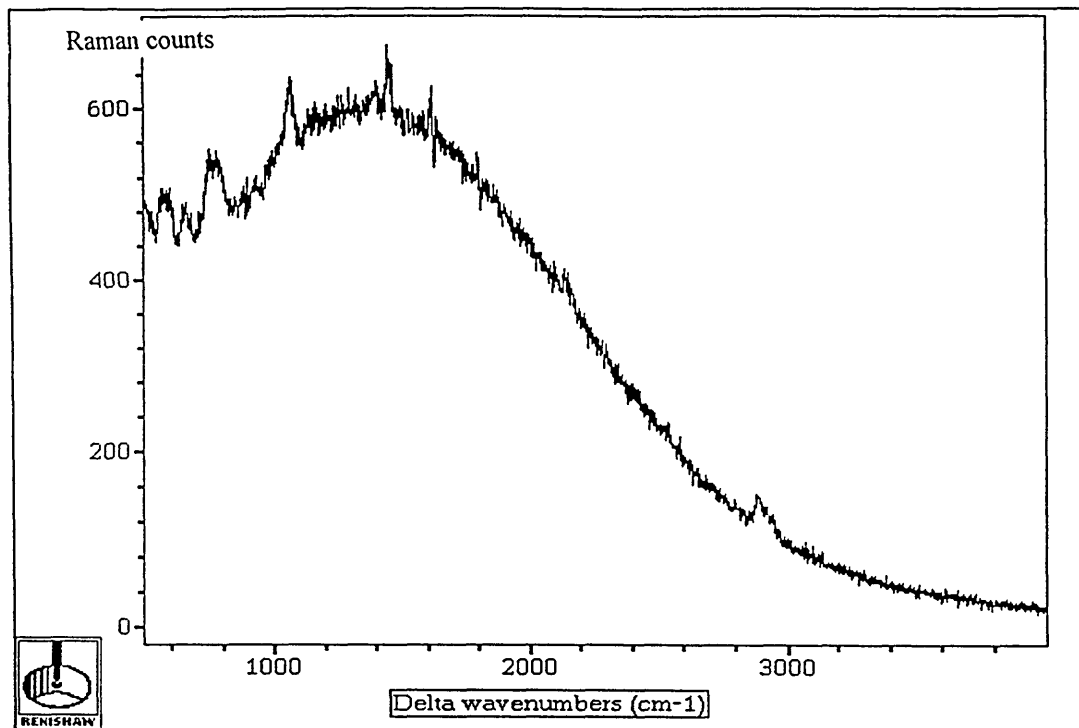


Figure.6.2. Raman Spectrum of Pure A1891 Film on Quartz.

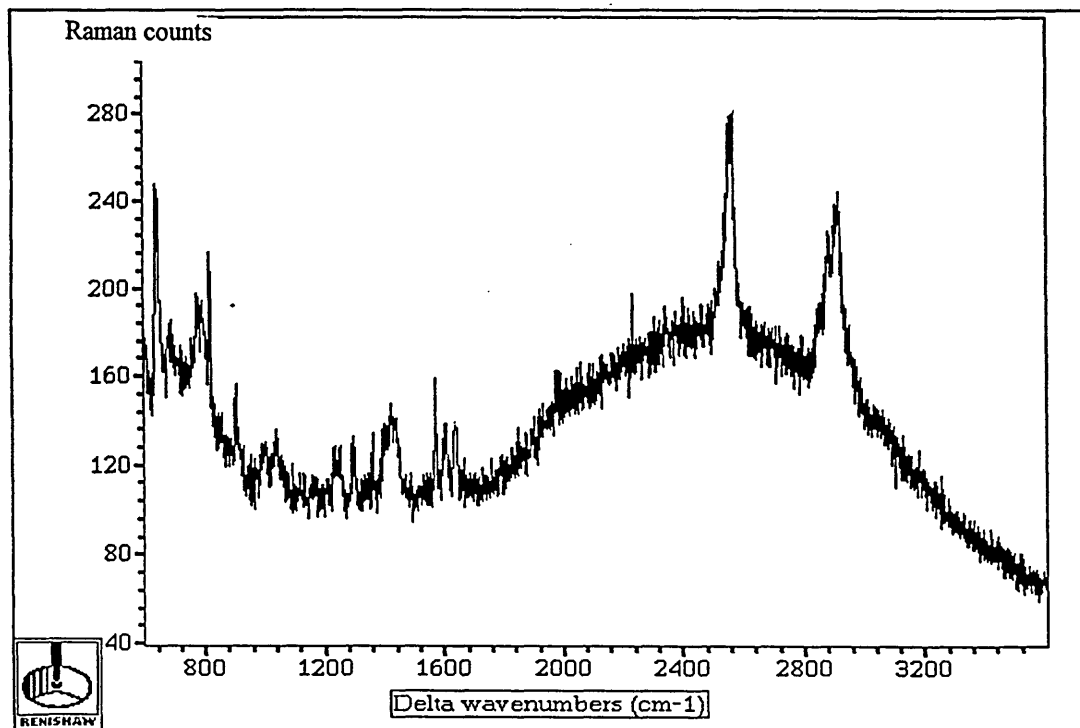
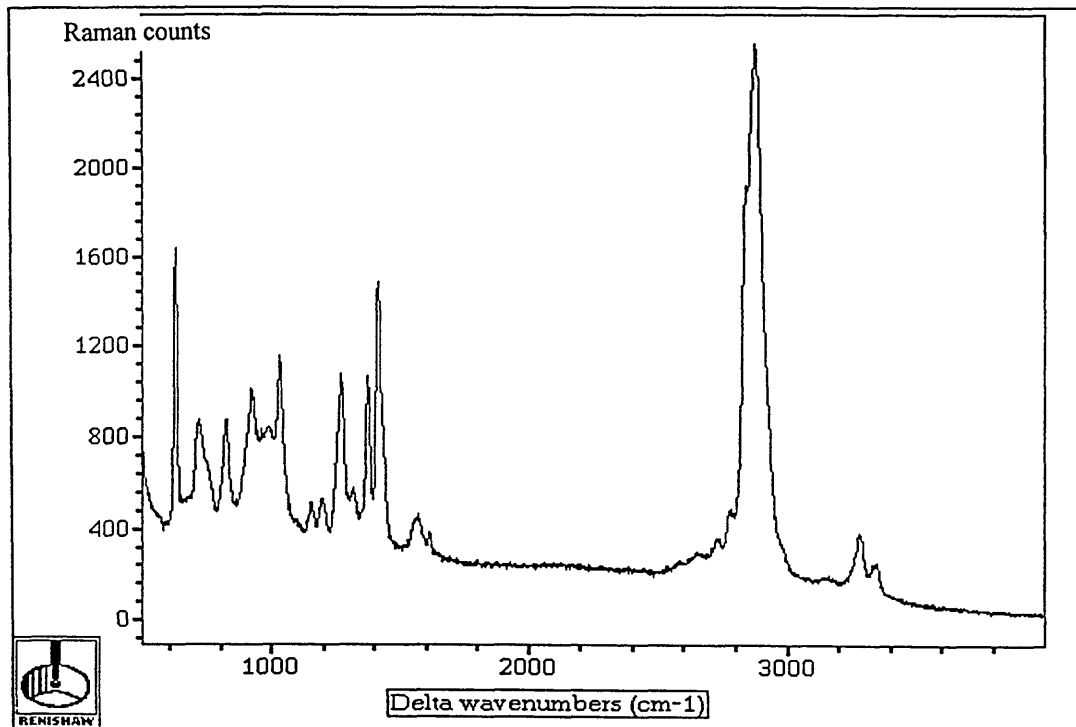


Figure.6.3. Raman Spectrum of Pure A1100 Film on Quartz.



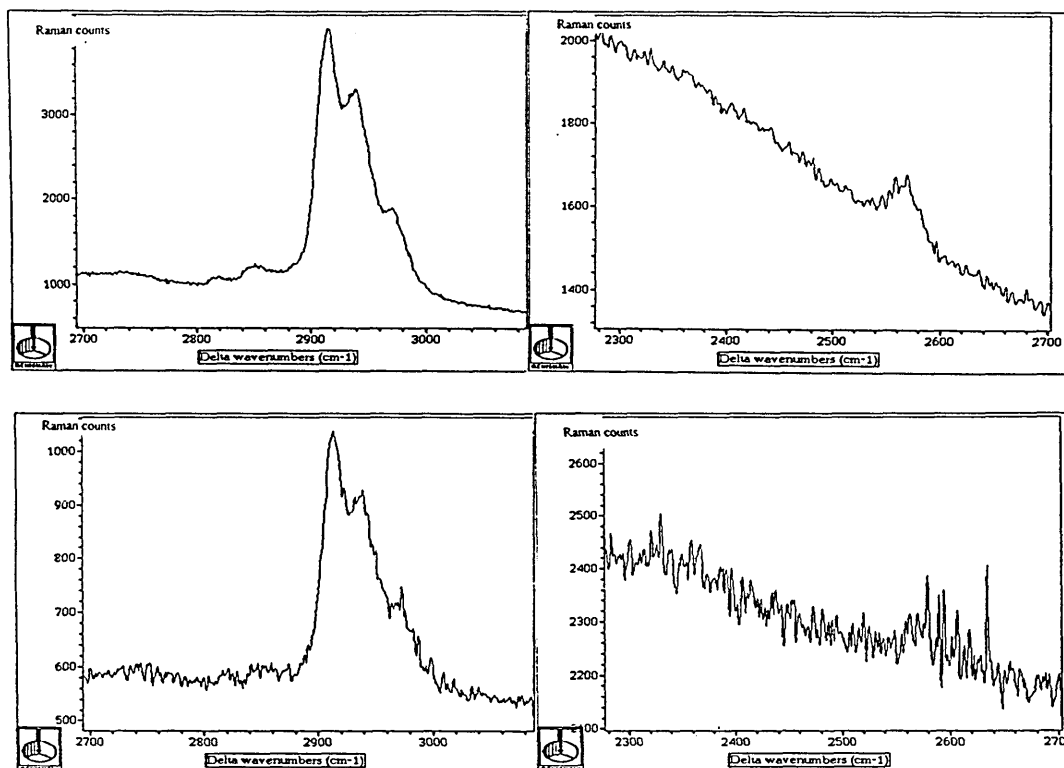
The important features in the spectrum, shown in figure.6.2, are the bands due to the $\nu(\text{SH})$ stretching vibration, at approximately 2550 cm^{-1} and the bands due to the $\nu(\text{CH}_2)$ and $\nu(\text{CH}_3)$ stretching vibrations at approximately 2900 cm^{-1} . It can be seen from figure.6.1. that there are no bands, due to PVC, in the region where the $\nu(\text{SH})$ stretching vibration occurs.

The important features in the spectrum, shown in figure.6.3, are the bands due to the $\nu(\text{NH}_2)$ stretching vibrations, which occur at approximately 3300 cm^{-1} and the bands due to the $\nu(\text{CH}_2)$ and $\nu(\text{CH}_3)$ stretching vibrations at approximately 2900 cm^{-1} . No bands at approximately 3300 cm^{-1} are observable in the pure PVC spectrum, (figure.6.1).

Therefore, when determining the presence of either silane in the samples, the band due to the $\nu(\text{SH})$ stretching vibration, (for A1891), and those due to the $\nu(\text{NH}_2)$ stretching vibrations, (for A1100), were monitored.

A laminate, comprising a quartz substrate, coated with a cast film of A1891, (from a 20% w/w solution), and a PVC overlayer, (dipped from a 10% w/w solution), was investigated using confocal Raman microscopy. The resulting spectra are shown in figure.6.4(a). The thickness of the PVC film was measured by the Talysurf profiler and was 3.5 μm . The Talysurf trace is shown in figure.6.4(b).

Figure.6.4(a). Successive Raman Spectra of a Depth Profile through a Quartz/ Cast A1891/Dipped PVC Laminate in the CH_2 and SH stretching vibration regions.



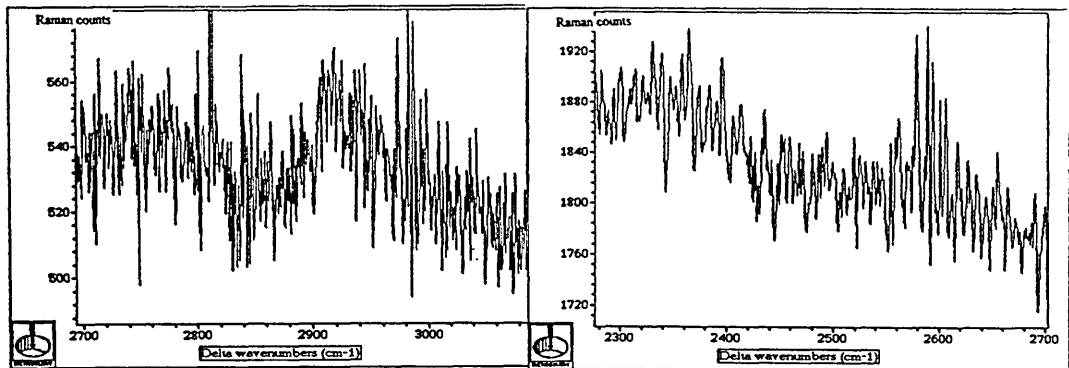
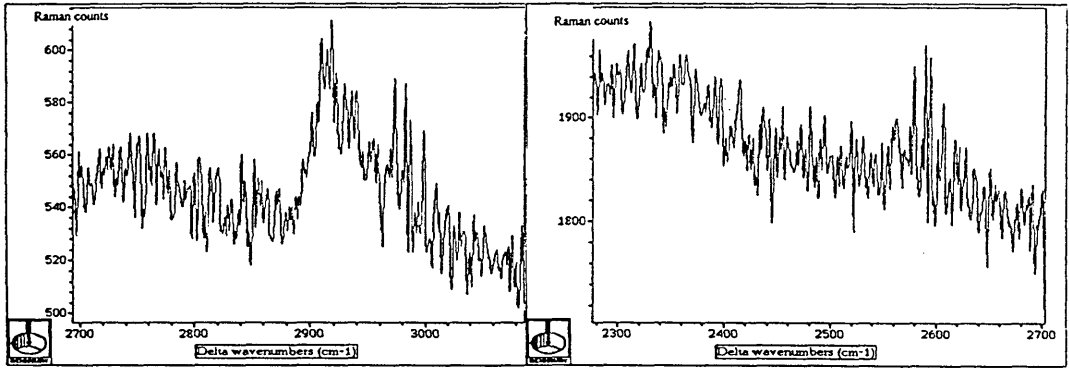
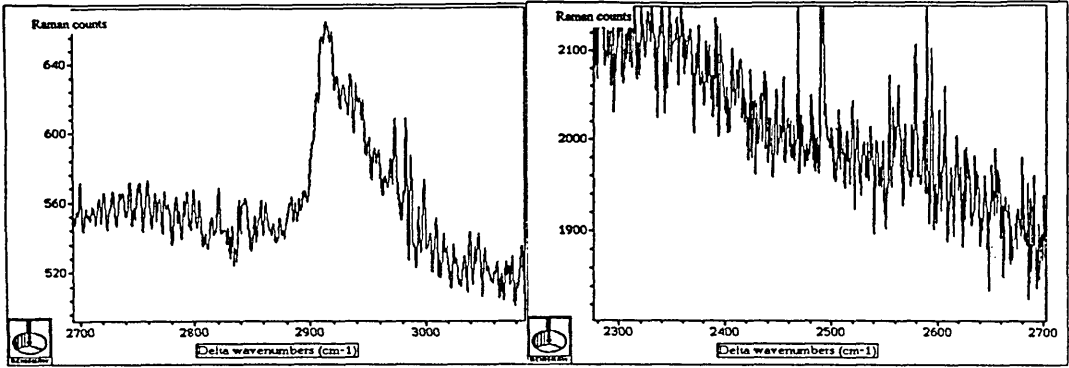
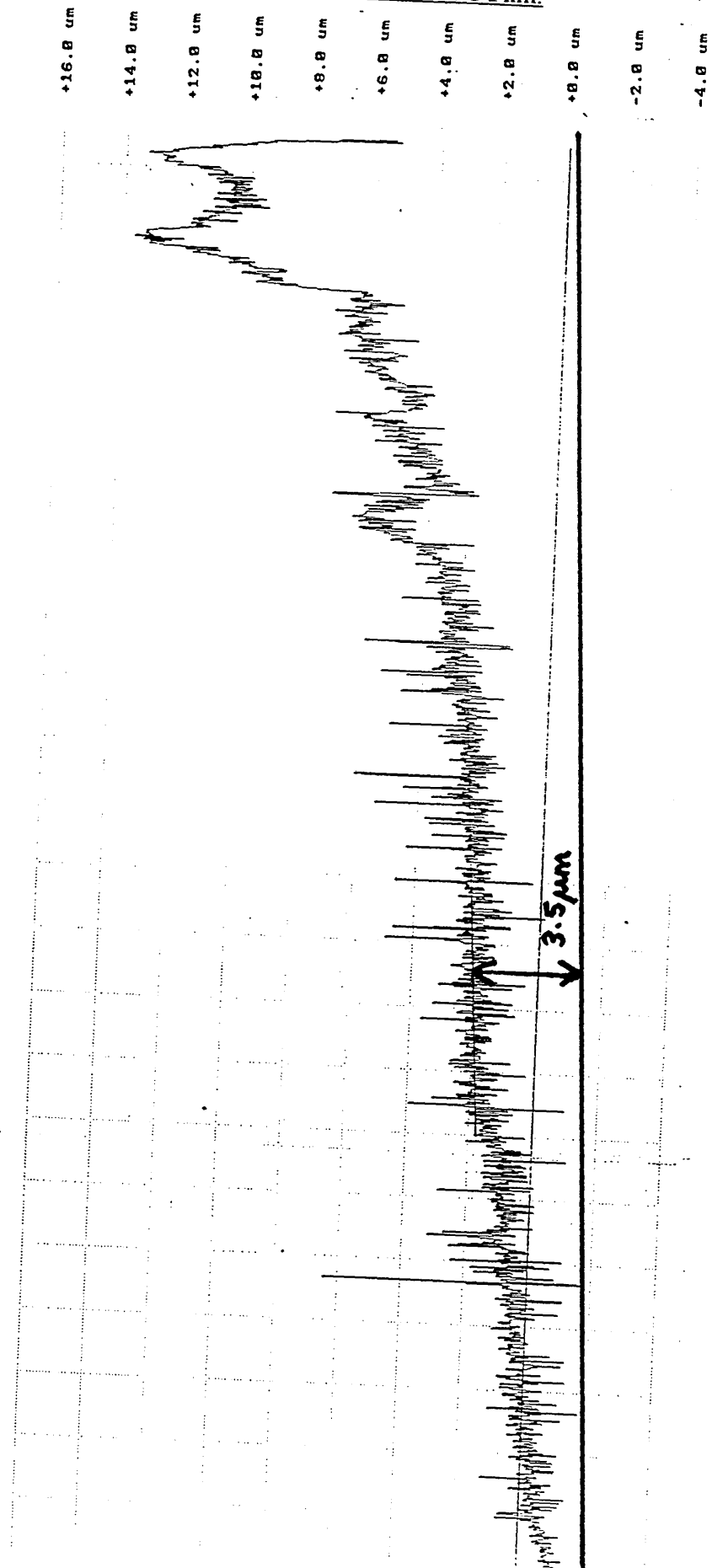


Figure.6.4(b). Talysurf Trace of PVC Film.



The spectra on the left hand side of the page, in figure.6.4, show the bands due to the $\nu(\text{CH}_2)$ stretching vibrations, (due to the PVC and the silane), and the spectra on the right hand side of the page show the bands due to the $\nu(\text{SH})$ stretching vibrations of the silane. The first pair of spectra were produced by focusing the laser onto the surface of the PVC with a resolution of approximately 4 cm^{-1} and scanning for 2 minutes. The second pair of spectra were produced by focusing the laser onto the surface of the PVC in confocal mode, (resolution of approximately $1 \times 1 \times 2 \text{ }\mu\text{m}^3$). The resolution depends on the set-up of the instrument and on the sample being depth profiled (see theory chapter). The following pairs of spectra were produced by moving the microscope down through the laminate in $1 \text{ }\mu\text{m}$ steps. The confocal spectra on the left hand side were obtained by scanning for 5 minutes, those on the right hand side were obtained by scanning for 30 minutes.

The band, due to the $\nu(\text{SH})$ stretching vibration can be seen in the first confocal spectrum, where the laser was focused onto the PVC surface. Considering the depth resolution of the experiment, ($2 \text{ }\mu\text{m}$), and the thickness of the PVC film, ($3.5 \text{ }\mu\text{m}$), it is clear that the mercaptosilane has diffused into the polymer.

The PVC film was then peeled away from the sample and both sides of the film were investigated in the microprobe mode. Figure.6.5. shows the Raman spectrum, (2320 to 2760 cm^{-1}), of the side of the PVC which was in contact with the silane in the laminate. Figure.6.6. shows the Raman spectrum, (2320 to 2760 cm^{-1}), of the top surface of the 'peeled' PVC film.

The band due to the $\nu(\text{SH})$ stretching vibration is observable in both figures.6.5 and 6.6. The silane has been shown to have diffused into the polymer overlayer.

Figure.6.5. Raman Spectrum of Dipped PVC Film, Bottom Surface.

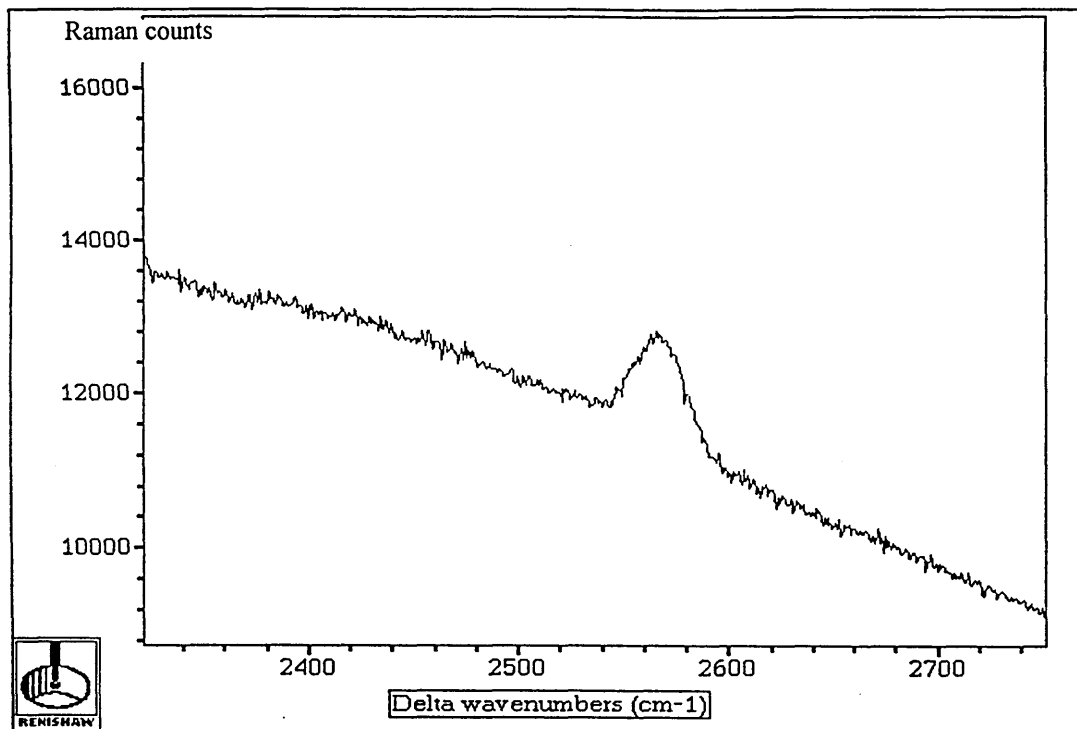
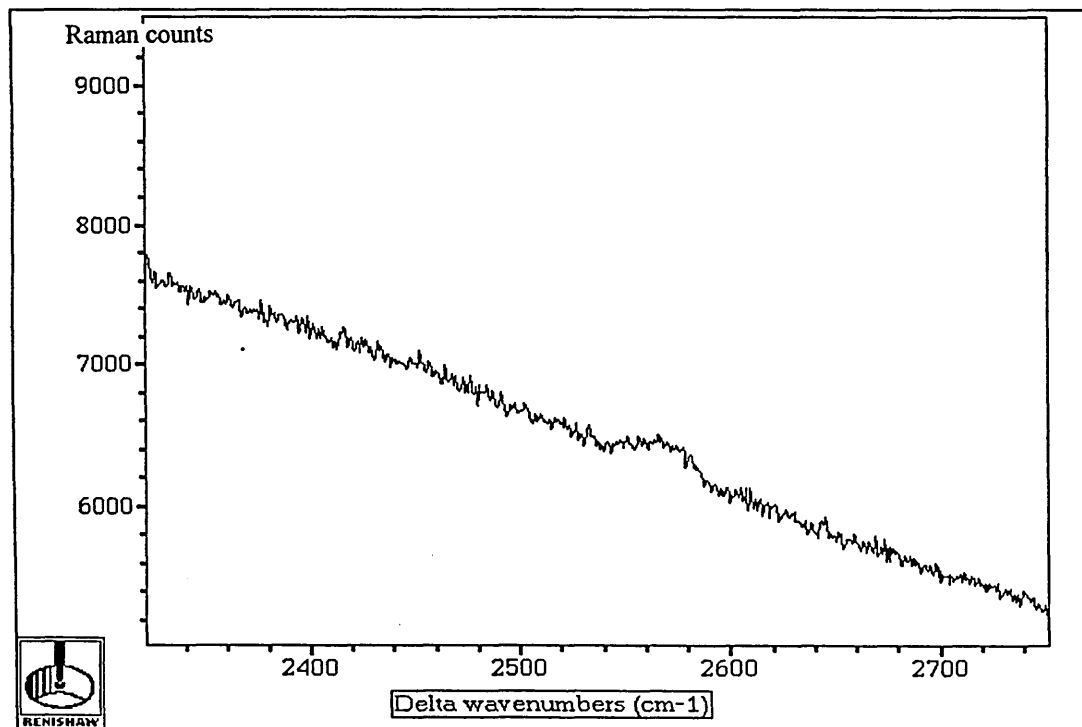


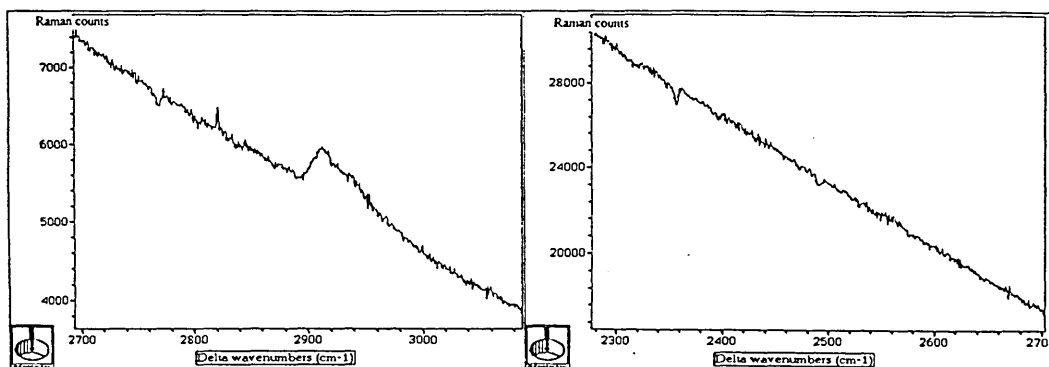
Figure.6.6. Raman Spectrum of Dipped PVC Film, Top Surface.

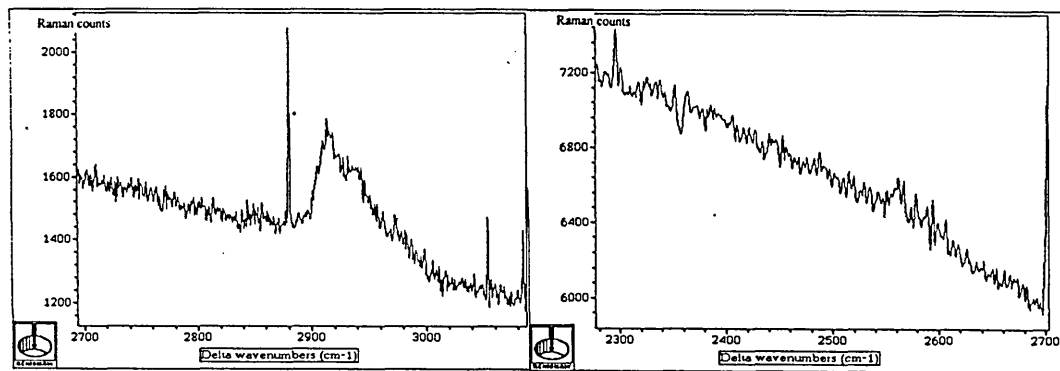
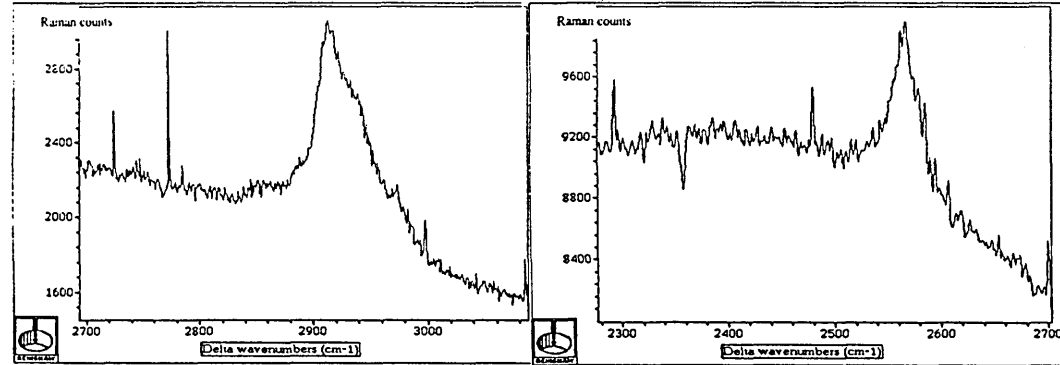
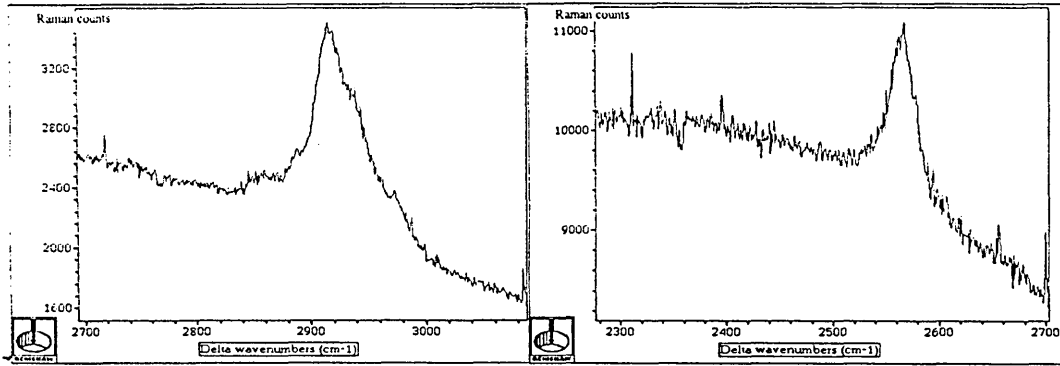
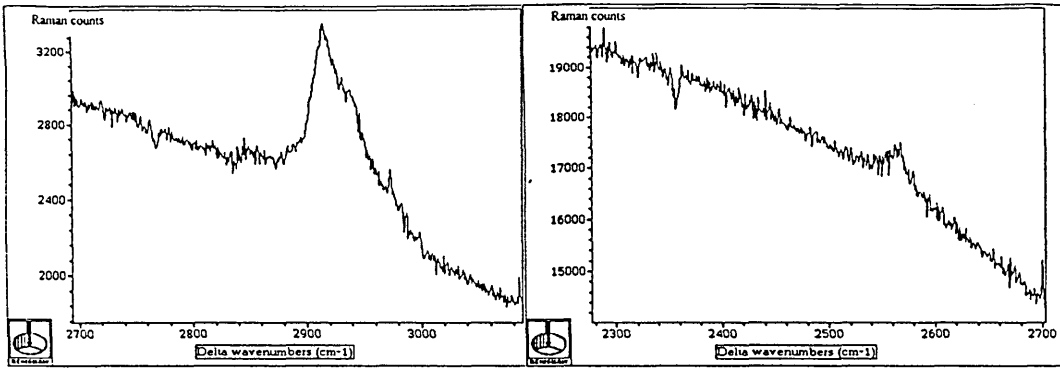


The effect of casting the polymer film as opposed to dipping the film over the silane layer was then investigated as follows:

A laminate consisting of a quartz slide, coated with a cast A1891 film, (from a 20% w/w solution), and a PVC overlayer, (cast from a 10% w/w solution), was investigated using the confocal Raman mode. The resulting spectra are shown in figure.6.7. The spectra on the left hand side show the bands due to the $\nu(\text{CH}_2)$ and $\nu(\text{CH}_3)$ stretching vibrations, (of the silane and the PVC), and the spectra on the right hand side show the band due to the $\nu(\text{SH})$ stretching vibration, of the silane. The thickness of the PVC was measured by the Talysurf profiler and was 4 μm . The first pair of spectra were produced by focusing the laser onto the PVC surface with a resolution of approximately 4 cm^{-1} and scanning for 2 minutes. The next pair of spectra were produced by focusing the laser onto the PVC surface in confocal mode. The following pairs of spectra were produced by moving the microscope down through the laminate in 1 μm steps, (confocal). The spectra on the left hand side were obtained by scanning for 20 minutes, and those on the right hand side were obtained by scanning for 1 hour.

Figure.6.7. Successive Raman Spectra of a depth profile through a Quartz/Cast A1891/Cast PVC Laminate in the CH_2 and SH stretching vibration regions.





A band due to the $\nu(\text{SH})$ stretching vibration of the silane is observable in the first confocal spectrum. Therefore, considering the depth resolution of the experiment, ($2\ \mu\text{m}$), and the thickness of the PVC film, ($4\ \mu\text{m}$), it was shown that the silane has diffused into the polymer.

The PVC film was then peeled away from the laminate and both sides were investigated, using the microprobe mode. Figure.6.8. shows the Raman spectrum, (2350 to $2750\ \text{cm}^{-1}$), of the side of the PVC film which was in contact with the silane in the laminate. Figure.6.9. shows the Raman spectrum, (2350 to $2750\ \text{cm}^{-1}$), of the top surface of the PVC film.

The band due to the $\nu(\text{SH})$ stretching vibration of the silane is observable in the spectra in both figures.6.8. and 6.9. Therefore, the silane has diffused into the polymer.

Figure.6.8. Raman Spectrum of Cast PVC Film, Bottom Surface.

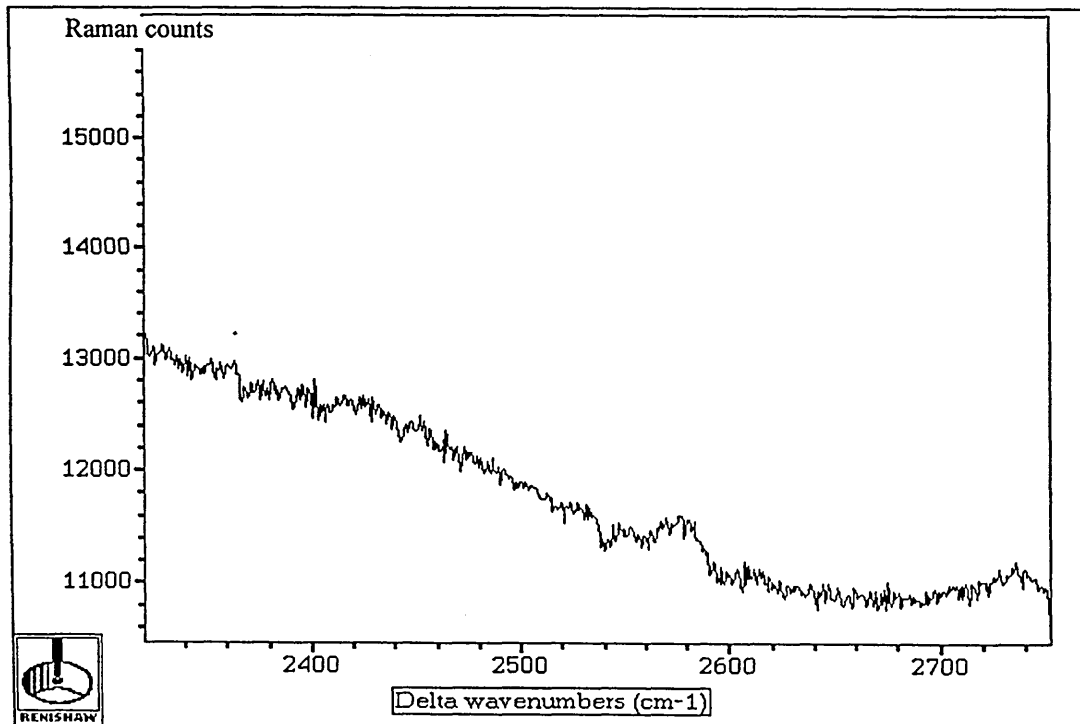
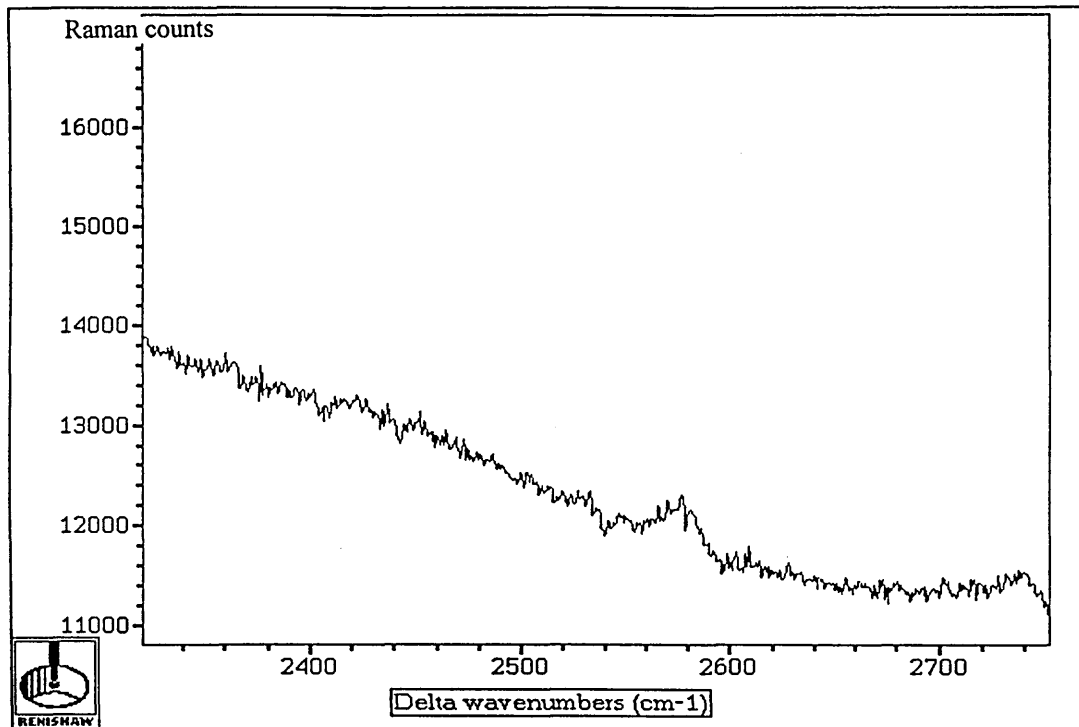


Figure.6.9. Raman Spectrum of Cast PVC Film, Top Surface.



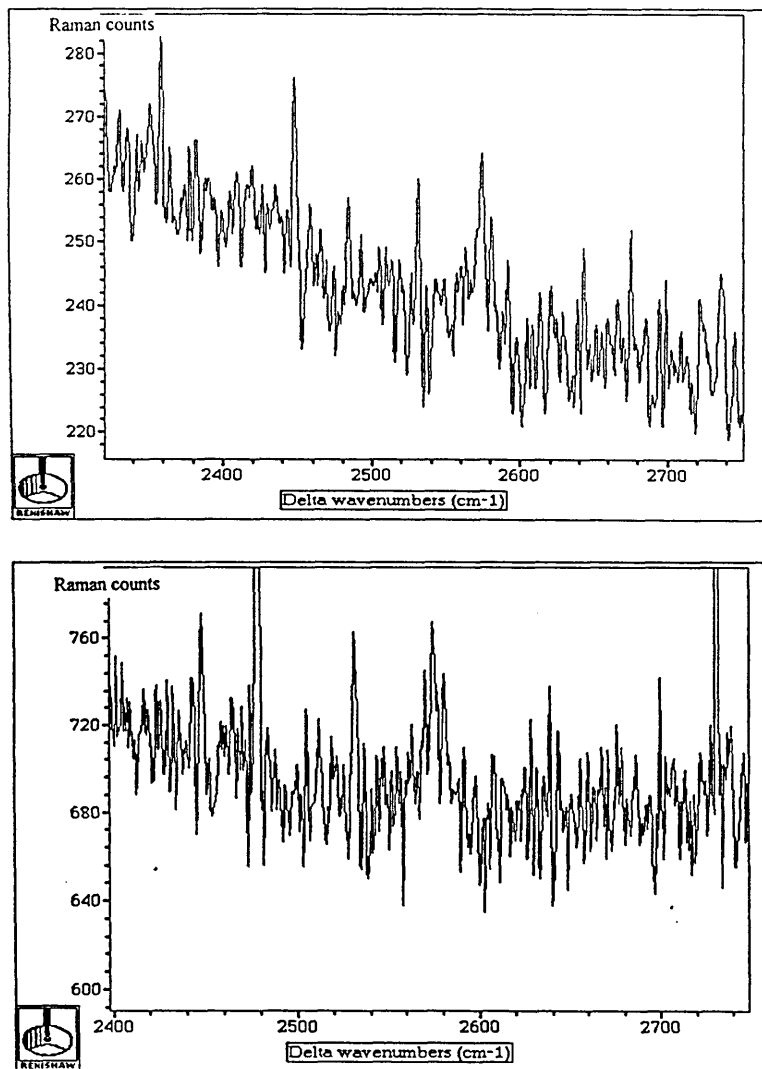
Because the depth resolution of the experiment was 2 μm , a polymer film thicker than 4 μm was considered more suitable for the confocal experiment, than a film of thickness equal to or less than 4 μm . Therefore, a thicker PVC film was deposited over the silane film. Uniform films are necessary for successful confocal experiments. However, there was a problem in producing uniform films of the required thickness. Therefore, the thickest uniform PVC film that could be deposited over the silane was 8 μm .

A laminate consisting of a quartz slide, coated with a cast A1891 film, (from a 20% w/w solution), and a cast PVC overlayer, (from a 10% w/w solution), was investigated using the confocal Raman mode. The resulting spectra are shown in figure.6.10(a).

The thickness of the PVC was measured using the Talysurf profiler and was 8 μm , (see figure.6.10(b)). The spectra show the band due to the $\nu(\text{SH})$ stretching

vibration of the silane. The first spectrum was obtained by focusing the laser onto the PVC in confocal mode and scanning for 10 minutes. The following spectra were obtained by moving the microscope down through the laminate in 2 μm steps, and scanning for 30 minutes.

Figure.6.10(a). Raman Spectra of Quartz/Cast A1891/Cast PVC Laminate.



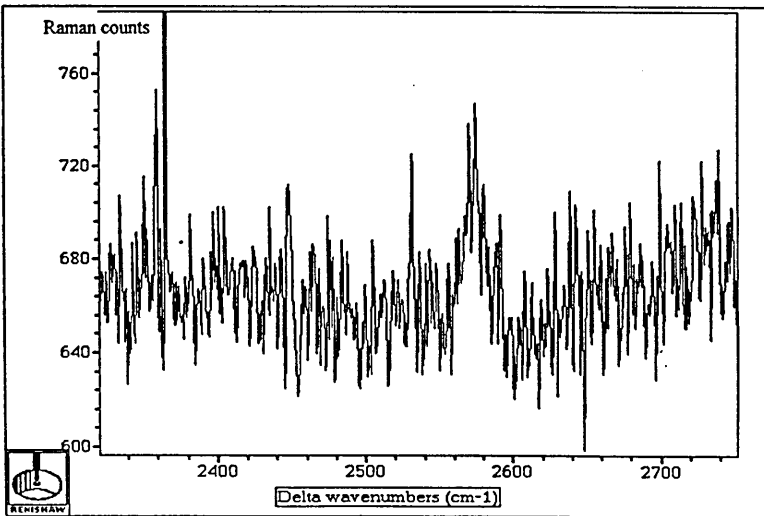
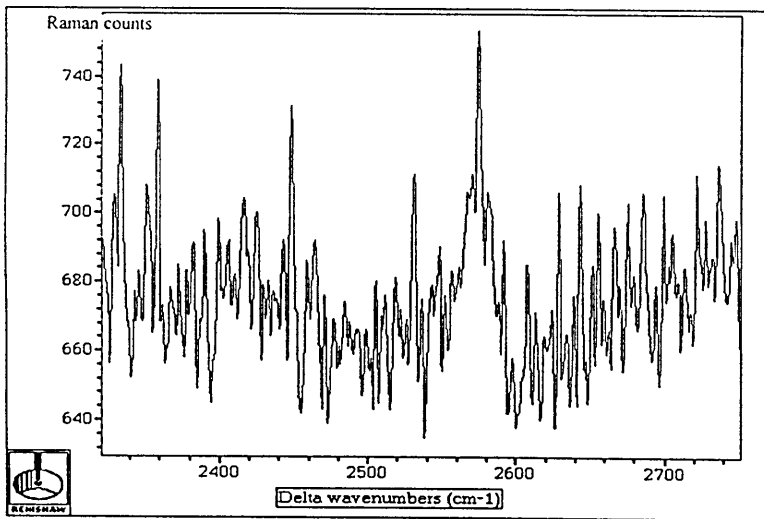
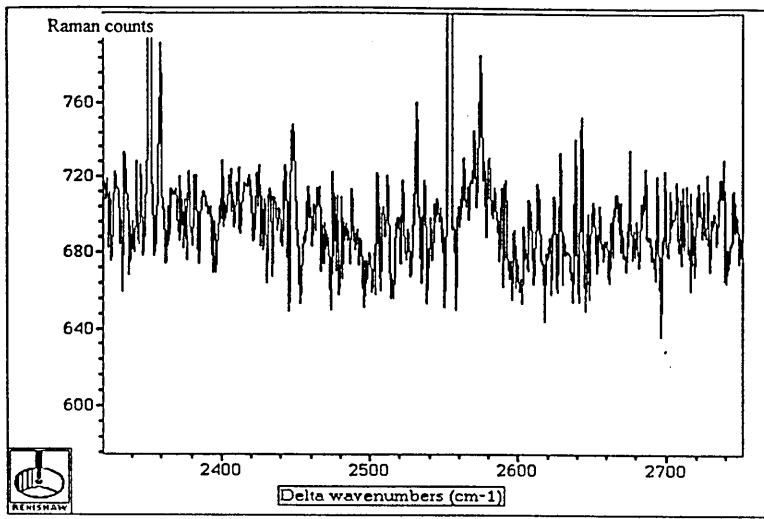
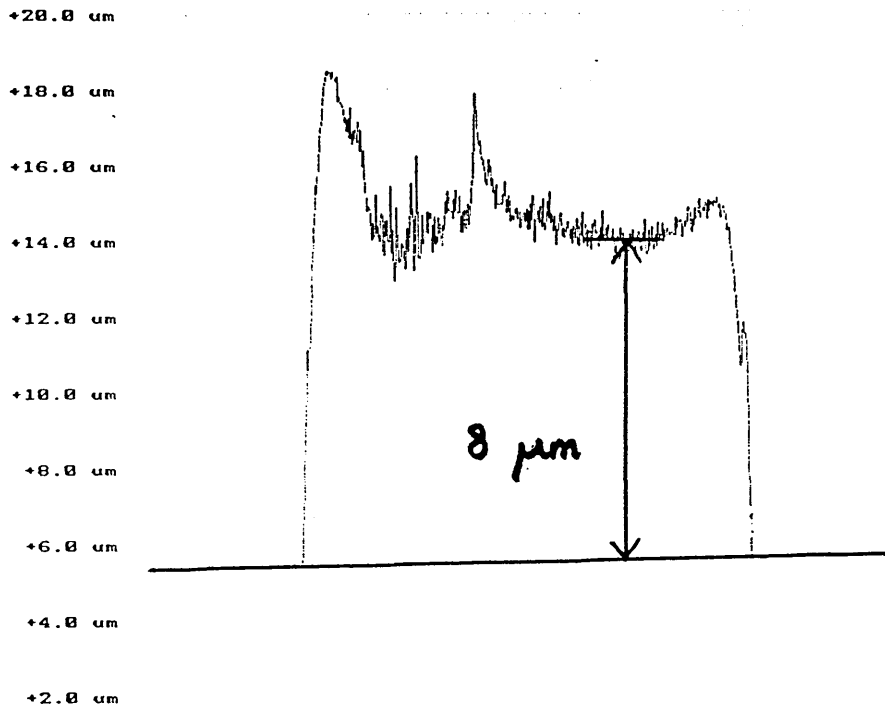


Figure.6.10(b). Talysurf Trace of PVC Film.



The band due to the $\nu(\text{SH})$ stretching vibration can be seen in all the confocal spectra. Therefore, the silane has diffused through the polymer. Further evidence of the mercaptosilane diffusion is given by the spectra of the PVC after it has been peeled away from the laminate. The microprobe mode was used to obtain spectra of both sides of the peeled PVC film. Figure.6.11. shows the Raman spectrum, (2350 to 2750 cm^{-1}), of the side of the PVC which was in contact with the silane, in the laminate. Figure.6.12. shows the Raman spectrum, (2350 to 2750 cm^{-1}), of the top surface of the peeled PVC film.

Figure.6.11. Raman Spectrum of Cast PVC, Bottom Surface.

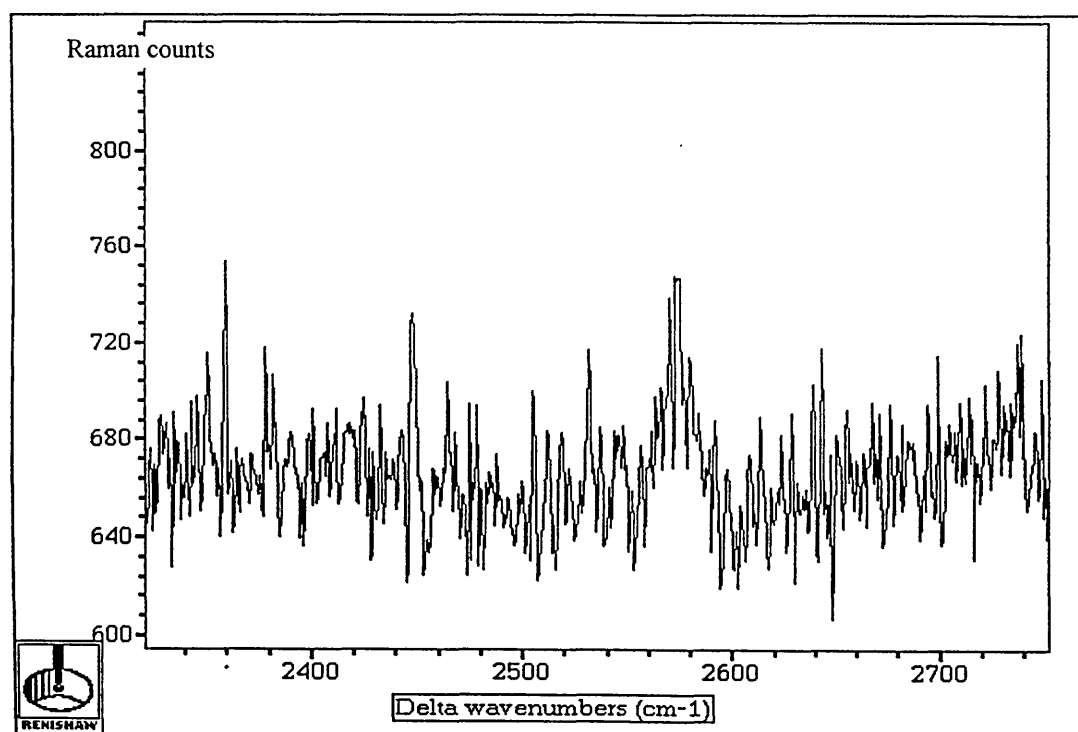
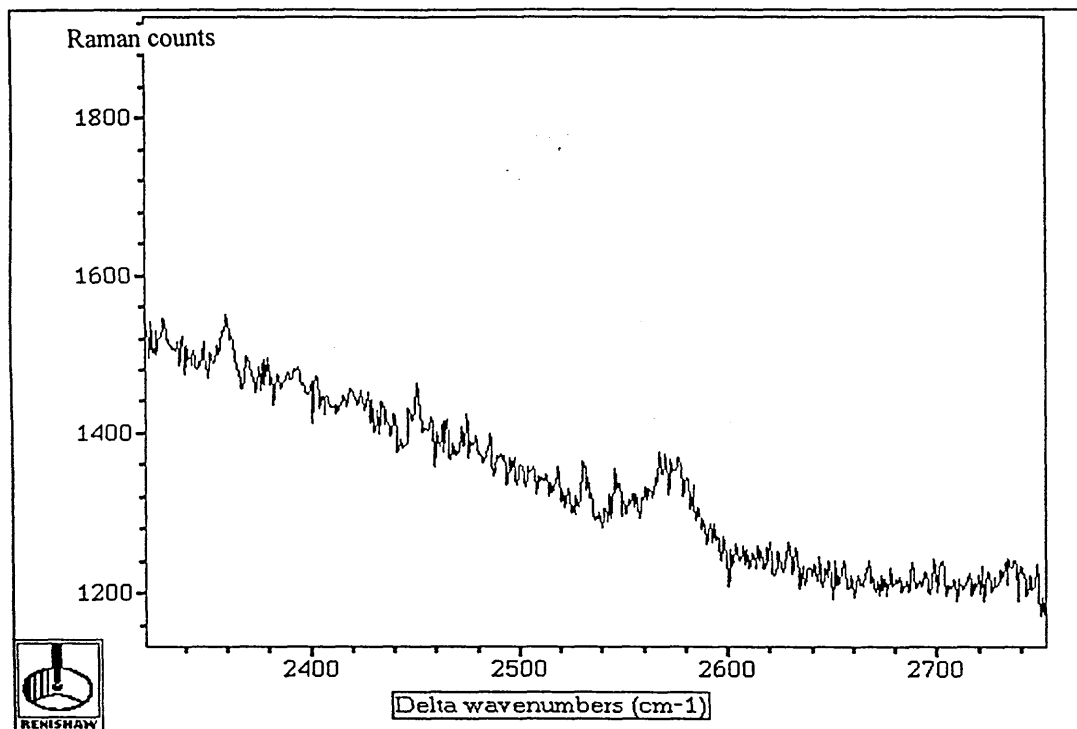


Figure.6.12. Raman Spectrum of Cast PVC, Top Surface.

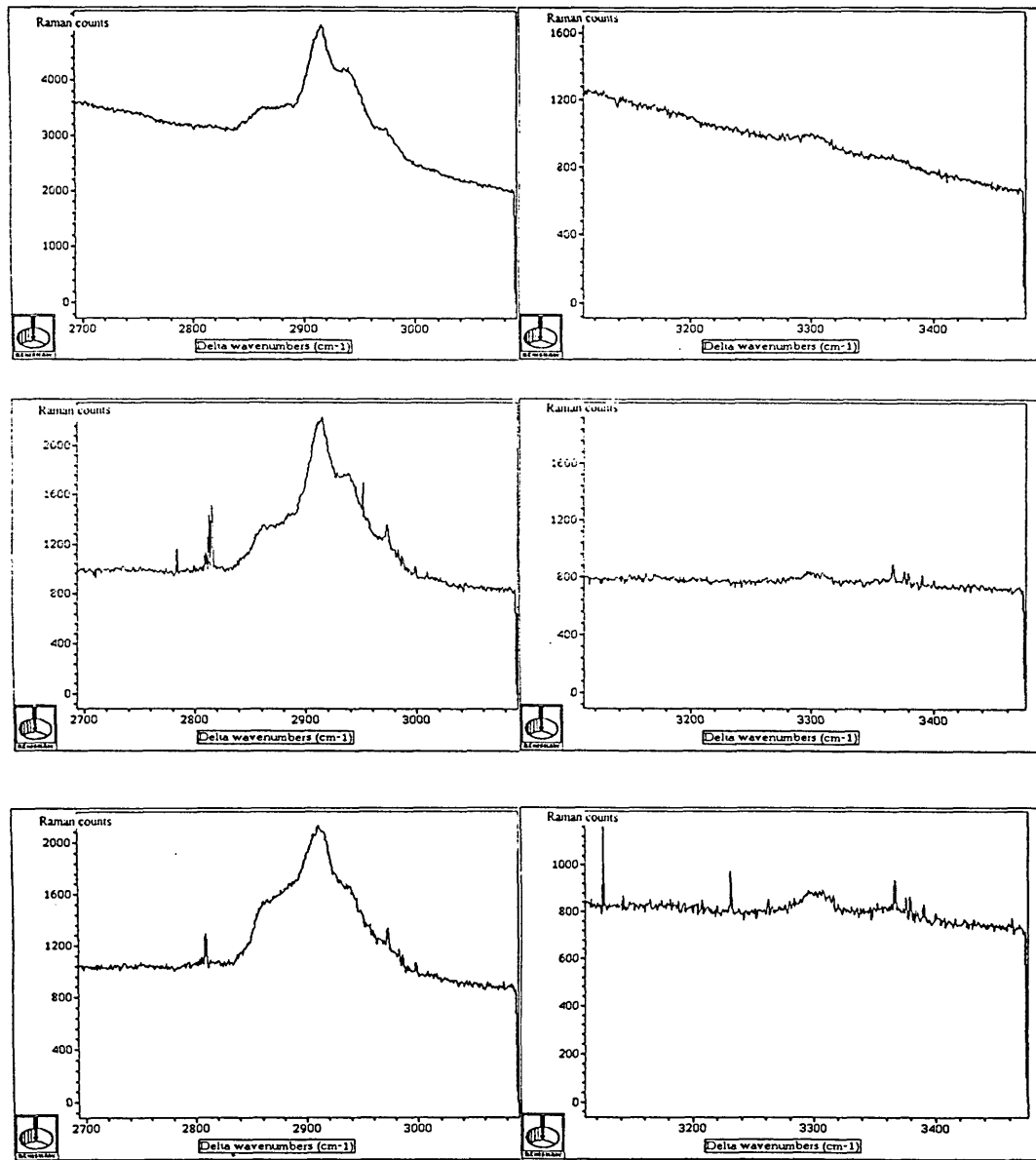


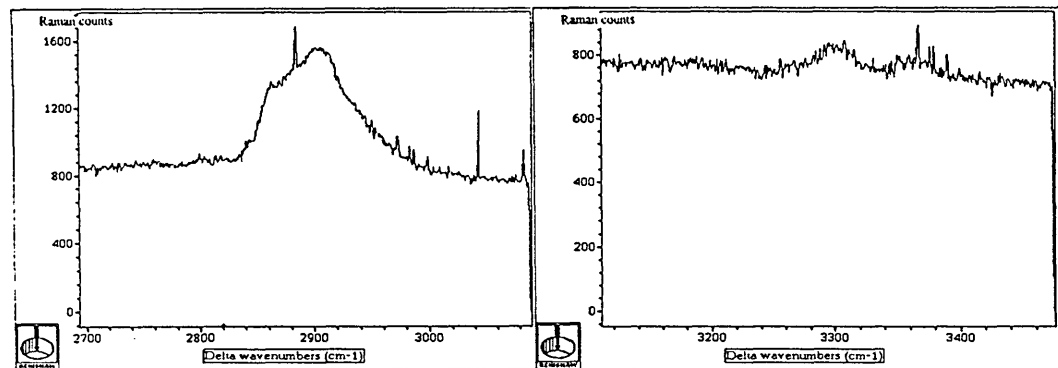
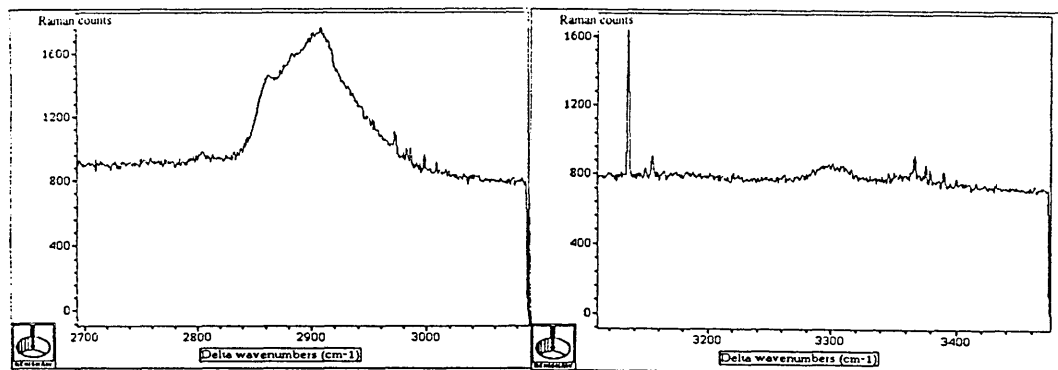
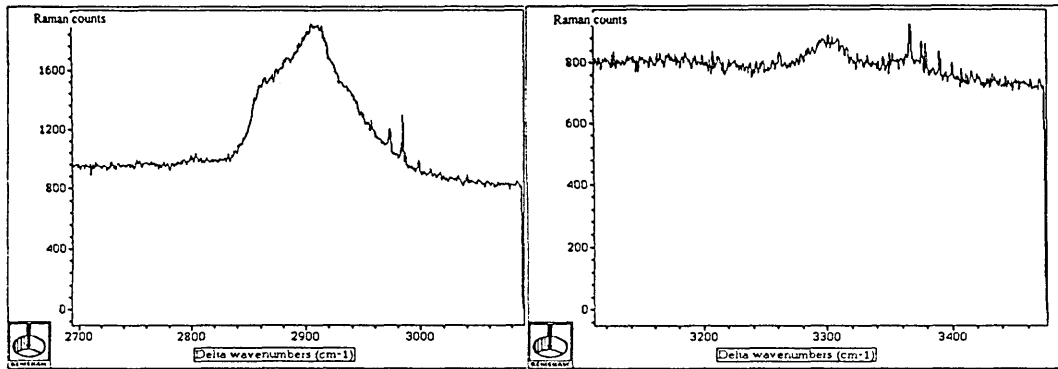
The band due to the $\nu(\text{SH})$ stretching vibration is observable in both figures.6.11. and 6.12. Therefore, it was shown that the A1891 has diffused through the PVC film.

Similar laminates were prepared using A1100 as the coupling agent, to determine whether this silane would also diffuse into the polymer, as follows:

A laminate, consisting of a quartz slide, coated with a cast A1100 film, (from a 20% w/w solution), and a PVC overlayer, (dipped from a 10% w/w solution), was investigated using the confocal Raman mode. The resulting spectra are shown in figure.6.13.

Figure.6.13. Raman Spectra of Quartz/Cast A1100/Dipped PVC Laminate.





The thickness of the PVC film was measured using the Talysurf profiler and was 2.5 μm .

The spectra on the left hand side of figure.6.13. show the bands due to the $\nu(\text{CH}_3)$ and $\nu(\text{CH}_2)$ stretching vibrations, (of the PVC and the aminosilane), and the spectra on the right hand side show the bands due to the $\nu(\text{NH}_2)$ stretching vibrations of the silane. The top pair of spectra were obtained by focusing the laser onto the PVC surface in the microprobe mode and scanning for 2 minutes. The second pair of spectra were obtained by focusing the laser onto the PVC surface in confocal mode. The following pairs of spectra were obtained by moving the laser beam down through the laminate in 2 μm steps. All the confocal spectra were obtained by scanning for 10 minutes.

Bands due to the $\nu(\text{NH}_2)$ stretching vibrations can be seen in the first confocal spectrum. Unfortunately because the depth resolution of the experiment was 2 μm , and the PVC thickness was only 2.5 μm , it cannot be definitely stated that the A1100 has diffused into the PVC. Unfortunately the PVC film was very difficult to remove from the laminate and so spectra of the peeled film were not obtained.

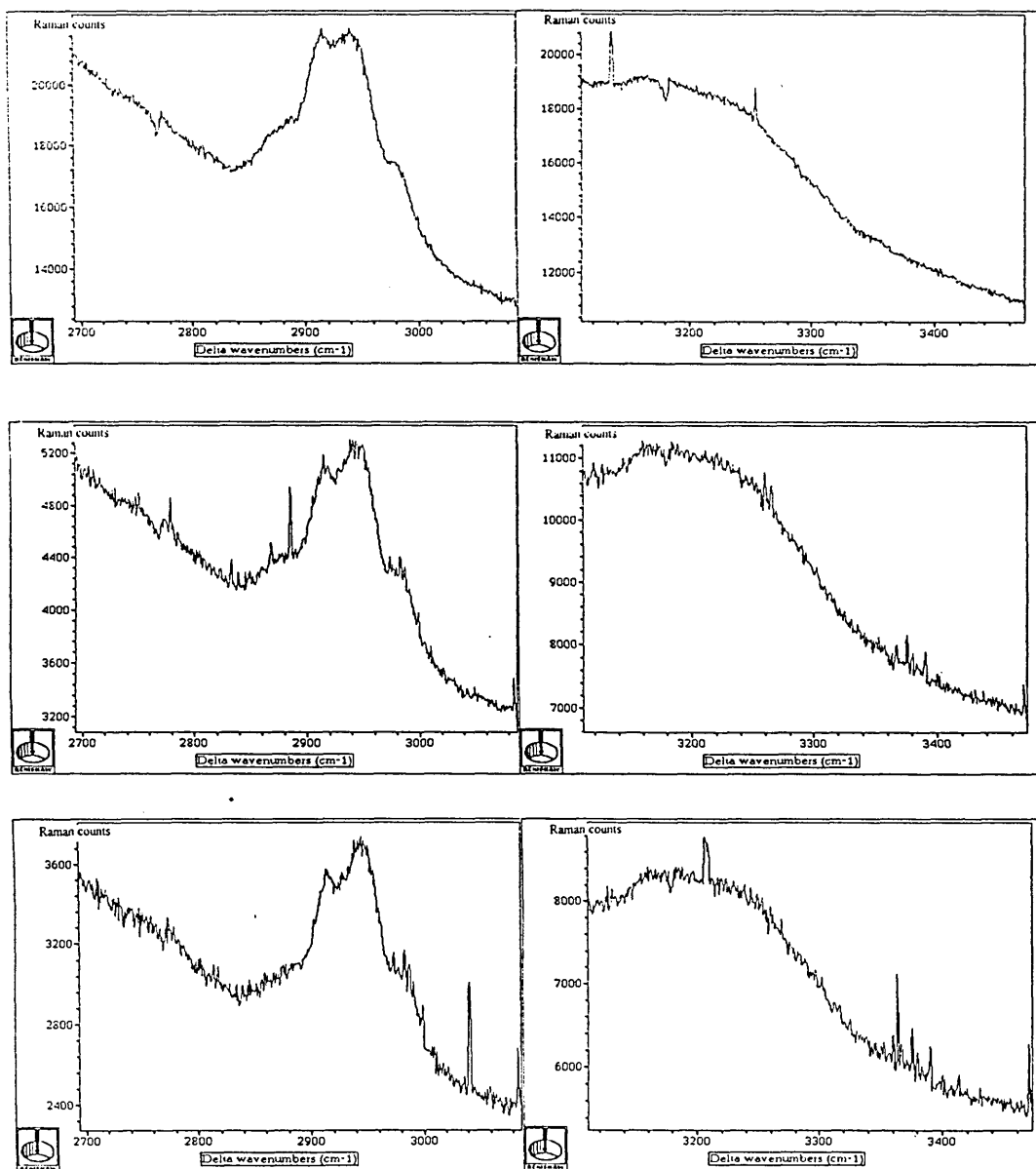
The effect of casting the polymer film as opposed to dipping it onto the silane layer was investigated as follows:

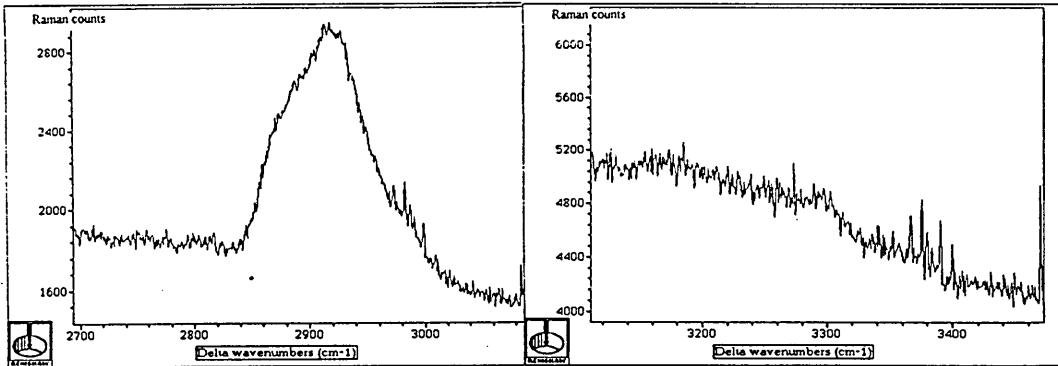
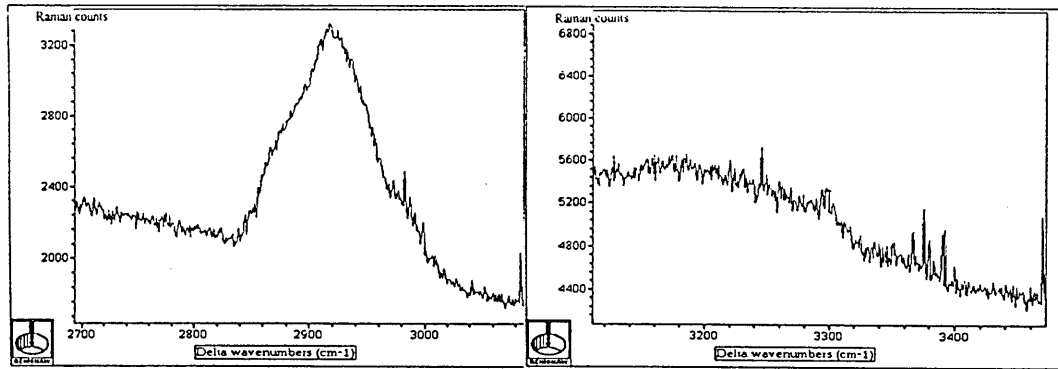
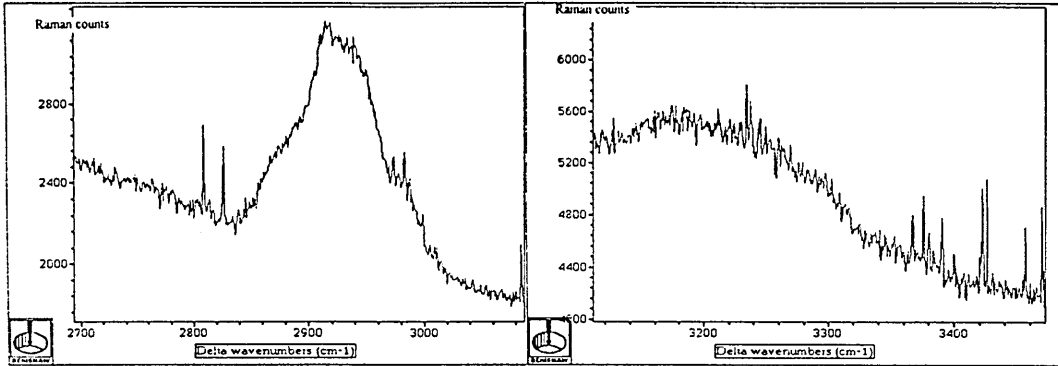
A laminate, consisting of a quartz slide, coated with a cast A1100 film, (from a 20% w/w solution), with a PVC overlayer, (cast from a 1% w/w solution), was analysed using Raman confocal microscopy. The resulting spectra are shown in figure.6.14. The thickness of the PVC layer was determined by the Talysurf profiler and was 3 μm .

The spectra on the left hand side of figure.6.14. show the bands due to the $\nu(\text{CH}_3)$ and $\nu(\text{CH}_2)$ stretching vibrations, (of the PVC and the aminosilane), and the spectra on the right hand side show the bands due to the $\nu(\text{NH}_2)$ stretching vibrations of the silane. The first pair of spectra were produced by focusing the laser onto the PVC surface in microprobe mode and scanning for 5 minutes. The

second pair of spectra were obtained by focusing the laser onto the PVC surface in confocal mode. The following pairs of spectra were obtained by moving the microscope beam through the laminate in 2 μm steps. The confocal spectra on the left hand side were obtained by scanning for 20 minutes and those on the right hand side were obtained by scanning for 1 hour.

Figure.6.14. Raman Spectra of Quartz/Cast A1100/Cast PVC Laminate.





Bands due to the $\nu(\text{NH}_2)$ stretching vibrations of the silane can just be distinguished in the first confocal spectrum at about 3300 cm^{-1} . These bands are difficult to see due to the fluorescence in the spectrum. Again, it cannot be categorically said that the A1100 has diffused into the polymer. As for the dipped PVC film, the cast film in the quartz/A1100/PVC laminate could not be peeled away from the quartz. Therefore, no spectra of the distribution of this silane on the polymer were obtained.

One of the peeled PVC films was then mapped over a $5 \times 5 \mu\text{m}^2$ area, using the confocal method, to determine the distribution of the silane molecules on the PVC bottom surface.

Figure.6.15. Raman Confocal Mapping Spectra of Quartz/Cast A1891/Dipped PVC Laminate.

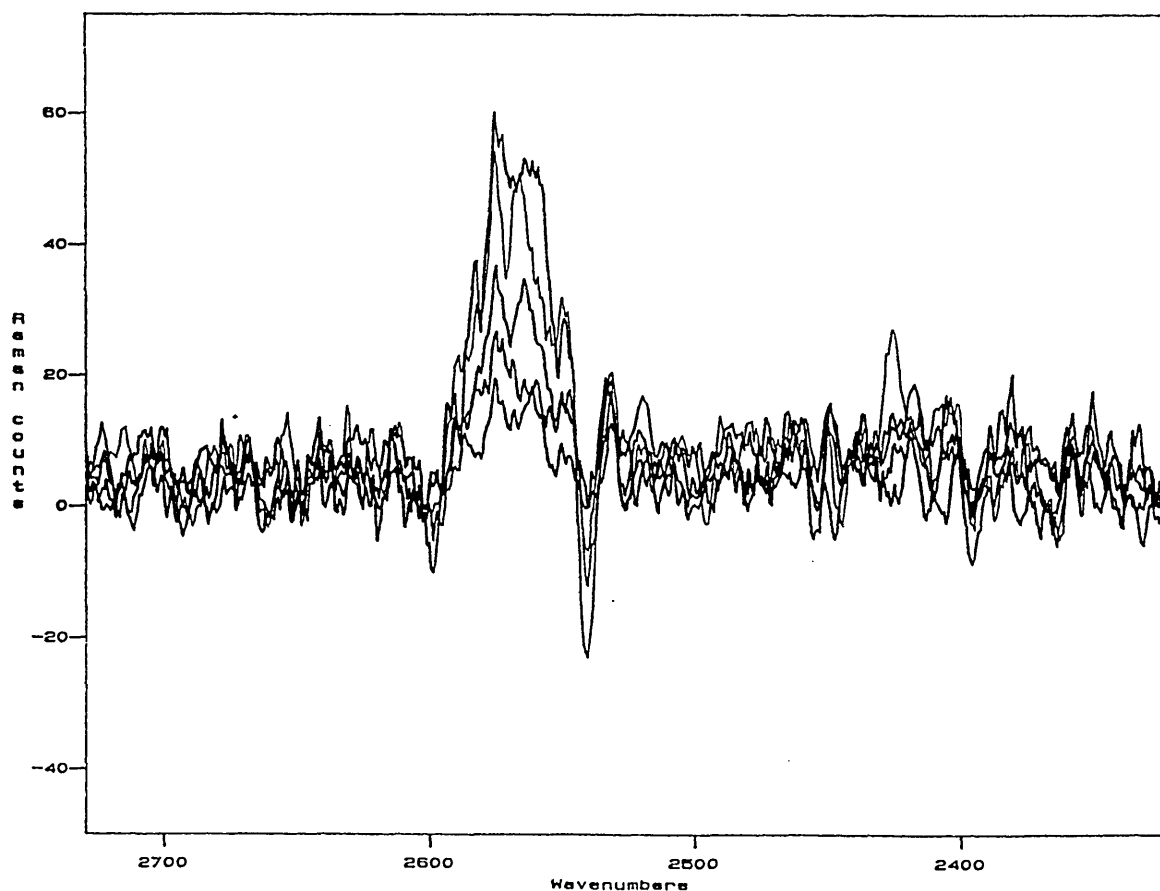


Figure.6.15. shows 5 spectra from a set of 25, obtained by scanning confocally over a $5 \times 5 \mu\text{m}^2$ area of the silane-side of the peeled film, (shown in figure.6.5). Each spectrum represents an area of $1 \times 1 \mu\text{m}^2$ and the scan times for each of these areas was 10 minutes. The band due to the $\nu(\text{SH})$ stretching vibration of A1891 can be seen in each spectrum. However, it can be seen that the intensity of this bands varies. Therefore there is not an even distribution of the silane molecules over the polymer film. This was also observed visually in the $1 \times 1 \text{ cm}^2$ film. Due to distortion of the peeled PVC film by the laser, it was not possible to obtain a map over a larger area of the film, which would have given more information on the distribution of the silane molecules.

For the quartz/silane/PVC laminates, analysed by Raman spectroscopy and microscopy, the formation of the PVC films depended on the nature of their preparation. Dipped films were seen to be 'wedge'-shaped while cast films were more uniform, (see figures 6.4(b) and 6.10(b)).

By studying the quartz/A1891/PVC laminates, it has been shown that the mercaptosilane diffused into polymer overlayers of 4 and 8 μms in thickness, after vacuum dessication and heat treatment. The silane appeared to diffuse into both the dipped and the cast PVC films. This is not surprising, since a molecule of this size, (10 Å), would be expected to diffuse into a polymer. The degree of this diffusion is interesting, since it appears that the silane has diffused all the way through both the 4 and 8 μm thick polymer layers. This may mean that there were gaps in the polymer network, possibly caused by solvent evaporation, which allowed the silane molecules to diffuse into the polymer film or simply that the silane molecules diffused through the polymer network. This effect has been observed by Koenig et al, [89], who observed the diffusion of A1110 into an epoxy resin to form an interpenetrating network.

It was necessary to obtain confocal spectra of a laminate which had a top, (PVC), layer greater than 4 μm . This was because at polymer thicknesses of less

than 4 μm , the spectra would have been collected at the depth resolution limit of the experiment and it could not have been necessarily deduced that diffusion had occurred. However, because spectra have been obtained that show that the mercaptosilane has diffused through 8 μm of PVC, the silane probably also diffused through the 4 μm PVC film. Further evidence of the diffusion of the mercaptosilane into the PVC was given from the spectra of the peeled PVC layers. Bands due to the mercaptosilane were observed in the spectra of both sides of the PVC. It also appeared both visibly and on a micron scale, (from a map of the peeled PVC film), that the distribution of A1891 over the quartz and PVC was non-uniform.

Unfortunately, due to problems with producing the required polymer thicknesses, fluorescence and removal of the PVC layers from the quartz/A1100/PVC laminates, it was not proven here that the aminosilane had diffused into the PVC. Because of work carried out by Koenig et al, [89], on similar systems it would be expected for the aminosilane, A1100, to diffuse through a polymer. Therefore, more work needs to be done on this system.

It was also observed that the A1100 formed smooth films while the A1891 formed 'globules' on the quartz substrates.

6.2.2. Infrared Spectroscopy Results.

The FTIR-ATR spectrum, (4000 to 1000 cm^{-1}), of a PVC film dipped onto a silicon prism from a 5% w/w solution in DMF, is shown in figure.6.16.

The transmission spectrum, (4000 to 500 cm^{-1}), of pure A1891 in a liquid cell, (KBr plates), is shown in figure.6.17. The transmission spectrum, (4000 to 500 cm^{-1}), of pure A1100 in a liquid cell is shown in figure.6.18.

The important infrared bands in figure.6.17. are those at approximately 2900 cm^{-1} , due to the $\nu(\text{CH}_3)$ and $\nu(\text{CH}_2)$ stretching vibrations and the band at 2550 cm^{-1} , due to the $\nu(\text{SH})$ stretching vibration. It can be seen from figure.6.16. that there are no bands in the PVC spectrum in the 2550 cm^{-1} region.

Figure.6.16. FTIR-ATR Spectrum of Pure PVC Film.

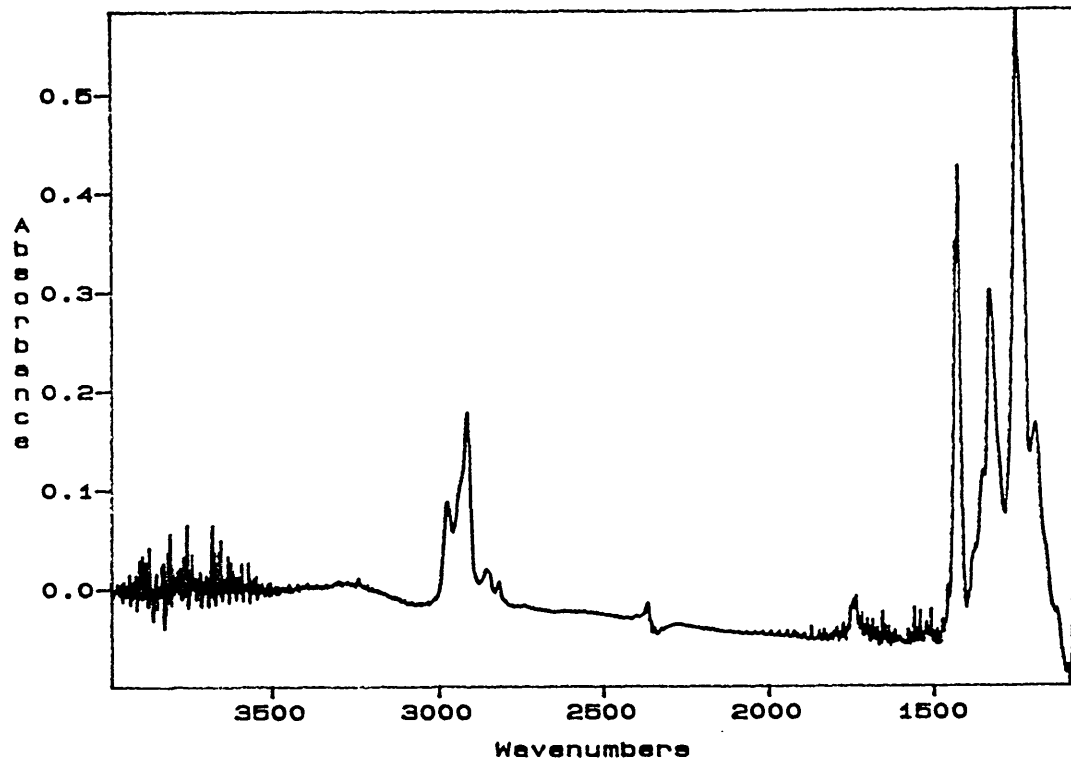


Figure.6.17. Transmission Spectrum of Pure A1891 Film.

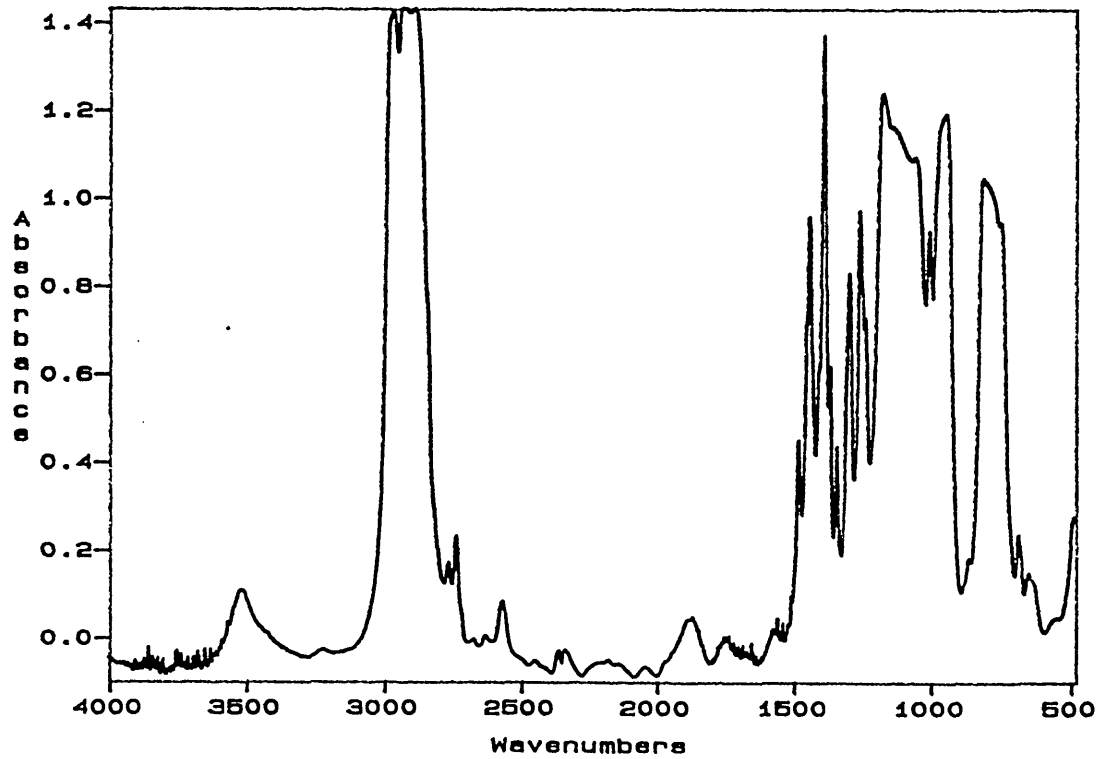
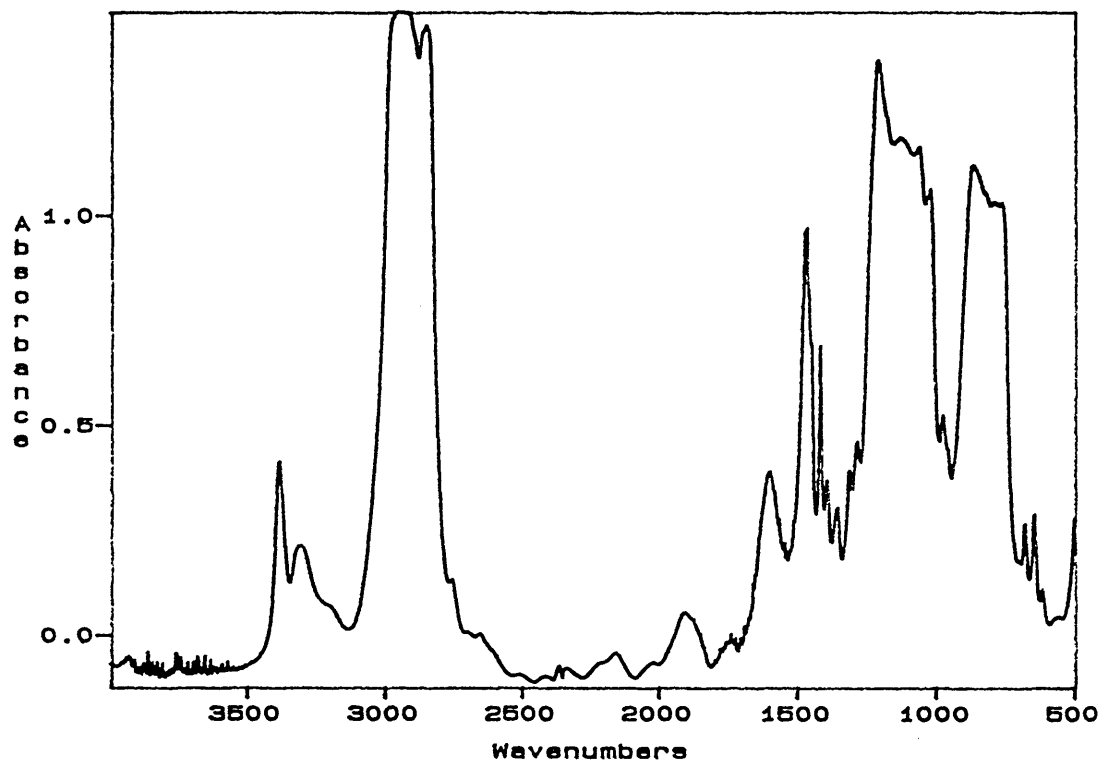


Figure.6.18. Transmission Spectrum of Pure A1100 Film.



The important bands in figure.6.18. are those at approximately 3300 cm^{-1} due to the $\nu(\text{NH}_2)$ stretching vibrations, those at approximately 3000 cm^{-1} due to the $\nu(\text{CH}_3)$ and $\nu(\text{CH}_2)$ stretching vibrations and those at approximately 1600 cm^{-1} due to the $\delta(\text{NH}_2)$ bending vibrations. The PVC spectrum in figure.6.16 does not have any bands in the 3300 and 1600 cm^{-1} regions of the spectrum, (except $\nu_s(\text{OH})$ of water at approximately 3400 cm^{-1}). Therefore for the samples containing A1891 as the silane, the band due to the $\nu(\text{SH})$ stretching vibration was analysed. For the samples containing A1100, the bands due to the $\delta(\text{NH}_2)$ bending vibrations were analysed. The bands due to the $\nu(\text{NH}_2)$ stretching vibrations were not chosen for infrared analysis, since integration of these bands proved difficult due to a sloping baseline in this region of the spectrum. The background arose from the bicarbonate salt formation, described in the introductory chapter.

A laminate, consisting of a silicon micro ATR prism, coated with a dipped A1891 film, (from a 4% w/w solution), with a dipped PVC layer, (from a 10% solution), of approximately 10 μm thickness, was investigated using FTIR-ATR spectroscopy. The resulting spectra, (before PVC deposition and 135, 185, 235, 285 and 335 minutes after PVC deposition), can be seen in figure.6.19. The solvents in the laminate were removed from the film by heat treatment. (This was necessary, because before solvent removal, evidence of hydrogen-bonding of the solvent to the silane was observed in the spectrum of the laminate, (see figure.6.20). Figure.6.20. shows two overlapping bands in the 2500 cm^{-1} region of the spectrum, which arise from the hydrogen-bonding of the SH group in the silane to the solvent in the PVC, (DMF)).

Figure.6.19. FTIR-ATR Spectra of Silicon/A1891/Dipped PVC Laminate.

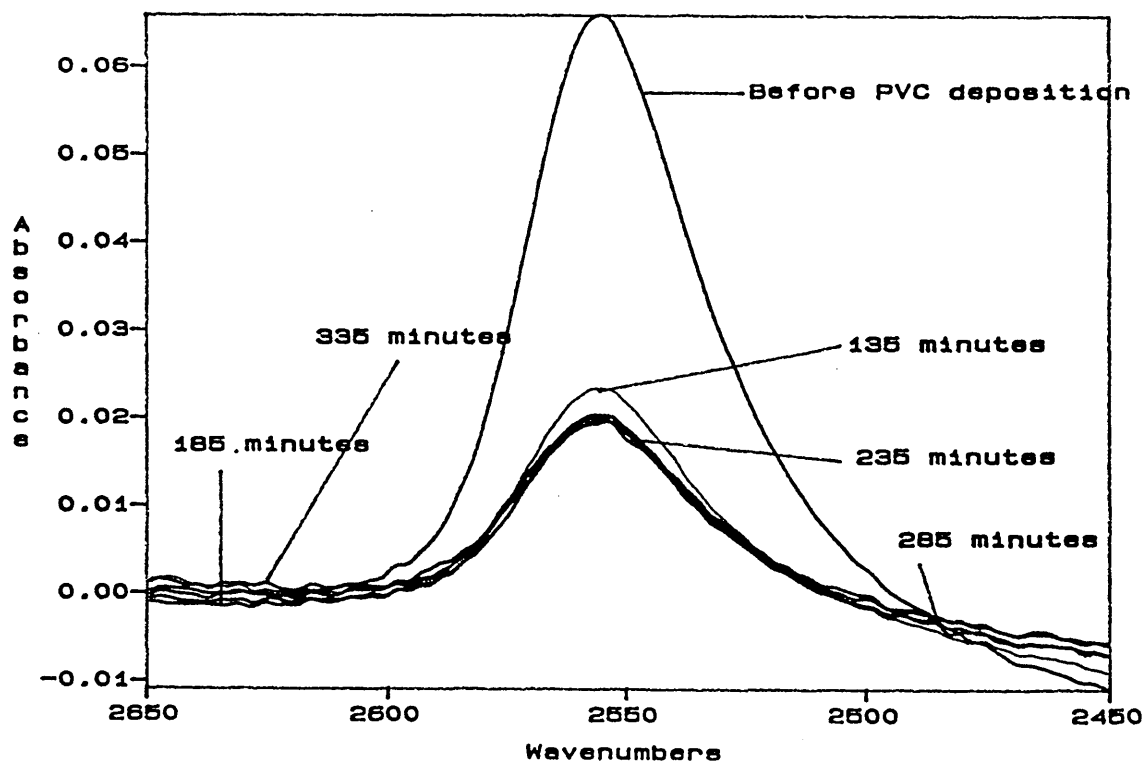
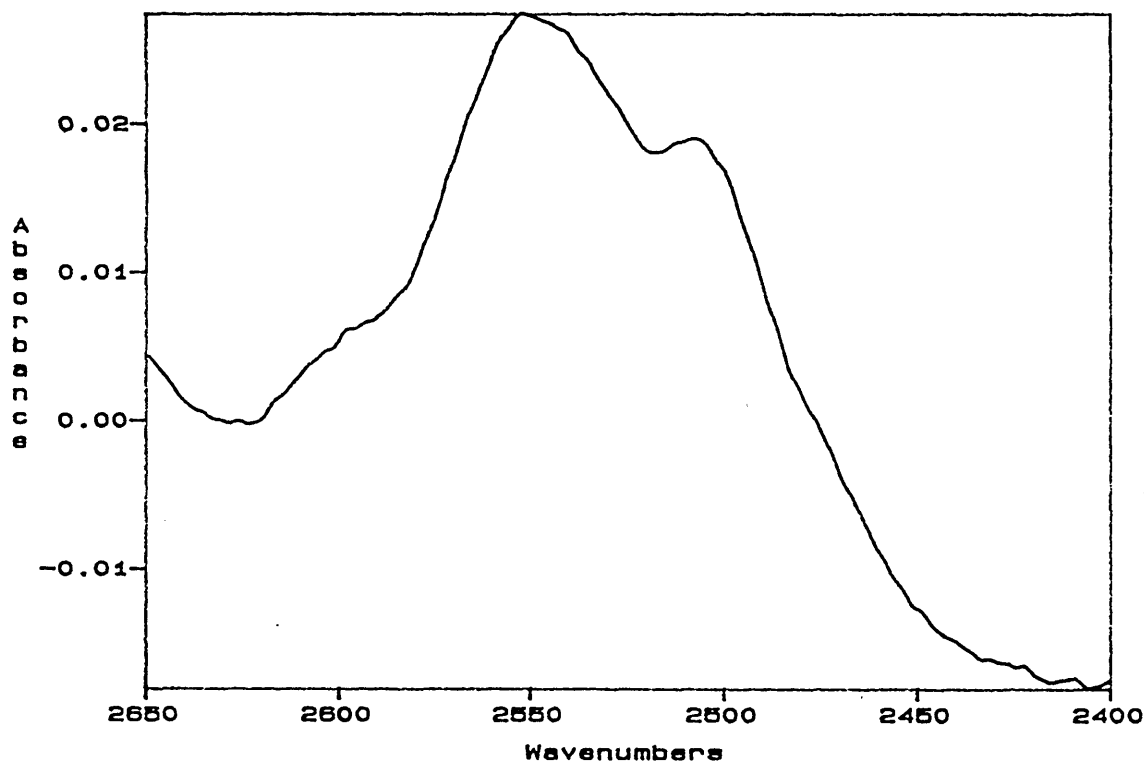


Figure.6.20. FTIR-ATR Spectrum of Silicon/A1891/PVC Laminate Before Solvent Removal.



It can be seen from the spectra in figure.6.19. that the intensity of the $\nu_s(\text{SH})$ bands decreases initially when the PVC is deposited, then decreases with increasing time. The integrated intensities under the $\nu_s(\text{SH})$ bands in figure.6.19. were measured and are reported in table.6.1.

It can be seen from the data in table.6.1. that the largest reduction in intensity of the $\nu_s(\text{SH})$ band occurs when the PVC is initially added. It appears that the diffusion after this time is very slow and that the main diffusion occurs after the PVC is deposited over the silane, during the curing procedure. However, the silane adhesive still remains at the interface.

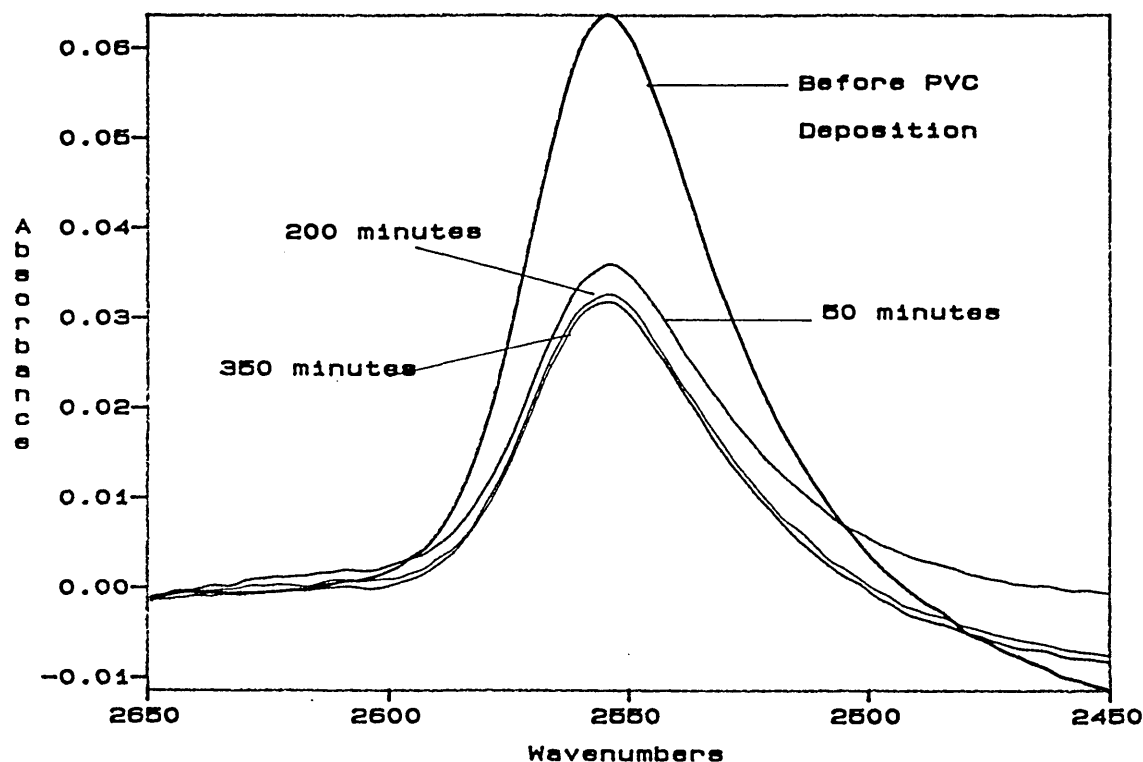
Table.6.1. Integrated Intensities Under the ν_{SH} Bands for Silicon/A1891/Dipped PVC Laminate.

Time /minutes after PVC Deposition	Integrated Intensity / cm^{-1} (2660 to 2460 cm^{-1})
Before PVC deposition	4.603
135	1.409
185	1.308
235	1.282
285	1.246
335	1.237

The effect of casting the silane and the PVC onto the silicon, as opposed to forming these films by the dipping technique was also investigated, as follows:

A laminate, consisting of a silicon micro ATR prism, coated with a cast A1891 film, (from a 20% solution), with a cast PVC overlayer, (from a 5% solution), was investigated using FTIR-ATR spectroscopy. The resulting spectra, (before PVC deposition and 50, 200 and 350 minutes after PVC deposition), are plotted in figure.6.21.

Figure.6.21. FTIR-ATR Spectra of Silicon/A1891/Cast PVC Laminate.



The integrated intensity of the areas under the $\nu_s(\text{SH})$ bands were determined, using the software, and the results are reported in table.6.2.

Table.6.2. Integrated Intensities Under $\nu_s(\text{SH})$ Bands for Silicon/A1891/Cast PVC Laminate.

Time / minutes after PVC deposition	Integrated intensity / cm^{-1} (2640 to 2450 cm^{-1})
Before PVC deposition	3.956
50	2.135
200	2.115
350	2.080

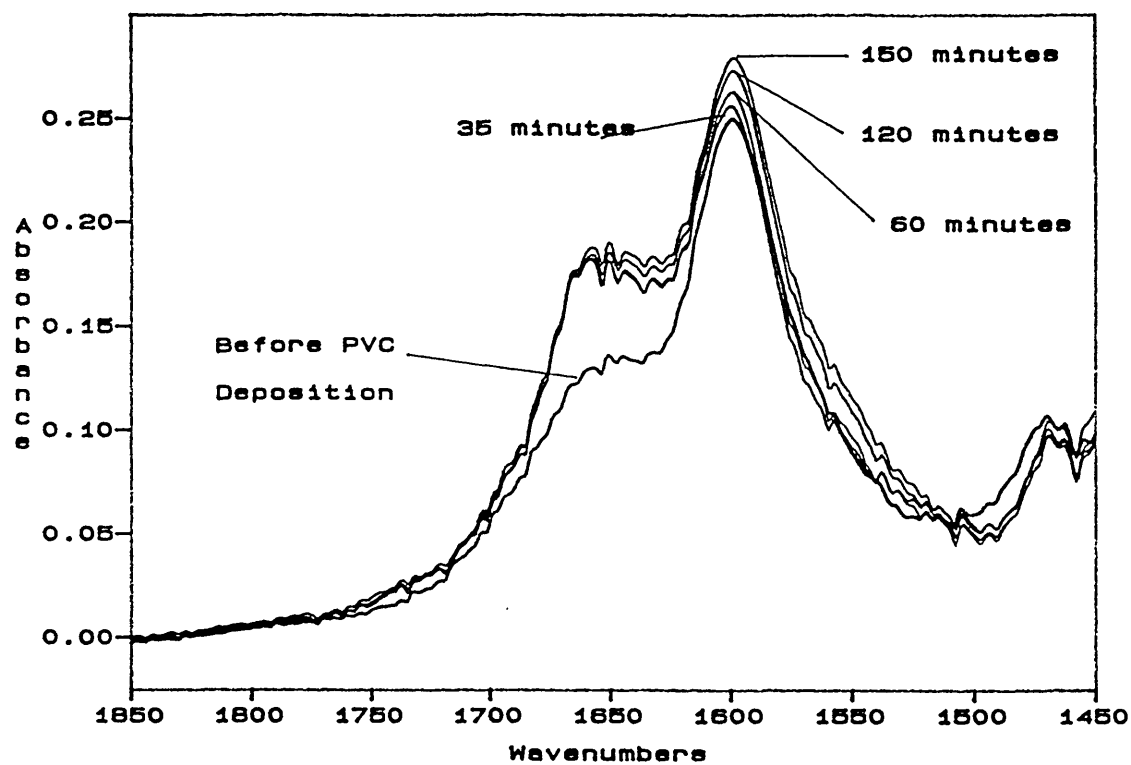
From the spectra in figure.6.21. and the data in table.6.2., it can be seen that the intensity in the $\nu_s(\text{SH})$ band initially decreased when the PVC was deposited over the silane layer and then slowly decreased with time. As for the dipped PVC film, it appeared that the main diffusion occurred shortly after the PVC deposition, possibly during the curing process.

There are other reasons why the silane intensity decreased so dramatically on addition of the polymer layer. The process of depositing the polymer over the silane could have removed silane from the silicon, particularly for the dipped PVC film. Also the silane may have been effected during the curing process of the laminate.

A similar laminate system with A1100 as the coupling agent was then investigated to see whether diffusion of this silane into the PVC could be detected and monitored, as follows:

A laminate, consisting of a silicon micro ATR prism, coated with a dipped A1100 film, (from a 4% w/w solution), with a dipped PVC overlayer, (from a 10% w/w solution), was investigated by FTIR-ATR spectroscopy. The resulting spectra, (before PVC deposition and 35, 60, 120 and 150 minutes after PVC deposition), can be seen in figure.6.22.

Figure.6.22. FTIR-ATR Spectra of Silicon/A1100/Dipped PVC Laminate.



The integrated intensities under the bands due to the $\delta(\text{NH}_2)$ bending vibrations have been calculated and are reported in table.6.3.

Table.6.3. Integrated Intensity Under $\delta(\text{NH}_2)$ bands for Silicon/A1100/Dipped PVC Laminate.

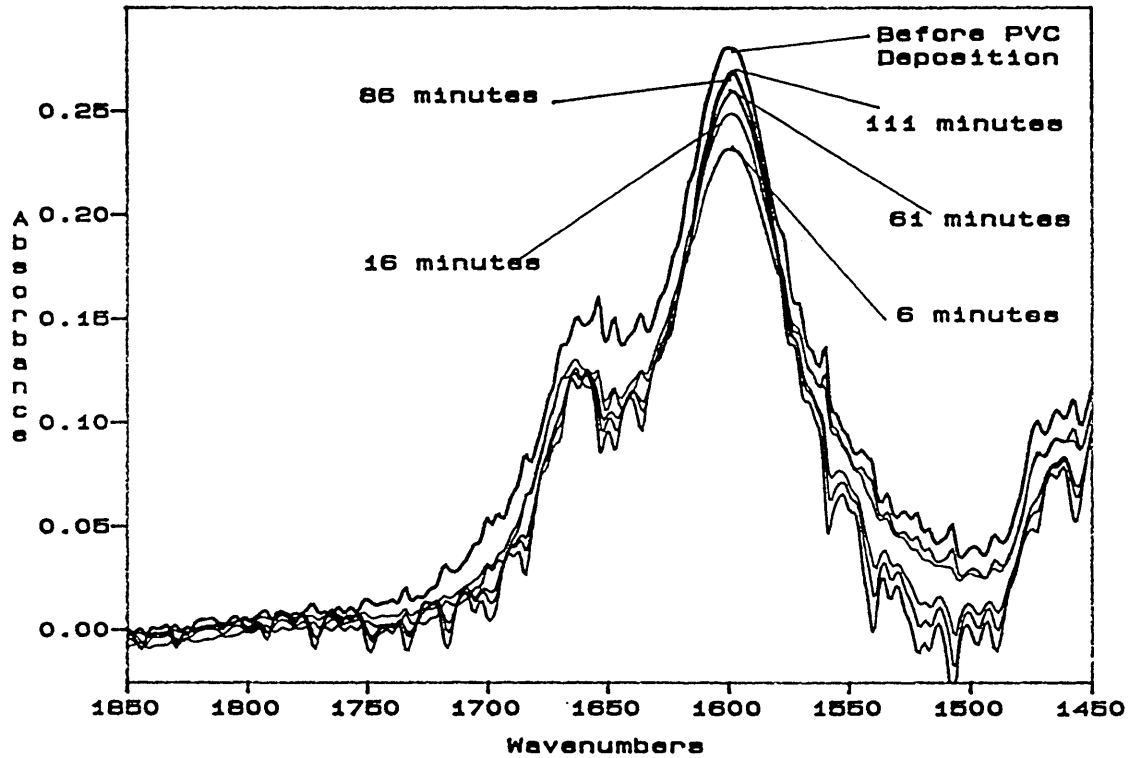
Time / minutes after PVC deposition	Integrated intensity / cm-1 (1730 to 1500 cm-1)
Before PVC deposition	17.697
35	20.781
60	21.909
120	22.117
150	22.458

From the spectra in figure.6.22 and the data in table.6.3, it can be seen that the integrated intensity of the bands due to the $\delta(\text{NH}_2)$ bending vibrations increases initially with the deposition of the PVC and then increases with increasing time. It is possible that not all the DMF , (from the PVC film), has evaporated, and that it has diffused into the silane film. Unfortunately, because there is a DMF band at approximately 1670 cm^{-1} , this may have contributed to the increase seen in the intensity of the $\delta(\text{NH}_2)$ bands. As for the laminates containing mercaptosilane, if any diffusion has occurred, it was probably during the initial stages of the experiment.

The effect of casting the silane and PVC films onto the silicon was then investigated, as follows:

A laminate, consisting of a silicon micro ATR prism, coated with a cast A1100 film, (from a 20% w/w solution), with a cast PVC overlayer, (from a 5% w/w solution), was investigated using FTIR-ATR spectroscopy. The resulting spectra, (before PVC deposition and 6, 16, 61, 86,111 minutes after PVC deposition), can be seen in figure.6.23.

Figure 6.23. FTIR-ATR Spectra of Silicon/A1100/Cast PVC Laminate.



The integrated intensity of the areas under the $\delta(\text{NH}_2)$ bands was determined, using the software and the results are reported in table.6.4.

Table.6.4. Integrated Intensity Under $\delta(\text{NH}_2)$ bands for Silicon/A1100/Cast PVC Laminate.

Time / minutes after PVC deposition	Integrated intensity / cm^{-1} (1730 to 1500 cm^{-1})
Before PVC deposition	22.089
6	19.605
16	20.092
61	21.063
86	21.522
111	22.286

From the spectra in figure.6.23. and the data in table.6.4, it can be seen that the intensity in the $\delta(\text{NH}_2)$ bands initially decreased when the PVC was deposited over the silane layer and then increased with increasing time. As for the laminates, with A1891 as the silane, it appears that if any diffusion had occurred it was in the early stages of the experiment, shortly after coating the silane with PVC. The increase in intensity in the $\delta(\text{NH}_2)$ bands may actually be due to the solvent, (DMF), diffusing into the silane from the PVC and contributing to the $\delta(\text{NH}_2)$ band intensity in the spectra.

As for the laminates analysed by Raman spectroscopy, formation of the PVC films produced in the silicon/silane/polymer laminates depended on their method of preparation. Dipped films were 'wedge-shaped' while cast films were uniform.

From the FTIR-ATR spectroscopy results of the silicon/A1891/PVC laminates, it appears that diffusion of the silane into the polymer overlayer may have occurred, because a reduction in intensity of the silane band was observed on addition of the PVC and then a further decrease in intensity was seen with

increasing time. However, the majority of the diffusion appeared to be in the initial stages of the experiment, during the curing stage. Other reasons why the silane intensity decreased so dramatically on addition of the PVC are that the polymer may have 'washed' away the silane or that the silane may have been affected during the curing process of the laminate. The heat treatment of the laminate, prior to FTIR investigation was necessary to remove solvents from the system, which otherwise gave rise to bands in the spectrum due to hydrogen bonding between the silane and the solvents. The heating time could not be decreased without causing inefficient solvent removal.

A similar problem arose with the silicon/A1100/PVC laminates. The solvent used to solubilise the polymer, DMF, had a band in a similar position to the δ (NH_2) bands, i.e. at approximately 1660 cm^{-1} . Therefore, incomplete removal of the DMF, gave rise to bands in the spectrum due to the solvent. This could be an explanation for why the intensity of the silane $\delta(\text{NH}_2)$ band was seen to increase with increasing time, when a decrease in silane intensity would be expected if the silane was diffusing into the polymer. This increase may have been caused by diffusion of the DMF into the A1100, for the sample that was only heated for 5 minutes prior to investigation. Even when one of these laminates was heated for 30 minutes at 150°C , prior to investigation, the effect of increasing intensity of the 'silane' $\delta(\text{NH}_2)$ band was still seen. Unfortunately, after 30 minutes heating time, if there was any silane diffusion it would probably have already occurred.

Because of the problems encountered with trying to detect the diffusion of the mercaptopropyl and aminopropyl silanes into a PVC overlayer, brought about by the necessity of removal of the solvents in the system, this experiment was not considered to be the best method of detection.

The Raman experiments, however, were not reliant upon fast removal of the solvents, (to determine rates of diffusion), but instead could be used to determine the evidence for diffusion after it had occurred. Evidence for diffusion of the mercaptosilane into the PVC was observed but evidence for diffusion of the

aminosilane into the PVC was not so successfully shown, due to problems with obtaining the required polymer thickness.

6.3. Conclusions.

Silicon, (or quartz)/silane/PVC laminates have been prepared for investigation by Raman and infrared spectroscopy and Raman microscopy. The silanes used in these laminates were (3-aminopropyl)trimethoxysilane, A1100 and (3-mercaptopropyl)triethoxysilane, A1891. The thickness of the silane films depended upon their pretreatment and use. More concentrated solutions produced thicker films and dipped films were thinner than cast films. The treatment after deposition was also important. Heating of the silane films was required to remove any solvent remaining. Both dipped and cast silane films were produced. The A1891 films formed 'globules' on the substrates while the A1100 films were even.

Both dipped and cast polymer films were deposited over the silane films. The dipped films tended to be 'wedge-like' in shape while the cast films were smoother and more uniform.

From the confocal Raman microscopy experiments, it was observed that the mercaptosilane diffused into the PVC overlayer. This would be expected since the mercaptosilane is such a small molecule and also because diffusion of a similar silane into a different polymer has been observed by previous researchers, [89]. The extent of diffusion was interesting. The silane seems to have diffused through 8 μm of polymer. This may have occurred by way of the silane and the PVC forming an interpenetrating network, also seen previously, [80, 89].

The PVC films of the samples containing A1891 were peeled away from the laminate. Investigation of these peeled films showed the presence of the silane on both sides of each film. The silane distribution on one side of a peeled film was determined by obtaining spectra over a 5 x 5 μm^2 area in 1 x 1 μm^2 steps. This showed that the silane distribution was uneven over this area. This uneven distribution of A1891 was also observed visibly over a 1 cm^2 area of sample, (i.e. the globule formation).

The aminosilane-containing laminate was also investigated using Raman confocal microscopy. Unfortunately, due to problems with obtaining PVC films of the required thickness, no real evidence of the diffusion of the aminosilane into the polymer was found. However it is highly likely that the aminosilane will have diffused into the PVC, since it is a similar size to the mercaptosilane, so there would have been no steric hindrance problems, and also because previous researchers have observed a similar aminosilane diffuse into a polyester to form an interpenetrating network, [80, 89].

Silicon/silane/PVC laminates, with A1891 and A1110 as the silanes, were investigated using FTIR-ATR spectroscopy in order to determine the diffusion time of the silanes into the polymer. The integrated intensities of bands specific to the silane in question were obtained as a function of time after PVC deposition. It was found for the laminates containing A1891, that the intensity of the silane band decreased dramatically on PVC deposition and then decreased slowly after that. These laminates had been cured for 55 minutes up to 2 hours at high temperature to remove the solvents in the system. Before removal of these solvents, bands due to hydrogen-bonding of the solvents and the silane molecules were observed in the spectra. It is likely that diffusion of the silane into the polymer occurred but that this was mostly during the initial curing stages of the experiment. It is possible that the PVC may have 'washed' away the silane during deposition or that the silane was effected during the curing of the laminate.

A different solvent-related problem was encountered with the laminates containing the aminosilane. The solvent for the PVC, (DMF), had bands in a similar position to the silane bands. Therefore when an increase in the silane intensity was observed with increasing time, after polymer deposition, this was attributed to the DMF diffusing into the silane. This may have masked any diffusion of the silane into the polymer. When the curing time of the laminates was increased from 5 to 30 minutes, this effect was still observed. At a curing

time of 30 minutes, (or greater), most of the diffusion will have probably already occurred. It is thought likely that the aminosilane diffused into the PVC because previous researchers have observed a similar silane diffusing into a different polymer. This diffusion probably will have occurred in the initial stages of the experiment, shortly after PVC deposition.

In summary, diffusion of A1891 into PVC in a Quartz/A1891/PVC laminate has been observed successfully, using Raman spectroscopy and microscopy. The diffusion of A1100 into PVC in a quartz/A1100/PVC laminate has not been definitely proven, although this probably also occurred. The results from the infrared analysis of silicon/silane /PVC laminates have shown that a different sample preparation is required if the rate of diffusion of the silanes into the polymer overlayers is to be followed.

More work is obviously needed in both the Raman and the infrared areas to try and overcome the problems outlined in this chapter. This will be discussed in chapter.7.

The following chapter brings together all the results from the whole thesis and compares and contrasts them. It also restates the aims and objectives of the project and discusses how well these have been achieved. Future work is also suggested.

CHAPTER.7. DISCUSSION AND CONCLUSIONS.

Introduction.

The main aim of this chapter is to compare and contrast the results reported in the rest of the thesis and to draw the major conclusions. The achievements versus the aims and objectives will be discussed and some future work will be suggested.

In chapter 3, the dipping times for formation of monolayers of n-octadecyltrichlorosilane, OTS and perfluorodecyl(ethyl)trichlorosilane, F8, on silicon ATR prisms were determined. The relative linear dichroic ratios of the cast and self-assembled films were also obtained, and the variation in linear dichroism for a self-assembled film of OTS on silicon, as a function of surface coverage was discussed. These findings will be compared to the results reported in chapters 4 and 5.

In chapter 4 the times for formation of monolayers of OTS and F8 on silicon ATR prisms were determined in an *in situ* environment, for varying silane concentrations. The areas per molecule of OTS and F8 on silicon were also obtained.

In chapter 5 atomic force microscopy was used to obtain information on the packing and distribution of OTS and F8 submono-, mono- and above mono-layer films on float glass substrates.

Chapter 6 examined a different system to the one described in chapters 3 to 5. Laminates consisting of quartz, (or silicon), substrates and polymer films, bound together by various silane layers were investigated by FTIR-ATR spectroscopy and by Raman spectroscopy and microscopy. The silanes in question were (3-aminopropyl)trimethoxysilane, A1100 and (3-mercaptopropyl)triethoxysilane,

A1891 and the polymer was poly(vinylchloride), PVC. The infrared experiments were carried out to try and determine the rate of diffusion of the silanes into the PVC. The Raman and infrared data reported in chapter 6 will also be compared in this chapter.

7.1. Adsorption of Long-Chain Silanes onto Silicon and Glass.

The adsorption of long-chain silanes, specifically, n-octadecyltrichlorosilane, OTS and perfluorodecyl(ethyl)trichlorosilane, F8, onto silicon and glass was followed by three techniques: *In situ* Fourier transform infrared attenuated total reflection, (FTIR-ATR), spectroscopy, *ex situ* FTIR-ATR spectroscopy and *ex situ* atomic force microscopy. The term *in situ* refers to analysis during silane adsorption onto the substrates and *ex situ* refers to analysis at various stages of silane adsorption, with the substrate removed from the silane solution. The main aims of the research were to determine the following:

- (i) The dipping time for formation of monolayers of the surfactants on silicon and glass substrates.
- (ii) The degree of orientational ordering of these silanes as a function of coverage on the substrate.
- (iii) The distribution of these silane molecules at various stages of submono-, mono- or multi- layer formation.

7.1.1. Comparison of *ex situ* FTIR-ATR Spectroscopy and Atomic Force Microscopy Results.

In chapter 3 the rates of formation of OTS and F8 monolayers on silicon ATR prisms were followed by FTIR-ATR spectroscopy. By plotting the integrated intensities under the chosen silane bands, ($\nu(\text{CH}_3)$ and $\nu(\text{CH}_2)$ bands for OTS and $\nu_{\text{as}}(\text{CF}_2)$ and $\nu(\text{CF}_2)$ bands for F8), against dipping time, the time required for monolayer formation of the two silanes on silicon were determined. For a 1 mM OTS solution in toluene, this time for monolayer formation was approximately 80 to 90 minutes. For a 0.5 mM F8 solution in freon 113, the dipping time for monolayer formation was approximately 6 to 8 minutes. These results agree well with previous researchers' work, [38, 46]. It may be concluded that for a lower concentration of F8 than OTS, the F8 monolayer formed much faster than the OTS monolayer. One of the differences between the two methods of sample preparation was that more water was removed from the F8 system than the OTS system, by drying the F8 and the freon 113, and also by preparing the F8 samples in a dry nitrogen environment. The reason why the F8 monolayer forms faster than the OTS monolayer is due to the relative rates of hydrolysis of the two molecules. The silane that can be hydrolysed the fastest would be expected to adsorb quicker onto the substrate. The rate of hydrolysis of the F8 molecules is faster than that of the OTS molecules. This is because the CF_3 and CF_2 groups in the F8 chain are more electron withdrawing than the CH_3 and CH_2 groups in the OTS chain and therefore the hydrolysis of the SiCl_3 group in the F8 chain, (nucleophilic substitution reaction of Cl with OH^- from water in the system), occurs faster than the rate of hydrolysis of the SiCl_3 headgroup in the OTS chain. The F8 monolayer was seen to form faster than the OTS monolayer, even though the F8 solution was a lower concentration than the OTS solution and more water had been removed from the F8 system than the OTS system.

Now that the Fourier transform infrared spectroscopy results have been compared to previous researchers' work, a comparison of the FTIR-ATR data to the atomic force microscopy results, reported in this thesis, will be now given:

In chapter 5, atomic force microscopy was indirectly used to determine the rates of formation of OTS and F8 monolayers on float glass substrates. The surfaces of silicon and of the float glass were considered to be fairly similar, since the silicon would naturally have an ambient silicon oxide layer, of approximately 5 nm thick on the surface, [29], with approximately 5 silanol groups per nm², [18]. The float glass would also be expected to have a similar distribution of surface silanol groups. Both surfaces are naturally covered with several layers of physisorbed water, with which some researchers have suggested the silane molecules react, [37].

The times for monolayer formation of OTS and F8 on float glass were determined from the roughness average values of the atomic force micrographs of these samples. For OTS, the monolayer was seen to form after approximately 90 minutes dipping time, while the F8 monolayer formed after about 5 to 8 minutes dipping time in the silane solution. These results agree very well with those obtained from the Fourier transform infrared spectroscopy experiments on silicon and with the results reported for monolayer formation times by other researchers, [38, 46]. The reasons why the F8 monolayer formed faster than the OTS monolayer have already been discussed.

The degree of orientational order, calculated from FTIR-ATR results for the silane films, can be used to help interpret the way the island formation, observed in the atomic force microscopy images, occurs, as follows:

In chapter 3, OTS films at submonolayer coverage were found to be more orientationally disordered than the OTS monolayer. At dipping times above that required to produce a monolayer, orientational order was seen to persist and

very little increase in the intensity of the bands due to the $\nu(\text{CH}_3)$ and $\nu(\text{CH}_2)$ stretching vibrations was observed. In chapter 5, the atomic force microscopy images and roughness average values showed that at below monolayer coverage, island formation was occurring and that at monolayer coverage no islands were observable in the images. The islands seen in the submonolayer AFM images were most likely due to orientationally disordered OTS molecules depositing over the glass surface. The lack of islands in the image obtained for the monolayer of OTS possibly implies that the OTS molecules are close packed and probably orientationally ordered. These results agree well with those determined for submono- and mono-layers of OTS on silicon, by FTIR-ATR spectroscopy. However, the difference in the FTIR-ATR and the AFM data on these systems can be seen when the dipping time is increased to a time greater than that required for monolayer formation. The AFM images show islands which again could be attributed to orientationally disordered OTS molecules depositing over the OTS monolayer. These islands would not necessarily be directly detected in the FTIR-ATR experiments but may have contributed to the variations in the linear dichroic ratios, observed for OTS. This discrepancy in the results may be explained by the fact that the areas probed in the two different techniques are not the same, (mm^2 in FTIR-ATR spectroscopy and nm^2 in AFM). The AFM experiments were carried out to gain a better understanding of the microscopic topographical details of these surfaces.

Although no linear dichroic ratio values were obtained for the formation of F8 submonolayers and monolayers onto silicon ATR prisms, the AFM experiments showed similar island formation to that reported for OTS. That is, at submonolayer coverage, the F8 molecules were seen to form islands attributed to orientationally disordered material, while the AFM image of the monolayer was smooth, with a few small islands. As the dipping time was increased above that required for monolayer formation, islands were again observed in the AFM

images for F8, which were attributed to orientationally disordered F8 molecules depositing over the F8 monolayer.

If multilayer formation had occurred, (for both OTS and F8), then the FTIR technique would have detected these multiple layers. However, the formation of isolated islands over a monolayer would not necessarily be detected by the FTIR experiment, except that such deposition may contribute to the statistical variations observed in the, (OTS), dichroic ratio results.

Samples for AFM investigation were prepared under class 100 clean room conditions and also in the open laboratory. Previous researchers have shown that samples not prepared under class 100 clean room conditions gave irreproducible AFM images, [60]. Therefore, only the roughness average values for the samples prepared under clean room conditions were analysed here.

7.12. Comparison of *ex situ* and *in situ* FTIR-ATR Spectroscopy Results.

The times for monolayer formation for OTS and F8 on silicon ATR prisms were determined for various silane concentrations by *in situ* FTIR-ATR spectroscopy. These were obtained by plotting the integrated intensities of the chosen silane bands, ($\nu(\text{CH}_3)$ and $\nu(\text{CH}_2)$ bands for OTS and the $\nu_{\text{as}}(\text{CF}_2)$ bands for F8), against exposure time to silane solution. Monolayer formation occurred at the point where the plot reached a constant maximum. The times for monolayer formation of OTS on silicon for solutions of concentration 1, 5.6 and 11.8 mM were 130, 70 and 40 minutes, respectively. For F8 solutions of concentration 0.25, 0.45 and 1 mM, the times for formation of the monolayers were 220, 52 and 16 minutes, respectively. All solutions were prepared in pre-dried deuterated toluene. For the same concentration of OTS and F8, the F8 monolayer was seen to form much faster than the OTS monolayer. The reasons for this have already been discussed. However, the time for formation of the OTS monolayer on silicon, at a concentration of 1 mM in deuterated toluene in the *in situ* experiment, was greater than that for the same concentration solution

in the *ex situ* FTIR-ATR experiment. This may be explained by the fact that in the *ex situ* experiment, the solvent was not pre-dried, whereas in the *in situ* experiment, the solvent was pre-dried. Also, in the *ex situ* experiment, the silicon prism was constantly being exposed to atmospheric humidity, while in the *in situ* experiment, once the prism was placed in the liquid cell, it was effectively sealed from the atmosphere. Therefore, more water was available for hydrolysis of the SiCl_3 headgroups in the *ex situ* experiment than in the *in situ* experiment. This is thought to be why the rates of adsorption for the same concentration OTS solutions, in the different environments varied.

A similar situation occurred with the F8 solutions. For an F8 solution of concentration 0.45 mM in deuterated toluene, the *in situ* adsorption time for monolayer formation on the silicon ATR prism was longer than that for a 0.5 mM solution in freon 113, in the *ex situ* FTIR-ATR experiment. This was partly due to the fact that in the *in situ* experiment, the concentration of the F8 solution was less than that in the *ex situ* experiment. The difference in monolayer formation times was probably also due to the fact that in the *in situ* experiment the sample was sealed from the atmosphere, once in the liquid cell, whereas in the *ex situ* experiment, the silicon prism was exposed to atmospheric humidity between dipping stages. Because of these differences, it was not surprising that the surfactant in the *in situ* experiment took longer to form monolayers than in the *ex situ* case.

7.13. Comparison of *in situ* FTIR-ATR Spectroscopy Data with XRD and AFM Results, (previous researcher's work).

The areas occupied by each silane molecule were determined from the *in situ* FTIR-ATR spectroscopy experiments. These were obtained by using Sperline's approach to calculate the Gibbs surface excess of a molecule on a substrate, [148]. The area per molecule was calculated for three different concentrations of

each silane. For OTS, deposited from solutions of concentration 1, 5.8 and 11.6 mM in pre-dried deuterated toluene, the areas per molecule determined at monolayer coverage were 24.05 ± 0.17 , 24.60 ± 0.10 and $24.66 \pm 0.08 \text{ \AA}^2$, respectively. This gave an average area per molecule of $24.44 \pm 0.12 \text{ \AA}^2$. The number of SiOH groups on a silicon oxide/silicon surface is 0.04 per \AA^2 , i.e. each silanol group occupies 25 \AA^2 , [18]. Therefore, the results found here suggest that complete coverage of the silicon oxide was achieved. The area per molecule of OTS on silicon oxide/silicon was previously reported by Whitesides et al, [39], from XRD measurements as $21 \pm 3 \text{ \AA}^2$. The results reported here agree well with this value. However, Fujii et al reported from AFM data, [57], that the area per molecule of OTS on silicon was $43 \pm 7 \text{ \AA}^2$. This value obviously disagrees with the results reported here and with those reported by Whitesides et al, [39]. FTIR-ATR data and XRD data might be expected to give similar results, since the areas probed in each of the two techniques are similar. However, FTIR-ATR and AFM results would not necessarily be expected to agree, since the areas probed in these two techniques are very different. Also the sample preparation by Fujii et al, (production of the silicon oxide layer by passing a dry stream of oxygen over the silicon substrate at high temperature), [57], may have produced a lower silanol group density on the silicon surface than that obtained by Whitesides et al, [39]. This is a possible reason why the areas per molecule observed by Fujii et al, [57], were smaller than those observed by Whitesides et al, [39], and smaller than those determined here.

The areas per molecule calculated for F8 molecules deposited from solutions of concentration 0.25, 0.45 and 1 mM in pre-dried deuterated toluene, were 30.86 ± 0.10 , 30.00 ± 0.04 and $29.21 \pm 0.09 \text{ \AA}^2$, respectively. These gave an average area per molecule for F8 of $30.02 \pm 0.08 \text{ \AA}^2$. The average area per molecule for F8 was 22.8% larger than the average area per molecule for OTS. This agrees relatively well with Fujii et al, [57], who found an area per molecule for F8 15%

larger than the OTS area per molecule, (both silanes adsorbed onto silicon). However, Fujii et al determined that the area occupied by an F8 molecule on silicon was $50 \pm 8 \text{ \AA}^2$. This value disagrees with the value reported here. As for the OTS samples, the ATR data would not necessarily be expected to agree with AFM data, due to the different sampling areas in the two techniques. As for the OTS samples, the density of the silanol groups on the silicon surface may have been less in Fujii's, [57], samples than in Whitesides', [39] samples and in the samples prepared here. This would give a larger area per molecule for F8 than that observed in the experiments here.

The reason why the F8 molecule occupies a larger area than the OTS molecule can be explained by two facts. Firstly, the CF_3 end group has a larger van der Waals radius than the OTS end group, CH_3 , and secondly the F8 chain forms a helix on the substrate, whereas the OTS adsorbs onto the substrate as an extended chain. Both the CF_3 end group and F8 helix would be expected to occupy a larger area than the OTS end group and straight chain, [57].

The dipping times for the monolayer formation of OTS and F8 onto silicon and glass and the degree of orientational order of OTS films on silicon were determined. However, the degree of orientational ordering of F8 on silicon was not established, even though cast films showed orientational disorder as expected.

Atomic force microscopy and *in situ* Fourier transform infrared attenuated reflection spectroscopy experiments were successful in obtaining an idea of the distribution of these silane molecules over silicon and glass surfaces.

7.2. Physical and Chemical Interactions in SiO₂/ Short-Chain Silane/

Polymer Laminates.

The interactions within quartz, (or silicon)/ short-chain silane/ polymer laminates were investigated by the following techniques: FTIR-ATR spectroscopy and Raman spectroscopy and microscopy. The main aims of the research were to determine the following:

- (i) The existence of and consequently the rate of diffusion of the silanes into the polymer.
- (ii) The distribution of the silanes over the polymer and substrate.

In chapter 6, Raman confocal microscopy was used to establish whether the silanes had diffused into the polymer overlayers. The silanes were (3-mercaptopropyl)triethoxysilane, A1891 and (3-aminopropyl)trimethoxysilane, A1100. The polymer was poly(vinylchloride), PVC and the Raman substrate was quartz. There were several problems in obtaining information on these systems. The first was the difficulty in producing uniform PVC films that were thick enough for the depth profiling experiment. This was achieved with the laminate containing the mercaptosilane, but not with the laminate containing the aminosilane. The mercaptosilane was seen to diffuse through an 8 μm film of PVC. The distribution of this silane on the quartz substrate, prior to PVC deposition, was observed to be 'globular' and uneven. In order to determine the distribution of the silanes over the polymer after deposition, the PVC film required peeling away from the laminate and then confocally analysing. This is where another problem arose. For the A1891, there was no problem peeling the PVC films away from the laminates, but the PVC films in the laminates containing A1100 were very difficult to remove and hence no Raman spectra were obtained of these films. By using the confocal mapping technique, the distribution of the mercaptosilane on the PVC was found to be uneven over a 25 μm^2 area. Another problem arose when trying to scan a larger area of the sample

for a longer time. The laser caused the sample to distort and therefore the silane distribution over larger areas could not be obtained.

The infrared experiments were carried out to determine the rate of diffusion of the silanes into the polymer overlayers, using silicon prisms as the substrates. The problems that arose were mainly solvent-related. In the case of the silicon/A1891/PVC laminate, the solvents in the system had to be removed because they hydrogen bonded to the silane SH end group and this produced bands in the $\nu(\text{SH})$ stretching vibration region of the spectrum. By the time these solvents were removed from the system, most of the diffusion had probably already occurred. However, a large decrease in silane band intensity was seen after deposition of the PVC. This may be due to diffusion of the silane into the polymer, the polymer 'washing' away some of the silane or the silane layer being effected during the laminate curing process. A similar problem was encountered in the silicon/A1100/PVC laminates. Again, complete removal of the solvents in the system was required to obtain useful results. This was because the solvent for PVC, (DMF), had a band in a similar position to the silane band and therefore contributed to the infrared spectra. As for the laminates containing A1891 as the silane, most of the diffusion would probably have already occurred by the time the solvents were removed.

It was observed that the mercaptosilane diffused into the poly(vinylchloride). The aminosilane probably also diffused into the polymer but this was not proven here. The distribution of the mercaptosilane over the polymer and quartz surfaces was found to be uneven probably due to the presence of insoluble oligomeric by-products in the original silane.

7.3. Conclusions.

Self-assembled monolayers of n-octadecyltrichlorosilane, OTS and perfluorodecyl(ethyl)trichlorosilane, F8, were formed on silicon ATR prisms and float glass substrates. These were monitored by *in situ* and *ex situ* Fourier transform infrared attenuated reflection spectroscopy and by atomic force microscopy.

The dipping times for formation of the monolayers were determined and the *ex situ* FTIR-ATR and AFM results were in good agreement with the each other and with previous researchers' work, [38, 46]. The linear dichroic ratio values of OTS submono- and monolayers were determined and showed an increase in orientational order with increased coverage. The island formation seen in the AFM submonolayer images supported the FTIR-ATR spectroscopy data. The islands observed in the images obtained for dipping times greater than that required to form a monolayer would not necessarily be expected to be directly seen in the FTIR-ATR spectroscopy experiments. However, these islands may have contributed to the variation in the linear dichroic ratio values seen for the OTS films.

The *in situ* FTIR-ATR spectroscopy experiments gave different times for monolayer formation than the *ex situ* experiments. This was due to the difference in the amount of water available to the silanes in the different techniques.

For the same concentration silane solutions, the F8 formed a monolayer before the OTS. This can be explained by the fact that the F8 head group hydrolyses faster than the OTS head group and therefore the F8 molecules adsorb onto the substrate faster than the OTS molecules.

The areas per molecule obtained from the *in situ* FTIR-ATR experiments agreed well with those reported in the literature, (from XRD experiments), [39]. The F8 molecule was seen to occupy a 22.8 % larger area than the OTS molecule, $30.02 \pm 0.08 \text{ \AA}^2$ as opposed to $24.44 \pm 0.12 \text{ \AA}^2$. This can be explained by the fact that the CF_3 end group in F8 has a larger van der Waals radius than

the CH₃ end group in OTS and also because the F8 forms a helix while the OTS adsorbs as an extended chain.

FTIR-ATR spectroscopy and Raman microscopy and spectroscopy were utilised to study the interactions within quartz, (or silicon)/silane/polymer laminates. The silanes were (3-mercaptopropyl)triethoxysilane, A1891 and (3-aminopropyl)trimethoxysilane, A1100 and the polymer was poly(vinylchloride). Quartz slides were used as the substrates for the Raman experiments and silicon ATR prisms were used for the FTIR-ATR experiments.

The mercaptosilane was seen to diffuse through the polymer in the laminate. However, due to sample preparation problems the diffusion of the aminosilane into the PVC was not proven. The distribution of the mercaptosilane over the quartz substrate was observed to be uneven.

A confocal map of a PVC film peeled from the laminate showed that the mercaptosilane was unevenly distributed over a 25 μm² area. The FTIR-ATR spectroscopic data, unfortunately did not yield many details on the rate of diffusion of the silanes into the polymer, due to sample preparation problems.

7.4. Future Work.

There are many systems which could be studied using the spectroscopic and microscopic analyses discussed in this thesis. Ones that are of relevance to the work here include the following:

- (i) Determination of the ordering of fluorinated silanes as a function of coverage on a silicon surface.
- (ii) The effect of the type of headgroup on the rate of adsorption of silanes onto silicon and glass.
- (iii) Obtaining Raman spectra of monolayers of OTS and F8 on silicon and quartz.
- (iv) Determining whether A1100 diffuses into a polymer overlayer, in a quartz/silane/PVC laminate.
- (v) Determination of the rate of diffusion of A1891 and A1100 into polymer overlayers in silicon/silane/PVC laminates.

In order to determine the orientational order as a function of surface coverage for fluorinated silanes, a silane with a longer fluorinated chain, (than the one used here), could be adsorbed onto silicon ATR prisms and then analysed using TE and TM polarised radiation. The effect of alkyl chain length on the formation of silane monolayers has already been investigated, [5], but the effect of changing the head group of fluorinated silanes on the rate of adsorption has not been investigated. FTIR-ATR spectroscopy could be utilised to see if the change of head group effects the rate of adsorption of the silane molecules.

Atomic force microscopy images could also be obtained of the samples mentioned above.

Raman spectra of monolayers of OTS on aluminium have been produced previously, [160]. However Raman spectra of OTS and of F8 monolayers on silicon or quartz have not been obtained. To do this a high powered laser,

(greater than 25 mW), and a scanning time of at least an hour would be necessary.

The diffusion of the aminosilane, A1100, into PVC could be followed by Raman microscopy by depositing a thick enough, (greater than 4 μ m), PVC layer over the silane. The distribution of this silane over the polymer could also be determined using the confocal mapping technique.

The rates of diffusion of the amino and mercaptosilanes into the polymer overlays requires monitoring. This may be possible by using a different solvent for the polymer which does not cause any interference with the silane, i.e. does not hydrogen bond to the silane end group and does not have any bands in the same position as the silane bands. Other possibilities of analysing these systems include preparing the laminate in a different manner, e.g. depositing the polymer over the silicon first then coating the polymer with silane. Then the diffusion of the silane into the polymer could be followed by monitoring the increase in silane band intensity as opposed to a decrease. This way all the solvent in the polymer could be removed prior to contact with the silane. Obviously, this would result in a laminate that was dissimilar to the required model but it may provide information on the rate of the silane diffusion into the polymer.

REFERENCES.

1. Angst, D.L.; Simmons, G.W. *Langmuir*.1991, 7, 2236-2242
2. Gun, J.; Sagiv, J. *J.Colloid Int.Sci.* 1986, 112, 457-472
3. Cheng, S.S.; Scherson, D.A.; Sukenik, C.N. *J.Am.Chem.Soc.* 1992, 114, 5436-5437
4. Maoz, R.; Sagiv, J. *J.Colloid Int. Sci.* 1984, 100, 465-495
5. Ulman, A.; Schildkraut, J.S.;Penner, T.L. *J.Am.Chem.Soc.* 1988, 110, 6136-6144
6. Netzer, L.; Iscovici, R.; Sagiv, J. *Thin Solid Films.* 1983, 100, 67-76
7. Le Grange, J.D.; Markham, J.L.; Kurkjian, C.R. *Antec.* 1993, 1148-1151
8. Banga, R.; Yarwood, J.; Morgan, A.M. *Langmuir.* 1995, 11(2), 618-619
9. Le Grange, J.D.; Markham, J.L.; Kurkjian, C.R. *Langmuir.*1993, 9, 1749-1753
10. Brandiss, S.; Margel, S. *Langmuir.*1993, 9, 1232-1240
11. Mathauer, K.; Frank, C.W. *Langmuir.*1993, 9, 3446-3451
12. Offord, D.A.; Griffin, J.H. *Langmuir.*1993, 9, 3015-3025
13. McGovern, M.E.; Kallury, K.M.R.; Thompson, M. *Langmuir.*1994, 10, 3607-3614
14. Tripp, C.P.; Veregin, R.P.N.; Hair, M.L. *Langmuir.*1994, 9, 3518-3522
15. Tada, H.; Nagayama, H. *Langmuir.*1994, 10, 1472-1476
16. Iler, R.K. *Colloid Chemistry of Silica and Silicates*, Cornell University Press, Ithaca, New York, 1955
17. Fowkes, F.M.;Burgess, T.E. *Clean Surfaces*, G.Goldfinger Ed, Symp.N.Carolina State Uni., Dekker, New York, 1970
18. De Boer, J.H.;Vleeskens, J.M. *K.Ned.Akad.Wet Proc.Ser B.* 1957, 60, 23, 45, 54;1958, 61, 2, 85

19. McFarlan, A.J. *J.Phys.Chem.* **1992**, *96*, 1395-1400
20. Shapiro, I.; Weiss, H.G. *J.Phys.Chem.* **1953**, *57*, 219
21. Lowen, W.K.; Broge, E.C. *J.Phys.Chem.* **1961**, *65*, 16
22. Davydov, V.Ya.; Kiselev, A.V.; Zhuralev, L.T. *Trans.Faraday Soc.* **1964**, *60*, 2254
23. Yoshinaga, K.; Rikitake, M.; Kito, T.; Yamamoto, Y.; Eguchi, H.; Komatsu, M. *Chem. Letters.* **1991**, *7*, 1129-1132
24. Fripiat, J.J.; Utteryloeven, J. *J.Phys.Chem.* **1962**, *66*, 800
25. Morimoto, T.; Naono, H. *Bull. Chem. Soc.Jap.* **1973**, *46*, 2000
26. Lange, K.R. *J.Colloid.Sci.* **1965**, *20*, 231
27. Armistead, C.G.; Tyler, A.J.; Hambleton, F.H.; Mitchell, S.A.; Hockey, J.A. *J.Phys.Chem.* **1969**, *73*, 3947
28. Rochow, E.G. *Chemistry of Silicon*, J.Wiley and sons, New York, **1947**
29. Stoneham, A.M. *Philisophical Magazine B.* **1987**, *55*, 201
30. Yamana, M. *J.Electrochem.Soc.* **1985** *137(2)*, 482, 1985
31. Di Maria, D.J.; Dong, D.W.; Kucza, J.A. *J.Appl.Phys.* **1980**, *51(7)*, 3860-3862
32. Cox, J.N.; Rastogi, R. *Mat.Res.Soc.Symp.Proc.* **1988**, *105*, 157-163
33. Ourmazd, A.; Bevk, J. *Mat.Res.Soc.Symp.Proc.* **1988**, *105*, 1-9
34. Bean, K.E. *IEEE Trans. on Electron Devices.* **1978**, *25(10)*, 1185-1193
35. Kern, W. *J.Electrochem.Soc.* **1990**, *137(6)*, 1887-1891
36. Silberzan, P. *Langmuir.* **1991**, *7*, 1647
37. Tripp, C.P.; Hair, M.L. *Langmuir.* **1992**, *8*, 1120-1126
38. Kallury, K.M.R.; Thompson, M.; Tripp, C.P.; Hair, M.L. *Langmuir.* **1992**, *8*, 947-954
39. Wasserman, S.R.; Tao, Y.-T.; Whitesides, G.M. *Langmuir.* **1989**, *5*, 1074-1087

40. Tripp, C.P.; Hair, M.L. *Langmuir*. **1991**, *8*, 1961-1967
41. Cohen, S.R.; Naaman, R.; Sagiv, J. *J.Phys.Chem.* **1986**, *90*, 3054-3056
42. Sagiv, J. *J.Am.Chem.Soc.* **1980**, *102*, 92
43. Kiselev, A.V.; Lisichkin, G.V.; Nikilin, Y.S. *Russ.J.Phys.Chem.* **1983**, *57*, 1113
44. Brzoska, J.B.; Azouz, I.B.; Rondelez, F. *Langmuir*.**1994**, *10*, 4367-4373
45. Geer, R.; Stenger, D.A.; Chen, M.S.; Calvert, J.M.; Shashidhar, R. *Langmuir*. **1994**, *10*, 1171-1176
46. Lindner, E.; Arias, E. *Langmuir*.**1992**, *8*, 1195-1198
47. Wasserman, S.R.; Whitesides, G.M.; Tidswell, I.M.; Ocko, B.M.; Pershan, P.S.; Axe, J.D. *J.Am.Chem.Soc.* **1989**, *111*, 5852-5861
48. Yoshino, N.; Yamamoto, Y.; Seto, T.; Tominaga, S.-I.; Kawase, T. *Bull.Chem.Soc.Jpn.* **1993**, *66*, 472-476
49. Chaudhury, M.K.; Owen, M.J. *Langmuir*.**1993**, *9*, 29-31
50. Ito, K.; Ariyoshi, Y.; Tarabiki, T.; Surahara, H. *Anal.Chem.* **1991**, *63*, 273-276
51. Parikh, A.N.; Allara, D.L.; Azouz, I.B.; Rondelez, F. *J.Phys.Chem.* **1994**, *98*, 7577-7590
52. Silberzan, P.; Léger, L.; Benattar, J.J. *Langmuir*.**1991**, *7*, 1647-1651
53. Tidswell, I.M.; Ocko, B.M.; Pershan, P.S. *Physical Review B*. **1990**, *41*, 1111-1128
54. Snyder, R.G. *J.Chem.Phys.* **1981**, *76(10)*, 5341-5346
55. Wunder, S.L.; Merajver, S.D. *J.Chem.Phys.* **1981**, *74(10)*, 5341-5346
56. Galbiati, E.; Zerbi, G. *J.Chem.Phys.* **1987**, *87(6)*, 3653-3659
57. Fujii, M.; Sugisawa, S.; Fukada, K.; Kato, T.; Shirakawa, T.; Seimiya, T. *Langmuir*.**1994**, *10*, 984-987
58. Rabinovich, Y.-I.; Yoon, R.-H. *Langmuir*.**1994**, *10*, 1903-1909

59. Flinn, D.H.; Guzonas, D.A.; Yoon, R.-H. *Colloids and Surfaces.A.* **1994**, *87*, 163-176
60. Bierbaum, K.; Grunze, M. *The Adhesion Soc.* **1994**, 213-216
61. Siedlecki, C.A.; Eppell, S.J.; Marchant, R.E. *J.Biomed.Mat.Res.* **1994**, *28*, 971-980
62. Bierbaum, K.; Grunze, M.; Baski, A.A.; Chi, L.F.; Schepp, W.; Fuchs, H. *Langmuir.* **1995**, *11*, 2143-2150.
63. Nakagawa, T.; Ogawa, K. *Langmuir.***1994**, *10*, 525-529
64. Okusa, H.; Kurihara, K.; Kunitake, T. *Langmuir.***1994**, *10*, 8-12
65. Kessel, C.R.; Granick, S. *Langmuir.* **1991**, *7*, 532-538
66. Schwartz, D.K.; Steinberg, S.; Israelachvili, J.; Zasadzinski, J.A.N. *Phys.Rev.Letts.* **1992**, *69*, 3354-3357.
67. Lin, F.; Meir, D.J. *Langmuir.* **1994**, *10*, 367-370
68. Liu, G.-Y.; Salmerson, M.B. *Langmuir.***1994**, *10*, 367-370
69. Alves, C.A.; Porter, M.D. *Langmuir.***1993**, *9*, 3507-3512
70. Pan, J.; Tao, N.; Lindsay, S.M. *Langmuir.***1993**, *9*, 1556-1560
71. Peltonen, J.P.K.; He, P.; Rosenholm, J.B. *J.Am.Chem.Soc.* **1992**, *114*, 7637-7642
72. Weisenhorn, A.L.; Römer, D.U.; Lorenzi, G.P. *Langmuir.***1992**, *8*, 3145-3149
73. Weisenhorn, A.L.; Egger, M.; Ohnesorge, F.; Gould, S.A.; Heyn, S.-P.; Hansma, H.G.; Sinsheimer, R.L.; Gaub, H.E.; Hansma, P.K. *Langmuir.***1991**, *7*, 8-12
74. Meyer, E.; Howlad, L.; Overney, R.M.; Heinzelmann, H.; Frommer, J.; Güntherodt, H.-J.; Wagner, T.; Scheir, H.; Roth, S. *Nature.* **1991**, *349*, 398-400
75. Snétivy, D.; Vansco, G.J. *Langmuir.* **1993**, *9*, 2253-2254
76. Goss, C.A.; Brumfield, J.C.; Irene, E.A.; Murray, R.W. *Langmuir.* **1993**, *9*, 2986-2994

77. Gould, S.; Marti, O.; Drake, B.; Hellemans, L.; Bracker, C.E.; Hansma, P.K.; Keder, N.L.; Eddy, M.M.; Stucky, G.D. *Nature*. **1988**, *332*, 332-334
78. Ishida, H.; Koenig, J.L. *Appl.Spectrosc.* **1978**, *32(5)*, 462-469
79. Van Blaadenen, A.; Vrij, A.; *J.Colloid.Int.Sci.* **1993**, *156(1)*, 1-18
80. Pluddemann; E.P. *Silane Coupling Agents*, second edition, Plenum Press, New York, **1991**
81. Vandenberg, E.T.; Bertilsson, L.; Liedberg, B.; Uvdal, K.; Erlandson, R.; Elwing, H.; Lundström, I. *J.Colloid.Int.Sci.* **1991**, *147(1)*, 103-118
82. Kern, W.; Puotinen; D.A. *RCA Review*. **1970** 187
83. Boerio, F.J.; Armogan, L.; Cheng S.Y. *J.Colloid.Int.Sci.* **1980**, *73(2)*, 416-424
84. Ishida, H.; Koenig J.L. *Polymer*. **1982**, *23*, 251-257
85. Koenig, J.L.; Culler, S.R.; Naviroj, S.; Ishida, H. *J.Colloid.Int.Sci.* **1983**, *96(1)*, 69
86. Shih, P.T.K.; Koenig, J.L. *Mat.Sci.Engineering*. **1975**, *20*, 144-154
87. Koenig, J.L.; Culler, S.R.; Naviroj, S.; Ishida, H. *J.Colloid.Int.Sci.* **1984**, *97(2)*, 308-317
88. Shih, P.T.K.; Koenig, J.L. *Mat.Sci.Engineering*. **1975**, *20*, 137-143
89. Koenig, J.L.; Culler, S.R.; Ishida, H. *J.Colloid.Int.Sci.* **1986**, *109(1)*, 1-10
90. Gnanasekaran, R.; Dang, T.A. *Chemically Modified Surfaces*. **1992**, *4*, 89-103
91. Domingue, A.; Piyakis, K.; Sacher, E.; Di Renzo, M.; Dénomée, S.; Ellis, T.H. *J.Adhesion*. **1993**, *40*, 151-162
92. Boerio, F.J.; Gosselin, C.A. *Polym.Characterisation*. **1983**, *31*,
93. Boerio, F.J. *Adv.Chem.Ser.* **1983**, *203*, 541-558
94. Furukawa, T.; Eib, N.K.; Mittal, K.L.; Anderson, Jr.H.R. *J.Colloid.Int.Sci.* **1983** *96(2)*, 322-337

95. Britcher, L.G.; Kehoe, D.C.; Matisons, J.G.; St.C.Smart, R.; Swincer, A.G. *Langmuir*. **1993**, *9*(7), 1609-1613
96. Sheedhara Murthy, R.S.; Blitz, J.P.; Leyden, D.E. *Anal. Chem.* **1986**, *58*, 3167-3172
97. Hook, D.J.; Vargo, T.G.; Gardella, Jr.J.A.; Litwiler, K.S.; Bright, F.V. *Langmuir*. **1991**, *7*, 142-151
98. Urban, M.W.; Koenig, J.L. *Appl.Spectrosc.* **1986**, *40*(4), 513-519
99. Xue, G.; Liu, S-Y.; Jin, Y.; Jiang, S-G. *Appl.Spectrosc.* **1987**, *41*(7), 1172- 1175
100. Vågberg, L.; de Potocki, P.; Stenius, P. *Appl.Spectrosc.* **1989**, *43*(7), 1240-1248
101. Porro, T.J.; Pattacini, S.C. *Appl.Spectrosc.* **1990**, *44*(7), 1170-1175
102. Culler, S.R.; Ishida, H.; Koenig, J.L. *Appl.Spectrosc.* **1984**, *38*1, 1-7
103. Chiang, C-H.; Koenig; J.L. *J.Colloid.Int.Sci.* **1981**, *83*(2), 361-369
104. Miller, J.D.; Ishida, H. *Langmuir*. **1986**, *2*, 127-131
105. McKenzie, M.T.; Culler, S.R.; Koenig, J.L. *Appl.Spectrosc.* **1984**, *38*(6), 786-790
106. Vrancken, K.C.; Van Der Voort, P ; Gillis-D'Hamers, I.; Vansant, E.F.; Grobet, P. *J.Chem.Soc.Faraday Trans*, **1992**, *88*(21), 3197-3200
107. Ishida, H.; Koenig, J.L. *J.Polym.Sci.:Polym.Phys.Edition.* **1979**, *17*, 1807-1813
108. Ishida, H.; Koenig, J.L. *J.Colloid.Int.Sci.* **1978**, *64*(3), 565-577
109. Kurth, D.G.; Bain, T. *Langmuir*. **1993**, *9*, 2965-2973
110. Krysztafkiewicz, A.; Rager, B. *Colloid and Polymer Sci.* **1988**, *266*(6), 484-493
111. Margalit, E.; Dodiuk, H.; Kosower, E.M.; Katzir, A. *SPIE Infrared Fiber Optics*. **1989**, *1048*, 145-152
112. Boerio, F.J.; Cheng, S.Y. *J.Colloid.Int.Sci.* **1979**, *68*(2), 252-259

113. Ishida, H.; Naviroj, S.; Tripathy, S.K.; Fitzgerald, J.T.; Koenig, J.L. *J.Polym.Sci.* **1982**, *20*, 701-718
114. Bascom, W.D. *Macromolecules.* **1972**, *5*, 792-798
115. Chiang, C-H.; Ishida, H.; Koenig, J.L. *J.Colloid.Int.Sci.* **1980**, *74(2)*, 396-404
116. Ishida, H.; Koenig, J.L. *J.Colloid.Int.Sci.* **1978**, *64(3)*, 555-563
117. Weigel, Ch.; Keller, R. *Fresenius Z.Anal.Chem.* **1989**, *335*, 663-668
118. Sheedhara Murthy, R.S.; Leyden, D.E. *Anal.Chem.* **1986**, *58*, 1228-1233
119. Koenig, J.L.; Shih, P.T.K. *J.Colloid.Int.Sci.* **1971**, *36(2)*, 247-253
120. Davis, C.A.; Graves, P.R.; Healy, P.C.; Myhra, S. *Appl.Surf.Sci.* **1993**, *72*, 419-426
121. Pluddemann, E.P. *J.Adhesion Tech.* **1991**, *5(4)*, 261-278
122. In honour of the 75th birthday of E.P.Pluddemann, Part3; *J.Adhesion Tech.* **1991**, *5(10)*, 771-946
123. Pluddemann, E.P. *Mod.Plastics.* **1962**, 135
124. Hearn, M.S.; Baird, J.D.; Nethsinghe, L.P.; Gilbert, M. *Polym. Comm.* **1990**, *31*, 194-197
125. Kelnar, I.; Schatz, M. *J.Appl.Polym.Sci.* **1993**, *48*, 669-676
126. Beckmann et al. *Method of Manufacturing Laminated Safety Glass.* U.S.Patent 4,277,538
127. Kelnar, I.; Schatz, M. *J.Appl.Polymer.Sci.* **1993**, *48*, 657-668
128. McNeill, I.C.; Basan, S. *Polym.Degradation and Stability.* **1993**, *39*, 139-144
129. Chiang, C-H.; Koenig, J.L. *Polym.Compos.* **1981**, *2(4)*, 192
130. Potts, W.J, Jr. *Chemical Infrared Spectroscopy.* J.Wiley and sons, New York, **1963**
131. Kiselev, A.V.; Lygin, V.I. *Infrared Spectra of Compunds.* J.Wiley, New York, **1975**

132. Hair, M.L. *Infrared Spectroscopy in Surface Chemistry*. Marcel Dekker, New York, 1967
133. Bellamy, L.J. *The Infrared Spectra of Complex Molecules*. Vol I and II. Chapman and Hall, London, 1975
134. Steele, D.; Yarwood, J. *Spectroscopy and Relaxation of Molecular Liquids*. Elsevier, Oxford, 1991
135. MacKenzie, M.W. *Advances in Applied Fourier Transform Infrared Spectroscopy*. J.Wiley and sons, Chichester, 1988
136. Chamberlain, J. *The Principles of Interferometric Spectroscopy*. Wiley-Interscience, 1978
137. Griffiths, P.R.; de Haseth, J.A. *Fourier Transform Infrared Spectroscopy*. Vol 83. J.Wiley and sons, 1986
138. Ferraro, J.R.; Basile, L.J. *Fourier Transform Infrared Applications to Chemical Systems*. 1-4. Academic Press. Inc, 1985
- 138a Bell, R.J.; *Introductory Fourier Transform Spectroscopy*. Academic Press, 1972
139. Newton, I. *Optiks II*. Book 8. 1817, 97
140. Harrick, N.J. *Phys.Rev.Letts*. 1960, 4(5), 224
141. Harrick, N.J. *J.Phys.Chem*. 1960, 64, 1110
142. Fahrenfort, J. *Spectrochimacta*. 1962, 698
143. Harrick, N.J. *Internal Reflection Spectroscopy*. Harrick Scientific Corp, New York, 1967
144. Muller, G.; Abraham, K.; Schaldach, M. *Appl. Opt.* 1981, 20(7), 1182
- 144a. Sperline, R.P.; Song, Y.; Freiser, H. *Langmuir*. 1992, 8(9), 2183 - 2191
- 144b. Crokek, D.M.; Bohn, P.W. *J.Phys.Chem*. 1990, 94(16), 6452 - 6457
145. Song, Y.P. *Electromagnetic Wave Considerations for FTIR and Waveguiding Raman Spectroscopy*. 1992, (unpublished).
146. Tompkins, H.G. *Appl.Spectroscopy*. 1974, 28, 335

147. Ohta, K.; Iwamoto, R. *Analytical Chemistry*. **1985**, *57*, 2491
148. Sperline, R.P.; Muralidharan, S.; Freiser, H. *Langmuir*. **1987**, *3*, 198
149. Nunn, S.N. *FTIR and Rheological Studies of Surfactant Adsorption onto Silica*. PhD Thesis, **1993**, Appendices A-C.
150. Gardiner, D.J.; Graver, R.R. *Practical Raman Spectroscopy*. Springer-Verlag, Berlin, **1989**
151. Garetz, B.A.; Lombardi, J.R. *Advances in Laser Spectroscopy*. Vol 3. J.Wiley and sons, New York, **1986**
152. Clark, R.J.H.; Hester, R.E. *Spectroscopy of Surfaces. Advances in Spectroscopy*. Vol 10. J.Wiley and sons, New York, **1988**
153. Hirschfield, T. *J.Opt.Soc.Am.* **1973**, *63*, 476
154. Williams, K.P.J.; Pitt, G.D.; Batchelder, D.N.; Kip, B.J. *RTS/AN/O12, (Application note)*. Issue 1, **1993**
155. Rugar, D.; Hansma, P. *Physics Today*. **1990**, *Oct*, 23-30
156. Tersoff, J.; Lang, N.D. *Methods of Experimental Physics*. Vol 27, chapter 1. Academic Press. Inc, **1993**
157. Binnig, G. *Ultramicroscopy*. **1992**, *42-44*, 7-15
158. Hamsma, P.K.; Elings, V.B.; Marti, O.; Bracker, C.E. *Science*. **1988**, *242*, 209-216
159. Dagnall, M.A. *Exploring Surface Texture*. Rank Taylor Hobson Ltd, Leceister, **1980**
160. Thompson, W.R.; Pemberton, J.E. *Langmuir*. **1995**, *11*, 1720-1725

CONFERENCES ATTENDED.

1. SCI: Second UK Colloid and Surface Science Student Meeting
University of Nottingham
18-21 April 1993

2. Spectra Tech Inc.: Fourth European Seminar on FT-IR Microscopy and
its Applications: "FT Microscopy- 10 Years On"
Manchester Airport
13 October 1993

3. Infrared and Raman Discussion Group: Martin and Willis Prize
Meeting
University of Nottingham
12 April 1994

Talk presented: "Determination of the Ordering of Alkylhalogenosilanes
on a Silicon Substrate using FTIR-ATR Spectroscopy", (Awarded joint
second prize)

4. The Institute of Materials Ceramic Industry Division: Convention 1994
University of York
13 April 1994

5. Faraday Discussion 98: Polymers at Surfaces and Interfaces
University of Bristol
12-14 September 1994

6. Infrared and Raman Discussion Group: 143rd Meeting
Renishaw plc
12 October 1994

7. MSG/MAG/IRDG: Imaging /Mapping using Vibrational Spectroscopy-
Microscopy
St.Catherine's College Oxford University
7 June 1995

8. LB7: The Seventh International Conference on Organized Molecular
Films
Numana (Ancona) Italy
10-15 September 1995

Poster presented: "FTIR and AFM Studies of the Adsorption of Silane
Surfactants onto Float Glass"

PAPERS PUBLISHED.

1. "Determination of the Ordering of Alkylhalogenosilanes on a Silicon Substrate using FTIR-ATR Spectroscopy"
Langmuir, 1995, 11, 618-622
Reena Banga, Jack Yarwood, Anthony M Morgan

2. "FTIR and AFM Studies of the Kinetics and Self-Assembly of Alkyl- and Perfluoroalkyl- Trichlorosilanes onto Glass and Silicon"
Langmuir, 1995, 11, 4393
Reena Banga, Jack Yarwood, Anthony M Morgan, Brian Evans, Jaqueline Kells

3. "*In Situ* FTIR Studies of the Kinetics and Self-Assembly of Alkyl- and Perfluoroalkyl- Trichlorosilanes on Silicon"
Thin Solid Films, 1995, Submitted
Reena Banga, Jack Yarwood, Anthony M Morgan, Brian Evans, Jaqueline Kells

4. "Molecular Mapping Using Confocal Raman Microscopy"
J.Raman Spectrosc, *To be submitted*
Russell Evans, Thomas Kasteleiner, Reena Banga, Sohail Hajatdoost, Jack Yarwood